# Long-term consequences of the redistribution of heat producing elements within the continental crust: Australian examples

**Sandra N. McLaren, B.Sc (Hons)**

Department of Geology and Geophysics
Adelaide University

This thesis is submitted in fulfilment of the
requirements for the degree of Doctor of Philosophy
in the Faculty of Science, Adelaide University

January 2001


ADELAIDE
UNIVERSITY
AUSTRALIA

# Table of Contents

## Part II - Anomalous heat source distributions: Geological consequences

# List of Figures

# List of Figures, continued



# List of Tables

# Abstract

Steady-state lithospheric thermal regimes are sensitive to the heat supplied from the convective mantle and the heat generated internally by the decay of radioactive isotopes. The focus of this thesis is on the impact of change in the distribution of heat producing elements on lithospheric thermal regimes and on temperature dependent processes such as metamorphism, magmatism and deformation, with application to Proterozoic Australia.

In many regions of Australian Proterozoic crust, analysis of surface heat flow and heat production data suggests that crustal heat sources contribute around 50-70 $mWm^{-2}$ to the lithospheric thermal budget, more than twice that normally expected for crust of this age. In these Proterozoic terranes granites and granite gneisses are extraordinarily enriched in the heat producing elements with calculated heat production for these rock types averaging 4.6 $\mu Wm^{-3}$ when normalized by area of outcrop. This value is almost twice that of the average granite and is even more extraordinary given that the total area of outcropping granite on which it is based is in excess of 100 000 $km^2$. This heat production appears to be strongly differentiated and concentrated in the upper 10 kilometres of the crust. This distribution is clearly a consequence of the processes that have shaped these regions of crust, such as deformation and magmatism, motivating an analysis of the time evolution of the distribution. Because lithospheric thermal regimes are sensitive to the presence and distribution of the heat producing elements, it is appropriate to ask (1) how these heat sources have impacted on the thermal, and hence tectonic history of these terranes through time, and (2) how the anomalous heat source distribution has been modified by these processes.

A simple parameterization which describes the distribution of heat sources using just two variables: $q_c$, the total contribution from crustal sources, and $h$, the length scale over which those heat sources are distributed, allows the thermal and mechanical effects of the presence and redistribution of crustal heat sources to be evaluated, and illustrated simply on the cartesian plane. Because this parameterization makes no assumption about the analytical form of the heat source distribution, it is ideal for investigating the long-term evolution of crustal heat sources through time as a consequence of various tectonic processes. The analysis presented in this thesis shows that the high concentrations of radiogenic heat sources present in many Australian Proterozoic terranes constitute an important, but previously unrecognized, source of thermal energy. Steady-state lithospheric thermal regimes and total lithospheric strength are highly sensitive to the presence of such high concentrations of heat sources and, importantly, to the way in which they are distributed. If heat source distributions are undifferentiated, and characterized by high values of $h$, significant thermal weakening results. For example, for a value of $q_c$ of 50 $mWm^{-2}$, increasing the heat production length scale from 6 km to 12 km results in an increase in lower crustal temperatures of more than 100°C (for typical thermal conductivities) and a decrease in effective strength by a factor of two to three.

The observation that the thermal and mechanical state of a high $q_c$ lithosphere is particularly sensitive to changes in the depth of the heat production has implications for thermal processes occurring on the scale of individual terranes. For example, the burial of granites enriched in the heat producing elements beneath an insulating sedimentary cover increases the heat production

length scale and allows high geothermal gradients to be sustained in the upper crust, while at the same time limiting lower crustal melting. This observation contributes to current debate on the origins of high temperature-low pressure metamorphism, and seems appropriate to metamorphism in the Palaeo-Mesoproterozoic Mount Isa inlier. In this case, the burial of the high heat producing Sybella batholith beneath the Isa Superbasin is capable of generating steep upper crustal thermal gradients immediately prior to the ~ 1530 Ma Isan orogeny. These gradients are appropriate to the observed peak metamorphic conditions (600°C and 3-4 kbar), such that the Isan orogeny required no significant additional heat input. This model helps to account for the otherwise anomalous ~ 130 Ma delay between intrusion of the Sybella Batholith and metamorphism of the surrounding rocks, the absence of lower crustal syn-metamorphic magmatism and also the curious observation that metamorphism followed an extended phase of post-rift thermal subsidence. This result is significant as it may provide a mechanism for understanding the origins of high-temperature metamorphism in other terranes where conventional paradigms, such as the advection of heat from depth during magma emplacement, are not appropriate.

The sensitivity of the crust to the distribution of heat sources also has implications for crustal evolution on much longer time scales. Given that the primary crustal processes of magmatism, extensional and shortening deformation effect the redistribution of these heat sources they also impact on steady state thermal regimes and lithospheric strength, and hence the propensity of that crust to localize future tectonic activity. Because these primary tectonic processes are themselves sensitive to lithospheric thermal regimes and, therefore, the distribution of crustal heat sources, an important feedback system exists. This feedback has impacted profoundly on the long-term evolution of the crust in Australian Proterozoic terranes.

Both models and case examples show that the long-term history of these terranes reflects the progressive concentration of heat sources into the upper crust, largely through magmatism, but also through the coupling of deformation and surface processes. The trend to decreasing both $h$ and $q_c$ leads to long-term deep crustal cooling, an increase in total lithospheric strength and eventually to effective cratonization. The long-term cooling and strengthening trend is locally countered by the role of subsidence during basin formation which, through burial of heat producing elements in the existing crust and the accumulation of more heat production in insulating sediments, may help to localise subsequent deformation. Until $q_c$ and $h$ have been reduced sufficiently to minimize the thermal and mechanical impacts of those heat sources, the crust will remain susceptible to applied tectonic loads. This aspect of the feedback system provides a means for understanding long histories of tectonic reactivation and the timing of effective cratonization, particularly in intraplate settings. It also provides insight into the origin of the modern heat source distribution. This model is appropriate for both the Mount Isa and Mount Painter inliers and provides a novel insight into the long-term behaviour of the crust.

# Declaration

This thesis contains no material which has been accepted for the award of any other degree or diploma in any university and, to the best of my knowledge and belief, contains no material previously published or written by any other person, except where due reference has been made in the text.

I give my consent for this copy of my thesis, when deposited in the University Library, being available for loan and photocopying.

.....
Sandra N. McLaren

# Acknowledgments

To Mum, Dad and craig! for being the best family I could hope for. Thankyou very very much for all your encouragement, support, love and concern.

To Mike Sandiford for overseeing the evolution of this project. Thankyou for your inspiration, guidance and patience, and for your countless attempts to try to teach me about 'the problem'. Thankyou for so many opportunities over the past few years. I am also grateful to Martin Hand who provided assistance in this last year.

I am indebted to Ian McDougall and Jim Dunlap for taking me on from a standing start and teaching me so much about argon thermochronology in a relatively short time. Thankyou both for your generosity and concern, and for sharing some of your knowledge and experience with me. Jim, thankyou for being so patient with me, and I hope that the future is everything you want it to be. To all the other members of the Noble Gas Group, Robyn, Xiaodong, Igor, Dave, Eleanor, John and Shane, I am grateful for all your support, assistance and good humour throughout my time at RSES.

Thanks to Lesley Wyborn and Irina Bastrakova of the Australian Geological Survey Organization who generously provided access to and assistance with the Proterozoic granites GIS. Thanks also to Deb Scott, Peter Southgate and others in the North Australian Basins Resource Evaluation group at the Australian Geological Survey Organization for many helpful discussions on the evolution of Isa Superbasin.

I am grateful to Mike Williams, Karl Karlstrom, Nick Oliver and Pete Betts for their reviews of work which now forms part of this thesis. I am also grateful to the Sprigg Family for access to Arkaroola, and to the many friendly landholders and townsfolk who made my time in Mount Isa much easier.

A big thankyou to all members of the Department of Geology and Geophysics, past and present. In particular I am grateful to the admin and technical staff, Yvonne, Gerald, Mary, Kim, Soph, Wayne, Sherry and John, for their prompt assistance and for making the Department a friendly place to work.

To friends past and present. To all those who have helped me stay (almost) sane over the past few years and to those who shared many Friday lunches and Friday nights. Many grateful thanks to Narelle Neumann for sharing an office with me, for many great times (and adventures) in the field, for answering my annoying geochemistry questions, and for being there in the good and bad times - 'good luck' for the next adventure! To Scott (thanks for saving the day with all my computer queries, and for listening to all my problems), Eike, Betina, John F, Karin, Kathy, Marlina, Kirsty, Jo, Miles, Rolf, Aaron, Stinger, Jerry and Trev ... and the Facit Phantom ... thankyou all for the good times, the advice and the encouragement. You have been a wonderful bunch of people to be with and I wish you all every success.

# Publications and conference abstracts

McLaren S.N., Dunlap W.J., Sandiford M. and McDougall, I. Thermochronology of high heat producing crust at Mount Painter, South Australia: Implications for tectonic reactivation of continental interiors. Submitted to *Tectonics*, December 2000.

McLaren, S.N. and Sandiford, M. (in press) Long-term thermal consequences of tectonic activity at Mount Isa, Australia: Implications for polyphase tectonism in the Proterozoic. *In*, Miller, J.A., Buick, I.S., Hand, M. and Holdsworth, R.E. (*eds.*), Continental Reworking and Reactivation, *Geological Society of London, Special Publications.*

McLaren, S.N., Sandiford, M. and Hand, M. 2000. High radiogenic heat-producing granites and metamorphism – An example from the Mount Isa Inlier, Australia: Reply to Comment by Foster, D., & Rubenach, M.J. *Geology,* 28, p. 672.

McLaren S.N., Sandiford, M., Dunlap, J. and McDougall, I. 2000. Carboniferous tectonism at Mount Painter - The Alice Springs Orogeny moves south. *In*, Skilbeck, C.G. and Hubble, T.C.T *(eds.)* Understanding Planet Earth, Searching for a sustainable future. Abstracts of the 15th Australian Geological Convention, University of Technology, Sydney. *Geological Society of Australia, Abstracts*, 59, p. 323.

McLaren, S.N., Sandiford, M. and Hand, M. 1999. High radiogenic heat-producing granites and metamorphism – An example from the Mount Isa Inlier, Australia. *Geology*, 27, p. 679-682.

McLaren, S.N., Neumann, N.L., Sandiford, M. and Wyborn L.A.I. 1999. Post-intrusion heating associated with high-heat producing Proterozoic granites — implications for mineralisation? *Australian Geological Survey Organization Research Newsletter*, 30, p. 23-26.

McLaren S.N. and Sandiford M. 1999a. Towards a new Proterozoic tectonic synthesis – an alternative view of the Proterozoic geology of Australia. *Geological Society of Australia, Abstracts*, 53, *Specialist Group in Tectonics and Structural Geology, Field Conference* (Halls Gap, Victoria), p. 153.

McLaren S.N. and Sandiford M. 1999b. Cyclicity in the Australian Proterozoic – Influences and controls. *Geological Society of Australia, Abstracts,* 54, *Specialist Group in Geochemistry, Mineralogy and Petrology, Orogenesis in the Outback Conference* (Alice Springs, Northern Territory), p. 66.

McLaren S.N., Sandiford M. and Hand M. 1998. Radiogenic heat production and high-temperature, low-pressure metamorphism in the Mount Isa Inlier, Queensland. *Geological Society of Australia, Abstracts,* 49, *Australian Geological Convention* (Townsville, Queensland), p. 305.

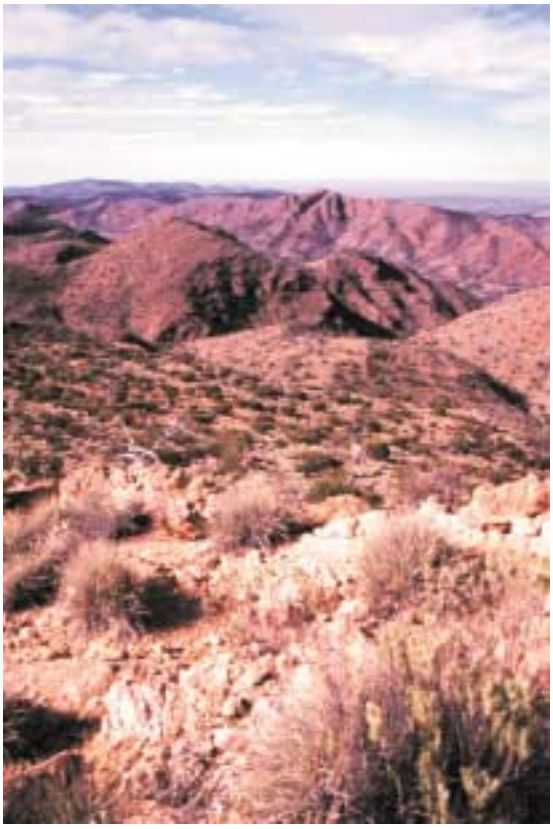

*... as he nears his destination, he discovers the great pleasure of contemplation while travelling backwards on a train. he longs to postpone his arrival and extend his dreams ...*

Great Rail Journeys, BBC Television, London to Arcadia, November, 1999

# Preamble

Understanding the controls and variations in lithospheric thermal regimes is fundamental to our knowledge of many geological processes. In the steady-state the thermal structure of the continental lithosphere is controlled by three primary variables, the heat flowing from the convective mantle, the heat produced within the lithosphere due to the decay of radiogenic isotopes, and the thermal conductivity structure. It is well understood that heat flow varies spatially as a function of lithology and tectonic setting and also temporally, although on very long time scales, as both the primordial heat from the formation of the Earth and the heat released from radiogenic decay have gradually declined through time. However, it is not so well understood that tectonic processes modify heat production distributions and therefore impact on the thermal structure of the crust on timescales of ~ 10-100 Ma.

The steady-state lithospheric thermal regime may be modified locally by transient effects including the advection of heat during magma emplacement, the flow of aqueous fluids, mantle plume activity, convective thinning of the mantle lithosphere and changes in lithospheric thermal regimes due to plate tectonic processes, such as continent-continent collision. Such transient phenomena are thought to be the primary source of thermal perturbations leading to many tectonic processes, including the localization of intraplate deformation (e.g., Neil and Houseman, 1999), the generation of crustal melts (e.g., England and Thompson, 1986; Koyaguchi and Kaneko, 1999) and the generation of high temperature-low pressure metamorphic belts (e.g., Wickham and Oxburgh, 1985; De Yoreo et al., 1991; Sandiford and Powell, 1991).

Although such models are widely accepted and are appropriate in a large number of cases, it has become increasingly clear that the long-term behaviour of the lithosphere must also be sensitive to the steady-state controls on thermal regime. In particular, as shown by England and Thompson (1984), thermal regimes will be sensitive to that heat produced by radiogenic decay, which in normal thickness crust contributes around half the observed surface heat flow (e.g., McLennan and Taylor, 1996). Since heat sources contribute to lithospheric thermal regimes in the long-term, they must impact on the strength of that lithosphere. Although this has been known for some time, the importance and implications of steady state heat sources and the way in which they impact on the long-term behaviour and evolution of the crust, have yet to be fully investigated. Indeed, as noted by Oxburgh in 1980, the "… problem of crustal heat production and its distribution and re-distribution by physical and chemical processes during crustal evolution is of fundamental importance, and is at present little understood."

Although more than 20 years have passed since Oxburgh's work, the problem of the redistribution of heat producing elements has received relatively little attention. This is due in part to the number of tectonic processes that can apparently be understood in terms of transient thermal pulses related to changing orogenic boundary conditions, and also because crustal heat generation rates are normally considered to be too low to promote heating. For average continental crust, radiogenic heat sources contribute 30 $mWm^{-2}$ to the observed surface heat flow (e.g., McLennan and Taylor, 1996). Much of this heat production resides within granites and granite gneisses which contain on average 3.9 ppm of Uranium, 16.0 ppm Thorium and 3.6 weight percent Potassium (e.g., Haenel et al., 1988; Fowler, 1990), giving an average heat production of 2.5 $\mu Wm^{-3}$. Other lithotypes

have heat production rates typically in the range 0-1 $\mu Wm^{-3}$, with the exception of shales which average 2.1 $\mu Wm^{-3}$. In recent times however, the effects of mild enrichments in crustal heat production on lithospheric thermal regimes have begun to be addressed. Critical to the development of this work was the observation by Chamberlain and Sonder (1990) that, when coupled with crustal thickening and a normal mantle heat flow, mild enrichments in crustal heat production (to a median value of 3.5 $\mu Wm^{-3}$) could provide sufficient thermal energy to drive mid crustal anatexis. Lathrop et al. (1994) applied this model to the rocks of the Acadian Appalachians and suggested that syntectonic monzonites of the New Hampshire Plutonic Series were the products of midcrustal partial melting due to the presence of high concentrations of heat producing elements. More recently Bea et al. (1999) suggested a similar model for the generation of Variscan batholiths in central Spain. Using two-dimensional thermal-kinematic models of collisional orogens Huerta et al. (1998, 1999) showed that mild enrichments of the heat producing elements may contribute to high temperature-low pressure metamorphic signatures and to the generation of inverted geothermal gradients. Gerdes et al. (2000) applied similar methods to a case study in the Bohemian Massif in central Europe. These workers proposed that the additional contribution of radiogenic heat in already thickened crust was consistent with the observed high temperature-low pressure metamorphic signature and that it can also account for the generation of post-collisional granites.

These studies have all been concerned with the additional contribution of only mild enrichments of the heat producing elements to thermal regimes in already thickened crust. Rocks in many Australian Proterozoic terranes however, are extraordinarily enriched in the heat producing elements, with internal heat sources contributing at least 50-70 $mWm^{-2}$ to the observed surface heat flow (e.g., Sandiford and Hand, 1998a). This value is more than twice that expected of the average continental crust and is highly anomalous when compared to equivalently aged terranes elsewhere in the world. Such concentrations of radiogenic heat sources constitute an important but previously unrecognized source of thermal energy, and it is appropriate to ask how such anomalous concentrations of heat sources have impacted on the thermal, and hence tectonic history of these terranes. Accordingly, the aims of this thesis are, (1) to evaluate the long-term thermal, mechanical and geological effects of the redistribution of anomalous concentrations of heat sources; and (2) to examine these effects through time and in a variety of tectonic settings. I do this from both a theoretical perspective, using simple physical models of crustal processes, and also by investigating several case examples.

Given that lithospheric thermal regimes and the mechanical state of the crust are sensitive to the presence and distribution of internal heat sources, the way in which heat sources are redistributed during tectonic processes may impact on the long-term stability of that crust. Consequently, the analysis presented here may bear on a number of general questions regarding the long-term evolution of the continental lithosphere. In particular:

- The controls on long-term reactivation of the continental crust, and
- The processes controlling the timing of effective cratonization and the origins of stable cratons.

On the scale of individual terranes it is also important to evaluate:

- The effects of the burial of high concentrations of heat sources within the upper crust, and
- The possible contribution of steady state heat sources to high temperature metamorphism.

## Thesis Outline

This thesis consists of 2 parts, each containing 3 chapters. Part I of this thesis is concerned with aspects of lithospheric thermal regimes and provides much of the theoretical background for the geological examples discussed in Part II.

Chapter One is a review of current ideas on the distribution of heat sources within the lithosphere. It outlines the information obtained from primary observables, including surface heat flow measurements, surface heat production data, and obliquely exposed crustal sections. A compilation of these data leads to the development of a general model for the distribution of heat sources within the modern continental crust. This compilation suggests that lithospheric heat sources contribute around 30 $mWm^{-2}$ to the surface heat flow and that this heat production is distributed over a length scale of ~ 10 km. This chapter also defines the $h$-$q_c$ parameterization which is used to describe heat source distributions throughout the remainder of the thesis.

Chapter Two describes the Central Australian Heat Flow Province, which is characterized by anomalous surface heat flow. An evaluation of the factors which contribute to surface heat flow suggests that Proterozoic terranes within this region are characterized by anomalous heat production distributions, in which crustal sources contribute around 50-70 $mWm^{-2}$ to the lithospheric thermal budget.

Chapter Three illustrates the long-term thermal and mechanical effects of the presence and redistribution of high concentrations of the heat producing elements within the crust using simple one-dimensional models of primary tectonic processes. The $h$-$q_c$ parameterization provides a simple scheme for evaluating and illustrating these effects. This analysis shows that the thermal and mechanical state of the lithosphere is highly sensitive to the presence of anomalous heat sources and particularly to the way in which they are redistributed during tectonic activity. However, because the processes which redistribute the heat sources are themselves temperature dependent a potentially profound feedback exists between the distribution of heat producing elements and the long-term tectonothermal history of the crust.

Part II of this thesis is concerned with the geological consequences of the redistribution of anomalous heat sources, using examples from terranes within the Central Australian Heat Flow Province. Chapter Four outlines the role of the redistribution of heat sources during the long-term evolution of the Mount Isa Inlier. This terrane is characterized by more than 300 million years of episodic tectonic activity prior to effective cratonization. Primary differentiation of crust initially enriched in heat producing elements has been achieved by felsic magmatism over much of the 300 million year history. The flux of heat producing elements from lower to mid-upper crustal levels associated with this magmatism was sufficient to cause long-term lower crustal cooling of at least 200°C while the accumulation of the radiogenic intrusives in the mid-upper crust resulted in a highly stratified heat production distribution. These observations, together with the results detailed in Chapter Three, suggest that the long-term evolution of the Mount Isa region reflects the progressive concentration of heat-producing elements into the upper crust leading to a long-term increase in lithospheric strength, and eventually to effective cratonization.

Chapter Five is concerned with the role of the high heat producing Sybella Batholith during high temperature-low pressure metamorphism in the Western Mount Isa Inlier. The origins of metamorphism (~ 600°C and 3-4 kbar) in this region have been controversial because no syn-

metamorphic intrusive bodies can be recognized, high temperatures appear to have been sustained for periods > 100 Ma, and metamorphism followed an extended phase of thermal subsidence. This chapter shows that the burial of granite batholiths enriched in radiogenic elements beneath the thick insulating sedimentary succession of the Mount Isa Group is capable of generating steep upper crustal thermal gradients immediately prior to the Isan Orogeny. These gradients are appropriate to peak metamorphic conditions, such that the ensuing orogeny requires no significant additional heat input. This result is significant as it may provide a mechanism for understanding the origins of high-temperature metamorphism in other terranes where the involvement of transient heating is not obvious.

Chapter Six investigates the record of long-term tectonic reactivation in the Mount Painter province and highlights the sensitivity of the thermal and mechanical state of the crust to small changes in the depth of the heat production. The rocks at Mount Painter provide an extreme example of the role of internal heat sources as, on average, basement rocks in this terrane contain more than four times the average compliment of heat producing elements. This chapter is also concerned with the origins of the intraplate Alice Springs Orogeny which affected a large area of the Australian continental interior, including the Mount Painter Province, around 400-300 Ma. The results presented in this chapter provide evidence that thermally modulated variations in lithospheric strength may control the distribution of intraplate deformation at the continental scale.

I conclude this thesis with a summary of the implications of these results for the long-term evolution of the Australian Proterozoic crust (Chapter Seven).

Several parts of this thesis have been published in various forms. Much of Chapter Four has been accepted for publication by the Geological Society of London in a volume of the Special Publications series entitled *"Continental Reworking and Reactivation"*. Much of Chapter Five has been published in manuscript form in *Geology*. In addition, a manuscript version of Chapter Six, discussing the role of crustal heat sources in localizing intraplate deformation, has recently been submitted to *Tectonics*. I have also been involved in several related projects published in *Earth and Planetary Science Letters*, and the Special Publications series of the Geological Society of London. A list of publications and conference abstracts is included in the introductory section of this thesis, and reprints of published manuscripts are included in Appendix C.

# PART ONE

## Lithospheric heat source distributions

# Chapter One

# Heat source distributions in the continental lithosphere

Lithospheric thermal regimes are largely controlled by conductive heat loss and reflect both the heat generated internally by the decay of radioactive isotopes and the heat supplied from beneath by the convective mantle (e.g., Turcotte and Schubert, 1982; England and Thompson, 1984). On geological time scales only 3 elements, and in particular 4 isotopes, $^{238}$U, $^{235}$U, $^{232}$Th and $^{40}$K, occur in sufficient abundance to contribute to the lithospheric thermal budget. Lithospheric thermal regimes are therefore sensitive to both the total abundance and distribution of these heat sources. In order to investigate this dependence we require some method by which to assess and describe the distribution of lithospheric heat sources.

Understanding the distribution of heat sources within the earth has long been the subject of much interest and endeavour (e.g., Lambert and Heier, 1967; Shaw, 1970; Lachenbruch, 1970; Lachenbruch and Bunker, 1971; Turcotte and Oxburgh, 1972; Singh and Negi, 1980; Schneider et al., 1987; Pinet and Jaupart, 1987; Cermak and Rybach, 1989; Furlong et al., 1995; Ketcham, 1996; Verdoya et al., 1998). The distribution and abundance of crustal heat sources is constrained by a number of geological, geochemical and geophysical datasets. The primary data include surface heat flow measurements and calculated surface heat production values, particularly from obliquely exposed crustal sections. In the following section I outline the information obtained from each of these sources. A compilation of these data leads to the development of a generalized model for the distribution of heat sources within the modern continental lithosphere.

## 1.1 Global heat flow data

Regional heat flow datasets provide important insights into the nature of lithospheric thermal regimes. In the steady state in the absence of erosion, tectonic deformation and groundwater circulation, surface heat flow provides a measure of the heat conducted through the outermost part of the lithosphere. As such, surface heat flow is a function of two fundamentally different sources, namely, the heat produced from sources within the lithosphere and the heat supplied to the base of the lithosphere by processes such as convection in the deeper mantle:

$$q_s = f(q_m, q_c) \tag{1.1}$$

In Equation 1.1 $q_S$ is the surface heat flow; $q_C$, the contribution of the lithospheric sources to the surface heat flow, and $q_M$, the heat flux supplied to the base of the lithosphere from the deeper convective mantle. In general $q_C$ and $q_M$ will be complex functions of space and thus the surface heat flow at any point will represent the sum of the two components averaged over some finite spatial and temporal domain. In the special case where there is no spatial variation in $q_C$ and $q_M$, and conduction is only in the vertical direction Equation (1.1) becomes,

$$q_s = q_m + q_c$$
$$= q_m + \int_0^{z_l} H_z \, dz \qquad (1.2)$$

where $z_l$ is the lithospheric thickness and $H_z$ is the distribution of heat sources with depth, $z$. This situation represents the one-dimensional approximation and has formed the cornerstone of much of our understanding of continental heat flow.

While routine measurement of well bore temperatures had long been possible, the first measurements of surface heat flow were not achieved until 1939 when a Cambridge University group, lead by E.C. Bullard, collected both thermal gradient and thermal conductivity data from the same well bore. Between this time and the mid-1950's, techniques for measuring heat flow in the oceanic crust were also established, and individual heat flow determinations were made in South Africa (Bullard, 1939), Great Britain (Benfield, 1939), Persia (Coster, 1947) and in California (Benfield, 1947) and Colorado (Birch, 1950) in the United States. Since that time, the global heat flow database expanded rapidly, especially from the late 1950's through until the 1970's (e.g., Birch, 1954; Birch et al., 1968; Roy et al., 1968; Lachenbruch, 1968; Lachenbruch, 1970; Sass and Lachenbruch, 1979). As a result of these and other studies, excellent datasets exist for many continental regions particularly the continental United States, Western Europe and the former USSR, where much effort has been expended in the collection and interpretation of surface heat flow data. In contrast however, surface heat flow is not well known in South America, Antarctica or Australasia where relatively few heat flow data exist. For example, the current United States National Geophysical Data Centre (NGDC) database lists some 4290 heat flow records from North America, 158 records from Australia and less than 10 from Antarctica. The distribution of global heat flow measurements is shown in Figure 1.1; a summary of the number of heat flow determinations, and the mean and standard deviation of these data for selected continental regions is given in Table 1.1.

As a result of the disproportionately large amount of data collected in the continental United States and Western Europe many of our generally held perceptions about surface heat flow (e.g., Nyblade and Pollack, 1993; Morgan, 1984) are strongly biased towards these regions. Indeed, as noted by Pollack et al. (1993), "one must be cautious about making ... global inferences ... because of the uneven geographic distribution of measurements". To overcome this problem, a number of empirical estimation techniques, largely based on the age of the last tectonothermal event in a

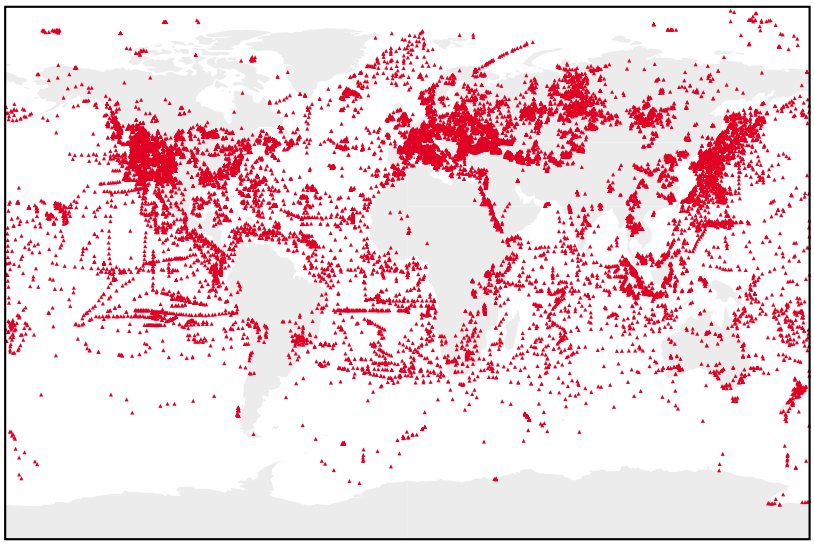

**Figure 1.1** Locations of heat flow determinations which make up the global heat flow dataset maintained by the International Heat flow commission (see also Pollack et al., 1993; *http://www.geo.lsa.umich.edu/IHFC/*). The total number of heat flow determinations is 24320. What is clear from this compilation is the paucity of data in many of the continental blocks, particularly Africa, South America, the middle east, Australia and Antarctica.

**Table 1.1** *Global heat flow data for selected regions*

| *Region* | *Number of measurements* | *Mean heat flow ($mWm^{-2}$)* | *Standard deviation* |
|---|---|---|---|
| Africa | 661 | **61** | 30 |
| Asia | 3144 | **63** | 33 |
| Australia | 158 | **67** | 26 |
| Europe | 3993 | **62** | 24 |
| Western Europe | 1412 | **76** | 26 |
| France | 650 | **81** | 26 |
| North America | 4290 | **77** | 41 |
| South America | 178 | **65** | 30 |
| former USSR | 3532 | **52** | 20 |

All data taken from United States National Geophysical Data Centre (NGDC) global heat flow database, maintained by the International Heat flow Commission, see *http://www.geo.lsa.umich.edu/IHFC/*

particular region, have been developed in order to calculate average heat flow values. This approach has proven popular (e.g., Chapman and Pollack, 1975; Chapman and Furlong, 1977; Morgan, 1984; Pollack et al., 1993), and in the remainder of this section I summarize the available heat flow dataset in terms of these global means.

The most recent compilation of global heat flow data (Pollack et al., 1993) suggests that modern continental crust is characterized by a mean heat flow of $65 \pm 1.6$ $mWm^{-2}$. Other estimates have variously placed this mean value at 61 $mWm^{-2}$ (Williams and von Herzen, 1974), 55 $mWm^{-2}$ (Davies, 1980) and 57 $mWm^{-2}$ (Sclater et al., 1980). These estimates are all significantly lower than the average heat flow of $101 \pm 2.2$ $mWm^{-2}$ through oceanic lithosphere (Pollack et al., 1993). This high oceanic heat flow reflects the bias associated with the extrusion of basaltic lava and the loss of heat through sea-floor hydrothermal systems at mid ocean ridges.

In terms of the continents, the available surface heat flow data show systematic differences with tectonic age (Table 1.2, Figure 1.2). Heat flow increases from the Archaean (41-46 $mWm^{-2}$) into the Proterozoic (49-54 $mWm^{-2}$), and again into the Phanerozoic (50-70 $mWm^{-2}$), where measurements often reflect the effects of transient thermal pulses which result from mantle upwelling or recent tectonic or magmatic activity.

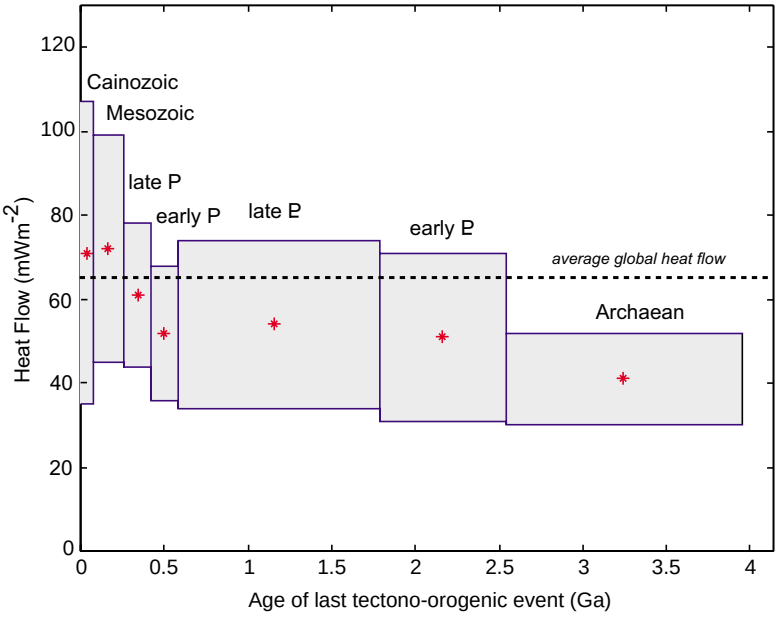


**Figure 1.2** Histogram of global continental heat flow data (e.g., from Morgan, 1984, after Chapman and Furlong, 1977). Heat flow measurements are grouped with age based on the timing of the last major tectonothermal event in the region of the measurement. Average heat flow by age is denoted by the star, boxes show regions of one standard deviation in the heat flow and the range of ages (Morgan, 1984). The number of data in each age group is given in Table 1.2. The average global heat flow value of ~ 65 $mWm^{-2}$, taken from the compilation of Pollack et al., (1993), is also shown. The high average surface heat flow reflects the large number of determinations made in regions of recent tectonic or magmatic activity.

**Table 1.2** *Average global and Australian Proterozoic heat flow data*

| *Region* | *Average heat flow ($mWm^{-2}$)* † | *Number of determinations* |
|---|---|---|
| Global Archaean | 41 ± 11 | 136 |
| Global (early) Proterozoic | 51 ± 20 | 78 |
| Global (late) Proterozoic | 54 ± 20 | 265 |
| Global (early) Palaeozoic | 52 ± 16 | 88 |
| Global (late) Palaeozoic | 61 ± 17 | 514 |
| Global Mesozoic | 72 ± 27 | 85 |
| Global Cainozoic | 71 ± 36 | 587 |
| ***GLOBAL AVERAGE*** | **60 – 65** | |
| Australian Proterozoic terranes | 82 ± 25 | 26 |

*Note:* Australian heat flow average taken from data in Cull, 1982, Houseman et al., 1989, and Gallagher, 1990. Many individual heat flow values represent the average of a number of determinations at a single locality

† Global heat flow averages taken from a compilation by Morgan, 1984 and Chapman and Furlong, 1977, with age taken as the time of the last tectonothermal event within a particular terrane.

## 1.2 The linear heat flow-heat production relation

One of the most significant results to stem from the pioneering studies into surface heat flow in the 1960's was the recognition of a linear relationship between surface heat flow and surface heat production data (Birch et al., 1968; Lachenbruch, 1968; Roy et al., 1968). Regions where this empirical relationship holds were termed "heat flow provinces", and have been studied extensively in an attempt to understand and recognize the implications of this relationship. The linear relationship was first documented in the continental United States and classic examples of such heat flow provinces include the New England region (Birch et al., 1968) and the Sierra Nevada (Lachenbruch, 1968).

The New England region of the United States has been the subject of the most detailed geothermal study, and Birch et al. (1968) show that there is a strong correlation between heat flow and local bedrock radioactivity (Figure 1.3a). Heat flow increases from 48 $mWm^{-2}$ in the Grenville aged Adirondack rocks, to 92 $mWm^{-2}$ in the Triassic Conway Granite of the White Mountain Plutonic Series. Through the same section heat productivity varies from 0.88 $\mu Wm^{-3}$ in the Precambrian rocks to 9.74 $\mu Wm^{-3}$ in the Conway Granite. After a detailed analysis of geological and topographic factors, Birch et al., (1968) concluded that the correlation was significant. In a companion study, Lachenbruch (1968) documented the variations in surface heat flow and heat production in the central Sierra Nevada, California. Here heat flow varies from 54 $mWm^{-2}$ in Cretaceous granites, to 17 $mWm^{-2}$ in Cainozoic volcanics. Heat production at the same sites varies from 3.76 $\mu Wm^{-3}$ to 0.36 $\mu Wm^{-3}$ (Figure 1.3b). Although these values are much lower than the New England region in absolute terms, the same strong linear correlation is evident.

Recognition of this linear relationship between surface heat flow and surface heat production suggests that surface heat flow, $q_S$, can be expressed in the following form:

$$q_s = q_r + h_r * H_s \tag{1.3}$$

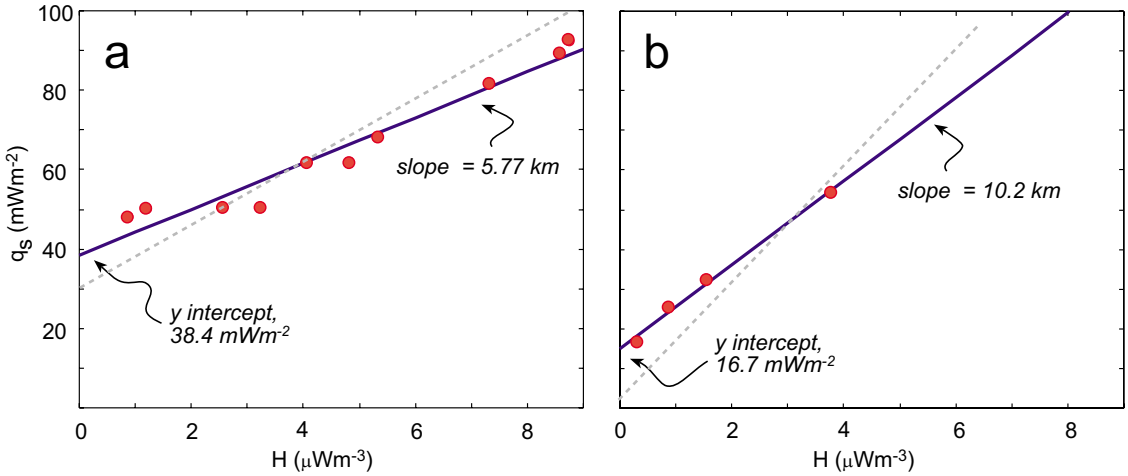


**Figure 1.3 (a)** Linear heat flow-heat production relationship for the New England, New York region of the USA. Data and figure reproduced from Birch et al., 1968. Heat flow data have been corrected for local geological factors, but not for topography. Solid line is a least squares linear regression. The parameters of the linear regression describe the parameters of the heat source distribution, where the *y*-intercept is the reduced mantle heat flow ($q_r$ ~ 38 mWm$^{-2}$) and the slope the characteristic length scale ($h_r$ ~ 5.7 km for the New England case). **(b)** Linear relationship for the Sierra Nevada region, California USA. Here the length scale of the heat source distribution is ~ 10 km while the reduced heat flow is ~ 16.7 mWm$^{-2}$. Data and figure from Lachenbruch, 1968. Where necessary data has been corrected for recent climatic and erosional effects. In each case the dashed line illustrates the general effect of lateral heat conduction on the linear heat flow-heat production relationship. Lateral heat conduction results in heat sources at depth being "averaged" over the region where heat flow is measured, and so consequently linear regression results in an underestimation of the length scale, $h_r$, and an overestimation of the reduced heat flow, $q_r$.

where $H_s$ is the surface heat production, $q_r$ is the reduced heat flow and $h_r$ the characteristic length scale for heat production in the lithosphere. For the New England case, the reduced heat flow is ~ 38 mWm$^{-2}$ and the length scale of the heat production is ~ 6 km. In the Sierra Nevada, $q_r$ ~ 17 mWm$^{-2}$ and $h_r$ ~ 10 km. The fact that $h_r$ is always much less than the crustal thickness implies that the characteristic near surface heat production cannot extend to depth throughout the crust, and that the crustal heat sources must be highly differentiated. Further implications of the linear relationship for models of crustal heat source distributions are discussed below.

The typical value for the reduced heat flow is also significant in that it allows us to place bounds on the contribution of crustal heat sources to the surface heat flow. For example, if $q_r$ is equated with the non-radiogenic component of the heat flow then it provides a measure of the value of heat flux supplied to the base of the lithosphere (i.e., $q_m$). While it is tempting to relate these equations, a number of authors including England et al., (1980), Jaupart (1983) and Vasseur and Singh (1986) have shown that the regression of surface heat production and heat flow data will necessarily overestimate the basal heat flux, and underestimate the length scale for crustal heat production (Figure 1.3a, b). This is because the lateral transfer of heat is significant in regions where there are significant lateral contrasts in heat productivity. Regions with relatively high heat production must "lose" heat by lateral conduction to the surrounding cooler regions such that the surface heat flow will underestimate the contribution of crustal and mantle sources directly beneath. Conversely, cool regions will "gain" heat by lateral conduction. Consequently, both $q_r$ and $h_r$ are dependent on the horizontal variation in heat production parameters, about which relatively little data is available, and cannot be interpreted simply in terms of 1-d (vertical) conduction in a medium subject to basal heat flow and internal heat production.

Notwithstanding these possible errors in the estimation of the parameters $h_r$ and $q_r$, a compilation of data across many heat flow provinces (Table 1.3) allows an important first-order signature to be identified. The average value of $h_r$ of 9.42 ± 3.5 km suggests that the crust is

**Table 1.3** *Compilation of estimates of the distribution parameters*

| *Terrane* | *Age of last tectonothermal event* | $q_r$ *(mWm$^{-2}$)* | $q_c$ *(mWm$^{-2}$)*‡ | $h_r$ *(km)** |
|---|---|---|---|---|
| Ukraine | Archaean | 25 | 12 | 7.1 |
| Western Australia | Archaean | 26 | 13 | 4.5 |
| Indian Shield | Archaean | 33 | 16 | 7.5 |
| Baltic | Archaean-Proterozoic | 22 | 14 | 8.5 |
| Eastern USA | Proterozoic | 33 | 24 | 7.5 |
| Central Australia | Proterozoic | 27 | 56 | 11.1 |
| Brazilian Coastal Shield | Proterozoic | 28 | 28 | 13.1 |
| Indian Shield | Proterozoic | 38 | 33 | 14.8 |
| Niger | Proterozoic | 11 | 9 | 7.5† |
| Zambia | Proterozoic | 40 | 27 | 7.5† |
| SE Appalachians | Palaeozoic | 28 | 21 | 7.2 |
| England and Wales | Palaeozoic | 23 | 36 | 16.0 |
| Indian Shield | Cenozoic-Mesozoic | 38 | 33 | 14.8 |
| Zambia | Cenozoic-Mesozoic | 40 | 27 | 7.5† |
| Basin and Range | Cenozoic | 69 | 23 | 10.0† |
| Sierra Nevada | Cenozoic | 18 | 19 | 10.1 |
| Bohemian Massif | Cenozoic | 44 | 29 | 3.8 |
| Eastern Australia | Cenozoic | 57 | 15 | 11.1 |
| | ***Average of all estimates*** | **33.3 ± 13.9** | **24.2 ± 11.2** | **9.4 ± 3.5** |
| | **Average Archaean** | 25.5 ± 0.7 | 13.7 ± 1.7 | 6.9 ± 1.7 |
| | **Average Proterozoic** | 29.5 ± 10 | 24.2 ± 9.0 | 10.1 ± 3.6 |
| | **Average Palaeozoic** | 25.5 ± 3.5 | 28.5 ± 10 | 11.6 ± 6.2 |
| | **Average Cenozoic-Mesozoic** | 44.5 ± 17 | 24.3 ± 6.6 | 9.5 ± 3.7 |

*Note:* Data from a compilation by Taylor and McLennan, 1985 (modified from Vitorello and Pollack, 1980 and Morgan, 1984). Errors in the estimation of $h_r$ are not shown, but generally lie in the range of 0.5-2.0 km (eg. Jaupart, 1983).

* estimates of the length scale of the heat production distribution have been calculated using the linear heat flow-heat production relationship; assuming this distribution is appropriate for each case, then calculated $h_r$ is also equivalent to the parameter, $h$, which we define in this contribution.

† values of length scale estimated, not calculated.

‡ values of $q_c$ are calculated assuming that $q_r$ can be equated with $q_m$, see text for discussion

differentiated with respect to the heat producing elements and that the bulk of these heat sources are concentrated in the upper crust. Further, if the average value of $q_r$ of 33.3 ± 13.9 mWm$^{-2}$ provides an upper bound on $q_m$, then the total contribution of these crustal heat sources, $q_c$, is around 30 mWm$^{-2}$ or slightly greater (Equation 1.2, Table 1.3).

Surface heat flow data can also be used in other ways to constrain the crustal contribution, $q_c$. Such methods are appropriate in cases where heat flow measurements are isolated or in regions where the paucity of heat flow and / or heat production data on the regional scale limit the potential application of the linear relationship. In such regions the lithospheric contribution can be estimated if there is additional independent (usually seismic) evidence to constrain Moho temperature (e.g., Black and Braile, 1982). This method, using terrane scale deep-seismic data (e.g., Zielhaus and Van der Hilst, 1996), has been applied to selected Australian heat flow measurements (see Chapter Two for further discussion) where the paucity of the heat flow field has hindered interpretation.

## 1.3 The distribution of crustal heat sources

As outlined in Section 1.2, surface heat flow-heat production data suggest that the lithospheric heat sources typically contribute around 30 $mWm^{-2}$ to observed continental heat flow and are concentrated in the upper crust over a length scale of ~ 10-15 km. Understanding the way in which these heat sources are distributed is important for our knowledge of the thermal structure of the crust, and may also reveal details about the processes which have controlled the redistribution of heat sources during crustal evolution.

In developing models for the distribution of crustal heat sources, it is important to recognize that the heterogeneous composition of the continental lithosphere implies that any heat source distribution will be complex and discontinuous, and broadly related to the distribution of lithotypes. A compilation of average heat productivity data for major lithotypes is given in Table 1.4. This compilation shows that by volume, the bulk of crustal heat sources are contained within felsic igneous rocks such as granites and granodiorites. These rock types have average heat production values of 2.5 $\mu Wm^{-3}$ and 1.5 $\mu Wm^{-3}$ respectively (Haenel et al., 1988). These values are significantly higher than mafic igneous rocks and most sedimentary rocks (with the exception of shales and siltstones whose average heat production is 2.1 $\mu Wm^{-3}$). It is significant that heat production in typical crustal rock types is much greater than that of undepleted mantle material, although metasomatized mantle associated with the accumulation of small melt-fraction partial melts may also contain significant heat production (McKenzie, 1989). These data concur with the notion that the bulk of lithospheric heat sources are concentrated in the crust, and particularly the mid-upper crust which is largely granitic in composition.

Regions where a significant proportion of the crust is exposed in oblique profile provide useful first-order constraints on the distribution of heat producing elements within the crust. While such exposures allow direct observation of the distribution of crustal heat sources, there are relatively few examples where near complete crustal sections are available. Moreover, there is always some concern that the preservation of these exposures may in some way reflect an unusual character, and the question remains as to what extent such examples are representative of the continental crust.

In the Vredefort region in South Africa, Archaean granite forms the core of an updomed and overturned sequence of strata which exposes a section equivalent to 15 km depth of Archaean

**Table 1.4** *Average heat production by lithology*

| *Lithology* | *U (ppm)* | *Th (ppm)* | *K (wt%)* | *Q ($\propto Wm^{-3}$)* |
|---|---|---|---|---|
| Granite/Rhyolite | 3.9 | 16.0 | 3.6 | 2.53 |
| Granodiorite/Dacite | 2.3 | 9.0 | 2.6 | 1.51 |
| Diorite/Andesite | 1.7 | 7.0 | 1.1 | 1.06 |
| Gabbro/Basalt | 0.5 | 1.6 | 0.4 | 0.29 |
| Peridotite | 0.02 | 0.06 | 0.006 | 0.01 |
| Undepleted mantle | 0.02 | 0.09 | 0.02 | 0.01 |
| Ocean Island Basalt | 1.02 | 4.0 | 1.2 | 0.67 |
| Limestone | 2.0 | 1.5 | 0.3 | 0.66 |
| Shales and siltstones | 3.7 | 12.0 | 2.7 | 2.10 |
| Quartzite | 0.6 | 1.8 | 0.9 | 0.37 |

*Note:* Heat production is that of the modern day, based on present abundances of the heat producing elements. U, Th and K data from Haenel et al., 1988.

crystalline basement (Nicolaysen et al., 1981). As discussed by Hart et al., (1981), this region provides an unparalleled opportunity to document the variation in heat sources with crustal depth, not in the least because its exposure is fortuitous (as the result of a mega meteoritic impact around 2000 Ma; Daly, 1947; Spray et al., 1995; Kamo et al., 1996) rather than due to any intrinsic unusual character. Average heat productivity-depth profiles suggest that U and Th concentrations fall off markedly with depth through the upper 7 km of crust. Consequently heat production falls from a maximum of 1.6 $\mu Wm^{-3}$ at 1 km depth to 0.86 $\mu Wm^{-3}$ at 7 km depth (Figure 1.4a). Below this depth the distribution becomes more complex, however in general the concentration of heat sources appears relatively constant to a depth of 14 km.

The Sudbury impact structure in the Canadian Superior Province exposes a similar depth profile to that seen in the Vredefort region and Schnieder et al., (1987) have evaluated the distribution of U, Th and K through this crustal section. Like the Vredefort section, there is considerable scatter in the Sudbury data so that a simple analytical expression for the heat production distribution is not evident. Despite this it is clear that heat productivity declines with depth through the crustal section (Figure 1.4b).

Another example is the vertical section through the Pennine Basement, Austria, where Hawkesworth (1974) documented heat production variations over ~ 4 km of equivalent vertical thickness through a sequence of Variscan intrusives. Although the spread of data and high level of background noise again do not allow any simple analytical form for the distribution to be resolved, it is clear in this region too that heat production is highest in the uppermost crustal column, around 6.5 $\mu Wm^{-3}$, and falls off markedly to around 2 $\mu Wm^{-3}$ at 4km depth.

On a larger scale, Fountain et al., (1987) evaluated the distribution of heat production across the Pitwitonei and Sachigo sub-provinces in central Canada. These provinces provide a cross-sectional view of the Archaean crust beneath the Superior Province and allow vertical and lateral heterogeneities in heat production to be documented. In this section Fountain et al. (1987) observe that heat productivity decreases with depth from around 1.2-1.5 $\mu Wm^{-3}$ in the upper crustal granite-greenstone units, to around 0.4-0.7 $\mu Wm^{-3}$ in the underlying high-pressure amphibolite and granulite terranes.

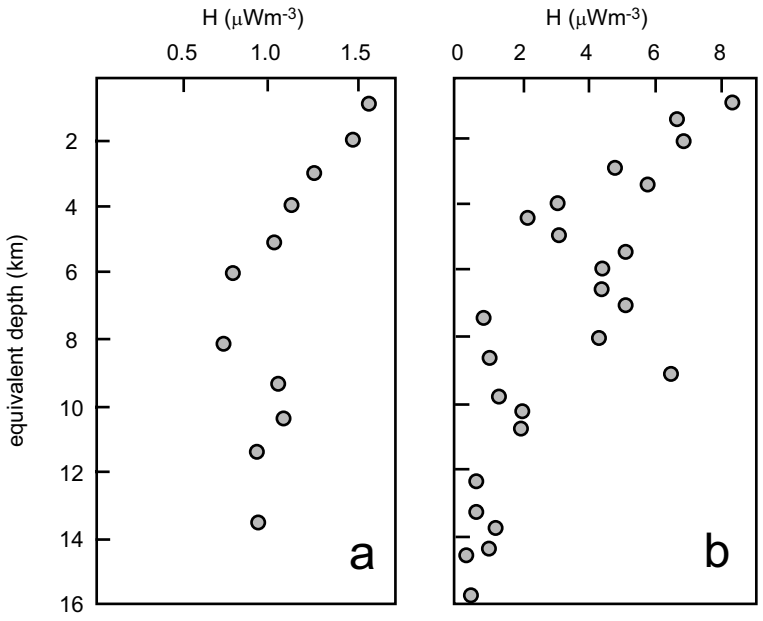


**Figure 1.4** Heat production-depth profiles for crustal sections exposed at **(a)** the Vredefort impact structure in South Africa (figure from Hart et al., 1981) and **(b)** the Sudbury impact structure, Ontario Canada (figure from Schneider et al., 1987). Both cases provide unique exposures of Archaean crustal sections, and show a clear trend of decreasing heat productivity with increasing crustal depth.

Ashwal et al., (1987) undertook a similar regional study to that of Fountain et al., (1987), in the Archaean Superior Province of Canada over an oblique cross section through some 25 km of equivalent vertical thickness. This section is interpreted to have been uplifted along a major thrust fault and so is likely to represent an unaltered and representative section of Archaean continental crust. The section runs from a mafic greenstone belt through a domal gneiss terrane into high pressure granulite facies rocks. The latter are in fault contact with greenschist and amphibolite facies volcanics of the Abitibi greenstone belt. The late stage granites within the gneiss belt showed the highest average heat production (1.37 $\mu Wm^{-3}$), a value more than twice that of the overlying greenstone belt (0.72 $\mu Wm^{-3}$), and three times that of the underlying granulite terrane (0.44 $\mu Wm^{-3}$). Such a distribution is different from the decrease in heat production with depth seen in the Vredefort, Sudbury and Alps examples outlined above, and Ashwal et al., (1987) suggest that this reflects a fundamental difference in crustal radioactivity profiles between granitic and more basic terranes; the latter characterized by relatively constant low heat production rates which show no systematic trend with depth.

A number of generalizations concerning heat production distributions may be deduced from these five examples. It is clear that gross lithological structure provides the primary first-order control on the distribution of heat sources and that the bulk of lithospheric heat sources are concentrated in felsic igneous rocks, particularly granites and granitic gneisses. Terranes with such units are characterized by a pronounced decrease in heat production with depth as the crustal section becomes increasingly mafic. This empirical relationship is also supported by similar studies by Lachenbruch and Bunker (1971), who documented the variation in heat production of rocks from deep boreholes, and Roy et al., (1968) who documented the variation of heat production in plutons from different emplacements levels.

## 1.4 Models for the distribution of crustal heat sources

Beyond the recognition that heat productivity is inversely dependent on crustal depth, there have been numerous attempts to describe the crustal heat production distribution in terms of an analytic function (e.g., Lachenbruch, 1968). Although Equation 1.3 implies that the regression of surface heat flow-heat production data provides a measure of the characteristic length scale, these data alone do not constrain the functional form of the distribution. As outlined above in Section 1.3, the spread of natural data in obliquely exposed crustal sections generally does not allow the analytical form of the distribution to be resolved. This is perhaps not surprising as the characteristic heterogeneous and discontinuous nature of continental geology would seem to preclude any simple analytic functional form for heat production distributions. Nevertheless, analytic models for heat production have proven useful, at least in as much as providing a pedagogical tool for calculating temperature fields. Here I describe three commonly accepted models for the distribution of heat sources within the crust: the exponential, linear and homogenous models.

Although the observation of a linear heat flow-heat production relation in a terrane does not provide any constraint on the way in which heat production varies with depth, the fact that that many heat flow provinces seem to be characterized by similar values of $h_r$ has lead to the proposal (Lachenbruch, 1968, 1970; Figure 1.5a) that continental heat production, $H$, must show an inverse exponential dependence on depth, $z$; a relation of the form:

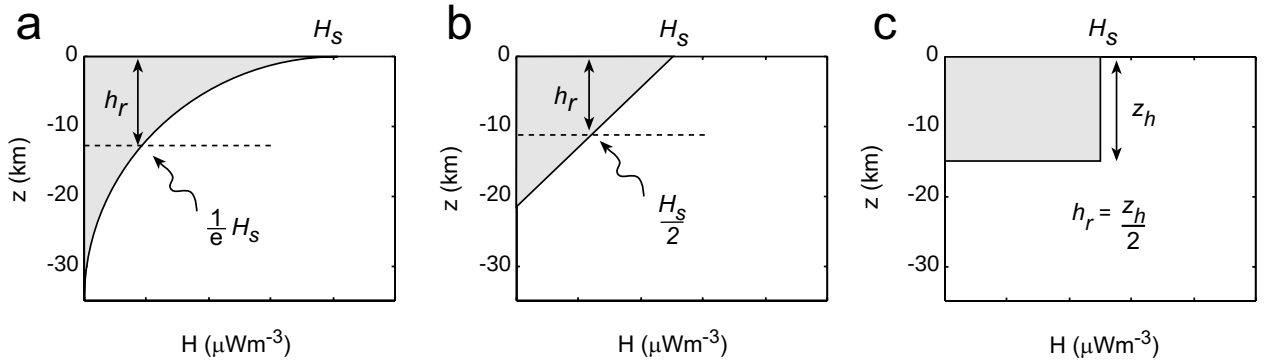


**Figure 1.5** Common models for the distribution of heat producing elements with depth within the modern continental crust **(a)** Exponential distribution proposed by Lachenbruch (1968, 1970); **(b)** Linear distribution and **(c)** homogeneous or step-like heat source distribution.

$$H = H_s e^{\frac{-z}{h_r}} \tag{1.4}$$

where $h_r$ is the length scale of the distribution and is defined as that depth at which the volumetric heat production, $H$, is $1/e$ of its surface value, $H_S$ (Figure 1.5a). Turcotte and Schubert (1982) showed that if there is no lateral variation in heat production and if the thermal conductivity, $k$, is independent of temperature, then the temperature field for the exponential model is given by,

$$T_z = -\frac{q_r z}{k} + \frac{H_s h_r^2 (1 - \exp(-z/h_r))}{k} \tag{1.5}$$

The exponential model for the distribution of crustal heat sources has found much favour, as it is the only functional form that allows a constant value of $h_r$ to be preserved after differential exhumation. As a result it has been widely adopted in many studies of continental thermal regimes. However, two alternative distributions, the linear and homogeneous models, are also commonly used to model the distribution of heat sources within the crust (Figure 1.5b, c). For the linear model, heat sources decay linearly with depth from a maximum, $H_S$, at the surface. The characteristic length scale of this distribution is the depth at which the heat production has decayed to half its maximum value. For the homogeneous model, heat production is constant to some depth, $z_h$, beneath which there are no heat sources. The characteristic length scale for this distribution is given by $z_h/2$.

## 1.5 A framework for the quantitative description of heat source distributions

The largely idealized heat production distributions shown in Figure 1.5 have proven popular, largely because they allow the formulation of simple analytical expressions for the temperature field. Although these models provide useful approximations for the distribution of heat sources in the modern continental crust, the lithophile nature of the heat producing elements suggests that they have been progressively concentrated into the upper crust during the segregation and upward migration of felsic melts from more mafic residuum during crustal growth. Consequently it is difficult to accept that any simple model for the distribution of heat sources in the modern continental crust could have applied throughout the entire history of that crust, particularly during its early stages of evolution. For this reason, it would be useful to have an alternative and more general description of the distribution of crustal heat sources that makes no explicit assumption about the analytical form of the distribution.

In the same way as for the idealized heat source distributions described above, treating the lithosphere as a one-dimensional column allows the distribution of heat sources within the crust

to be described using just two parameters. These parameters describe some characteristic heat production value, and some characteristic length scale for this heat production. For any general heat source distribution, these parameters are termed $q_c$ and $h$ respectively (see also, Sandiford and McLaren, in press; McLaren and Sandiford, in press; Sandiford et al., in press).

The first distribution parameter, $q_c$ (mWm$^{-2}$) represents the vertically-integrated heat production (see also Equation 1.2) and is a measure of the total abundance of crustal heat sources. It is formally defined as:

$$q_c = \int_0^{z_c} H(z)dz \tag{1.6}$$

The second parameter, $h$ (km), is a measure of the effective depth of the heat production, and, in terms of the heat source distribution, is formally defined as:

$$h = \frac{1}{q_c}\int_0^{z_c}(H(z)z)dz \tag{1.7}$$

As outlined in the previous section, the heat production length scale has previously been defined for each particular analytical form of the heat production distribution. The advantage of the above definition of $h$ is that it makes no explicit assumption about the form of the heat production distribution. As such, $h$ can be understood as the depth at which concentrating all heat sources does not alter the thermal structure at or beneath the base of the crust. This definition allows the redistribution of crustal heat sources, for example during various tectonic processes, to be shown quantitatively on the $h$-$q_c$ plane. Furthermore, by recognizing that the temperature field ($T$) is a function of the temperature contribution from both mantle ($T_{qm}$) and crustal ($T_{qc}$) sources, i.e,

$$T = T_{qc} + T_{qm} \tag{1.8}$$

we can define the maximum contribution of crustal heat sources. This maximum contribution, termed $T'_{qc}$, occurs at or beneath the base of the heat producing parts of the lithosphere (i.e., the

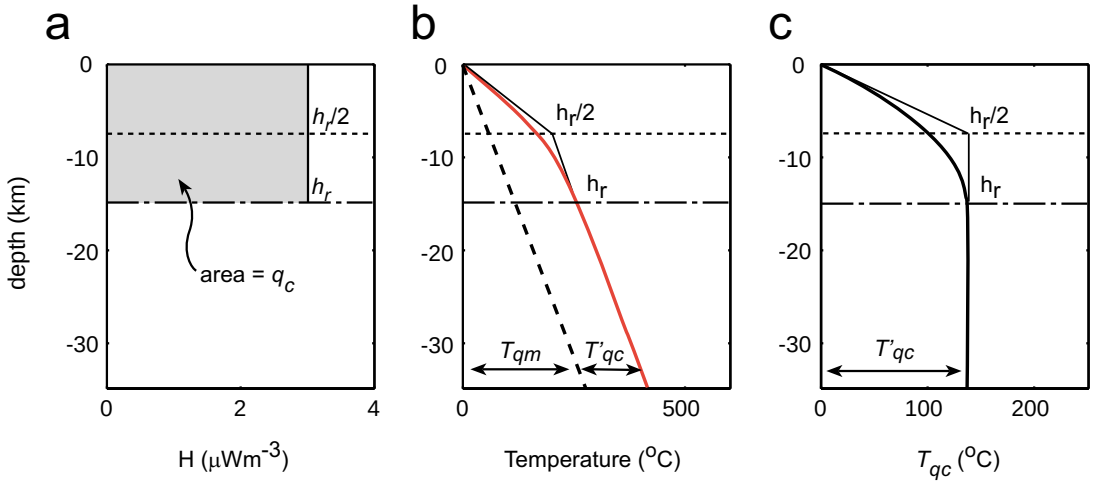


**Figure 1.6 (a)** a simple crustal heat source distribution in which heat productivity is constant at 3 μWm$^{-3}$ throughout the crust to a depth of 15 km. At deeper crustal levels there are no heat sources. **(b)** the effect of the presence of the heat source distribution shown in (a) on the crustal geotherm. The dashed line is the geotherm that would apply in crust containing no heat producing elements (ie. the mantle contribution). As shown in Equation (7) the difference between the actual geotherm and the mantle contibution is the effect of the crustal heat source distribution, $T_{qc}$, and this is shown in **(c)**. $T_{qc}$ has a maximum value, $T'_{qc}$, at the base of the heat producing layer (that is, the depth $h_r$). $h$ is the effective depth of the heat production and can be expressed as a function of $T'_{qc}$, $q_c$ and $k$, as shown in Equation 8. For the simple homogeneous heat source distribution shown, $h = h_r / 2$.

Moho) and can be considered as the thermal contribution caused by the presence of the heat source distribution relative to an otherwise identical lithosphere containing no heat sources (Figure 1.6). In terms of the parameters $h$ and $q_C$, $T'_{qC}$ can be expressed as a simple linear function:

$$T'_{qc} = \frac{q_c h}{k} \tag{1.9}$$

where $k$ is the thermal conductivity. In general, a strongly differentiated crust (in which much of the crustal complement of heat producing elements resides in the uppermost crust) is characterized by low values of $h$; similarly an undifferentiated crust will be characterized by high values of $h$. Because the $h$-$q_C$ parameterization makes no assumption about the analytical form of the heat production distribution, it is particularly useful for the description of ancient heat production distributions and for this reason the $h$-$q_C$ parameterization is adopted throughout the remainder of this thesis.

# Chapter Two

# Examples of anomalous heat source distributions

As shown in the previous Chapter, in terms of global means, the modern continental crust typically contributes ~ 30 $mWm^{-2}$ to the observed surface heat flow with this heat production mainly concentrated in the upper ~ 10 km of the continental crust. However as highlighted in the previous chapter, the modern surface heat flow dataset is strongly biased geographically, with the great majority of measurements taken from just three continents: Europe, North America and Africa. In contrast, relatively few heat flow measurements have been made in South America, Antarctica, Australia and Asia, and in these regions the modern surface heat flow field is only poorly constrained. Moreover, many of the heat flow measurements in Africa come from either Archaean cratons or within the East African rift system with the heat flow field known only very poorly outside these provinces. Recognizing that the available global heat flow dataset is representative of only a small fraction of the total area of continental crust (Figure 1.1) raises doubt about how representative this data is. Any analysis of the heat flow dataset should therefore be cognisant of this geographic bias and also recognise that, at least potentially, regions where relatively few heat flow determinations have been made or where surface heat flow differs significantly from the global average may provide additional information about the variability of the crustal heat source distribution.

Surface heat flow data can be used to make inference on the total amount and distribution of crustal heat sources through the use of the linear relationship between surface heat flow and heat production data. A compilation of estimates of the total crustal contribution to surface heat flow, $q_c$, and the length scale over which those heat sources are distributed, $h_r$, allows the variability of the crustal heat source distribution to be assessed, at least at the first order. A compilation of estimates of these parameters (Table 1.3) suggests that certain terranes appear to be characterized by significantly different heat source distributions than “typical” or “average” continental crust. Particularly, while the natural range in the heat production length scale, $h_r$, seems to be remarkably narrow ($9.4 \pm 3.5$ km, Table 1.3), the relative mantle and crustal contributions are significantly more variable. Some regions, including those which have suffered Cenozoic-Mesozoic tectonic activity, are characterized by high mantle contributions, while other areas, such as Proterozoic terranes of central Australia and the Indian Shield, and the Palaeozoic crust of England and Wales, are characterized by above average crustal contributions.

As outlined in Chapter One of this thesis, the total abundance of crustal heat sources provides one of the primary controls on crustal thermal regimes. As shown in the remainder of this thesis, recognizing variations in $q_c$ may be significant for understanding the way in which these regions have evolved, both thermally and mechanically. This is particularly the case for regions with higher than average values of $q_c$, as the presence of anomalous concentrations of heat sources is almost certain to have impacted on the long term thermal history of such crust.

Notable examples of regions with higher than average values of $q_c$ include the western Canadian Cordillera (e.g., Lewis and Hyndman, 1999), Palaeozoic terranes across England and

Wales (e.g., Richardson and Oxburgh, 1978) and Proterozoic terranes of central Australia (Sass and Lachenbruch, 1979). In the Canadian Cordillera exceptional surface heat flows in the range 118-136 $mWm^{-2}$ (Hyndman and Lewis, 1999) in the Proterozoic Omienca Belt are probably due to a high crustal contribution (Lewis and Hyndman, 1999) with this heat production contained within late granites which intrude the Slave Province. In these regions Majorowicz (1996) suggests that as much as 60 $mWm^{-2}$ is contributed by crustal sources. In a less extreme example, Richardson and Oxburgh (1978) present heat flow and heat production data for 40 sites within England and Wales and show that on average the crust contributes 35 $mWm^{-2}$ to the observed heat flow, around 20% higher than the average crustal value (Table 1.3). While on average heat production in both granites and sediments is about average, at $2.2 \pm 1.6$ $\mu Wm^{-3}$, some granites and granite gneisses are significantly enriched in the heat producing elements with heat production rates as high as 6.5 $\mu Wm^{-3}$. Richardson and Oxburgh (1978) also note that while the crustal heat production is about average, this heat production extends to greater depth than in many other regions, giving a higher total integrated crustal contribution.

Heat flow data from Australian Proterozoic terranes suggests that this crust is characterized by highly anomalous concentrations of the heat producing elements. By simply equating $q_r$ with $q_m$ the linear relationship between surface heat flow and heat production suggests that in this region $q_c$ is on average 56 $mWm^{-2}$. In this chapter I discuss the evidence for anomalous surface heat flow field in Australian Proterozoic terranes, and present the first detailed analysis of surface heat production and other data to constrain the relative contributions to the observed heat flow. This analysis shows that in this region the average surface heat flow of 85 $mWm^{-2}$ reflects a crustal contribution of at least 50 $mWm^{-2}$ and as high as 70 $mWm^{-2}$; that is, about twice that of “average” continental crust!

## 2.1 The Australian heat flow field

While much effort has been expended in the collection and interpretation of heat flow data in many continental settings, the Australian heat flow field is defined by only ~ 120 data points. The first heat flow determination was published by Newstead and Beck in 1953, and much of the current dataset was collected from this time through until the late 1970’s, lead largely by the pioneering work of J.C. Jaeger and J.H. Sass. These early data were compiled by Cull (1982). Since 1982 only a handful of additional heat flow determinations have been published (Houseman et al., 1989; Gallagher, 1990). The main features of the Australian heat flow field at the continental scale are shown in Figure 2.1a.

Sass and Lachenbruch (1979) divided the heat flow field into the Eastern, Central and Western provinces (Figure 2.1b) each characterised by somewhat different heat production parameters. This is revealed by the regression of surface heat flow and heat production data (Lachenbruch, 1968, 1970). The tripartite division is closely allied to tectonic age. The dominantly Archaean Western Province has an average heat flow of $39 \pm 8$ $mWm^{-2}$. The central province comprises the region of the Australian continent formed mostly during the Proterozoic and has an average surface heat flow of $82 \pm 25$ $mWm^{-2}$. The Eastern Province, where the major period of crustal growth occurred in the Palaeozoic and where widespread Cainozoic magmatic and tectonic activity is concentrated (Sass and Lachenbruch, 1979), has an average heat flow of $72 \pm 27$ $mWm^{-2}$. Average heat flow in both the Western and Eastern Provinces is consistent with accepted global averages for equivalently

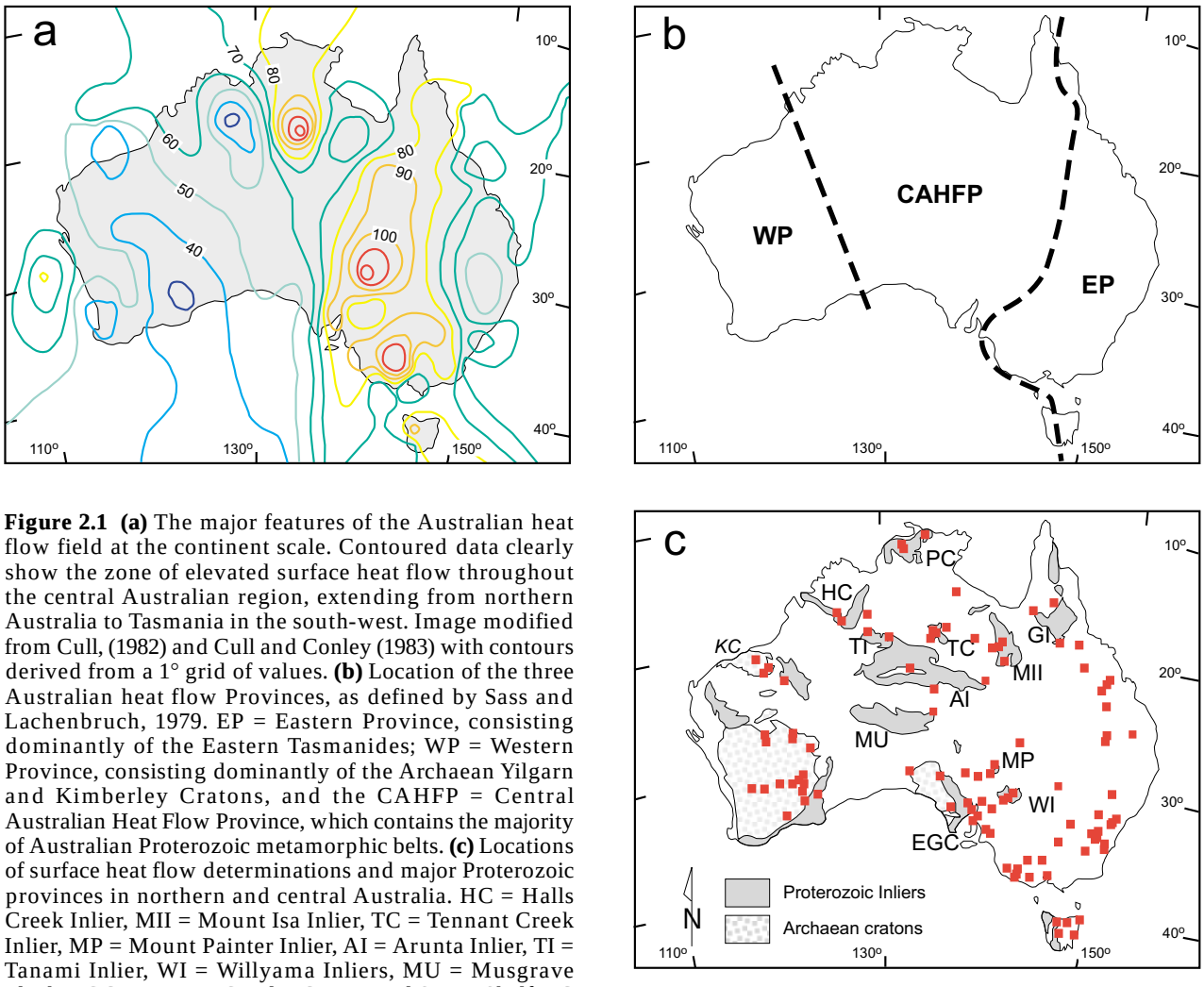


**Figure 2.1** **(a)** The major features of the Australian heat flow field at the continent scale. Contoured data clearly show the zone of elevated surface heat flow throughout the central Australian region, extending from northern Australia to Tasmania in the south-west. Image modified from Cull, (1982) and Cull and Conley (1983) with contours derived from a 1° grid of values. **(b)** Location of the three Australian heat flow Provinces, as defined by Sass and Lachenbruch, 1979. EP = Eastern Province, consisting dominantly of the Eastern Tasmanides; WP = Western Province, consisting dominantly of the Archaean Yilgarn and Kimberley Cratons, and the CAHFP = Central Australian Heat Flow Province, which contains the majority of Australian Proterozoic metamorphic belts. **(c)** Locations of surface heat flow determinations and major Proterozoic provinces in northern and central Australia. HC = Halls Creek Inlier, MII = Mount Isa Inlier, TC = Tennant Creek Inlier, MP = Mount Painter Inlier, AI = Arunta Inlier, TI = Tanami Inlier, WI = Willyama Inliers, MU = Musgrave Block, EGC = Eastern Gawler Craton and Stuart Shelf, PC = Pine Creek Inlier, GI = Georgetown Inlier. Archaean cratons are shown in light shading, YC = Yilgarn Craton, KC = Kimberley Craton. Solid geology modified from Wyborn et al., (1987). Squares denote surface heat flow determinations, location data from Cull, (1982), Houseman et al., (1989) and Gallagher, (1990).

aged terranes (Table 1.1). For the Western province regression of surface heat flow-heat production data yields a value of $q_r$ of 26.3 mWm$^{-2}$ and a value of $h_r$ of 4.5 km. In the Eastern Province these values are 57.3 mWm$^{-2}$ and 11.1 km respectively (Sass and Lachenbruch, 1979).

## 2.2 Central Australian heat flow province (Sass and Lachenbruch, 1979)

The Central Province (the so-called “Central Shield Province” of Sass and Lachenbruch, 1979, and here termed the Central Australian heat flow province – CAHFP) is a belt ~ 500 km wide which extends from the Northern Territory south-east to Tasmania (Figure 2.1b). This region includes all major Proterozoic metamorphic belts and records the highest average surface heat flow of the three provinces identified by Sass and Lachenbruch (1979), typically in the range 70-100 mWm$^{-2}$ with an average of ~ 82 ± 25 mWm$^{-2}$. This value is well in excess of the global average of around 50-55 mWm$^{-2}$ for Proterozoic terranes, and must arise as a consequence of either:

- systematic error in the heat flow determinations
- anomalous mantle heat flow, $q_m$
- recent tectonic, magmatic or hydrologic activity, or
- an anomalous contribution from crustal heat sources, $q_c$.

In this section I first describe the character of the CAHFP and assess the factors that contribute to its extraordinary heat flow. This analysis indicates that the crust throughout the CAHFP is enriched in the heat producing elements and characterized by an anomalous heat source distribution.

The distribution of heat flow data within the Proterozoic metamorphic terranes which comprise the CAHFP is variable (Figure 2.1c, Table A.17). Coverage is best in the south, in central and southern South Australia and western New South Wales. In this area the Gawler Craton, Stuart Shelf and Willyama Inliers have each been the subject of several heat flow studies, with heat flow measurements available for 19 separate localities. As discussed by Neumann et al., (2000), these data allow a detailed heat-flow transect to be constructed ranging across the Archaean-Proterozoic Gawler Craton, the Adelaide Fold Belt (which consists dominantly of Neoproterozoic sediments), the Archaean-Proterozoic Curnamona Craton and the Palaeo-Mesoproterozoic Willyama and Broken Hill Inliers (Figure 2.1c). One of the most detailed heat flow datasets within this group is taken from the region around the Olympic Dam Cu-U-Au deposit where Houseman et al. (1989) made 7 heat flow determinations. Together the amount and quality of heat flow data from South Australian terranes allows the regional heat flow character of this portion of the CAHFP to be well defined.

The Mount Isa, Georgetown, Pine Creek and Tennant Creek Inliers in northern Australia have also been the focus of a number of determinations. The Mount Isa Inlier has been the subject of 4 heat flow determinations, with measurements available for the Western Fold Belt and Kalkadoon-Leichhardt Fold Belt (Hyndman and Sass, 1966) and also the Eastern Fold Belt (Cull and Denham, 1979; see also Chapters Four and Five of this thesis). The Georgetown Inlier, lying near the boundary of the CAHFP and the Eastern Province has been the subject of a 3 determinations by Cull and Denham (1979) and Cull (1982). Good heat flow datasets are also available for both the Pine Creek Inlier (Howard and Sass, 1964; Sass et al., 1976; Cull, 1982) and the Tennant Creek Inlier (Howard and Sass, 1964; Hyndman, 1967; Sass et al., 1976; Lilley et al., 1978), in part because the occurrence of world class mineral deposits in both localities has meant many suitable boreholes are available. In the case of the Pine Creek Inlier however, the proximity of several heat flow measurements to large uranium resources casts some doubt on just how valid these measurements are. Despite these concerns, the excellent coverage through the Mount Isa, Georgetown and Tennant Creek inliers allows the regional heat flow character of the north-eastern portion of the CAHFP to be reasonably well constrained.

However, a number of other areas of Proterozoic crust remain quite poorly characterized. These terranes include the Musgrave Block in northern South Australia, where heat flow is totally unknown; the Arunta Inlier, in central Australia where only two heat flow measurements are available; and the Halls Creek Inlier in Western Australia and the Tanami Inlier in the Northern Territory, where only one good quality heat flow determination is available in each case. These terranes comprise the central-western portion of the CAHFP and the absence of direct heat flow determinations throughout this region represents a major limitation to our understanding of the regional thermal structure.

Those data which are available within the CAHFP do allow a significant first-order signature to be identified, that is, that measurements from Proterozoic basement terranes are highly anomalous in the context of averages reported for other Proterozoic terranes (Table 1.2). The mean and standard deviation of all 49 heat flow determinations throughout all the regions of Proterozoic crust which comprise the CAHFP is $81.9 \pm 24.7$ mWm$^{-2}$. This value is one and a half times the global average

(Table 1.2) and twice the value recorded in Grenville province in North America. The latter is probably the best characterized Proterozoic province where 30 separate heat flow determinations yield an average of 41 ± 11 $mWm^{-2}$ (Jaupart and Mareschal, 1999). Several basement terranes within the CAHFP, including the Tennant Creek and Mount Painter Inliers and the Eastern Gawler Craton, record surface heat flow > 100 $mWm^{-2}$; well in excess of the average CAHFP value (Table 2.1).

Much of the Proterozoic metamorphic basement in the CAHFP is covered by Neoproterozoic and Palaeozoic intra-cratonic basins and heat flow and thermal gradient measurements in these regions support the high values of surface heat flow reported from Proterozoic basement inliers. Examples include a single heat flow measurement of 116 $mWm^{-2}$ from the Eromanga basin in south-western Queensland (Gallagher, 1990) and thermal gradient determinations of 45-55°$Ckm^{-1}$ from

**Table 2.1** *Surface heat flow and heat production of selected terranes within the CAHFP*

| *Metamorphic Terrane* | *$q_s$ ($mWm^{-2}$)* | *H p* ($\mu Wm^{-3}$)* | *Total area ($km^2$)†* |
|---|---|---|---|
| Willyama Inliers‡ | 80, 68, 64, 75 | **2.88** | 1920 |
| | **average = 72** | | |
| Mount Painter Inlier | **126** | **12.49** | 555 |
| Eastern Gawler Craton & Stuart Shelf | 91, 101, 109, 96, 88, 91, 73, 120 | **4.79** | 20888 |
| | **average = 96** | | |
| Mount Isa Inlier | 82, 78, 72, 98 | **4.82** | 10935 |
| | **average = 83** | | |
| Georgetown Inlier | 77, 100, 77 | **5.06** | 6411 |
| | **average = 85** | | |
| Tennant Creek | 89, 100, 161, 100, 75 | **3.89** | 4131 |
| | **average = 105** | | |
| Pine Creek + environs | 86, 84, 80 | **4.73** | 8626 |
| | **average = 83** | | |
| Arunta Complex | 62, 56 | **5.24** | 27233 |
| | **average = 59** | | |
| Tanami Inlier | 34, 56 | **5.79** | 790 |
| | **average = 45** | | |
| Halls Creek + environs | 26, 65, 67 | **3.15** | 12073 |
| | **average = 53** | | |
| Musgrave Inlier | **–** | **2.68** | 5499 |
| ***CAHFP AVERAGE*** § | ***81.9 ± 24.7*** | ***4.58*** | ***100477*** |

*Note*: All available surface heat flow measurements within (or immediately adjacent) each terrane are listed. In many cases an individual measurement may represent the average of a number of determinations at a single site. Data is taken from a compilation by Cull, (1982). Details of each individual heat flow measurement, including location and reference, are listed in Table A.17 (in Appendix A). Locations of terranes are shown in Figure 2.1c

*H p** = present heat production, calculated from present concentrations of U, Th, and K. These values of heat production are terrane averages which represent weighted averages based on proportional outcrop area. Note that because radioactive decay causes a reduction in the concentration of heat-producing elements through time, the value of the calculated heat production during the Proterozoic is on average ~25–30% higher than the present day value. Raw geochemical data used in the calculation of average heat production values from Wyborn et al., (1998a).

† Total area is that area of outcrop of felsic igneous rocks for which heat production data are available. Total area listed is used in the calculation of area normalized heat production averages. Note that the total area includes some regions of Proterozoic crust not included in the table above. A complete summary of all available CAHFP heat production data is included in Appendix A.

‡ The Willyama Inliers include the Broken Hill and Olary regions.

§ The CAHFP averages are calculated including all heat flow determinations and surface heat production data within the CAHFP.

water bores in the Great Artesian Basin and oil prone wells in the Cooper-Eromanga Basin system (e.g., Cull and Conley, 1983; Somerville et al., 1994). These data provide useful insights into the nature of the heat flow field and support the notion that the elevated surface heat flow measurements are truly representative of a high heat flow province, and are not merely artefacts of the determinations in anomalous regions.

Although surface heat flow is anomalously high throughout the CAHFP, several measurements are significantly lower than the average suggesting considerable regional (> 100 km) variation within the CAHFP. Such measurements include an isolated and exceptionally low heat flow determination of 48 $mWm^{-2}$ at Camooweal on the Northern Territory-Queensland border between the high heat flow Proterozoic terranes of Mount Isa (where heat flow averages 83 $mWm^{-2}$) and Tennant Creek (where heat flow averages 105 $mWm^{-2}$). Relatively low heat flow is also recorded in the Arunta and Tanami Inliers in central Australia, and in the Halls Creek Inlier in Western Australia, the only anomalous basement terranes in the province. In the Arunta Inlier, thermal gradients of 20-30 $°Ckm^{-1}$ from bottom hole temperatures along the northern margin of the Amadeus Basin (Gorter, 1984) support the notion of comparatively low heat flow in this region. While the average surface heat flow in both the Arunta and Halls Creek Inliers is low when compared to other terranes within the CAHFP (averaging 59 and 53 $mWm^{-2}$ respectively) the measured surface heat flow is still above the global Proterozoic average (Table 1.2). Only the Tanami Inlier (45 $mWm^{-2}$) has an average heat flow lower than the accepted global mean.

## 2.3 Reconciling Australian Proterozoic heat flow

As outlined in Section 2.2, in order to understand the significance of the heat flow measurements in the CAHFP it is necessary to assess the extent to which the anomalous surface heat flow recorded throughout much of the CAHFP is the result of systematic error in the heat flow determinations, recent tectonic, magmatic or hydrological activity, or an anomalous contribution from either crust or mantle sources.

### 2.3.1 The contribution of systematic error

Because many of the heat flow measurements throughout the CAHFP are so anomalous when compared to global averages, they lead us first to question the accuracy of heat flow determinations throughout this region.

In order to evaluate the possible contribution of systematic error associated with the mechanics of the heat flow determinations, we recognize that the measurement of surface heat flow is based on the application of Fouriers Law, that is:

$$q = k * gradT \tag{2.1}$$

where $q$ is the heat flow per unit area, $k$ is the thermal conductivity and $gradT$ is the temperature gradient. As such, surface heat flow is calculated directly from measurements of absolute temperature and thermal conductivity through the borehole section, and potential errors are associated with the collection of both datasets. Firstly, geothermal gradients are calculated from measurements of subsurface temperature at intervals < 5 m. The thermistor probes commonly used for this task give excellent resolution (Cull and Sparksman, 1977), however, there are frequent departures from ideal linear temperature gradients, caused largely by heterogeneities in the subsurface lithostructure. As a result, approximation of a linear thermal gradient throughout the section may introduce minor

errors to the subsequent calculation. To add to this generally only a few conductivity determinations are made for any particular borehole, and this sampling bias will also introduce errors into the calculated heat flow. Cull and Denham (1979) suggest that this is probably a greater source of error than instrumental or thermal gradient problems. In light of these errors heat flow is generally averaged over several intervals to provide an estimate of the potential error.

A third source of error relates to the quality of the borehole used for the heat flow determination. The Australian heat flow dataset contains measurements from tunnels, mines, flowing bores and cased and uncased boreholes of various depths (Cull and Denham, 1979), and in each case the condition of the borehole and its physical environment impact on the quality of the heat flow measurement. Preferably the hole should have returned to thermal equilibrium after drilling (Cull, 1982, recommends an equilibration period of at least 6 months) and it should be fluid filled but with no hydrological flow. The region should also be characterized by flat topography and uniform stratigraphy to minimize the error associated with measurement of thermal conductivity and thermal gradient (Cull, 1982).

Based on these considerations, Cull (1982) estimates that more than 60% of the heat flow measurements from the CAHFP are of “good” quality or better. This value increases to around 75% for the whole Australian heat flow dataset. Given these results, and the number of data available for the CAHFP, it seems unlikely that all measurements from Proterozoic terranes in the CAHFP could have been subject to the same magnitude and polarity of systematic error. In other words, it seems unlikely that the errors associated with the measurement of thermal gradients or thermal conductivity, inadequate borehole equilibration or the effects of lateral heat transfer (e.g., Jaupart, 1983) would result in consistent over-estimation of surface heat flow throughout the CAHFP. Consequently I suggest that the consistency and homogeneity of Proterozoic heat flow data at both the continent and terrane scale almost certainly reflects a unique first-order signature.

### 2.3.2 Recent magmatic, tectonic and hydrological activity

As outlined in Chapter One of this thesis, measurements of surface heat flow in the absence of erosion, deformation or groundwater flow, represent the sum of the lithospheric heat sources (which are mostly concentrated in the crust) and the heat flowing into the lithosphere from the deeper mantle.

Many regions of elevated surface heat flow on the modern earth can be associated with transient thermal pulses resulting from recent tectonic or magmatic activity, or an anomalous contribution from the convective mantle. One such region is the Basin and Range Province in south-western USA, where surface heat flow averages 80-100 $mWm^{-2}$ (Sass et al., 1994). Blackwell (1978) first suggested that this high heat flow was the result of thermal transients accompanying recent magmatic activity, and Sass et al. (1994) demonstrated this to be the case by noting a strong correlation between zones of high heat flow and areas of late Tertiary (middle Miocene) igneous activity. Lachenbruch et al. (1994) suggested further that the high heat flow was a direct result of increased mantle heat flow (as much as twice the average contribution) associated with regional extension and asthenospheric upwelling. Saltus and Thompson (1995) presented models in support of this hypothesis and showed that it was consistent with observed surface heat flow measurements, topographic and gravity data.

As one example, the most anomalous region of the Basin and Range is the Salton Trough in which surface heat flow averages an extraordinary 150 $mWm^{-2}$ and in some areas is in excess of 1 $Wm^{-2}$ (e.g., Newmark et al., 1988). This region is the most rapidly evolving extensional basin within the Basin and Range and its high heat flow is readily explicable in terms of rapid extension and magmatic and hydrothermal processes associated with the presence of a basaltic underplate (Sass et al., 1994). In minor sub-terranes within the Basin and Range region, evidence for a magmatic source is not so compelling, and in these cases high observed heat flow can readily be associated with deep hydrological circulation (Sass et al., 1994).

Vasseur and Nouri (1980) report a similar scenario for the origin of elevated surface heat flow in France. Here surface heat flow is also anomalous when compared to global averages, with a large country-wide anomaly centred on the Central Massif region, where heat flow averages $107 \pm 17.5$ $mWm^{-2}$. In the same region the lithosphere is significantly thinned and interpretation of seismic and gravity data suggest the presence of an asthenospheric plume ~ 50 km in diameter. Vasseur and Nouri (1980) present a quantitative model showing that large scale mantle convection at rates approaching 5 $mmy^{-1}$ for around 40 Ma is consistent with observed variations in surface heat flow, and known lithospheric thickness. They also suggest that transient phenomena such as recent volcanism probably also contribute to the heat flow anomaly.

Unlike these examples, the Australian Proterozoic heat flow anomaly cannot be understood in terms of some transient thermal contribution. Aside from a small region in South Australia which has suffered mild neotectonic reactivation associated with the formation of the Flinders Ranges (e.g., Tokarev et al., 1999), there is little evidence for recent tectonic or magmatic activity throughout CAHFP, and the vast majority of this crust has remained relatively tectonically inactive for the last few hundreds of millions of years.

A compilation of both refraction and reflection seismic data suggests that Proterozoic terranes throughout central Australia (encompassing a large proportion of the CAHFP) contain the thickest crust within the Australian continent, with the Moho discontinuity imaged at around 45-50 km (Collins, 1991; Drummond, 1988). This crust is associated with negative teleseismic travel time residuals, suggesting that the lithospheric thickness is also anomalous. This notion is supported by recent deep seismic imaging (Figure 2.2) as part of the continent-wide SKIPPY project (e.g., Van der Hilst et al., 1994; Kennett and Van der Hilst, 1996; Zielhaus and Van der Hilst, 1996). As part of this study, Zielhaus and Van der Hilst (1996) note an abrupt contrast in the seismic velocity of the upper mantle between the Eastern Australian region and Proterozoic terranes lying to the west (and forming part of the CAHFP) (Figure 2.2a, b). This contrast is inferred to represent a major discontinuity in mantle structure. The upper mantle beneath Eastern Australia is characterized by low seismic velocities, a thin lithosphere and positive *p*-wave travel-time residuals, reflecting high mantle temperatures and steep thermal gradients. These data are consistent with the locus of recent (Cainozoic) volcanism, and petrological analyses of mantle xenoliths in this region (e.g., O'Reilly and Griffin, 1985; Sutherland et al., 1994), and suggest that the high surface heat flow recorded in this zone reflects an anomalous mantle contribution; as indeed was suggested by Sass and Lachenbruch (1979) on the basis of their regression of surface heat flow heat production data. In contrast however, the Proterozoic terranes of Northern Australia are characterized by higher seismic velocities, around 8.2 $kms^{-1}$ (Collins 1991). The southern part of the CAHFP is characterized by slightly lower seismic velocities, averaging ~ 8.0 $kms^{-1}$, and corresponding to Moho depths of 37-40 km (Collins 1991).

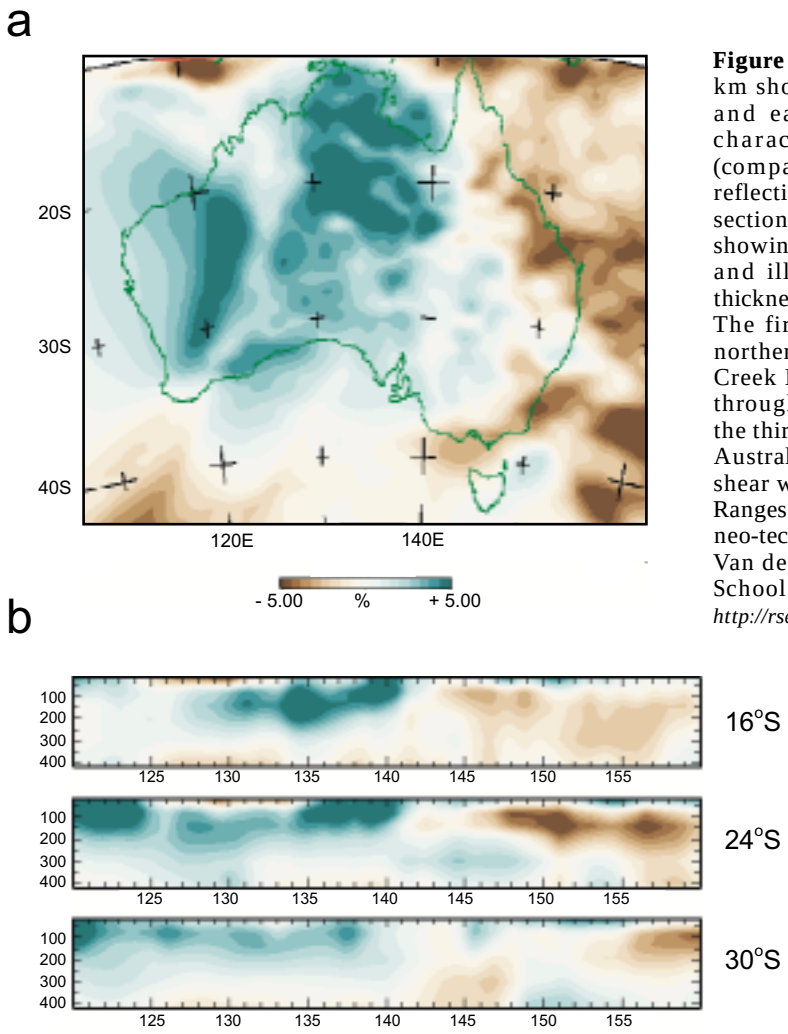


**Figure 2.2** **(a)** Model of shear wave speed at 140 km showing the sharp contrast between central and eastern Australia. Central Australia is characterized by high shear wave speeds (compared to a reference velocity of 4.50 $kms^{-1}$) reflecting an unusually cool mantle. **(b)** Vertical sections through the model of shear wave speed showing the contrast in seismic velocity with depth and illustrating the variation in lithospheric thickness between the Central and Eastern regions. The first section (at 16°S) passes through the northern Australian region, just south of the Pine Creek Inlier; the second section (at 24°S) passes through the central Australian Arunta Inlier and the third section (at 30°S) through northern South Australia. The latter section shows a region of low shear wave velocity corresponding to the Flinders Ranges. This region is also characterized by ongoing neo-tectonic activity. All figures from Zielhaus and Van der Hilst (1996) and taken from the Research School of Earth Sciences Seismology Group, at *http://rses.anu.edu.au/seismology/skippy97/skippynew.html*

The high seismic velocities recorded at the Moho in the CAHFP, and particularly the northern CAHFP, are likely to reflect relatively low mantle temperatures, probably less than about 500°C. For example, detailed seismic surveys in the Mount Isa Inlier by Goncharov et al. (1996), Goncharov et al. (1998) and Drummond et al. (1998) suggest that the average $P_n$ velocity in this terrane (at Moho depths of ~ 50 km) is 8.1 $kms^{-1}$. Using the empirical $P_n$ velocity-moho temperature relation derived by Black and Braile (1982), upper mantle temperatures beneath the Mount Isa Inlier are calculated to be 488°C. If the average $P_n$ velocity were 8.2 $kms^{-1}$, which Collins (1991) suggests is appropriate for much of the CAHFP, then the relation of Black and Braile (1982) yields an average upper mantle temperature of 350°C. Although these calculations give an estimate of upper mantle temperatures, the Black and Braile (1982) relation is strictly applicable only for North America, and the calculated temperatures are therefore only a guide. Zielhaus and Van der Hilst (1996) suggest that this thick crust is also coupled with unusually thick lithosphere with the transition between high and low seismic velocities at around 250 km marking the base of the continental lithosphere.

The existence of thick, cold mantle lithosphere beneath much of the CAHFP is at odds with the observed surface heat flow and, together with the absence of recent tectonic or magmatic activity, points toward low mantle heat flow throughout the CAHFP. For example, for a thermal conductivity of 3 $Wm^{-1}K^{-1}$ appropriate to mantle peridotite at elevated temperatures (e.g., Haenel et al., 1988) and a moho temperature of 500°C at 40 km depth, a lithospheric thickness of 250 km implies modern day mantle heat flows of 12 $mWm^{-2}$. Such low mantle heat flows, together with the absence of recent

tectonic and magmatic activity, suggest that the anomalous surface heat flow recorded throughout the CAHFP must reflect anomalous crustal heat production, with crustal sources contributing as much as 70 $mWm^{-2}$ to the measured surface heat flows.

### 2.3.3 Crustal heat production in Proterozoic metamorphic belts

A total complement of heat producing elements that contributes 70 $mWm^{-2}$ to the surface heat flow implies an average crustal heat production of around 2 $\mu Wm^{-3}$. However, as outlined in Chapter One, lower crustal rock types are typically depleted in heat producing elements relative to middle and upper crustal rocks (e.g., Fowler, 1990; Table 1.2) and so, if crustal heat production was the source of the anomalous heat flow, we may expect significantly higher heat production rates in the upper crust. Moreover, we may also expect that these surface heat production values are significantly greater than normal lithological averages in order that the measured surface heat flow is so high. This notion was supported by a preliminary compilation of surface heat productivity data by Lambert and Heier (1968) who showed that Australian rocks were more radioactive than similar rocks on other continents. More recently the compilation of an extensive geochemical database of Australian Proterozoic felsic igneous rocks by Wyborn et al. (1998a) enables a detailed analysis of the variations in surface heat productivity of these units to be made. I have used this database to calculate an area normalized surface heat production value for all felsic igneous rocks in each Proterozoic terrane within the CAHFP. Throughout this discussion I am concerned with heat production rates in granites, granite gneisses and felsic volcanics only. This is principally because these lithotypes are by far the most representative, volumetrically, of the middle to upper crust, and so are most likely to contain any anomalous crustal heat production. These lithologies also comprise a significant proportion of Australian Proterozoic terranes, both in outcrop and in the subsurface, as revealed by seismic profiling. In many terranes these granites, which are dominantly I-(granodioritic) types, comprise around 20 % of the total area of outcropping Proterozoic rocks (Table 2.2). In the Mount Isa Inlier, for example, granites and felsic volcanics outcrop over ~ 11 000 $km^2$, and constitute 27% of the total area of the inlier. Similar values are also noted for other terranes, including the Arunta Inlier where > 27 000 $km^2$ of outcropping granite and granite gneiss constitutes 18% of the total area of the inlier (Table 2.2).

In this analysis I use all of the data compiled by Wyborn et al., (1998a) for which average U, Th and K analyses are available. In total, 462 individual felsic rocks have such data available. Heat production values were calculated using the known decay parameters of each of the radiogenic isotopes, using the formulae outlined in Appendix A. At this stage I do not discriminate between analyses on any basis. By calculating averages based on proportional area of outcrop any possible bias arising from high radiogenic but small volume lithologies is removed. I assume that all analyses are subject to the same analytical error and that all samples are representative of the granites from which they are taken and of their source regions. We see later that this second point is valid as the areal average Thorium to Uranium ratio is 4.7 when calculated over the entire CAHFP granite database. This value is a primary magmatic ratio and so these granites are likely to be representative of the chemical state of the crust at the time of their intrusion. It is therefore unlikely that the observed concentrations of heat producing elements reflect later mobilisation during chemical alteration.

The results of these heat production calculations are summarized in Tables 2.1 and 2.2. Detailed analyses for each Proterozoic terrane within the CAHFP, and for additional Proterozoic

**Table 2.2** *Average heat production of major granite suites in selected Australian Proterozoic terranes within the CAHFP*

| *Terrane* | *Granite Type* | *Age range* | *Area of outcrop ($km^2$)* | *% area of outcrop* | *U (ppm)* | *Th (ppm)* | *K (wt%)* | *Q ($\mu Wm^{-3}$)* |
|---|---|---|---|---|---|---|---|---|
| Mount Isa | Williams & Naraku | 1490 – 1545 | 1883 | 5 | 13.5 | 55.5 | 3.90 | **7.93** |
| | Rift-related | 1620 – 1790 | 4323 | 11 | 6.6 | 33.5 | 5.60 | **4.69** |
| | Kalkadoon | 1800 – 1860 | 4686 | 12 | 5.3 | 25.6 | 4.71 | **3.71** |
| | **All granites** | | **10935** | **27** | | | | |
| Pine Creek | Burnside | 1750 – 1800 | 300 | 0.6 | 11.1 | 38.1 | 4.85 | **6.15** |
| | Cullen | 1810 – 1890 | 8325 | 17 | 7.3 | 31.9 | 4.53 | **4.68** |
| | **All granites** | | **8626** | **18** | | | | |
| Arunta Inlier | Mount Webb | 1615 – 1480 | 6155 | 4 | 9.8 | 43.0 | 4.52 | **6.14** |
| | Southwark | 1680 – 1560 | 6720 | 4 | 4.1 | 30.0 | 3.77 | **3.62** |
| | Jervois-Jinka | 1820 – 1710 | 12587 | 8 | 8.4 | 48.4 | 4.96 | **6.19** |
| | Narwietooma | ~ 1880 | 1770 | 1 | 1.8 | 9.8 | 3.27 | **1.50** |
| | **All granites** | | **27233** | **18** | | | | |
| Tennant Creek | Warrego | 1670 – 1720 | 443 | 2 | 8.7 | 36.4 | 5.23 | **5.45** |
| | Tennant Creek | 1830 – 1870 | 2195 | 10 | 5.5 | 23.4 | 4.60 | **3.60** |
| | **All granites** | | **4131** | **18** | | | | |
| Kimberley | Sally Downs | 1780 – 1830 | 2592 | 5 | 3.6 | 19.0 | 3.46 | **2.65** |
| | Paperbark | 1845 – 1860 | 9415 | 6 | 5.2 | 20.6 | 4.48 | **3.29** |
| | Sophie Downs | ~ 1910 | 64 | 1 | 2.2 | 16.9 | 5.10 | **2.29** |
| | **All granites** | | **12073** | **22** | | | | |
| ***TOTAL*** | | | **100477** | | **6.8** | **32.1** | **4.62** | **4.58** |

*Note:* Heat production is that of the modern day, based on present abundances of the heat producing elements. Granites listed in each terrane are major granite suites (loosely grouped using age data and supersuite terminology from Wyborn et al, 1998a). The granites shown in this table do not include all granites known from each terrane. Average U, Th and K data summarized from Wyborn et al., (1998a).

The Kimberley terrane includes both the Halls Creek and King Leopold Orogens

TOTAL values are determined from an average of all analyses (and include analyses from terranes not included in the summary compilation above) Appendix A contains a detailed listing of all heat production data.

% area occupied by each major granite group is an estimate based on the accurate outcrop area of the granite, and an estimated area of the entire inlier. Estimates of total inlier area are likely to overestimate the area of outcrop, so the values shown here are likely to be a minimum estimate of the percentage of granite *vs.* total outcrop.

terranes outside the CAHFP, are given in Appendix A (Tables A.1-A.15).

In terms of the regional dataset, heat production of felsic granites and volcanics in all Proterozoic terranes within the CAHFP averages 4.58 $\mu Wm^{-3}$ when normalized by area of outcrop (Tables 2.1, 2.2). This value is almost twice that of the average granite (Table 1.4) and is even more extraordinary given that the total area of outcropping granite on which it is based is in excess of 100 000 $km^2$! For comparison, the extensive Peninsular Ranges Batholith in California has average heat production of just 1.1 $\mu Wm^{-3}$ (Silver and Chappell, 1988), increasing to a maximum of only 1.56 $\mu Wm^{-3}$ in the eastern Sierra Nevada Range.

Amongst the CAHFP dataset, volumetrically significant granites in many terranes have heat production rates much higher than the CAHFP average, with values commonly in the range 5-10 $\mu Wm^{-3}$ (Tables 2.1, 2.2, A1-A15). The fundamental importance of these heat production values is highlighted by recognizing that a granite only 5 km thick with heat production of 6 $\mu Wm^{-3}$ is required to produce what is by conventional wisdom considered to be the entire crustal contribution

to measured surface heat flow!

In the southern part of the CAHFP heat production increases from the Eastern Gawler Craton and Stuart Shelf eastward to the Mount Painter Inlier before decreasing in the Willyama Inliers. While the average heat production in the Mount Painter Inlier is extreme, at 16.1 $\mu Wm^{-3}$, this region occupies only a very small fraction of total outcrop in the southern CAHFP, covering an area on only around 800 $km^2$. In contrast, granites of the Eastern Gawler Craton and Stuart Shelf occupy in excess of 20 000 $km^2$ and are dominated by the extensive Hiltaba Supersuite in which heat production averages 4.79 $\mu Wm^{-3}$. In the northern part of the CAHFP average heat production across the Georgetown, Mount Isa and Pine Creek Inliers is relatively constant with average values of 5.06 $\mu Wm^{-3}$, 4.82 $\mu Wm^{-3}$ and 4.73 $\mu Wm^{-3}$ respectively.

The central portion of the CAHFP shows greater variability, with heat production ranging from 5.79 $\mu Wm^{-3}$ in the Tanami Inlier to just 2.68 $\mu Wm^{-3}$ in the Musgrave Inlier, the latter only slightly greater than the average granite value. Heat production in the Arunta Inlier, where granites outcrop over a total area of > 27 000 $km^2$, is well above the CAHFP average at 5.24 $\mu Wm^{-3}$. This value is strongly influenced by the areally extensive Mount Webb and Napperby Suites in which heat production averages 5.92 $\mu Wm^{-3}$ and 7.61 $\mu Wm^{-3}$ respectively. Together these two granite suites comprise 42% of total granite outcrop in the Arunta Inlier. Heat production is significantly lower in the Halls Creek-Kimberley region where granites and felsic volcanics average only 3.15 $\mu Wm^{-3}$.

Granites within Proterozoic terranes outside the CAHFP, including the Albany-Fraser, Gascoyne and Paterson Orogens in Western Australia, are also characterized by above average heat production rates. For the Gascoyne Province heat production averages 3.45 $\mu Wm^{-3}$ over 11 794 $km^2$, while in the Albany Fraser Orogen heat production averages 3.84 $\mu Wm^{-3}$ over 9229 $km^2$. The much smaller Paterson Orogen, at only 737 $km^2$, has an average heat production of 4.82 $\mu Wm^{-3}$. The consistency of high values of average heat production throughout many Australian Proterozoic terranes suggests that a time dependent process, or source, of enrichment was active during the Palaeo-Mesoproterozoic growth of the Australian continent.

As noted earlier, while the values of heat production that characterize many Australian Proterozoic granites are highly anomalous when compared to global averages, these granites are also generally characterized by Thorium to Uranium ratios in the range 3-5 (Appendix A, Tables A.1-A.15). Such ratios are thought to be magmatic (e.g., Durrance, 1986) and so these granites are likely to represent primary crustal additions. This observation highlights an extraordinary geochemical problem, in so much as it is difficult to understand how such extraordinary enrichments may have resulted. Particularly, are these enriched granites products of some extraordinarily enriched source region, or the result of an unusual fractionation process? Aspects of this problem have been addressed by Neumann et al., (2000), but the origin of these granites still remains enigmatic.

Wyborn et al., (1992) present data to show that many of the I-(granodioritic) type granites which dominate the Australian Proterozoic crust are Sr-depleted and Y-undepleted, reflecting derivation from moderately shallow sources in which plagioclase, but not garnet, was stable. These data suggest that many of these Proterozoic granites have experienced a significant crustal prehistory, and for the most part reflect crustal recycling rather than new additions from the mantle. Wyborn et al., (1987) suggest that these granites have Proterozoic rather than Archaean precursors, and this

is also supported by isotopic data of McCulloch (1987). One popular, but not yet proven hypothesis for the sources of these granites is that suggested by Etheridge et al., (1987) and Wyborn et al., (1987) who proposed that they were derived from a fractionated mantle-derived underplate accreted to the base of the crust around 2000 Ma. One consequence of the apparent lengthy crustal pre-history of these granites is that successive generations of granite must have required higher temperatures to form. This notion is supported by Wyborn et al., (1998b) who, on the basis of geochemical trends, asserted that the temperature of formation of the Proterozoic I-type granites generally increased with time between 1880 and 1500 Ma. The temperature increase of the granite melts is at odds with a general decrease in the temperature of mafic melts with time, with high Mg-tholeiites dominating before ~ 1850 Ma and continental tholeiites after ~ 1850 Ma (Wyborn et al., 1998b).

Heat production rates also show trends with intrusive age, with the youngest granites in a particular terrane not only the hottest melts, but generally also the most enriched in the heat producing elements. This trend is perhaps not surprising as the heat producing elements, particularly U and Th, are strongly incompatible and will therefore be preferentially partitioned into the melt during progressive fractional crystallization. Again the large dataset compiled by Wyborn et al. (1998a) affords an examination of these variations, and in Table 2.2 I present a summary of heat production-age data for selected terranes.

The oldest granites in the CAHFP, the 1800-1850 Ma Barrumundi Igneous Suite (Etheridge et al., 1987), are the lowest heat producing with rates ranging from 1.5 $\mu Wm^{-3}$ in the Arunta Inlier, to 3.6 $\mu Wm^{-3}$ in the Tennant Creek Inlier (Table 2.2). From this time, heat production rates tend to increase, with the highest heat producing granites generally those of the early to middle Mesoproterozoic. Examples include the 1545-1490 Ma Williams and Naraku Batholiths in the Mount Isa Inlier (where heat production averages 7.9 $\mu Wm^{-3}$), 1570-1555 Ma granites and granite gneisses of the Mount Painter inlier (16.1 $\mu Wm^{-3}$) and the 1615-1480 Ma Mount Webb granite suite in the Arunta Inlier (6.1 $\mu Wm^{-3}$).

The heat flow-heat production dataset discussed here is also internally consistent, as regions of low to average surface heat flow are generally characterized by low to average surface heat production. For example in the Arunta Inlier the only available surface heat flow measurements are taken from the northern margin of the terrane. These values are relatively low when compared to the CAHFP average. In this part of the inlier these low heat flow values are likely to reflect significant Phanerozoic denudation which resulted in the removal of a large proportion of the high heat producing granitic upper crust and the exposure of the largely depleted deep crust. In contrast, many of the higher heat producing units outcrop in the south and west of the inlier and it is these granites which are responsible for the average surface heat production value of 5.24 $\mu Wm^{-3}$. Evidence for the presence of high heat producing units above the current exposure surface in the area of the heat flow measurements is recorded in the form of uranium rich sequences of the foreland Devono-Carboniferous Mount Eclipse sandstone in the Ngalia Basin (Wells and Moss, 1983). Removal of the high heat producing upper crust is also likely to account for the low normalized surface heat production value of 2.68 $\mu Wm^{-3}$ in the Musgrave Inlier. In this terrane geobarometry suggests that the deepest parts of the orogen have been exhumed from 20-30 km (Scrimgeour and Close, 1999), implying very deep levels of post-metamorphic denudation, particularly when compared to other Australian Proterozoic terranes. Low to average heat flow in the Halls Creek Orogen reflects the predominance of the lower heat production Palaeoproterozoic Barramundi granite suite (Table 2.2,

and Table A.6 in Appendix A).

It is worth reiterating at this point that the values quoted above and listed in the accompanying tables are modern heat production rates. This is important in order that they can be compared to the modern day surface heat flow data. Because the heat producing elements decay through time, average heat production values would have been significantly higher in the Mesoproterozoic and Palaeoproterozoic at the time of intrusion of the granites. For example, the average modern surface heat production in the Halls Creek Inlier is 3.1 $\mu Wm^{-3}$ but at the time of intrusion of these granites (~ 1800 Ma) this value would have been at least 4.6 $\mu Wm^{-3}$ – an increase of 48%. Similarly in the Mount Isa Inlier, where most granites are Mesoproterozoic, the average surface heat production at the time of intrusion would have been at least 6.5 $\mu Wm^{-3}$ when averaged over the entire inlier – an increase of 34% over the present day value.

These calculations are significant because they mean that the total contribution of crustal heat sources to the surface heat flow would have been significantly higher than suggested by modern surface heat flow measurements. For a modern $q_c$ of 70 $mWm^{-2}$ increased heat productivity in the past means that the total contribution from the same average crustal section at 1600 Ma would have been 89 $mWm^{-2}$ and at 1800 Ma would have been 93 $mWm^{-2}$! These calculations further highlight just how extraordinary the heat source distribution is within the CAHFP.

## 2.4 Distribution of crustal heat sources in Australian Proterozoic terranes

Recognizing that regions of anomalous surface heat flow in the CAHFP are the result of high heat production in crustal rocks impacts on our views about the crustal heat source distribution. First, the high values of surface heat production throughout many Proterozoic terranes must be restricted to the upper crust in order to be consistent with the known range of surface heat flow. This implies that the crust throughout the CAHFP is strongly differentiated with regard to the heat producing elements, an interpretation supported by regression of surface heat flow and heat production data. As outlined by Sass and Lachenbruch (1979) such a regression suggests that the heat source distribution in this region has a characteristic length scale, $h_r$, ~ 11 km (Figure 2.3). While such a distribution length scale is not dissimilar from other Proterozoic and Phanerozoic terranes (Table

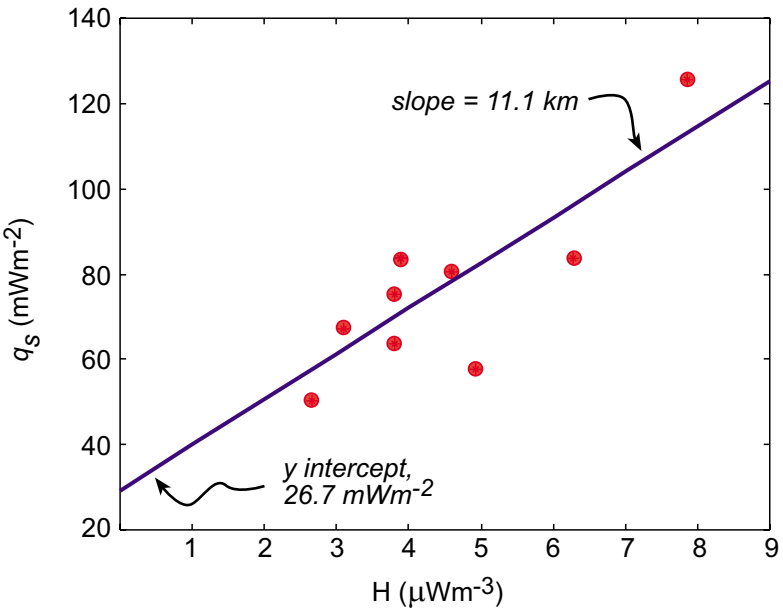


**Figure 2.3** Linear surface heat flow-heat production relationship for the Central Australian Heat Flow Province (from Sass and Lachenbruch, 1979). Regression does not include less reliable data pairs from Blockade (Queensland), Whyalla or Iron Knob (South Australia). The parameters of the regression give a heat production length scale, $h_r$, of 11.1 km and a reduced heat flow, $q_r$, of 26.7 $mWm^{-2}$. Although the parameters of this linear regression are very sensitive to the presence or absence of particular heat flow data, this analysis does support the notion that much of the surface heat flow recorded in Australian Proterozoic terranes is the result of an anomalous contribution from crustal heat sources, and that these heat sources are largely concentrated in the uppermost crust.

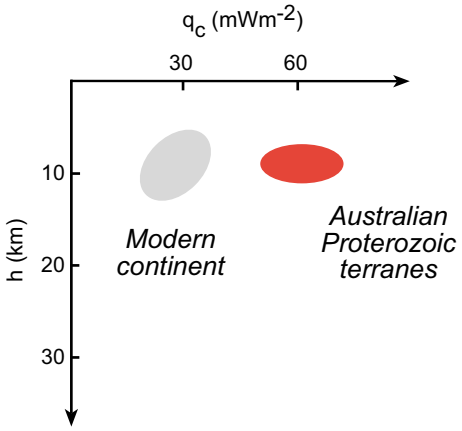


**Figure 2.4** *h*-$q_c$ diagram showing the area occupied by average modern continental crust, with $h$ ~ 10 km and $q_c$ ~ 30 mWm$^{-2}$, and that area occupied by modern Australian Proterozoic crust. The latter is characterized by similar values of the heat production length scale, but much greater values of $q_c$, commonly in the range 50-70 mWm$^{-2}$.

1.3), the total crustal contribution from internal heat sources of ~ 50-70 mWm$^{-2}$ is around twice that of average continental crust and implies that the distribution of heat sources in the CAHFP is anomalous by global standards. In terms of the *h*-$q_c$ parameterization outlined in Chapter One of this thesis, these values suggest that Australian Proterozoic terranes occupy a distinctly different region of *h*-$q_c$ space than do regions of modern continental crust (Figure 2.4).

More detailed models for the distribution of crustal heat sources may be developed for terranes in which detailed information on the thickness and distribution of units in the sub-surface is available. In the Palaeo-Mesoproterozoic Mount Isa region where detailed deep seismic data is available, the contributions of individual units to the heat flow anomaly can be constrained, allowing the development of a relatively well constrained model for the distribution of heat sources, including estimates of the parameters $h$ and $q_c$. This model is developed in Chapters Four and Five of this thesis.

As noted earlier, anomalous crustal heat source distributions characterized by high values of $q_c$ are not exclusive to Australian Proterozoic crust, although this region is to date the best example of a continental scale heat flow anomaly resulting from anomalous crustal heat production.

## 2.5 Implications for heat production distributions in the Proterozoic

Data from modern Australian Proterozoic terranes shows that anomalous surface heat flow is the result of enrichments in the heat producing elements to about twice the bulk crustal average. Because internal heat sources represent an important contribution to the lithospheric thermal budget, and in order to understand how this may have impacted on the thermal history, it is essential to characterize the contribution of these heat sources at the time at which the crust was evolving.

In order to do this it is appropriate to consider both the absolute abundance of crustal heat sources in the past, and also their distribution prior to metamorphism, magmatism and crustal differentiation. We have seen in the preceding discussion that for typical present day surface heat flows of around 80-85 mWm$^{-2}$ the crustal contribution is on average 50-70 mWm$^{-2}$. During the Proterozoic the contribution from crustal sources is likely to have been greater because:

- Barometric estimates suggest that some 10-15 km of the upper crust has been removed from many Australian Proterozoic terranes by post-metamorphic exhumation (e.g., Bodorkos et al., 1999; Rubenach, 1992; Scrimgeour and Close, 1999). Assuming a heat production rate of between 1-2 μWm$^{-3}$ (consistent with average sedimentary material, e.g., McLennan and Taylor, 1996) the presence of such crust would contribute an additional 10-30 mWm$^{-2}$ to the

total lithospheric thermal budget.

- The decay of the main heat producing elements (U, Th and K) results in a significant decrease (around 20-25 % for typical granitic compositions) in heat production over the appropriate time intervals (1500-1800 Ma). This would contribute a further 15-20 $mWm^{-2}$ to the total crustal contribution at times in the past.

On the other hand however, significant crustal shortening recorded in many terranes prior to effective cratonization is likely to have increased the thickness of upper and middle crustal lithologies and consequently structural repetition is likely to cancel the second point above, at least at the first order. Notwithstanding these considerations, constraints outlined throughout this chapter suggest that the tectonic evolution of Proterozoic terranes in Australia should be viewed in the context of a total crustal heat production, $q_c$, in excess of 50 $mWm^{-2}$ and possibly as high as 100 $mWm^{-2}$.

Such high concentrations of heat sources have important implications for every crustal process which shows fundamental dependence on thermal regime, including metamorphism, deformation and magmatism. In the remainder of this thesis, I evaluate the role and impact of the presence of such anomalous heat sources during the tectono-thermal history of selected Australian Proterozoic terranes. This first requires some knowledge of the thermal and mechanical consequences of the redistribution of heat producing elements within the crust and in the following Chapter I present such an analysis, using simple models of physical processes. This analysis is presented in terms of the parameters $h$ and $q_c$, defined in Chapter One of this thesis.

# Chapter Three

# Long-term thermal and mechanical consequences of the redistribution of heat sources within the continental crust

The previous section has shown that the anomalous surface heat flow recorded in the Central Australian heat flow province can be attributed to exceptional concentrations of the heat producing elements within the crust. In many of the Proterozoic terranes which comprise the CAHFP these crustal heat sources are thought to contribute at least ~ 50-70 $mWm^{-2}$ to the total thermal budget: more than twice that of average continental crust. Much of this heat production is contained within granites and granite gneisses in the upper 10 km or so of the crust. These observations suggest that the crust is strongly differentiated. The distribution of heat producing elements is clearly a consequence of the tectonic processes that have shaped these regions. Moreover, because lithospheric thermal regimes are sensitive to the amount and distribution of the heat producing elements, it is likely that the redistribution of heat sources has impacted on the ongoing tectonic evolution of these terranes through time. Because the $h$-$q_c$ parameterization outlined in Chapter One is independent of the analytical form of the heat source distribution, it can be used to track changes in the distribution of heat sources with time as a consequence of various crustal processes. Such changes are shown by vectors on the $h$-$q_c$ plane. The $h$-$q_c$ plane also provides a useful tool for illustrating the thermal and mechanical responses of the crust to such changes.

In this chapter I illustrate the thermal and mechanical effects of the redistribution of heat sources within the continental crust emphasising the effects which could be expected in Australian Proterozoic-like crust, where $q_c$ is in the range 50-70 $mWm^{-2}$. I first describe, both qualitatively and quantitatively, the way in which the crustal heat sources are redistributed by various tectonic processes, using simple one-dimensional models. Identifying the long-term changes in the heat source distribution arising from these tectonic processes allows the resultant thermal and mechanical responses of the crust to be quantified. As discussed at the end of this chapter, this analysis affords important insights into the factors that control the long-term behaviour of the crust, and also contributes to our understanding of how the present-day distribution of crustal heat sources has arisen.

## 3.1 Tectonic modification of crustal heat source distributions

Tectonic processes associated with reworking of the continental lithosphere (such as magmatism, deformation, sedimentation and erosion) effect changes in the distribution of heat producing elements within the crust, and thus must impact on its long-term thermal and mechanical state. In this section I first describe the qualitative changes in the distribution of heat sources which result from various tectonic processes. This introductory section is concerned only with the effects of these tectonic processes as they occur in isolation, such that magmatism and deformation are unaccompanied

by associated surficial responses or coupled deformation. The sections which follow consider the more complex changes accompanying more realistic crustal deformations. Implicit in all of these models is a one-dimensional approximation that assumes no lateral variation in the thermal parameters and, importantly, no lateral heat transfer.

The heat producing elements, and particularly the trace elements U and Th, are "incompatible" in melt systems and thus are partitioned preferentially into the product melt phase. Consequently, the generation and segregation of felsic magmas constitutes a primary mode of transport of the heat producing elements from the deep crust to the upper crust. In terms of the $h$-$q_c$ parameterization, the impact of magma generation on the heat source distribution is relatively easy to understand. When unaccompanied by coupled deformation or surficial responses, the generation and migration of magma within the crust involves no net change in crustal volume, such that crustal material is neither added or removed. Consequently the total abundance of crustal heat sources ($q_c$) will remain constant. At the same time however, the migration of the heat producing elements into the upper crust in the form of the granites results in a reduction in the heat production length scale $h$. Together these changes result in a simple vertical path on the $h$-$q_c$ plane (Figure 3.1a).

Crustal shortening deformation (where β, which is defined as the ratio of the thickness of the crust prior to and following deformation, is less than 1) unaccompanied by erosion, results in two changes to the heat source distribution. The total complement of heat sources within a crustal column will be increased, due to structural repetition, and at the same time buried to deeper crustal levels. These concomitant changes result in an increase in both $h$ and $q_c$. In contrast, crustal thinning deformations (where $\beta > 1$) which are unaccompanied by basin formation and sedimentation, will tend to attenuate the pre-existing heat production and move it to shallower levels. Such deformations therefore result in a reduction in both $h$ and $q_c$. The effects of both types of deformation are shown

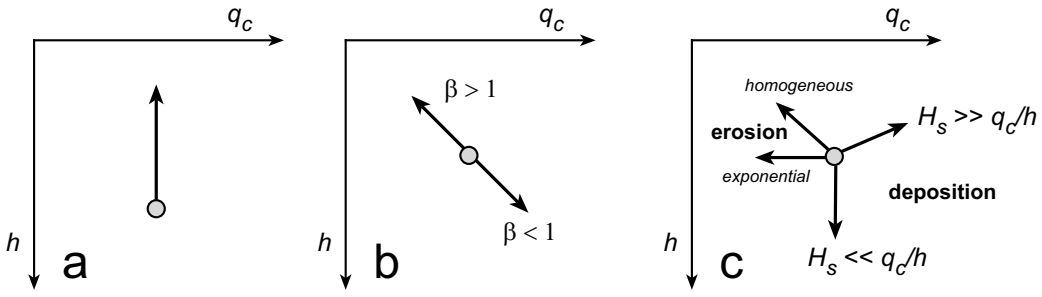


**Figure 3.1** Illustration of the qualitative changes in the heat source distribution (in terms of the parameters $h$ and $q_c$) which accompany various tectonic processes. **(a)** Illustration of the effects of magma extraction. Because the heat producing elements, and particularly U and Th, are incompatible, they will be partitioned preferentially into the melt and moved to higher crustal levels. Consequently this process results in a reduction in the length scale of the heat source distribution, $h$, while maintaining the total $q_c$. **(b)** Illustration of the effects of crustal deformation, both crustal extension ($\beta > 1$) and crustal shortening ($\beta < 1$). During crustal extension the heat source distribution will become attenuated and generally become less deeply buried; these changes resulting in a reduction in both the length scale and the total crustal contribution. Conversely, the heat source distribution will be concentrated and moved to deeper levels during crustal shortening, with these changes resulting in an increase in both the length scale and the total crustal contribution. The impact of the coupled surface processes are illustrated in **(c)**, and, if they accompany the changes occurring in **(b)**, will result in more complex changes to the heat source distribution. In both cases the impact of erosion and sedimentation depend on a number of factors. The effect of erosion on the length scale depends on the initial distribution of heat producing elements. Illustrated here are the effects of erosion on an exponential model (in which the length scale is essentially preserved on erosion) and a homogeneous model (where the length-scale is reduced in direct proportion to the reduction in $q_c$). The effect of sedimentation is also dependent on the initial distribution of heat sources, and is also dependent on the amount of heat production contained within the sediments ($H_s$) relative to the average heat production of the stretched crust ($H_c$). If $H_s$ is much greater than $H_c$ then sedimentation will result in an increase in $q_c$ and possibly a reduction in $h$ (as much of the heat sources are concentrated in the upper crust). Conversely, if $H_s << H_c$ then sedimentation will lead to a decrease in the length scale (as those heat sources already present will be buried to deeper crustal levels) and only a minor increase in $q_c$.

on the $h$-$q_c$ plane in Figure 3.1b.

The general effects of the surficial responses of erosion and sedimentation on the distribution of heat sources are illustrated in Figure 3.1c, however the actual changes resulting from these processes will depend on the initial distribution of the heat producing elements. For example, if the crustal heat sources are initially concentrated in the upper crust (i.e., low $h$), erosion will reduce the total $q_c$ via the removal of a significant proportion of the heat sources from the crustal system. Conversely, if the crustal heat sources are initially concentrated in the deeper crust (i.e., high $h$) erosion will have little effect on $q_c$. The changes in the length scale will also be dependent on the initial form of the distribution. For an exponential distribution the length scale is preserved upon erosion (see Chapter One) however erosion of a simple homogeneous or step-like distribution results in a reduction in $h$ in direct proportion to the reduction in $q_c$. Similarly, the effect of sedimentation following crustal stretching is dependent on the initial heat source distribution, but also on the ratio of the heat production added in the form of the sedimentary cover ($H_s$), and that heat production attenuated in the pre-existing crust ($H_c$). If the heat production contained within the sediments is significantly greater than that of the stretched crust, then sedimentation will result in a significant increase in $q_c$. Moreover, the presence of high concentrations of crustal heat sources within the sedimentary cover may result in a reduction in the heat production length scale, as a greater proportion of the crustal heat sources reside in the uppermost crust. Conversely, if $H_s << H_c$, then sedimentation will facilitate the burial of the pre-existing heat production, resulting in an increase in $h$ and only a minor change in $q_c$.

This simple analysis highlights the fact that the long-term redistribution of heat sources accompanying any deformation is sensitive to the way in which deformation and surface processes are coupled. The following section attempts to quantify these effects for various tectonic processes. In all models deformation and surface processes are linked isostatically such that constant surface elevation is maintained in the long-term (Figure 3.2). Consequently, crustal extension is coupled with basin formation, and crustal shortening with erosion. Long-term changes are those that remain following dissipation of all thermal transients which accrue from the advective heat transport that

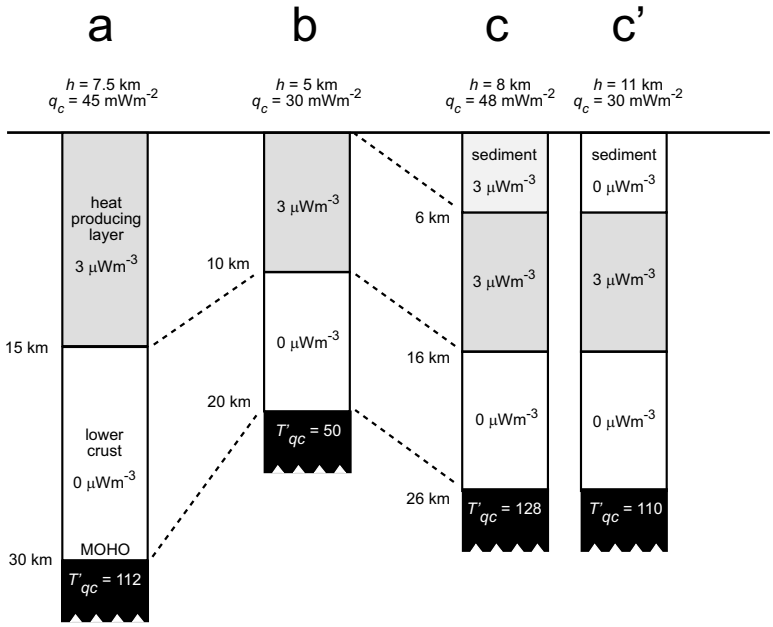


**Figure 3.2** Illustration of the effect of extensional deformation, coupled with an isostatic response, on the crustal heat source distribution. Given an initial lithospheric column (shown in **a**), stretching (shown in **b**) results in attenuation of pre-existing heat production, while the surface response of basin formation (shown in **c**) moves it to deeper levels, resulting in an increase in $h$. The final heat production distribution following restoration of the original surface elevation depends on the amount of heat production contained in the basin-filling sediments, $H_s$. As noted in Figure 3.1 this may result in either an increase or decrease in $q_c$.

normally accompanies the deformation. This discussion also assumes that there are no new additions of the heat producing elements during deformation or magmatism and that any deformation operates homogeneously throughout the crustal column. Models are presented for two initial configurations of crustal heat sources – the exponential and homogeneous (step-like) models, which were discussed in Chapter One of this thesis (Figure 1.5).

### 3.1.1 Quantitative changes in the heat source distribution due to felsic magmatism

The generation and segregation of magma allows significant vertical reorganization of the crust and is an important agent of crustal differentiation. As outlined above, the heat producing elements, and particularly the trace elements U and Th, are highly incompatible with respect to mantle minerals and so are likely to be partitioned preferentially into the melt phase. Consequently felsic magmas contain much of the crustal complement of heat production (Table 1.4); as has been shown to be the case for the Australian Proterozoic examples discussed in Chapter Two (Tables 2.1, 2.2). Given that the isotopic and geochemical characteristics of these Proterozoic granites suggest that much of the heat production contained within them was scavenged largely from crustal sources (e.g., Wyborn et al., 1992), then the generation and upward migration of these granites must have effected profound changes in the distribution of heat sources.

Figure 3.3 shows the effect of the generation of a granitic melt from the middle-deep crust for various initial exponential (Figures 3.3a and 3.3c) and homogeneous (Figures 3.3b and 3.3d) heat source distributions. These figures are based on a highly simplified model of magma extraction in which melting is assumed to occur throughout some known thickness of the deep-middle crust, with a specified proportion of the heat sources available in this source region scavenged by the product melt. In the models shown in Figures 3.3a and 3.3b, the source region comprises the lower 10 km of the crust while for Figures 3.3c and in 3.3d, melting occurs in the lower 15 km of the crust.

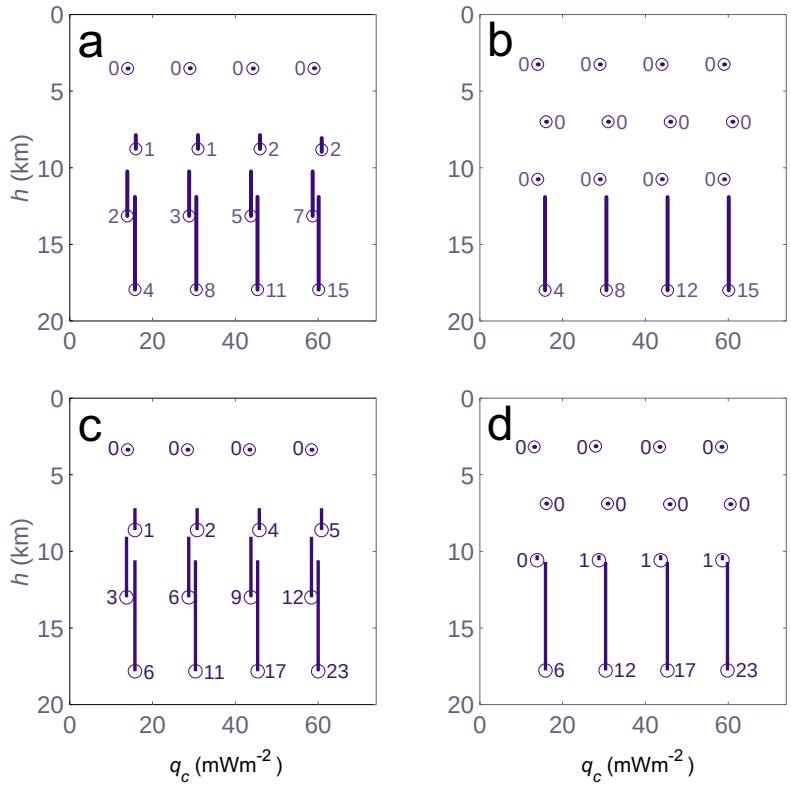


**Figure 3.3** Illustration of the effects of magma extraction from the deep-middle crust. In all examples shown 85% of the heat sources available in the source region are scavenged into the melt, meaning that these models reflect very efficient magma extraction processes. **(a)** and **(c)** are constructed for an initial exponential distribution and **(b)** and **(d)** for an initial homogeneous distribution. The circles represent the initial heat source distributions, in terms of the parameters $h$ and $q_c$, while the thick lines show the way in which the heat source distribution changes as a consequence of the melt extraction. The figures alongside each circle show the amount of heat production carried in the product granite, expressed in terms of its contribution to the surface heat flow. In figures **(a)** and **(b)** melting occurs in a source zone which comprises the lower 10 km of the crust, in figures **(c)** and **(d)** melting occurs in the lower 15 km of the crust; this second configuration illustrates the sensitivity of the amount of melting observed to the size of the source region.

The parameters chosen for this model reflect very efficient magma extraction, as in all examples 85% of the available heat sources present in the source region are scavenged into the melt. The product melt is then assumed to migrate out of the source region and into the upper crust. The circles show the initial heat source distribution prior to melt extraction and the vectors show the $h$-$q_c$ path followed by the crust on the way to its post-melt configuration. The final value of $h$ is taken from calculating the reduction in the length scale of the heat source distribution resulting from the removal of that amount of heat production contained within the product melt. The precise value of $h$ after melt generation will depend on the crustal level at which the product melt is emplaced, which is in turn dependent on the density and buoyancy of the melt and the country rocks.

In the same way as shown in Figure 3.1, simple melt extraction of the type described here results in a vertical path on a $h$-$q_c$ diagram, as the total crustal compliment of heat sources remains constant. For any given source region the greatest change in the heat source distribution occurs for initial distributions characterized by high values of $h$, i.e., heat source distributions where a significant proportion of the heat sources reside in the lower crust. In contrast, deep to middle crustal melting has little impact on the distribution of heat sources in crust where the initial distribution is characterized by low values of $h$. It is clear that such results should be the case when the geometry of the model and source region are considered. In other words, deep to middle crustal melting can only change the distribution of crustal heat sources if a significant proportion of those heat sources initially reside within the melt source region. The most obvious corollary of this result is that once the heat sources have been redistributed into the upper crust as a result of melting, a similar melting event later in the history of that crust would not result in further significant redistribution of the crustal heat sources.

### 3.1.2 Quantitative changes in the heat source distribution due to extension and convergent deformation

The effect of a 10% crustal extension (i.e., $\beta = 1.1$) on the distribution of heat sources is illustrated for the exponential and homogeneous heat source distributions in Figures 3.4a, and 3.4b. The effect of the same magnitude crustal shortening deformation (such that $\beta = 0.9$) is illustrated in Figures 3.5a and 3.5b. Following the conventional definition, as appropriate for a one-dimensional lithospheric column, the parameter $\beta$ is used as a measure of the deformation given by the ratio of the initial to the deformed crustal thickness. What is clear from these diagrams is that the greatest changes in the parameters of the heat source distribution result when deformation acts on a heat source distribution initially characterized by high values of $h$, high values of $q_c$, or high values of both parameters.

Figures 3.4c, 3.4d and 3.5c, 3.5d show the effects of the associated surficial response, i.e., erosion in the case of the crustal extension depicted in Figure 3.4, and sedimentation in the case of the crustal shortening deformation illustrated in Figure 3.5. In each case the surface response restores the original surface elevation assuming local isostatic balance. As noted by Sandiford and McLaren (in press) this condition is implicit in all models which treat the lithosphere as a one-dimensional column, and while obviously simplistic, is sufficient to capture the first-order dynamics of the continental lithosphere for processes that operate on spatial scales which are large when compared

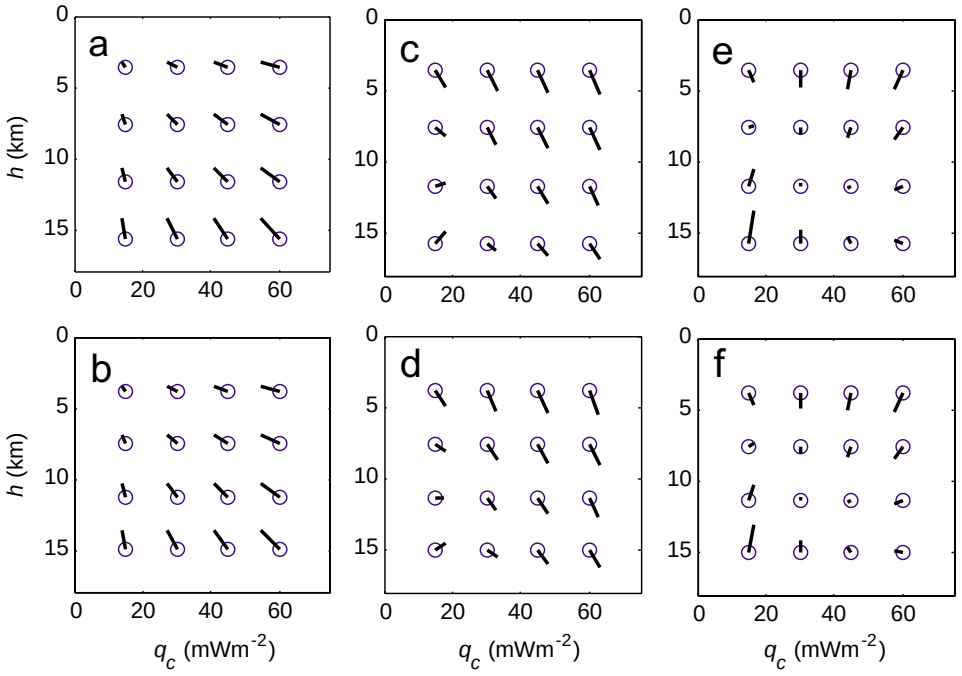


**Figure 3.4** Illustration of the effects of a 10% crustal extension (β = 1.1) on the distribution parameters $h$ and $q_c$ for **(a, c** and **e)** an initial exponential distribution and **(b, d** and **f)** an initial homogeneous distribution. **(a)** and **(b)** show the effect of the deformation, **(c)** and **(d)** show the effect of deposition sufficient to restore the original value of surface elevation. In this case 1.9 km of sedimentation is required. **(e)** and **(f)** show the combined effect of stretching and basin formation.

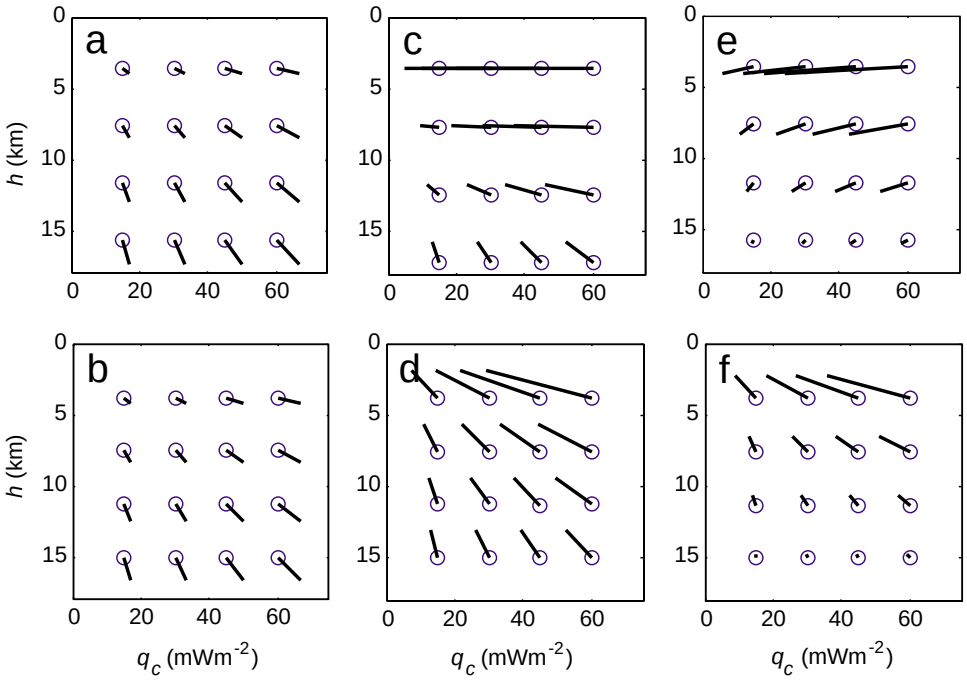


**Figure 3.5** Illustration of the effects of a 10% crustal shortening deformation (β = 0.9) on the distribution parameters $h$ and $q_c$ for **(a, c** and **e)** an initial exponential distribution and **(b, d** and **f)** an initial homogeneous distribution. **(a)** and **(b)** show the effect of the deformation, **(c)** and **(d)** show the effect of erosion sufficient to restore the original value of surface elevation. In this case 3.7 km of erosion is required. **(e)** and **(f)** show the combined effect of shortening and erosion.

to the thickness of the lithosphere, i.e., greater than several hundred kilometres. In order to preserve the surface elevation a number of assumptions are made about the density structure of the crust. First, there is assumed to be no significant density difference between the upper and lower crust. The important implication of this assumption is that following crustal shortening the amount of erosion required to restore the original surface elevation will also, to a first approximation, restore the original crustal thickness. Second, the basin filling sediments are assumed to be significantly less dense than the crust. A consequence of this second assumption is that the crust shows significant long-term thinning following extension.

Figures 3.4e, 3.4f and 3.5e, 3.5f show the combined effects of the deformation and linked surface responses. The difference in the paths depicted in these diagrams from those in the simple models shown in Figures 3.4a, 3.4b, 3.5a and 3.5b highlights the importance of the way in which deformation and surface responses interact in determining the long-term changes in the heat

production parameters. While heat source distributions characterized by low values of $h$ and $q_c$ are relatively unaffected by deformation when it acts alone, a coupled surficial response has a much more dramatic impact. This is particularly so for crustal shortening deformations as much of the heat production is removed via erosion. For extensional deformation the change is greatest for distributions of high $h$, but low $q_c$.

The results discussed here show that the coupling of crustal shortening and erosion provides an effective means for modifying the crustal heat source distribution, particularly when the crustal heat production is already significantly differentiated, i.e., for initial heat source distributions which are characterized by low values of $h$. While crustal shortening tends to increase $q_c$, by thickening the heat producing layer, erosion tends to reduce it. Consequently, if the existing heat production is already concentrated near the surface (i.e., small $h$) the loss of heat production during erosion will be much greater than the increase in heat production due to the thickening. This results in a significant decrease in $q_c$ and reflects the fact that the coupling of crustal shortening and erosion essentially removes upper crustal material and replaces it with lower crustal material. The change in the length scale, $h$, is dependent on the form of the initial distribution of heat sources. As shown in Figure 3.5, for distributions approximating the homogeneous model, $h$ will be reduced as a consequence of combined homogeneous shortening and erosion. For an exponential distribution, providing $h << z_c$, $h$ will increase by $1/\beta$, because, as shown by Lachenbruch (1968) erosion preserves the exponential length-scale established by the deformation. An important result shown in Figure 3.5 is that the coupling of crustal shortening and erosion is much less effective in changing the heat source distribution when the deformation acts upon largely undifferentiated (i.e., large $h$) crust. In this case the heat production character of the lower crust is essentially the same as the upper crust so thickening and erosion effect little change to the heat source distribution.

In contrast to crustal shortening deformations, crustal extension and sedimentation are not as effective in modifying the heat production distribution; although the effects shown in Figure 3.4 are strongly dependent on the chosen model parameters. For the models shown here crustal extension has the greatest effect on heat source distributions which are characterized by low $h$, or by high $h$ and low $q_c$. For other distributions, and particularly distributions characterized by high values of both $h$ and $q_c$, extension and basin formation have little impact on the distribution of heat sources.

As noted earlier however, deformation in all the models discussed here is assumed to operate homogeneously on the crustal column. Rather different $h$-$q_c$ paths may result when large-scale discontinuities in the deformation pattern are allowed, such as crustal scale thrust faulting, for example. Typically such discontinuities are an important component of deformation when large strains accumulate, but are less likely to be important when finite strains are small, as is typical of intraplate deformation associated with reworking of continental interiors. Examples throughout the remainder of this thesis show that this analysis is particularly relevant to the role played by intra-continental deformation.

## 3.2 Thermal effects of the redistribution of heat producing elements

The changes in the heat source distribution affected by the various tectonic processes outlined above will impact on the thermal structure of the crust. This section illustrates these changes. Again for the sake of simplicity both idealized homogeneous and exponential models are used.

The temperature field for the exponential model is calculated according to Equation 1.4 (in Chapter One), with the length scale of the exponential distribution, $h_r$, equivalent to the parameter $h$ used here. The temperature field of the homogeneous model is a simplification of the formulation for a multilayer model given by Liu and Zoback (1997), where the temperature at the base of a layer, $T_{i+1}$, is a function of the temperature at the top of that layer, $T_i$, the heat flow at the top of the layer, $q_i$, and the thermal conductivity, $k_i$, thickness, $z_i$, and heat production, $H_i$, of that layer. This can be written:

$$T_{i+1} = T_i + \frac{q_i}{k_i} z_i - \frac{H_i z_i^{\,2}}{2 k_i} \tag{3.1}$$

where

$$q_{i+1} = q_i - H_i z_i \tag{3.2}$$

This formulation allows the temperature field of any arbitrary layered model to be evaluated, provided the heat production and thermal conductivity are constant throughout each layer and the latter is temperature independent. For the case of the single layer model used here, the length scale $h$ is equivalent to half the thickness of the layer, $h_r$.

As outlined in Chapter One of this thesis, the temperature distribution arising from various heat source distributions can be compared to that which would arise in the absence of all heat sources, with the maximum difference defining the contribution from crustal heat sources, here termed $T'_{qc}$. Calculating the temperature field for a number of different heat source distributions allows the $h$-$q_c$ plane to be contoured for $T'_{qc}$, as shown for the exponential model in Figure 3.6. This analysis shows the sensitivity of deep crustal thermal regimes not only to the total heat contributed by crustal sources, $q_c$, but also to the distribution of these heat sources. For example, for a value of $q_c$ of 30 mWm$^{-2}$, as appropriate for the average modern continental crust, changing the length scale from 2.5 to 10 km results in an increase in lower crustal temperatures of 75°C (assuming an average thermal conductivity of 3 Wm$^{-1}$K$^{-1}$).

The shape of the contours shown in Figure 3.6 emphasizes the dramatic effect of the presence of high concentrations of heat sources within the crust, an observation pertinent to the Australian Proterozoic examples discussed here. For a given distribution with $h$ equal to 10 km, changing the total compliment of crustal heat sources from 30 mWm$^{-2}$ to 60 mWm$^{-2}$ results in an increase in lower crustal temperatures of around 100°C. Lower crustal temperatures in crust characterized by such high $q_c$ distributions also show the strongest dependence on the distribution length scale, with only minor variations in $h$ causing significant long-term changes in the thermal regime.

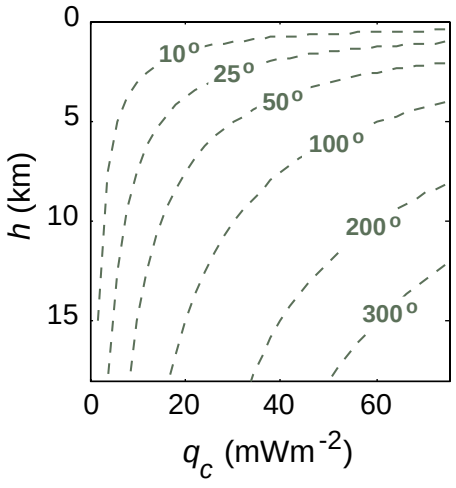


**Figure 3.6** $h$-$q_c$ space contoured for the long term change in the thermal structure of the deep crust, $T'_{qc}$. Figure calculated for an exponential distribution, and a 40 km crustal column.

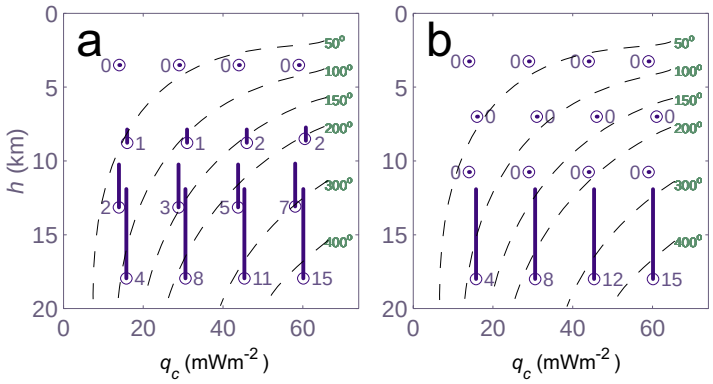


**Figure 3.7** As for Figure 3.3, but also contoured for $T'_{qc}$. **(a)** is for an exponential distribution and **(b)** is for a homogeneous distribution. The melt source region comprises the lower 10 km of the crust.

Because changes in the heat production distribution arising from various tectonic processes can be quantified, the $h$-$q_c$ diagram contoured for $T'_{qc}$ allows the long-term thermal effects accompanying these processes to be calculated. In the following section I present these results, for the same simple models of deformation and magmatism discussed in the previous section.

### 3.2.1 Thermal effects accompanying magmatism

As shown in Figure 3.7, the thermal effects accompanying magmatism are strongly dependent on the initial distribution of heat sources, and particularly the total abundance of crustal heat sources, $q_c$. For distributions of the same initial $h$, but different values of $q_c$, the change in the distribution length scale occurring as a result of magmatism will be the same, however the long-term thermal effects accompanying that magmatism will be significantly different. For example, for an initial heat production distribution of length scale $h$ equal to 18 km and $q_c$ equal to 15 mWm$^{-2}$, the change in lower crustal temperatures following magmatism is ~ 40°C. For an initial distribution of the same length scale but with a total crustal contribution of 60 mWm$^{-2}$, this change is around 150°C. This observation highlights the sensitivity of crust containing anomalous concentrations of the heat producing elements.

The results summarized in Figure 3.7 suggest that magmatism is an effective means of redistributing crustal heat sources in crust of high initial $h$, and that significant long-term lower crustal cooling will accompany this redistribution. This long-term cooling is most significant for crust also characterized by high values of $q_c$.

### 3.2.2 Thermal effects accompanying deformation

For the theoretical deformations discussed in the previous section, i.e., a 10% crustal stretch and a 10% crustal shortening, the long-term changes in the thermal structure of the deep crust can be quantified. Figures 3.8 and 3.9 show, respectively, the thermal effects of these deformations using $h$-$q_c$ diagrams contoured for $T'_{qc}$. In each Figure (a), (c) and (e) are appropriate for an exponential heat source distribution, while (b), (d) and (f) are constructed for a homogeneous single layer model.

For crustal thinning deformations where $\beta < 1$, the long-term thermal consequences are strongly dependent on whether basin formation occurs and, if it does, on the thermal parameters of the basin filling sediments. In Figures 3.4 and 3.8 the basin fill is assumed to have crustal heat production of 1.5 μWm$^{-3}$, which McLennan and Taylor (1996) suggest is typical of the upper crust.

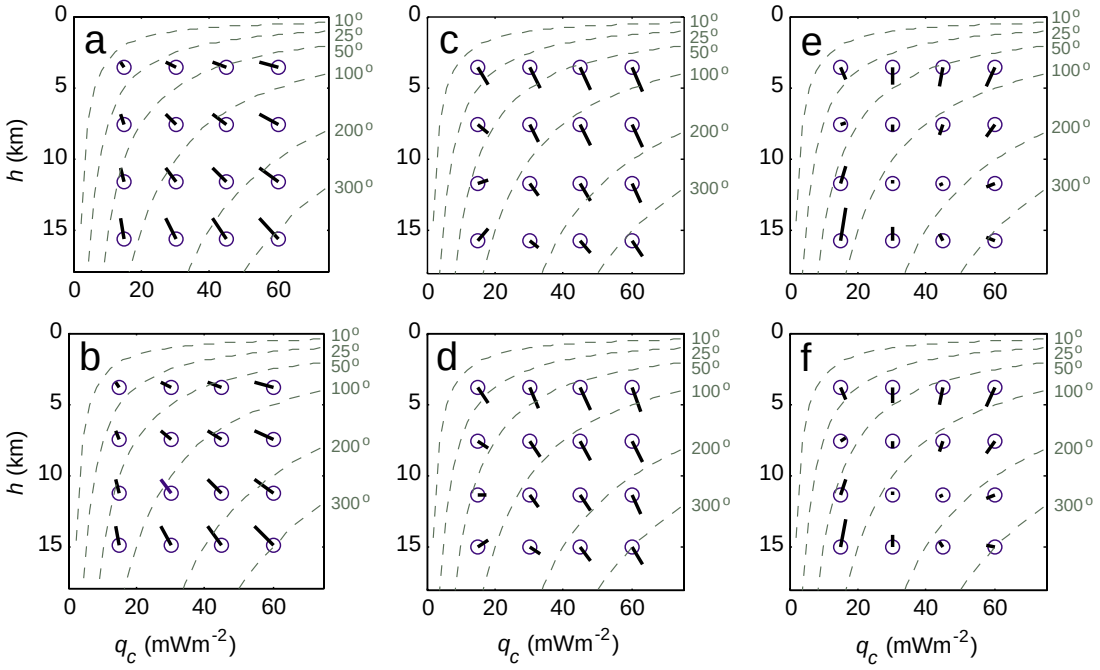


**Figure 3.8** As for Figure 3.4, but also contoured for $T'_{qc}$.

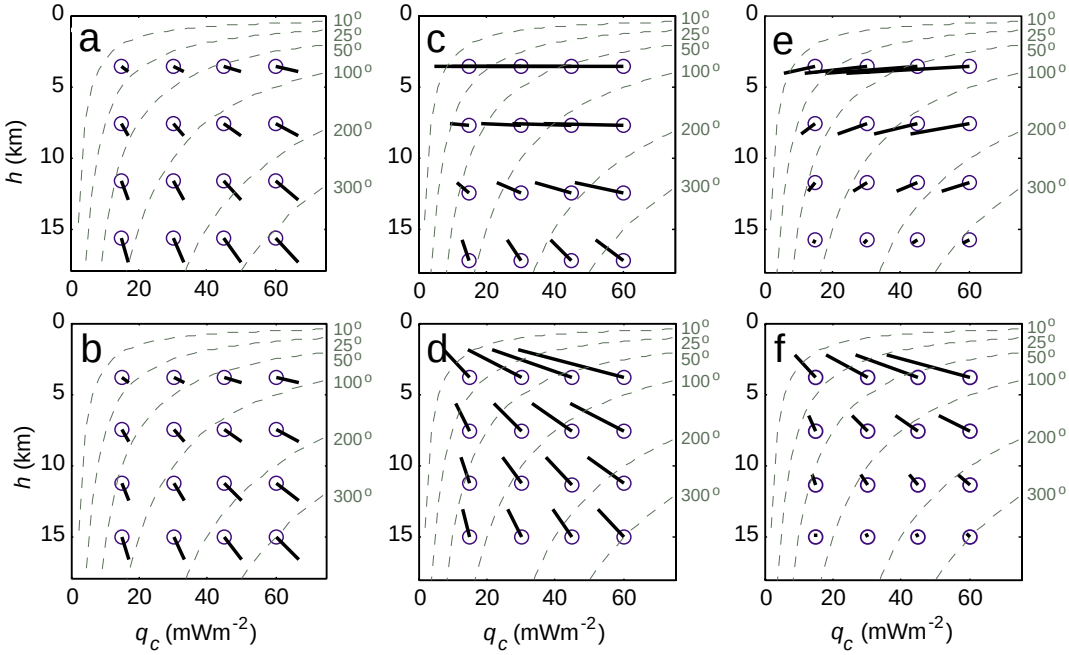


**Figure 3.9** As for Figure 3.5, but also contoured for $T'_{qc}$.

If crustal thinning occurs without basin formation, as shown in Figures 3.8a and 3.8b, then both $h$ and $q_c$ will be reduced by the factor $1/\beta$ for all heat source models, with these changes resulting in long-term lower crustal cooling. The greatest cooling effect is seen for heat source distributions of high $h$ and high $q_c$.

If the subsidence resulting from the crustal thinning is accompanied by sedimentation, the resulting changes in $h$ and $q_c$ may lead to either an increase or a decrease in $T'_{qc}$ (e.g., Sandiford, 1999). As shown in Figure 3.8e and 3.8f, increases in $T'_{qc}$ are expected when the length scale of the pre-orogenic heat source distribution is less than about 10 km. For initial configurations characterized by higher values of $h$ the combination of stretching and basin formation can lead to long-term reductions in $T'_{qc}$ of up to 10°C for the simple 10% extension shown in these models. Importantly though, these values are dependent on the assumed density and heat production character of the

basin sediments, with more dense and / or more radiogenic sediments leading to increased values of $T'_{qc}$ for a given deformation. In the models which are shown here the basin filling sediments are significantly less dense than the attenuated crust. This relationship is expressed in terms of relative densities, thus:

$$\rho' = \frac{\rho_c \pm \rho_s}{\rho_m \pm \rho_c} \approx 0.66 \tag{3.3}$$

A consequence of this relationship (which is standard for typical basin fill densities) is that the crust shows significant long-term thinning following extension. Consequently the calculated values of $T'_{qc}$ shown in Figure 3.8 cannot be related directly to long-term changes in moho temperature. Additional cooling of the Moho due to its long-term shallowing will be dependent on the geothermal gradient at Moho depths.

Figure 3.9 shows that the long-term changes in the thermal structure of the deep crust resulting from shortening and erosion can be quite significant. If crustal shortening occurs without an associated surface response (Figures 3.9a, 3.9b) then both $h$ and $q_c$ will increase by the factor $1/\beta$ for all heat source models. Such changes in the heat source distribution result in long-term lower crustal heating. Again, the greatest change in lower crustal temperatures is seen for heat source distributions characterized by high values of both $h$ and $q_c$.

If the shortening is accompanied by erosion sufficient to restore the pre-orogenic thickness, the precise changes in the long-term thermal structure are strongly dependent on the pre-orogenic heat source distribution. Deformation of crust characterized by either an initial homogenous heat source distribution or an initial exponential distribution will lead to significant lower crustal cooling, particularly for values of $h$ less than 10 km. This is largely because a significant proportion of the available heat sources will be removed by the erosion accompanying the deformation. For higher values of $h$ long-term cooling is also seen, although not to the same extent as for distributions of low initial $h$. For typical crustal heat production parameters, i.e., $h \sim 10$ km and $q_c \sim 30$ mWm$^{-2}$, 10% shortening followed by erosion will lead to a reduction in deep crustal temperatures by 10-30°C. Because the Moho will be returned to its original depth following erosion, it will be expected to experience all of this predicted cooling.

## 3.3 Heat source distributions and the mechanical state of the crust

The previous section has shown that the redistribution of lithospheric heat sources effected by deformation and magmatism may result in changes in the thermal regime of the deep crust. Such changes are quite significant, even for relatively minor deformations. Moreover, because the rheological parameters of the crust are generally considered to be temperature dependent, with upper mantle temperatures providing a useful proxy for lithospheric strength (e.g., Sonder and England, 1986), the changes in the deep crustal thermal structure following the redistribution of crustal heat sources will influence the long-term mechanical state of the lithosphere. This section attempts to quantify the effects of such long-term changes using a “Brace-Goetze” model rheology.

### 3.3.1 Background to calculations of lithospheric strength

As noted by Molnar (1992) the laboratory work of W.F. Brace, C.G. Goetze and their colleagues has provided the basis for much of the current knowledge about the strength of the crust and upper

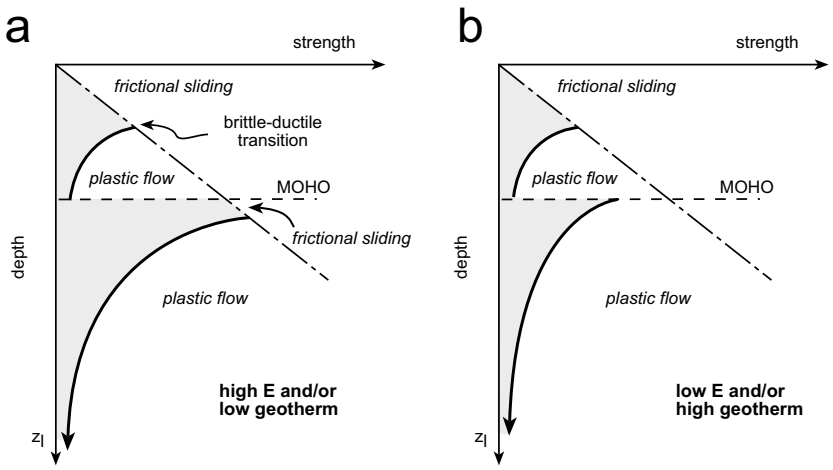


**Figure 3.10** Schematic illustration of the variation in lithospheric strength with depth. The brittle-ductile transition marks the onset of plastic flow. Deformation by frictional sliding generally operates only in the brittle zone. The total strength of the lithosphere is given by the area under the strength-depth curve. The strength is a function primarily of the vertical compositional structure of the lithosphere, the geotherm and the strain rate (*E*). **(a)** is appropriate to a low geotherm or a high strain rate. This means that the lithosphere is strong and the strongest part is the brittle upper mantle, **(b)** is appropriate to a high geotherm or low strain rate, that is, a weaker lithosphere where there is no brittle mantle. Note that the proportion of the total strength of the lithosphere which is concentrated in the crust increases with increasing geotherm.

mantle. The "Brace-Goetze" rheology, in which the lithosphere is assumed to deform by a combination of frictional sliding and ductile creep, is the most widely accepted model for the variations in lithospheric strength, and is described in detail by Brace and Kohlstedt (1980). Implicit in the model is the recognition that rocks composed of silicate minerals are characterized by rheological properties which vary as a function of both temperature and pressure. Consequently crustal strength varies with depth. A typical "Brace-Goetze strength profile" for the continental crust, as shown in Figure 3.10, consists of three main segments: (1) a brittle upper crust in which strength increases with depth, (2) a ductile lower crust in which strength decreases rapidly with depth, and (3) a ductile, but much stronger, upper mantle where strength also decreases with depth (Molnar, 1992).

The upper part of the strength profile, corresponding to rocks at low to moderate pressures and depths of < 15 km is best constrained, largely as conditions in this zone can be readily replicated by laboratory experiments. In this region of the crust brittle deformation occurs and the rocks undergo fracture. Frictional sliding on such fractures is the dominant mechanism controlling yield strength. Laboratory experiments suggest that for the great majority of lithologies a linear frictional criterion applies (Figure 3.10). This relationship is known as Byerlee's Law (from the work of Byerlee, 1978) and is based primarily on observations of frictional resistance on rock-rock surfaces (Carter and Tsenn, 1987). It can be written as:

$$\frac{S_1 - P_p}{S_3 - P_p} = f(\mu) = [(1+\mu^2)^{1/2} + \mu]^2 \qquad (3.4)$$

where $S_1$ and $S_3$ are the maximum and minimum compressive stresses respectively, μ is the coefficient of friction and $P_p$ is the pore pressure. Several models for the linear failure criteria exist and are commonly invoked in calculations of lithospheric strength, these models generally assume hydrostatic pore pressure and a coefficient of friction of ~ 0.6 (Byerlee, 1978). These two parameters, as well as the orientations of the principal stresses, determine the rate at which strength increases with depth.

Beyond the depths where frictional sliding can be considered the dominant failure mechanism, models for lithospheric strength require knowledge of the petrologic composition and temperature structure (e.g., Liu and Zoback, 1997). In these deeper regions of the lithosphere ductile creep is the

dominant deformation mechanism and is strongly dependent on temperature. In most cases the ductile creep strength is assumed to conform to a power law creep model and so can be written as:

$$\sigma_1 - \sigma_3 = \left(\frac{E}{A}\right)^{\frac{1}{n}} \exp\left(\frac{Q + PV^*}{nRT}\right) \tag{3.5}$$

where $E$ is the strain rate, $R$ is the gas constant, $T$ is the temperature (K), $A$ is a material constant, $n$ is the power law exponent, and $Q$ is the activation energy (Liu and Zoback, 1997 and references therein). The exponential term expresses the inverse exponential dependence of strength on temperature and is responsible for the curved portion of the strength profile (Figure 3.10). In the above equation the $PV^*$ term is generally small compared to $Q$ and so the relationship is usually approximated by:

$$\sigma_1 - \sigma_3 \sim \left(\frac{E}{A}\right)^{\frac{1}{n}} \exp\left(\frac{Q}{nRT}\right) \tag{3.6}$$

The parameters $A$, $n$ and $Q$ are stress and temperature independent (e.g., Kirby and Kronenberg, 1987) and this observation has allowed a number of models for the strength of various sections of the lithosphere to be developed. Such models are the result of laboratory experiments on different lithotypes, and several have become widely accepted as type examples for weak, intermediate and strong rocks. The Adirondack and Pikwitonei granulites are considered to typify “weak” and “strong” lower crust respectively (Wilks and Carter, 1990), while different dunite samples are used to describe “weak”, “intermediate” and “strong” upper mantle rocks (Chopra and Paterson, 1981, 1984). Table 3.1 lists some commonly used rheological parameters and the regions of the lithosphere they are used to model.

Although these models are widely accepted and are in common use, their application to lithospheric conditions is considerably uncertain. Paterson (1987) presents a discussion of such uncertainties highlighting the problems introduced by the extrapolation of various rheological flow laws from laboratory conditions to the geological realm, and the uncertainties associated with our incomplete understanding of the compositional and mineralogical structure of the lithosphere. The latter may introduce uncertainties in assigning which particular flow laws apply at different lithospheric depths. In addition to these factors, the uncertainties in measuring the rheological parameters in the laboratory introduce errors to the strength calculation. For example, as shown in Table 3.1, the uncertainties in the activation energy alone are commonly ~ 5%-10%. Molnar (1992) shows that these levels of uncertainty introduce a factor of 10 in the uncertainty in the calculated

**Table 3.1** *Commonly used rheological parameters describing ductile creep*

| *Rock or mineral type* | *Flow parameter, A ($MPa^{-n}s^{-1}$)* | *Power Index, n* | *Activation energy, Q ($kJmol^{-1}$)* | *Models* | *Source* |
|---|---|---|---|---|---|
| Westerly granite (wet) | $1.995 \times 10^{-4}$ | 1.9 | 140.6 | UC | Hansen & Carter (1983) |
| Adirondack granulite (felsic) | $7.943 \times 10^{-3}$ | 3.1 | 243 | Weak LC | Wilks & Carter (1990) |
| Pikwitonei granulite (mafic) | 12589 | 4.2 | 445 | Strong LC | Wilks & Carter (1990) |
| Anita Bay dunite (wet) | 10000 | $3.35 \pm 0.2$ | $444 \pm 24$ | Weak UM | Chopra & Paterson (1981) |
| Aheim dunite | 398.11 | $4.5 \pm 0.3$ | $498 \pm 38$ | Intermediate UM | Chopra & Paterson (1981) |
| dry dunite | 31623 | $3.6 \pm 0.2$ | $535 \pm 33$ | Strong UM | Chopra & Paterson (1984) |

Data summarized from a compilation by Carter & Tsenn (1987) and Liu & Zoback (1997); UC = Upper crust, LC = Lower crust; UM = Upper mantle.

strength at temperatures of 700°C. A third source of error is related to uncertainties in the absolute thermal structure of the lithosphere, arising from our incomplete knowledge of the thermal properties, particularly thermal conductivity and heat production.

Together these uncertainties introduce significant error into any calculation of absolute lithospheric strength and suggest that Equation 3.6 cannot be usefully applied in a quantitative manner. Recognizing this, the analysis shown in the following section emphasizes the relative changes in lithospheric strength that accompany various temperature changes. While the absolute magnitude of these changes will be dependent on the precise composition and thermal structure, it seems likely that the relative changes in lithospheric strength are more robust than any absolute calculation because many of the uncertainties outlined above will cancel.

### 3.3.2 Mechanical consequences of the redistribution of heat producing elements

Given the relationships outlined above, recognizing that the $h$-$q_c$ plane can be contoured for thermal structure (as shown in Figure 3.6) means that it can also be contoured for lithospheric strength (Figure 3.11). Figure 3.11a shows the variations in the strength of lithosphere forced to deform at a constant strain rate. Figure 3.11b shows variations in the effective strain rate for the lithosphere when subject to an imposed tectonic load. Both figures highlight the sensitivity of the integrated lithospheric strength and the effective strain rate to the parameters of the heat source distribution. For example, varying either $h$ or $q_c$ by a factor of 2 leads to a variation in effective strength by a factor of 2-3, and effective strain rates by 1-2 orders of magnitude.

This analysis highlights the temperature dependence of the "Brace-Goetze" rheology, and together with the observations outlined in Section 3.2, suggests that through the redistribution of heat producing elements the primary tectonic processes may impact significantly on the long-term

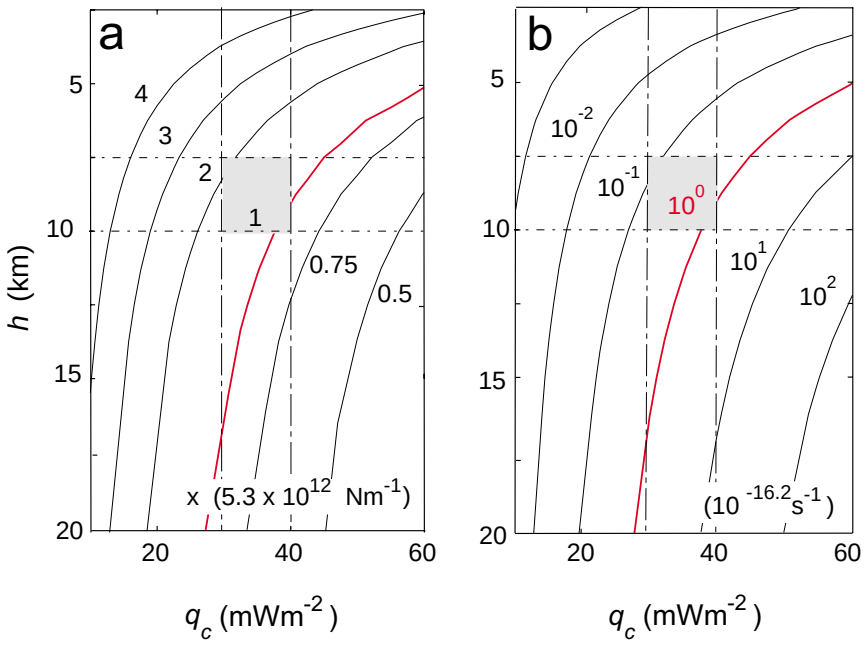


**Figure 3.11** Heat source distributions and the mechanical state of the crust **(a)** shows the $h$-$q_c$ plane contoured for integrated lithospheric strength, **(b)** shows the $h$-$q_c$ plane contoured for rate of deformation subject to an imposed tectonic load. As discussed in the text a "Brace-Goetze" lithospheric rheology is assumed. In this model deformation occurs by a combination of frictional sliding and temperature-dependent creep. The strength parameters shown in (a) are normalized against a configuration characterized by $q_c$ = 45 mWm$^{-2}$ and $h$ = 7 km. The shaded area illustrates that, with all other factors equal, a 25% reduction in both $h$ and $q_c$ will result in an increase in strength by a factor of 2, or a decrease in strain rate in response to an imposed load by one order of magnitude. The calculations are sensitive to a large number of assumed parameters as well as the material parameters constraining creep and frictional sliding. In these models thermal conductivity, $k$, is 3 Wm$^{-1}$K$^{-1}$ while the mantle heat flow, $q_m$, is 30mWm$^{-2}$.

stability of the crust. Again these effects can be quantified using the $h$-$q_c$ plane.

The previous section has shown that magmatism, particularly when occurring in crust which is characterized by high initial values of $h$, results in significant lower crustal cooling. Figure 3.11 suggests that such cooling will be accompanied by an increase in total lithospheric strength. Importantly though, while the relative change in the distribution of heat sources for given $h$ is the same for all values of $q_c$ (Figure 3.4), the resultant mechanical effect is not the same. The greatest relative change is seen in crust characterized by lower initial $q_c$. For example, for $h$ equal to 12.5 km and $q_c$ equal to 15 $mWm^{-2}$, the magma extraction shown in Figure 3.3a results in an increase in effective strength by a factor of 1.25. In contrast, if $q_c$ was 50 $mWm^{-2}$, effective strength would increase by a factor of just 1.1.

The long-term cooling accompanying crustal shortening deformations and subsequent erosion also leads to crustal strengthening, which is most significant for crust whose heat source distribution is already differentiated. Shortening deformation does not lead to any significant long-term change in total strength for crust characterized by high initial $h$.

This result also holds for crustal extension, where the most significant changes in crustal strength accompany deformation of crust characterized by low initial $h$. For distributions of high $q_c$, small increases in the length scale of the heat production distribution as a consequence of burial result in marked decreases in crustal strength. In contrast, extension occurring in crust of high initial $h$ has no significant effect on the long-term mechanical state of that crust, despite impacting significantly on the distribution of those heat sources (particularly for distributions of high initial $h$, but low initial $q_c$) (c.f., Figures 3.3, 3.11). For crust with high initial values of both $h$ and $q_c$, crustal extension is accompanied by only very minor increases in total lithospheric strength. However, as noted in Section 3.2.2 above, the changes in lithospheric strength during extension are very sensitive to the change in Moho depth, which is in turn dependent on the relative density of the sediments which infill the basin ($\rho_s$) and the density of the crust which is attenuated ($\rho_c$). Sandiford (1999) provides a detailed evaluation of these effects.

Therefore, in general terms, when they effect changes in the heat production distribution magmatism and crustal shortening deformation lead to long-term lower crustal cooling and strengthening while crustal extension may result in an increase in lower crustal temperatures and a decrease in total crustal strength. Magmatism has the greatest effect on crust of high initial $h$; extension and shortening deformations effect the greatest changes on crust of low initial $h$. Recognizing these relationships allows several important conclusions to be made about the controls on the long-term strength of the crust.

In particular, the spacing of the contours shown in Figure 3.11a suggests that dramatic increases in lithospheric strength occur as the parameters of the heat source distribution are reduced. Heat source distributions of low $h$ and low $q_c$ are the most stable and are least sensitive to small changes in the parameters of the heat source distribution.

Conversely, for heat source distributions characterized by high values of $q_c$ and $h$, small changes in the heat production parameters do not result in significant changes in total lithospheric strength. A consequence of this is that such crust will remain weak for a much longer period as significant and prolonged tectonic reworking is required to effect a significant increase in crustal strength. In these cases the most effective way of increasing the total lithospheric strength is via

magma extraction, and this is the principal mechanism by which to stabilize such crust. Unless the density of the basin filling sediments is significantly lower than the density of the attenuated crust (in which case the Moho becomes significantly shallower) extensional and shortening deformations do not effect significant increases in strength. However, crust that has already become strongly differentiated (i.e., low $h$) but retains a high value of $q_c$ does remain sensitive to the small changes in the heat source distribution effected by extensional and shortening deformations. Small changes in the depth of burial of the heat production maximum can result in significant changes in the total crustal strength. Both observations provide insight into the long-term evolution of high $q_c$ terranes, and are discussed in more detail in Section 3.4.

While this analysis has shown that variations in the parameters of the heat source distribution may significantly affect the strength of the lithosphere, a number of other factors also influence lithospheric strength. For example as noted above, Sandiford (1999) suggested that the long-term changes in the depth of the Moho which may be expected following basin formation will also contribute to variations in lithospheric strength. In this case cooling associated with the shallowing of the Moho will increase the strength of the lithosphere, while the changes in the heat source distribution will tend to decrease its strength (c.f., Figures 3.4 and 3.11).

Nevertheless, the analysis presented in these sections shows that the thermal and mechanical state of crust containing anomalously high concentrations of the heat producing elements is extremely sensitive to the way in which those heat sources are distributed, with this factor exerting a primary first order control on the total lithospheric strength. Given that the tectonic processes which modify the heat source distributions are themselves dependent on the lithospheric thermal regime and the consequently the distribution of heat sources, a potentially profound feedback system exists. This relationship is explored in the following section.

## 3.4 Tectonic feedback and the differentiation of the continental crust

While the models shown in this Chapter are dependent on many different input parameters, they do suggest that the mechanical response of the lithosphere to an applied tectonic load is extremely sensitive to distribution of heat sources. The temperature dependence of the "Brace-Goetze" rheology suggests that deformation is likely to be localized in continental regions which are characterized by elevated thermal regimes, such as would arise for heat source distributions characterized by high $q_c$ and / or $h$ values. Consequently, with all other factors being equal, continental crust with a heat source distribution characterized by low $h$ and / or $q_c$ values would be expected to be significantly stronger and therefore less likely to deform in response to an applied tectonic load than crust characterized by high $h$ and / or $q_c$ values.

These observations, together with those outlined throughout this Chapter, have important consequences for the long-term evolution of the continents and highlight a potentially profound role that tectonic reworking may play in modulating the heat production distributions within the continental crust. Sandiford and McLaren (in press) have explored the way in which this feedback system operates by investigating how a succession of small-scale deformation events might serve to modify the distribution of heat producing elements and how these variations might impact on the lithospheric strength. As outlined in Section 3.3.1, these calculations were based on a lithospheric rheology in which plastic failure occurs either by frictional sliding or ductile creep (e.g., Brace and

Kohlstedt, 1980). Sandiford and McLaren (in press) carried out a set of numerical simulations (summarized in Figures 3.12 and 3.13) using a series of idealized one-dimensional lithospheric columns. These columns were subject to identical loading histories and differ only in terms of their heat source distribution parameters. The three simulations shown in Figure 3.12 are characterized by an initial exponential heat source distribution with distribution parameters, $q_c$ = 37, 42 and 27 $mWm^{-2}$, and $h$ = 13.5, 11.8 and 11.8 km, respectively (Figure 3.12b). In contrast, the three simulations shown in Figure 3.13 are characterized by initially homogeneous distributions.

The load history, as shown in Figures 3.12d and 3.13d, is scaled to provide a mildly compressional stress regime (as suggested by the potential energy differences between mid-ocean ridges and normal continental crust, e.g., Coblentz et al., 1994), with a series of fluctuations of up to ~ $10^{13}$ $Nm^{-1}$ over a range of time scales up to around 500 Ma. Deformation rates are relatively insignificant (Figures 3.12d and 3.13d) especially when compared to modern plate margin deformation rates. As a consequence the strain increments during any given episode are only small (individual stretch increments are < 15%; Figures 3.12e, 3.13e). The isostatic response to changes in crustal thickness either elevates or depresses the surface (e.g., Figures 3.12a and 3.13a), inducing a surface response which tends to restore the surface to sea level (e.g., Figures 3.12f and 3.13f) on a characteristic time scale.

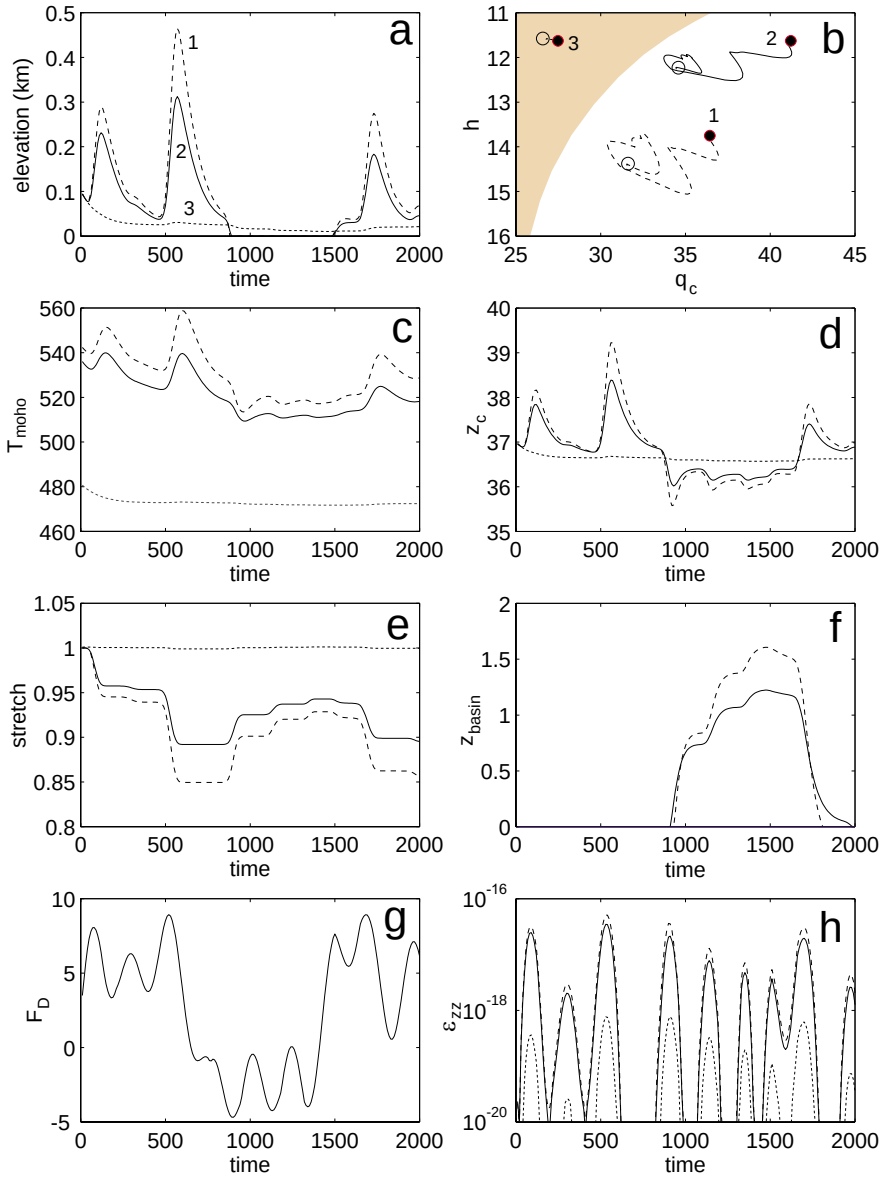


**Figure 3.12** Numerical simulations of Sandiford and McLaren (in press), in which one-dimensional "Brace-Goetze" lithospheric columns are subject to a variable tectonic load **(g)**. The response of three lithospheric columns is shown; thee columns being identical in all respects apart from the initial heat source distribution parameters **(b)**, which translated to variations in the initial thermal regime **(c)**. The initial heat source distribution is exponential. The tectonic response is measured in terms of vertical strain rate **(h)**, as well as incremental stretching history **(e)**. The interaction of deformation and surface response leads to long-term changes in surface elevation **(a)** and crustal thickness **(d)**. Accumulation of sediments in basins, and its subsequent removal during basin-inversion, is shown in **(f)**. The change in the heat source distribution parameters is shown in **(b)**. Time is measured in millions of years with the thermal response of the lithosphere **(c)** calculated using a finite elements algorithm. In **(b)** closed circles in show initial heat source parameters, open circles show final heat source parameters; shaded region represents the range in $h$-$q_c$ parameters which shows stable (or cratonic) behaviour throughout the imposed loading history. Simulations are discussed further in the text, and more details are given by Sandiford and McLaren (in press).

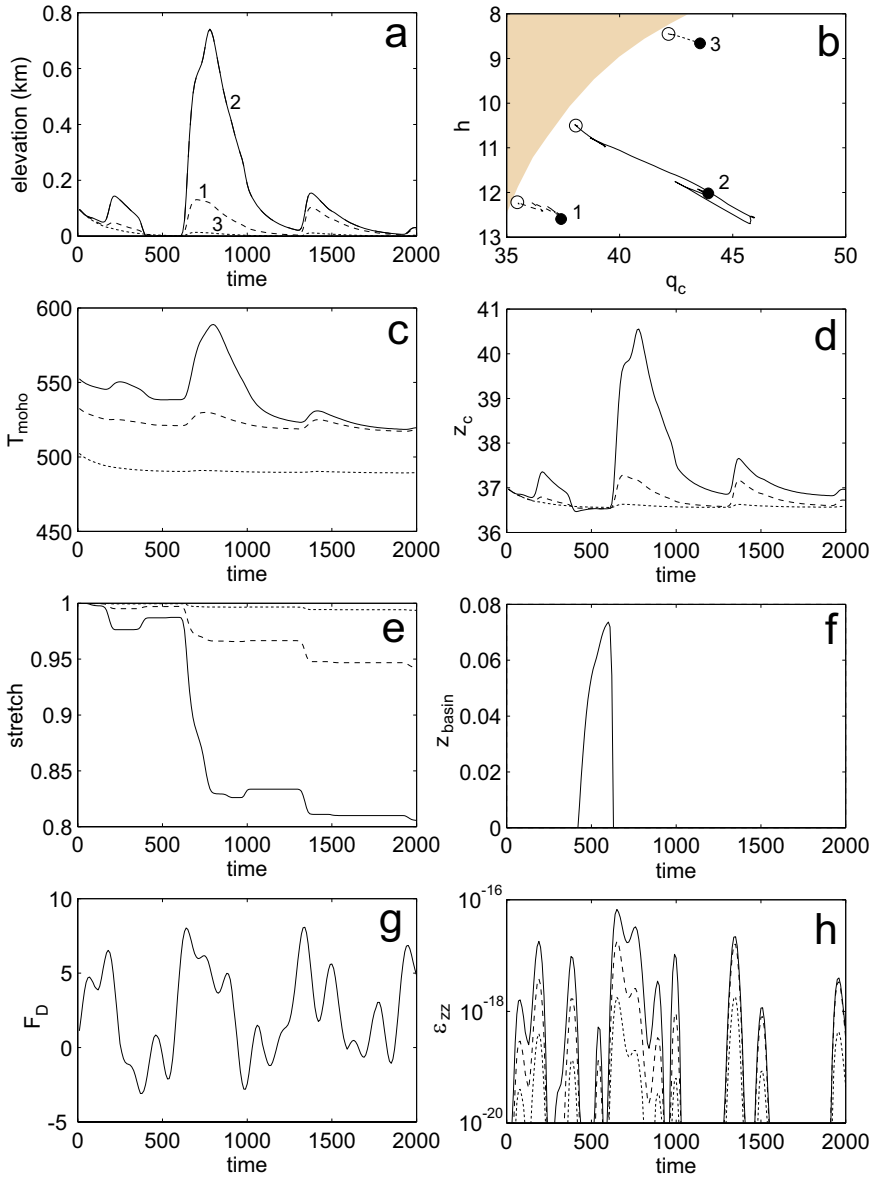


**Figure 3.13** Numerical simulations of Sandiford & McLaren (in press), as for Figure 3.12, but with an initially homogeneous heat source distribution.

These detailed models corroborate the earlier observations by showing that (1) the response of the lithosphere is sensitive to its thermal state, and that (2) the distribution of heat sources within the lithosphere will be significantly modified by repeated small-scale tectonic reworking. Lithosphere initially characterized by elevated $q_c$ and / or $h$ will, through the isostatic coupling of deformation and surface processes, tend to redistribute those heat sources until the total lithospheric strength increases sufficiently that that crust ceases to respond to normal fluctuations in applied tectonic stresses. In terms of the parameters of the heat source distribution this corresponds to a reduction in $q_c$ and, depending on the form of the initial distribution, a reduction in $h$. In particular these models have shown that initial configurations characterized by high $q_c$ (> 35 $mWm^{-2}$) experience significant reductions in $q_c$ during repeated tectonic reworking, even though the scale of the reworking is very minor (note that in the models of Sandiford and McLaren, the amplitude in variations in surface elevation is usually less than 500 m). This $q_c$ reduction effects a significant decrease in lower crustal thermal regimes and an increase in total lithospheric strength. For an initial exponential distribution, the erosion dominated reduction in $q_c$ tends to largely preserve the initial value of $h$, as shown in Figure 3.5. Figure 3.13b shows that initial homogeneous distributions can show significant reductions in both $h$ and $q_c$ during reworking. In contrast, the initial configurations

with low $q_c$ and low $h$ (e.g., case 3 in Figure 3.12b) show no significant response to the imposed loads by virtue of their inherent mechanical strength.

This feedback system provides insights into why the crust should have become differentiated over geological time scales, and also to the origins of the characteristic heat source distribution. As outlined in Chapter One of this thesis, heat sources in the continental crust contribute on average ~ 30 $mWm^{-2}$ to the observed surface heat flow and are generally concentrated in the upper 10-15 km. These parameters are remarkably consistent across terranes of different age and different tectonic histories (Table 1.3). While the lithophile nature of the heat producing elements means that primary magmatic dominated crustal growth will lead to heat production length-scales which are significantly less than the characteristic crustal thickness, there is no compelling reason why such processes should lead to a characteristic length scale or to a characteristic abundance of heat producing elements.

The observations outlined here however, show that the gross chemical and structural architecture of the crust is not only a function of primary crustal accretion, but also reflects complex tectonic reworking in zones of continental deformation (both at plate boundaries and in intraplate settings). In such settings tectonic reworking provides an additional mechanism for ordering heat producing elements in the continental lithosphere (Figures 3.12, 3.13). Because this reworking is dependent on thermal regime and therefore on the distribution and abundance of heat producing elements, the observations outlined in this Chapter provide a new insight into the origin of the characteristic heat production distribution. This is best shown in Figure 3.11b which shows the way in which the heat source distribution influences the rate of deformation of the "Brace-Goetze" lithosphere in response to an applied tectonic load.

As outlined earlier, this diagram shows that for a given complement of heat sources (i.e., constant $q_c$), relatively undifferentiated crust (characterized by high $h$) is very much weaker than differentiated crust (characterized by low $h$). An important consequence of the inherent weakness of high $h$-$q_c$ configurations is that they are susceptible to tectonic reworking. Even though such distributions are expected to show only modest changes in the heat production parameters per unit increment of deformation (i.e., Figures 3.4 and 3.5), this susceptibility implies that tectonic loading will result in very much greater strains and thus may, in the long-term, effect significant redistribution of the heat producing elements providing there is some primary magmatic differentiation. Indeed only once reworking has effectively removed much of the heat production from the crust, or moved it to shallow levels, will such lithosphere be stabilized.

The correlation between the distribution of heat producing elements and the strength of the continental lithosphere implies that the differentiation of heat producing elements into the upper crust is essential for the long-term stability of the continental lithosphere. Moreover, these observations suggest that crustal scale differentiation of the heat producing elements is a necessary precursor to cratonization. While cratons are manifest by long-term tectonic stability, cratonization is usually preceded by a lengthy early history involving not only primary crustal growth, but also extensive crustal reworking during episodic tectonism spanning many hundreds of millions of years. From a thermal and mechanical sense such reworking can be viewed in terms of the way in which it redistributes the heat producing elements.

Terranes characterized by high initial $q_c$ will undergo a lengthy history of both magmatic

dominated differentiation and tectonic reworking before achieving a state of increased thermo-mechanical stability. Moreover, if such crust retains a high value of $q_c$ after the length scale of the heat production distribution has been reduced (such as that which would result for a tectonic history dominated by magmatic differentiation) it will remain sensitive to small changes in the depth of the heat production (see Section 3.3.2). This means that such crust may never achieve a truly stable craton-like state. In contrast, crust of lower $q_c$ will become stabilized much earlier after only limited tectonic reworking; such crust will also be significantly less sensitive to small changes in the heat production parameters.

In Part II of this thesis I investigate the way in which the redistribution of heat producing elements has impacted on the long-term history of terranes within the CAHFP. I use two examples, the Mount Isa and Mount Painter inliers which, as outlined in Chapter Two, are both characterized by crustal contributions greater than 50 $mWm^{-2}$.

# PART TWO

## Anomalous heat source distributions: Geological consequences

# Introduction

The previous section, using simple physical models, has shown that lithospheric thermal regimes are extremely sensitive to the redistribution of crustal heat sources occurring during primary tectonic processes. Moreover, because these primary tectonic processes are themselves sensitive to lithospheric thermal regimes a profound tectonic feedback system exists. These observations suggest that this feedback has important implications for the long-term history of crust characterized by high concentrations of the heat producing elements. The three chapters of this section are concerned with the implications of radiogenic heating and tectonic feedback on the long-term behaviour of crust within the CAHFP, using examples from the Mount Isa and Mount Painter inliers. Each of the three chapters have been written as self-contained manuscripts.

The Mount Isa and Mount Painter terranes have been chosen for a number of reasons. First, as outlined in Chapter Two of this thesis, they form part of the CAHFP and are characterized by high surface heat flow and high concentrations of the heat producing elements, contained principally within granites and granite gneisses. At Mount Isa crustal heat sources contribute at least 50 $mWm^{-2}$ to the modern surface heat flow and at Mount Painter this value is at least 70 $mWm^{-2}$ and may be as high as 100 $mWm^{-2}$. Given that these crustal contributions are highly anomalous, more than twice that of the average continental crust, these terranes are ideally suited to an evaluation of the role of radiogenic heating and provide excellent templates on which to assess the predictive thermo-mechanical models discussed in the previous Chapter. Second, a number of aspects of the long-term evolution of these terranes remain unanswered and so the approach taken here has the potential to provide novel solutions to some ongoing problems of crustal evolution, both in the Australian context and in more general terms.

The Mount Isa terrane is large and volumetrically significant, and has been the subject of numerous detailed investigations (e.g., Blake and Stewart, 1992; Rubenach, 1992; Eriksson et al., 1993; Connors and Page, 1995; Wyborn et al., 1996; O'Dea et al., 1997a, b; Spikings et al., 1997; Betts et al., 1998; Page and Sweet, 1998, Page and Sun, 1998; Wyborn, 1998; Drummond et al., 1998; Perkins et al., 1999). The region is characterized by a lengthy record of tectonic activity extending for more than 300 million years through the Palaeoproterozoic and Mesoproterozoic. Effective cratonization followed the middle Mesoproterozoic Isan Orogeny. The history of tectonic activity is characterized by a series of rift-related extensional events, which are often associated with voluminous granitic magma extraction, and by episodes of convergent deformation and high temperature-low pressure metamorphism.

Chapter Four is concerned with the role of tectonic feedback in modulating the long-term tectonic evolution of the Mount Isa crust. The tectonic history recorded at Mount Isa has resulted in dramatic changes in the crustal heat source distribution and this redistribution must have been accompanied by long-term changes in the thermal regime. Results in this Chapter show that primary differentiation of the Mount Isa crust was achieved principally by felsic magmatism over much of its 300 million year history. The flux of heat producing elements from the lower to the upper crust associated with this magmatism was sufficient to cause long-term lower crustal cooling of at least 200°C, and resulted in a highly stratified heat source distribution. This high $q_c$, low $h$ distribution,

remained sensitive to small changes in the depth of the heat production effected by processes such as deformation, erosion and sedimentation. This redistribution lead to significant changes in deep crustal thermal temperatures and impacted on lithospheric strength. These results suggest that the long-term evolution of the Mount Isa crust reflects the progressive concentration of heat producing elements into the upper crust, which has lead to an increase in lithospheric strength and eventually to effective cratonization.

Chapter Five is concerned with the possible role of internal heating during high temperature-low pressure metamorphism in the western Mount Isa Inlier. The origins of metamorphism (~ 600°C and 3-4 kbar) in this region have been controversial because no syn-metamorphic intrusive bodies can be recognized, high temperatures appear to have been sustained for periods > 100 Ma, and metamorphism followed an extended phase of thermal subsidence. This chapter investigates the thermal effects of the burial of the high heat producing Sybella Batholith, and shows that this burial, beneath the thick insulating sedimentary succession of the Mount Isa Group, is capable of generating step upper crustal thermal gradients prior to the Isan Orogeny. This model may provide a basis for understanding the origins of high-temperature metamorphism in other terranes where transient heating models do not apply.

In contrast to the Mount Isa region, the Mount Painter province in northern South Australia represents one of the smallest volume fractions of Australian Proterozoic crust and has been the subject of relatively few detailed studies (e.g., Teale, 1993) although an ongoing research program at Adelaide University has lead to a significant increase in what is known about this terrane (e.g., Johnson, 1980; Thornton, 1980; Smith, 1992; O'Halloran, 1992; Schaefer, 1993; Neumann, 1996; Paul, 1998; Sandiford et al., 1998a, b; Paul et al., 1999). Despite being located well within the continental interior from the Mesoproterozoic to the present day, this province records a long, complex and ongoing history of deformation. The factors which have controlled this ongoing tectonic history are poorly understood, and there appears to be no satisfactory explanation as to why this crust has not undergone cratonization during its history.

Chapter Six is concerned with the origins of the long-term tectonic reactivation recorded at Mount Painter, and particularly the factors which controlled the localization of deformation in this intraplate setting. As thermal regime is one of the most likely factors contributing to the spatial and temporal variations in the mechanical state of the lithosphere detailed reconstruction of thermal histories can be used to understand the links between thermal regime and tectonic activity. Chapter Six uses modern thermochronological methods, including both K/Ar and $^{40}Ar/^{39}Ar$ analyses, to reconstruct the Palaeozoic thermal history of Mount Painter region. These results show that in addition to deformation during the Cambro-Ordovician Delamerian Orogeny, the Mount Painter province was also reactivated during the Carboniferous Alice Springs Orogeny. The thermochronological data show that throughout the Palaeozoic the Mount Painter crust was characterized by elevated thermal gradients, with the basement rocks above 300°C throughout this period. The presence of such elevated thermal gradients must have equated with dramatic lithospheric weakening. This observation suggests that the localization of Palaeozoic intraplate deformation at Mount Painter was a primary response to thermally modulated variations in the strength of the continental lithosphere. This result bears on general models for the localization of deformation within the continental interiors.

# Chapter Four

# Long-term thermal consequences of tectonic activity at Mount Isa, Queensland

Proterozoic crustal evolution is typically characterized by polyphase tectonism and tectonic reactivation (e.g., Dallmeyer and Keppie, 1993; Kalsbeek, 1995; O'Dea et al., 1997a; Betts et al., 1998). In many instances, semi-continuous tectonic activity seems to have occurred over many hundreds of millions of years prior to effective cratonization. Such extended periods of tectonic activity exceed that which can easily be ascribed to a single "plate-tectonic cycle" and suggest that these terranes have either been at active plate margins for very extended periods, or that at least part of the record reflects tectonism in an intraplate setting. Neither explanation is particularly satisfactory. The former case raises questions concerning the very nature of active plate boundaries in and around Precambrian continents, while in the latter case we recognize a distribution and style of deformation that, on face value at least, is very different from that evident in the continent interiors today.

Major deformation, both at plate boundaries and within continental interiors, requires that the tectonic stresses exceed yield strength through much of the lithosphere. Consequently the distribution of active deformation of the lithosphere can be understood as a consequence of either stress amplification or strength reduction. In the modern Earth both factors seem to apply at plate boundaries where substantial stress amplification is related to processes such as subduction and continental collision, while significant thermal weakening occurs in response to subduction-related magmatism as well as crustal thickening and, possibly, shear heating. It is not surprising that much (but not all) of the deformation on the modern Earth is located along plate margin zones!

Conversely, the factors responsible for the distribution of intraplate deformation evident in the modern Earth are not so well understood. It is difficult to see how stresses can be greatly amplified in intraplate settings, although localised mantle down-welling associated with convective instability beneath continental interiors may provide an important source of tectonic stress amplification (e.g., Neil and Houseman, 1999; Houseman et al., 1981; Beaumont et al., 1994). One problem here is that the magnitude and source of stresses that apply in any particular geological scenario are only poorly constrained. On the other hand, the mechanical properties of continental interiors are likely to vary significantly because of subtle variations in the thermal and compositional structure of the lithosphere (e.g., Neil and Houseman, 1997). Because of the coupling between the thermal state and mechanical strength of the lithosphere, constraints on the way in which crustal thermal regimes have evolved through time may therefore provide particularly useful insights into the evolution of lithospheric strength, and the role it has played in contributing to tectonism.

The recognition that lithospheric strength and thermal regime are coupled may provide a solution to the old problem of long-lived tectonic activity in Precambrian terranes. Rather than attempting to reconcile whether such activity is strictly "plate-tectonic" (in the sense that we understand the modern Earth, e.g., Myers et al., 1996) or "intraplate" (e.g., Etheridge et al., 1987; Wyborn, 1988), it may prove more rewarding to view it in terms of the way in which the history of tectonic activity has modified the thermal and mechanical properties of the lithosphere, and so

influenced its subsequent tectonic evolution. The objective of this chapter is to provide some understanding of how the evolution of thermal regime and, by inference, lithospheric strength may have influenced the tectonic development of the Palaeo-Mesoproterozoic Mount Isa Inlier (MII) in northern Australia. The Mount Isa region is particularly well suited to such an analysis because its protracted history of magmatism, sedimentation and deformation (both extensional and convergent) has been constrained at the outcrop scale by a number of detailed geochronological, structural and tectonic studies (e.g., Eriksson et al., 1993; Connors and Page, 1995; O'Dea et al., 1997a, b; Betts et al., 1998; Page and Sweet, 1998). The region records a ~ 300 million year polyphase tectonic history prior to effective cratonization and this chapter is particularly concerned with the role of strength changes in this transition from persistent active tectonics to craton-like behaviour. Also, unusually good exposure allows for detailed characterisation of the thermal properties of outcropping lithologies. Together with existing heat flow determinations, these data provide constraints on the present-day thermal structure of the Mount Isa crust and the way in which it has evolved through the various tectonic processes that have shaped it. By exploring the way in which the distribution of heat sources has evolved at the crustal scale as a function of tectonic activity, we are able to place constraints on the long-term thermal evolution of the Mount Isa crust, and thus infer likely changes in its strength through time.

I begin this chapter with a brief outline of the record of polyphase tectonism in the Mount Isa region. This summary will also serve as in introduction to Chapter Five of this thesis. I then describe the way in which the distribution of heat sources evolved during this history. The insights provided by these first-order observations suggest that the tectonic evolution of Mount Isa reflects, at least in part, long term crustal cooling and consequently strengthening, due to the progressive differentiation of heat producing elements within the crust.

## 4.1 A review of the tectono-stratigraphic history of the Mount Isa region

The Mount Isa Inlier is a metamorphic and igneous complex in north-west Queensland (Figure 4.1) consisting dominantly of Palaeo-Mesoproterozoic sedimentary sequences, felsic plutonic rocks and bimodal volcanics. The inlier records a complex and protracted history of magmatic and orogenic

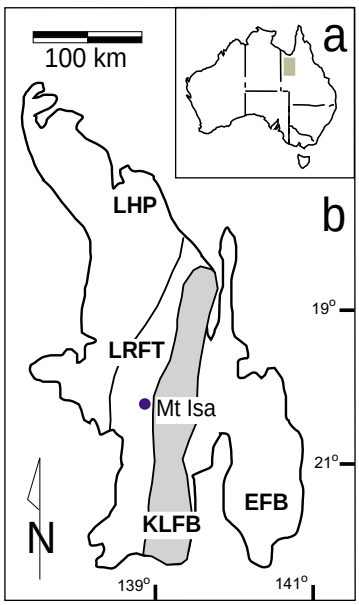


**Figure 4.1** (**a**) Location of the Mount Isa Inlier (MII) in north-western Queensland, Australia. (**b**) Structural domains of the Mount Isa area (after Blake and Stewart 1992). MI = Murphy Inlier, LHP = Lawn Hill Platform, LRFT = Leichhardt River Fault Trough, KLFB = Kalkadoon-Leichhardt Fold Belt, EFB = Eastern Fold Belt. Together the Leichhardt River Fault Trough and Lawn Hill Platform comprise the Western Fold Belt (WFB).

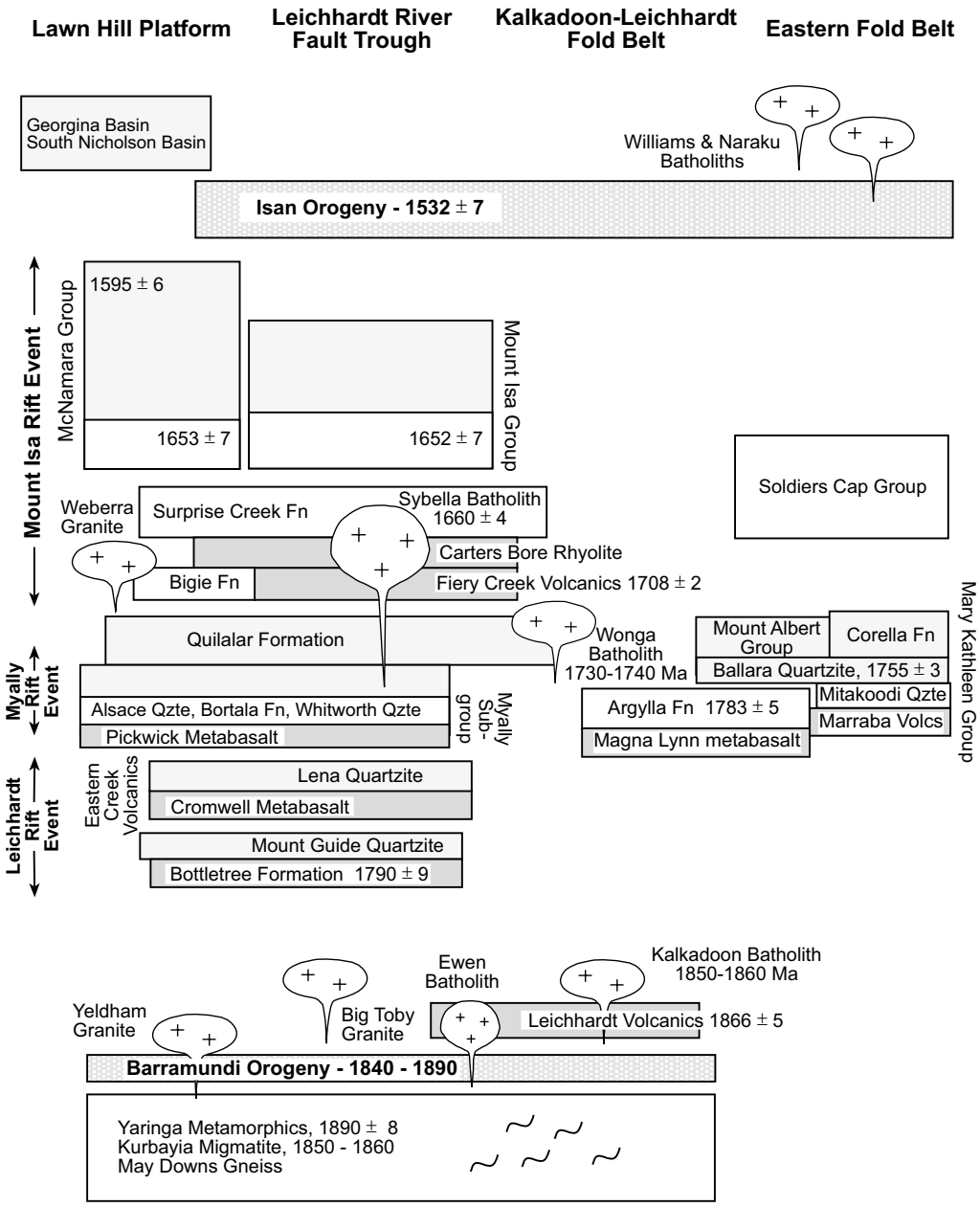


**Figure 4.2** Tectono-stratigraphic history of the Mount Isa Inlier. Major magmatic, and deformational events are shown for the Lawn Hill Platform, Western, Kalkadoon-Leichhardt and Eastern Fold Belts. Unshaded units denote rift-related sedimentary packages, light shading sag-related sediments, and dark shading volcanic sequences. Geochronological data from Connors and Page, 1995 (Sybella Batholith and Isan Orogeny); Page and Sun, 1998 (Eastern Fold Belt); Page and Sweet, 1998 (Mount Isa Group and McNamara Group). All other geochronology from Wyborn et al., 1988 and Wyborn et al., 1998a.

activity extending throughout an interval of more than 300 million years (Figure 4.2). The Inlier can be divided into three main tectonic domains, the Western Fold Belt (WFB; including the Lawn Hill Platform, LHP, and Leichhardt River Fault Trough, LRFT), the Kalkadoon-Leichhardt Fold Belt (KLFB) and the Eastern Fold Belt (EFB) (Figure 4.1). The following section reviews the geological history of the Mount Isa region through the description of those major events that have lead to the long-term geochemical and structural reorganization of the crust. Particular emphasis is placed on the description of the history of the Western Fold Belt where the most lengthy history of reactivation has been recorded, and where excellent exposure has permitted a number of detailed investigations (e.g., Blake, 1987; Blake and Stewart, 1992; Eriksson et al., 1993; Connors and Page, 1995; O'Dea et al., 1997a, 1997b; Betts et al., 1998; Page and Sweet, 1998).

The earliest history of the Western and Kalkadoon-Leichhardt Fold Belts is associated with deposition and subsequent metamorphism of Palaeoproterozoic sedimentary packages (Yaringa Metamorphics, May Downs Gneiss and Tewinga Group) during the Barramundi Orogeny. This widespread orogenic event, occurring between 1840 and 1890 Ma (with peak metamorphism ~ 1875 Ma; Page and Williams, 1988; Wyborn, 1988) is also recorded through other Australian Proterozoic terranes (e.g., Etheridge et al., 1987; Wyborn, 1988). Metamorphism is typically high temperature and generally low pressure (< 5 kbar) amphibolite to granulite facies. This event was associated with voluminous, extensive and dominantly felsic magmatism, characterized by emplacement of I-type granites (Wyborn 1988). At Mount Isa these include the Kalkadoon, Big Toby and Ewen Batholiths (e.g., Wyborn 1988). These granites share common Nd model ages of *ca.* 2200 Ma (Wyborn, 1998), suggesting a crustal prehistory of ~ 300-400 million years. Etheridge et al., (1987), Wyborn et al., (1988), and Wyborn (1998) have argued that they were derived from the melting of mafic rocks accreted to the base of the crust. Units associated with the Barramundi Orogeny form local basement throughout much of the MII and are best exposed in the deeply exhumed KFLB. Recent deep seismic results (e.g., Drummond et al., 1998) suggest Barramundi-aged rocks also underlie the WFB and EFB. The Barramundi Orogeny is inferred to have concluded around 1840 Ma (e.g., Page and Sun 1998) and from this time until *ca.* 1790 Ma the terrane experienced a period of relative tectonic quiescence, particularly when compared to its later tectonic history.

Lying unconformably upon the metasediments and plutonic rocks of the Barramundi Orogeny are sequences of sediments and volcanics related to cycles of rifting and post-rift subsidence. These sequences form a series of 3 major stacked and unconformity bound basins in which the deposition of each package of sag related sediments is terminated by a further stage of rift-related extension (e.g., O'Dea et al., 1997b). Volcanics associated with each rift basin are characteristically bimodal, consisting predominantly of continental tholeiites and ignimbrites. Basin development accompanying rifting was best developed through the Western Fold Belt, although sedimentation associated with post-rift subsidence was continuous from the Lawn Hill Platform to the Eastern Fold Belt (e.g., Derrick et al., 1980).

Within the Western Fold Belt, rifting was strongly partitioned into the Leichhardt River Fault Trough (LRFT), a N-S trending fault bounded fold belt which represents the deformed axis of a major Proterozoic rift zone (O'Dea et al., 1997a,b). The two-stage Leichhardt Rift Event (LRE, 1790-1765 Ma, Page 1983; O'Dea et al., 1997b) follows the Barramundi Orogeny in this region. The first phase of LRE extension was associated with the deposition of a thick rift-sag sequence – the Bottletree Formation and Mount Guide Quartzite. The second phase of rifting resulted in the extrusion of voluminous continental tholeiites of the Eastern Creek Volcanics, and deposition of the sag-related Lena Quartzite. The Leichhardt Rift Event was terminated by a second major period of intermittent rifting and subsidence – the Myally Rift Event (MRE) (1765-1740 Ma) (Betts et al. 1998). Overlying sediments of the upper Myally Subgroup and Quilalar Formation are associated with post-rift subsidence and reflect a period of relative tectonic stability (Derrick et al. 1980).

A further period of major extension, the two-phase Mount Isa Rift Event (MIRE) (O'Dea et al., 1997a; Betts et al., 1998), was characterised by the reactivation of many earlier formed, mainly extensional faults (Betts et al., 1998). The first stage (1708 ± 2 Ma, Page and Sweet 1998) was associated with extrusion of the felsic Fiery Creek Volcanics, and deposition of the Bigie Formation; the second resulted in the deposition of the rift-related Surprise Creek Formation and the sag-related shale and

dolomite rich sequences of the Mount Isa Group (*ca.* 1653-1595 Ma, Page et al., 1994; Page and Sweet 1998). The Mount Isa Group forms a thick (~ 12-14 km) package of sediments (Andrews, 1998) across the Western Fold Belt and the Lawn Hill Platform (where it is termed the McNamara Group). The Mount Isa Rift Event was also associated with the intrusion of a number of voluminous granitic batholiths (and comagmatic volcanics) in the LRFT, including the Sybella Batholith (*ca.* 1655 Ma, Connors and Page 1995), Carters Bore Rhyolite (1678 ± 2 Ma, Page and Sweet 1998), and the Weberra Granite (*ca.* 1698 Ma, Wyborn et al., 1988).

The Leichhardt Rift Event is manifest in the KFLB by extrusion of the Magna Lynn Metabasalt, and in both the KLFB and EFB by the sag-related Argylla Formation (*ca.* 1783 ± 5 Ma, Page and Sun 1998). The Myally Rift Event in the EFB is represented by rift-related Marraba Volcanics and Mitakoodi Quartzite. Associated sag related sediments of the Mary Kathleen Group are present across both the EFB and KLFB. There are no post-Myally Rift Event sequences preserved in the KLFB. The Eastern Fold Belt records little evidence of the thick post-rift sedimentary sequences associated with the MIRE in the Western Fold Belt and Lawn Hill Platform. Stratigraphic studies however, imply the presence of a temporally equivalent pre-orogenic basin in this region (e.g., Southgate et al., 2000).

The rift-related depositional record of the Western, Kalkadoon-Leichhardt and Eastern Fold Belts was terminated by basin inversion during the Isan Orogeny (*ca.* 1590-1500 Ma, Blake 1987, O'Dea et al., 1997a,b; peak metamorphism at 1532 ± 7 Ma, Connors and Page 1995). In the WFB, compressional deformation was partitioned strongly into the LRFT, which contained the thickest rift-related sequences, however it is also recorded throughout the KLFB and EFB. The latter suffered particularly intense deformation and associated high temperature-low pressure metamorphism (e.g., Loosveld and Etheridge, 1990; Reinhardt, 1992).

In the Western Fold Belt, compressional deformation during the Isan Orogeny terminated the record of Mesoproterozoic tectonic activity. In the Eastern Fold Belt tectonic activity terminated with the emplacement of the I-type Williams and Naraku Batholiths at ~ 1510 Ma (Page and Sun, 1998) the youngest granitic bodies in the MII. In contrast to the histories of the both the WFB and EFB, and despite recording a similar early sedimentary history, the Lawn Hill Platform was relatively unaffected by the Isan Orogeny. Furthermore, it remained an active depocentre until at least the middle Cambrian. The Lawn Hill Platform is also characterised by a virtual absence of felsic magmatism.

The protracted, but spatially and temporally variable, tectonic history of the MII records a series of rift-related extensional events associated with the generation of voluminous felsic magmas, as well as convergent deformation. Granites throughout the terrane, from the Barramundi Igneous Association to the young granites of the EFB, show remarkable geochemical and isotopic homogeneity (e.g., Wyborn 1988, 1998). Consistency of Nd-isotopic data through time (Wyborn, 1988) seems to reflect lithospheric recycling during major crustal tectonism rather than significant additions from the mantle. A lengthy period of crustal prehistory is further supported the characteristic granite geochemical signature of Sr-depletion, implying derivation from crustal protoliths in which plagioclase was stable (Wyborn, 1998).

The remainder of this chapter investigates how crustal thermal regimes have evolved as a consequence of the major periods of crustal activity recorded at Mount Isa. In order to understand

this it is useful to first consider the thermal regime of the modern Mount Isa crust, as reflected by modern heat flow and surface heat production data.

## 4.2 The modern thermal regime in the Mount Isa Inlier

Surface heat flow has been determined at four localities within the MII: Mount Isa in the Western Fold Belt; Blockade, ~ 40 km east of the city of Mount Isa in the Kalkadoon-Leichhardt Fold Belt; and Dugald River and Mount Dore in the Eastern Fold Belt (Table 4.1). The mean heat flow at each of these locations is 82 $mWm^{-2}$, 78 $mWm^{-2}$ (Hyndman and Sass, 1966), 72 $mWm^{-2}$ and 98 $mWm^{-2}$ (Cull and Denham, 1979) respectively. In contrast to these measurements, a single surface heat flow measurement from Camooweal, near the western limit of the Lawn Hill Platform, is much lower at 48 $mWm^{-2}$ (Hyndman, 1967). As discussed in Chapter Two of this thesis, the MII data are anomalous in terms of global averages (Table 1.2) but are by no means unusual in the context of Australian Proterozoic terranes, where heat flow averages 82 $mWm^{-2}$ (Cull, 1982; Table 2.1). In the Mount Isa case, the relative contributions of mantle and crustal sources to these elevated high heat flow regimes can be inferred using several lines of evidence. In the first instance, seismic data indicate that the lithosphere beneath the MII is characterized by relatively high upper mantle velocities associated with an exceptionally thick lithosphere of ~ 250-300 km (e.g., Kennett and Van der Hilst, 1996; Zielhaus and Van der Hilst, 1996). For such thick lithosphere, we might expect mantle heat flows of 10-20 $mWm^{-2}$. For this to be consistent with the high surface heat flows, the crust must be enriched in heat production, contributing as much as 60-70 $mWm^{-2}$ of the observed surface heat flow.

Such crustal contributions to surface heat flow are exceptional when compared with other terranes of equivalent age (e.g., Chapman and Furlong, 1977). Because there are only two regions from which heat flow measurements are available in the MII it is not possible to rigorously examine potential sources of error. However, one source of error which may be important is heat refraction associated with contrasting thermal conductivities. This is likely in the case of the Mount Isa measurements which lie close to the surface exposure of the contact between the Sybella Granite

**Table 4.1.** *Surface heat flow data from the Mount Isa Inlier*

| *Region* | *Average heat flow ($mWm^{-2}$)* | *Number of determinations* |
|---|---|---|
| Mount Isa, Western Fold Belt[1] | 82 | 25 |
| Blockade, Kalkadoon-Leichhardt Fold Belt[1] | 78 | 3 |
| Dugald River, Eastern Fold Belt[2] | 72 ± 3 | |
| Mount Dore, Eastern Fold Belt[2] | 98 ± 4 | |
| Australian Proterozoic terranes | 88 ± 22 | 26 |
| Global (early) Proterozoic* | 51 ± 20 | 78 |
| Global (late) Proterozoic* | 54 ± 20 | 265 |

*Note:* Australian heat flow average taken from data in Cull (1982); Houseman et al. (1989), and Gallagher (1990). Mount Isa heat flow measurements from [1] Hyndman and Sass (1966), and [2] Cull and Denham (1979).

* Global heat flow averages taken from a compilation by Morgan (1984) and Chapman and Furlong (1977), with age taken as the time of the last tectonothermal event within a particular terrane. See Table 1.2 for further details of the global heat flow field

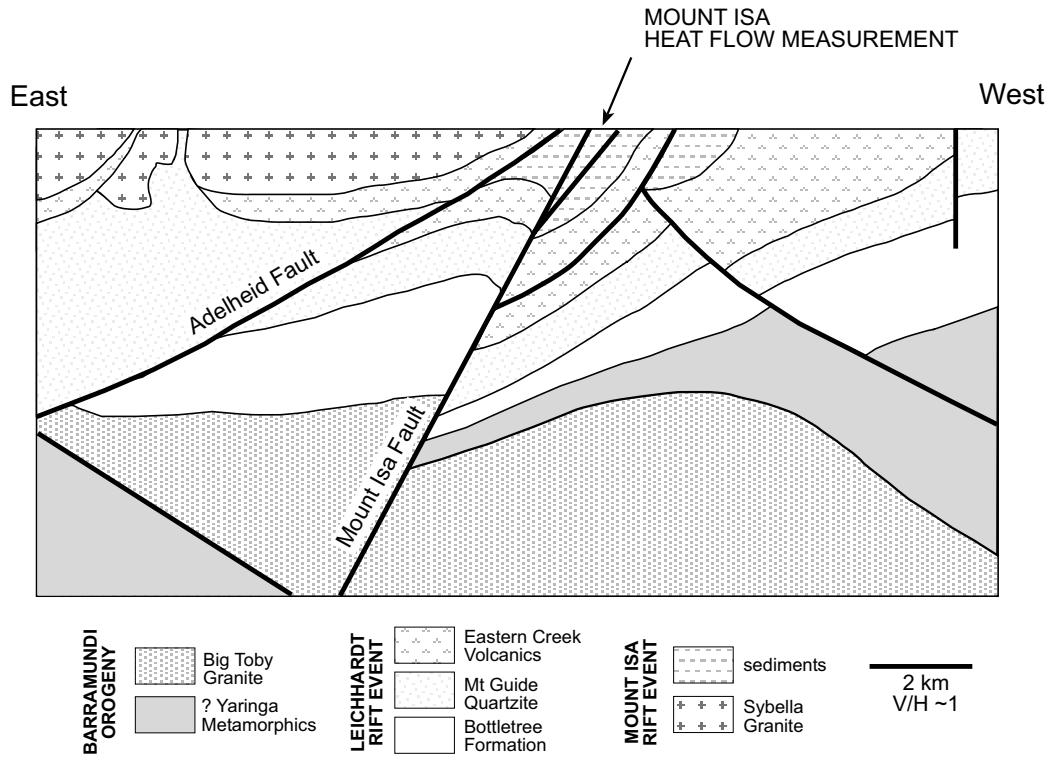


**Figure 4.3** Interpreted seismic section from the WFB, MII (compiled from Drummond et al., 1998 and Wyborn et al., 1996). In this region the Yaringa Metamorphics and Big Toby Granite comprise local Barramundi basement. Sediments form part of the Isa Superbasin. Note that the heat flow measurement at Mount Isa city (~ 82 $mWm^{-2}$; Hyndman and Sass 1966) lies immediately to the east of the Adelheid and Mount Isa Faults, near the contact of the Sybella granite, Eastern Creek Volcanics and younger sedimentary cover.

and the metasediments of the Isa Superbasin (Figure 4.3). In theory, heat refraction due to conductivity contrasts can lead to substantial local amplification of heat flow density, possibly by as much as 10-20 $mWm^{-2}$ (e.g., England et al., 1980). In light of this possibility here a more conservative estimate, of 50 $mWm^{-2}$, is taken for the mean contribution of crustal heat sources to the observed heat flow at the regional scale throughout the MII. It is noted that the crustal contribution is likely to be higher for crustal sections which include the high heat producing granites.

Calculated heat production values (Tables 4.2 and 4.3; Figure 4.4) support the notion that the MII crust is exceptionally enriched in heat producing elements, and suggest that much of this enrichment is localized in granite rocks now near the present surface. Throughout the terrane, the average heat production of all Proterozoic granites (by area) is 5.2 $\mu Wm^{-3}$ (Table 4.2, Figure 4.4). This is approximately two times the "average" granite (Table 1.4). This value is all the more extraordinary given that the area of outcropping granite on which this estimate is based is ~ 11 000 $km^2$ (~ 23% of the total outcrop area of the inlier) and, as noted earlier, Barramundi granites are known to underlie the Palaeoproterozoic supracrustal sequence. Examples of these high heat production granites include the Sybella Batholith in the LRFT (Figure 4.4) where heat production averages 5.1 $\mu Wm^{-3}$ and in some individual stocks is as high as 10 $\mu Wm^{-3}$. Similarly, the late-stage Williams and Naraku Batholiths in the EFB have average heat production values of 7.8 and 7.1 $\mu Wm^{-3}$, respectively (Table 4.2; Figure 4.4). High values of heat production are not associated exclusively with granites and granite gneisses, with much of the sedimentary and volcanic basin fill also anomalously enriched in heat producing elements, when compared to "average" values (Table 4.3).

**Table 4.2** *Geochemistry and heat production of selected granites of the Mount Isa Inlier*

| *Granite unit* [§] | *Age* | *# of samples* | *Area of outcrop ($km^2$)* [‡] | *U * (ppm)* | *Th * (ppm)* | *$K_20$ * (wt%)* | *Th:U* | *H p* [§] *($\mu W\ m^{-3}$)* | *H e* [§] *($\mu W\ m^{-3}$)* |
|---|---|---|---|---|---|---|---|---|---|
| Kalkadoon Batholith | 1856 ± 10 | 5 | 3478 | 5 | 26 | 4.6 | 5.2 | **3.6** | **5.3** |
| Big Toby Granite | 1804 ± 15 | 4 | 29 | 5 | 19 | 3.6 | 3.8 | **3.0** | **4.4** |
| Ewen Batholith | ~ 1820 | 1 | 321 | 9 | 31 | 4.8 | 3.6 | **5.0** | **7.3** |
| Wonga Batholith – main phase | 1758 ± 8 | 30 | 335 | 8 | 46 | 5.2 | 5.7 | **5.9** | **8.1** |
| Wonga Batholith – microgranite | 1671 ± 8 | 11 | | 11 | 66 | 5.5 | 6.0 | **8.2** | **10.9** |
| Weberra Granite | 1698 ± 24 | 5 | 47 | 5 | 34 | 7.8 | 6.8 | **4.5** | **6.5** |
| Sybella Batholith – main phase | 1655 ± 4 | 31 | 1231 | 8 | 35 | 5.1 | 4.3 | **5.1** | **7.0** |
| Sybella Batholith – BQ phase | | 14 | | 8 | 33 | 5.4 | 4.1 | **5.0** | **6.9** |
| Sybella Batholith – microgranite | | 12 | | 12 | 54 | 5.8 | 4.5 | **7.6** | **10.2** |
| Naraku Batholith – main phase | 1505 ± 5 | 19 | 395 | 10 | 57 | 3.5 | 5.7 | **7.1** | **8.9** |
| Naraku Batholith – microgranite | | 3 | | 19 | 58 | 4.9 | 3.1 | **9.6** | **12.6** |
| Williams Batholith | 1505 ± 5 | 44 | 1900 | 13 | 55 | 3.9 | 4.3 | **7.8** | **9.9** |
| **Average (by area)** [†] | | | **7736** | **8** | **37** | **4.5** | | **5.2** | **7.1** |
| **Average granite** [‖] | | | | **4** | **15** | **3.5** | **3.8** | **2.5** | |

*Note:* Intrusive ages of granites are those determined by U-Pb zircon geochronology; SHRIMP data quoted where available. Kalkadoon and Ewen Batholith ages from Wyborn et al., 1998a; Weberra and Big Toby Granite ages from Wyborn et al., 1998a; Wonga Batholith ages from Page 1983, Pearson et al., 1992 and Wyborn et al., 1998a; Sybella Batholith age from Connors and Page 1995; Williams and Naraku Batholith ages taken as that age of the Malakoff granite (from Page and Sun 1998).

* Average geochemical analyses from Wyborn et al., 1988, Wyborn 1988, and Wyborn et al., 1998a.

† Terrane averages are weighted averages based on proportional outcrop area. Note that ungrouped granites constitute a further ~ 3600 $km^2$ area of the inlier and are not included in this calculation.

‡ Area of outcrop includes all granites within that batholith, where applicable. Area of outcrop from Wyborn et al., 1998a.

§ *H p* = present heat production, calculated from present concentrations of U, Th, and K. *H e* = heat production at the time of granite emplacement. As radioactive decay causes a reduction in the concentration of heat-producing elements through time, the value of the calculated heat production at the time of intrusion of each batholith is on average ~25–30% higher than the present day value.

‖ average granite heat productivity from Fowler, 1990

**Table 4.3** *Geochemistry and heat production of major sedimentary units of the Mount Isa Inlier*

| *Sedimentary unit* | *# of samples* | *U (ppm)* | *Th (ppm)* | *$K_20$ (wt%)* | *H ($\mu W\ m^{-3}$)** |
|---|---|---|---|---|---|
| Basin fill – sands and conglomerates* | 288 | 2.3 | 8.3 | 2.0 | 1.39 |
| Basin fill – siltstones and shales* | 317 | 6.4 | 17.7 | 4.3 | 3.37 |
| Basin fill – carbonates* | 1176 | 1.5 | 3.0 | 1.5 | 0.75 |
| Average sandstone† | | 0.6 | 1.8 | 0.9 | 0.37 |
| Average siltstone and shale† | | 3.7 | 12 | 2.7 | 2.10 |
| Average carbonate† | | 2.0 | 1.5 | 0.3 | 0.66 |

*Note: H* = present heat production, calculated from present concentrations of U, Th, and K.

* Basin fill geochemistry from Australian Geological Survey Organization geochemical databases

† Average sedimentary heat productivity data from Haenel et al. (1988).

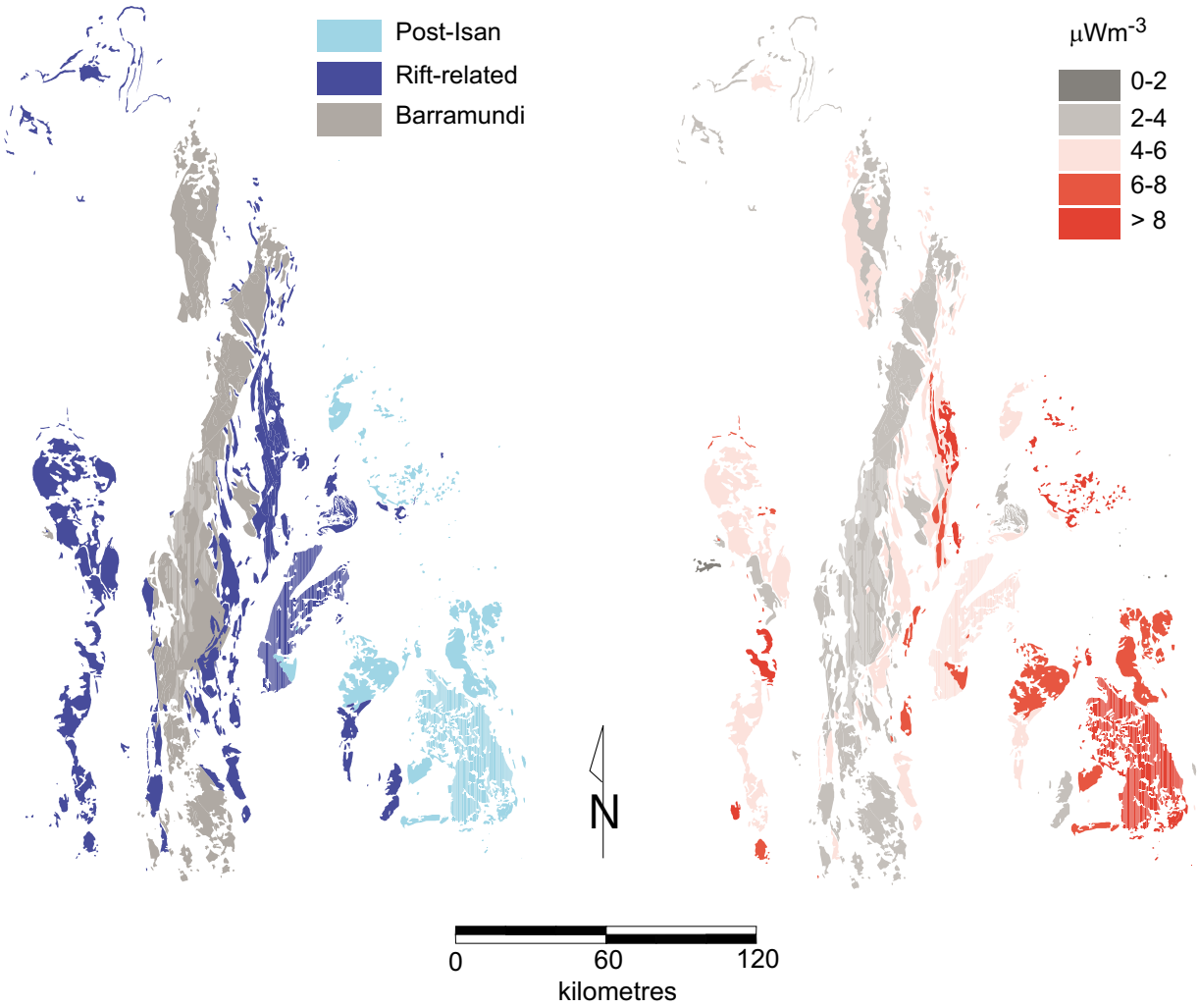


**Figure 4.4** Granites and comagmatic volcanics of the Mount Isa Inlier. (**a**) Granites are grouped according to age into three main subdivisions – Barramundi Granites (e.g., Wyborn et al., 1988); Rift-related granites (which include the Sybella granite and equivalents associated with the MIRE, and the Wonga Granite and equivalents associated with the Myally Rift Event) and the latest syn-post tectonic post-Isan Granites (including the Williams and Naraku Batholiths). (**b**) Granites are grouped by heat productivity. Heat production values are assigned to individual plutons from the average of a number of geochemical analyses from that pluton. Data and figure compiled from Wyborn et al., (1998). As discussed in Chapter Two, the "average" granite has heat production ~ 2.5 $\mu Wm^{-3}$.

These high values of surface heat production must be restricted to the upper crust in order to be consistent with the known range of surface heat flow, implying a strongly differentiated crust with regard to heat producing elements. For example, assuming that the average contribution of crustal heat producing elements across the terrane is 50 $mWm^{-2}$ (as discussed above) then a layer of average MII granite some 9.6 km thick would account for the crustal contribution without any additional heat sources in the deeper crust. The crust in the MII is around 40 km thick (e.g., Drummond et al., 1998) and if we allow that the mid to deep crust contributes on average 0.6 $\mu Wm^{-3}$ (e.g., Fowler, 1990), then the thickness of the average MII granite required to account for the surface heat flow is ~ 6 km. This is consistent with available seismic evidence from the WFB (Figure 4.3), where the Big Toby Granite is imaged as a unit at least 5 km thick.

The strongly differentiated distribution of heat production outlined above is clearly a consequence of the processes that have shaped the MII crust. In particular, it is clear that the distribution of heat producing elements must have been very different prior to major periods of

magmatism and has certainly been modified during deformation and crustal extension and associated erosion and sedimentation. As the majority of heat producing elements are carried by granites that formed as a result of crustal recycling, granite generation and transport from the deep crust must have been particularly significant in redistributing the heat producing elements. In order to understand the thermal consequences of this redistribution, the next section outlines a simple framework for the quantitative description of the distribution of crustal heat sources.

## 4.3 The distribution of crustal heat sources in the Mount Isa crust

As outlined earlier in this thesis, the distribution of crustal heat sources can be described using two parameters, termed $h$ and $q_c$. The parameter $q_c$ represents the crustal contribution to measured surface heat flow (i.e., the depth integrated heat production) and, as outlined above, a mean regional value of $q_c \sim 50$ mWm$^{-2}$ is considered appropriate for the MII. It is noted that this is almost twice what other workers have suggested is typical of Proterozoic crust (Table 1.3; Chapman and Furlong, 1977; Nyblade and Pollack, 1993; McLennan and Taylor, 1996). Geological constraints outlined earlier in this Chapter also allow the likely distribution of these heat sources to be constrained (Figure 4.5). Knowing this, the length scale of the heat production distribution, $h$, in modern Mount Isa crust is estimated in the range ~ 7-11 km.

As outlined in Chapter Three of this thesis, the $h$-$q_c$ parameterization is particularly useful in that it allows us to "map" the way the distribution of heat sources changes with time during major tectono-orogenic processes. As a result, we are able to illustrate the thermal (and hence mechanical) consequences of the primary crustal processes. In the following section I investigate the way in which each major period of crustal activity recorded in the MII and described above, impacts on the distribution of heat producing elements in the crust. Following the analysis presented in Chapter Three, deformation and surface processes are linked through an isostatic response that, in the long-term, maintains crustal thickness. Thus, crustal thickening is coupled with erosion, while crustal extension is coupled with subsidence and basin formation.

In the following discussion I make few assumptions about the starting configuration of the crustal system prior to tectonism (i.e., the initial values of $h$ and $q_c$). One assumption I do make is that the heat producing elements were added to the crust from the lithospheric mantle relatively early in its history and have subsequently been redistributed during crustal scale processes. This assumption is supported at Mount Isa by both Nd and Sr-isotopic data from granites throughout the EFB, KLFB and WFB (Wyborn, 1998). Given that the modern crust is strongly differentiated in the heat producing elements and so characterized by low $h$, it must have evolved with decreasing $h$ through time.

## 4.4 Magmatic differentiation

Since much of the heat production in the MII is within granites, the generation, segregation and emplacement of these granites is central to the development of the inferred heat production distribution, with $h \sim 7$-11 km (Figure 4.5). In this section I consider some simple models for source region distributions in order to quantify the long-term thermal effects of such magmatism. For the sake of simplicity modern day heat production values are used. The equivalent temperature changes

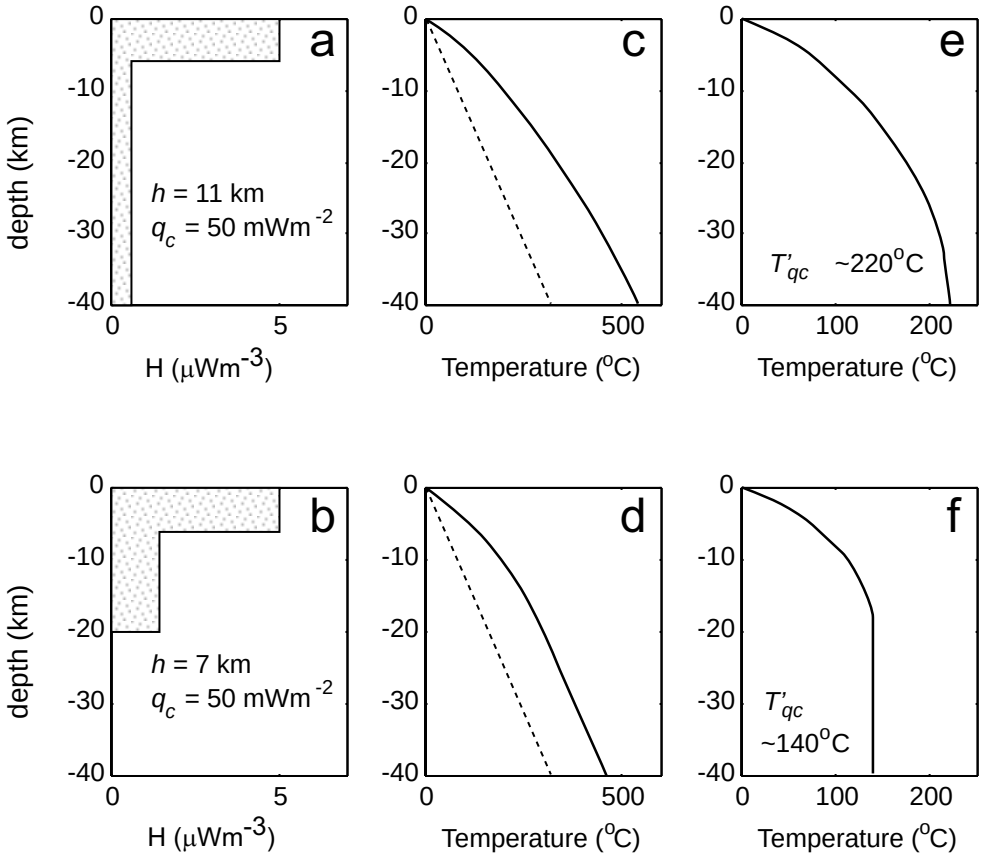


**Figure 4.5** Two alternative models for the distribution of heat sources in the modern crust in the MII. Both distributions give a total crustal contribution to surface heat flow $q_c$ ~ 50 mWm$^{-2}$ (see text for discussion). In both cases the upper layer represents the assumed thickness of average Mount Isa granite with ~ 5 μWm$^{-3}$ (see text), while the lower layers represent the largely depleted middle and lower crust. In (**a**) lower crustal heat production extends to the Moho with average productivity of 0.59 μWm$^{-3}$. For this distribution $h$ = 11 km. In (**b**) the middle crust contributes 1.2 μWm$^{-3}$ while the lowermost crust contains no significant heat sources. For this distribution $h$ = 7 km. Both models are consistent with known surface heat flow and heat production. (**c**) and (**d**) show the geotherm resulting from the heat production described by Models A and B, respectively. The dashed line is the geotherm that would apply in crust containing no heat producing elements (i.e., the mantle contribution). (**e**) and (**f**) show the additional temperature contribution, $T_{qc}$, due to the crustal heat sources distribution shown in (**a**) and (**b**) respectively. $T'_{qc}$ occurs at a point beneath which there are no additional heat sources and is ~ 220°C for Model A and ~ 140°C for Model B (see Chapter One for definitions).

in the Palaeoproterozoic to early Mesoproterozoic would be ~ 30% greater than listed below. Moreover, the calculations below assume a modern crustal contribution of ~ 50 mWm$^{-2}$ and so represent a minimum estimate of $T'_{qc}$ as $q_c$ may well have been much higher prior to the lengthy history of extensional deformation which occurred later in the tectonic history (see below for discussion).

As the MII granites are interpreted to represent lower crustal melting (e.g., Wyborn, 1998), heat producing elements carried by these granites must have been concentrated at much deeper levels prior to granite generation. I begin by exploring two simple scenarios that could explain the distribution of heat sources in the source region prior to granite generation. In the first I consider a distribution in which the granitic melt was generated from a layer of equivalent thickness (and hence enrichment) in the lower crust yielding $h$ ~ 30 km (Figure 4.6a). In this scenario the change in the length scale required to generate the inferred present day distribution of heat producing elements is $h$ ~ 19-23 km, implying a corresponding reduction in $T'_{qc}$ of 380-460°C, assuming a thermal conductivity, $k$, of 2.5 Wm$^{-1}$K$^{-1}$. However, it seems improbable that the lower crust was ever significantly more enriched in the heat producing elements than the upper crust, especially if it were largely mafic as suggested by Wyborn (1998), and a more reasonable scenario might have

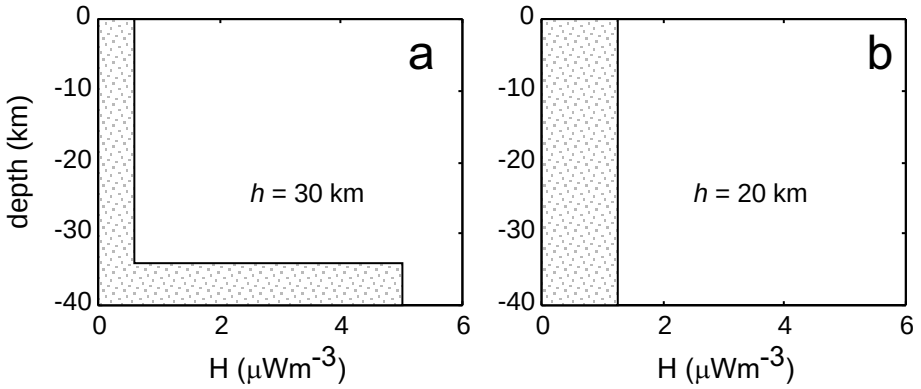


**Figure 4.6** Different heat source distributions as discussed in the text. Distributions (**a**) and (**b**) represent possible end-member starting configurations prior to crustal differentiation. *h* is the characteristic length scale of each distribution.

been an initially homogeneous distribution with $h \sim 20$ km (Figure 4.6b). In this case a differentiation equivalent to $h \sim 9$-13 km is required to generate the inferred present day distribution of heat producing elements, which equates to a long-term reduction in $T'_{qc}$ of 180-260°C (Figure 4.7).

These observations suggest that in the Mesoproterozoic the long-term cooling associated with the differentiation attributable to all magmatic processes in the MII is of the order of several hundred degrees. However, as noted previously this magmatism was the result of several distinct episodes, namely the Barramundi granites, the pre-Isan granites (Myally and Mount Isa Rift Events) and post-Isan granites (Figure 4.4). This section attempts to constrain the relative contributions of each of the three main pulses of magmatism (Table 4.4).

The volumetrically most significant of these granite pulses was the Barramundi Igneous Association (e.g., the Kalkadoon, Big Toby and Ewen Batholiths). While these granites form only about 18% of the total surface exposure in the MII, seismic profiles show that Barramundi granites extend at depth beneath the WFB (Figure 4.3), they are well exposed in the central KLFB where they comprise ~ 50% of surface outcrops, and they most likely form basement to the younger sedimentary packages in the EFB (e.g., Drummond et al., 1998). Consequently the "footprint" of these granites is assumed to be close to 100% of the area of the MII. Available geochemical data indicates an average heat production of ~ 3.7 $\mu Wm^{-3}$ (Tables 4.2, 2.2). Assuming that these Barramundi granites comprise ~ 5 km of the crust throughout the MII then they would account for approximately ~ 37%

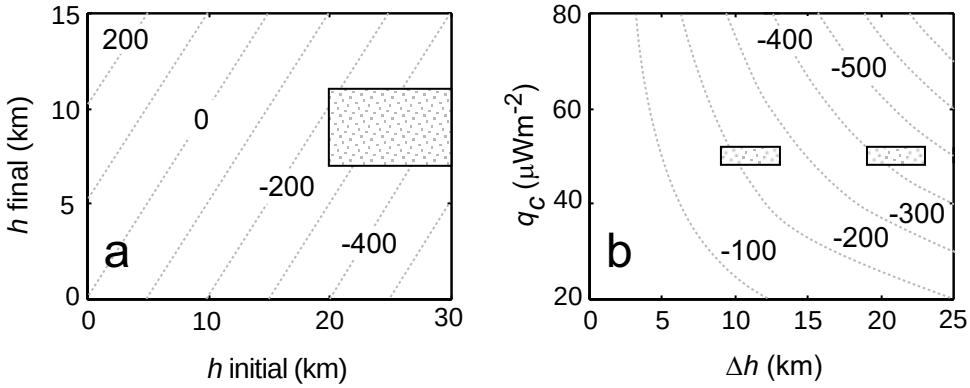


**Figure 4.7** Effects of changing heat source distribution on lower crustal temperature. (**a**) is contoured for the change in $T'_{qc}$ (°C) for different relative changes in length scale, *h*, and is constructed for $q_c \sim 50$ $mWm^{-2}$ as appropriate to the Mount Isa Inlier. Thermal conductivity is assumed to be constant and temperature independent, $k \sim 2.5$ $Wm^{-1}K^{-1}$. Negative $\Delta(T'_{qc})$ represents lower crustal cooling, such as would accompany magmatism (where $h_{initial} > h_{final}$). Positive $\Delta(T'_{qc})$ is equivalent to lower crustal heating resulting from, for example, the burial of a heat producing layer beneath a sedimentary basin (which has heat production such that $h_{initial} < h_{final}$). The shaded regions show the change in $T'_{qc}$ for the inferred starting configurations (as shown in Figure 4.6) and present-day configurations (as shown in Figure 4.5).

of the total complement of crustal heat production in the MII. The flux of heat producing elements associated with the generation of these granites equates with a ~ 7°C reduction in $T'_{qc}$ for each kilometre of transport. For a vertical transport distance of 20 km, appropriate to transport from the deep to shallow crust, the reduction in $T'_{qc}$ is around 140°C.

Younger granites in the MII (i.e., the pre-Isan rift related granites and the post-Isan granites), although often extraordinarily high heat producing, are not as significant volumetrically as the older Barramundi granites. In particular, these granites are of limited areal extent comprising about 16% of the surface exposure in the MII (Table 4.4). While the current erosion surface only samples a proportion of all the granites generated at these times, it is unlikely that their total "footprint" was vastly more extensive than represented in the current surface. In the following discussion we consider the total "footprint" for these granites to be no more than 2 times their representation in the current surface. Seismic profiles (e.g., Drummond et al. 1998) and previous workers suggest that the Sybella Batholith is a thin sill-like body which intruded essentially parallel to stratigraphy, with a preserved thickness of ~ 1.5-2 km in the plane of the seismic profile (Figure 4.3). A number of observations suggest that the batholith was considerably thicker at the time of intrusion (McLaren et al., 1999; see also Chapter 5 of this thesis), and here a typical thickness of ~ 3 km is assumed. By area the pre-Isan rift-related granites account for about 11% of all exposure in the MII. An average heat production of 5.1 $\mu Wm^{-3}$ (Tables 4.2) and an average thickness of 3 km implies that these granites account for 3.4%-6.8% of the total heat production of the MII crust (the upper limit assuming a footprint twice the current surface exposure, Table 4.4). The generation of these granites would account for a reduction in $T'_{qc}$ of 0.7-1.4°C per ascent kilometre, averaged over the area of the entire inlier. Locally the significance would have been much greater. For example, assuming that the "footprint" of the source area for individual granites was of the same dimension as the granite, then their segregation would lead to a reduction in $T'_{qc}$ of 6.1°C per ascent kilometre, with a 20 km ascent

**Table 4.4** *Characteristics of main phases of magmatism in the Mount Isa Inlier*

| *Parameter* | *Barramundi granites* | *Rift-related granites* | *Post-Isan granites* |
|---|---|---|---|
| Area ($km^2$) | 7130 | 4310 | 1830 |
| Area (%) | 18 | 11 | 5 |
| Thickness (km) | 5 | 3 | 3 |
| Heat Production ($\propto Wm^{-3}$) | 3.7 | 5.1 | 7.7 |
| HP (1) (%) | 6.7 | 3.4 | 2.2 |
| HP (2) (%) | 20.2 | 6.7 | 4.6 |
| Contribution to $q_c$ (%) | 37 | 30.6 | 46.2 |
| $T'_{qc}$ (1)* | 1.3 | 0.7 | 0.4 |
| $T'_{qc}$ (2)* | 7.4 | 6.1 | 9.2 |

*Note:* HP (1) is the percentage of total heat production in the MII crust based on the current area of outcrop and assumed thickness. As such HP (1) represents the minimum contribution of each pulse of granites to the total heat production in the MII. HP (2) is an estimate of the maximum percentage of total heat production in the MII based on the following estimates of the original "footprint" of each granite pulse: for the Post-Isan and Rift-related granites HP (2) is calculated for an area twice that which is outcropping; the Barramundi granites three times that area of outcrop (i.e., 54% of the terrane).

* $T'_{qc}$ (1) is the change in lower crustal temperature per kilometre of magma ascent when averaged over the entire inlier. $T'_{qc}$ (2) is the local change in lower crustal temperature per kilometre of magma ascent (i.e., that change in the immediate vicinity of each granite).

path corresponding to a reduction in $T'_{qc}$ of 122°C.

Similarly the post-Isan Orogeny granites such as the Williams and Naraku Batholiths are confined to the uppermost crust within the EFB, constituting about 5% of the total surface exposure of the MII. Seismic interpretation (McCready, 1997) suggests that these late-orogenic granites are sill-shaped and around 3-4 km in thickness. As such the granites host between 2.2%-4.4% of the total MII crustal heat production (Table 4.4), and are estimated to have contributed to a regional reduction in $T'_{qc}$ of 0.4-0.8°C per ascent kilometre. Locally their generation would have contributed to a reduction in $T'_{qc}$ by as much as 9.2°C per ascent kilometre.

## 4.5 Extension and convergent deformation

Although the very enriched nature of granites in the MII implies that granite magmatism provided the principal means of crustal differentiation, both extension and convergent deformation are also likely to have significantly modified the distribution of crustal heat sources. Of particular importance is the recognition that crustal thermal regimes are sensitive to small changes in the distribution parameters that result from deformation and associated surface processes of erosion and deposition.

As outlined in Chapter Three of this thesis, crustal extension, when accompanied by basin formation and sedimentation, results in two fundamental changes to the distribution of heat sources within the crust. The relative magnitude of each is dependent on the amount and symmetry of basement extension, and the thickness and heat production of the basin-fill. In general terms, the effect of stretching during crustal extension is to attenuate the pre-existing heat production while at the same time moving it to deeper levels (via burial beneath the sedimentary cover deposited in response to the extension). It thereby results in an increase in $h$. The change in $q_c$ is dependent on the amount of stretching and the heat production of basin-fill relative to the attenuated basement. Figure 4.8 illustrates that for a basin-fill with average heat production of 2.5 $\mu Wm^{-3}$ as appropriate to the LRFT (McLaren et al., 1999; Table 4.3), crustal extension and basin formation will lead to an increase in both $h$ and $q_c$ (dashed lines in Figure 4.8). For a stretching sufficient to produce a 7 km

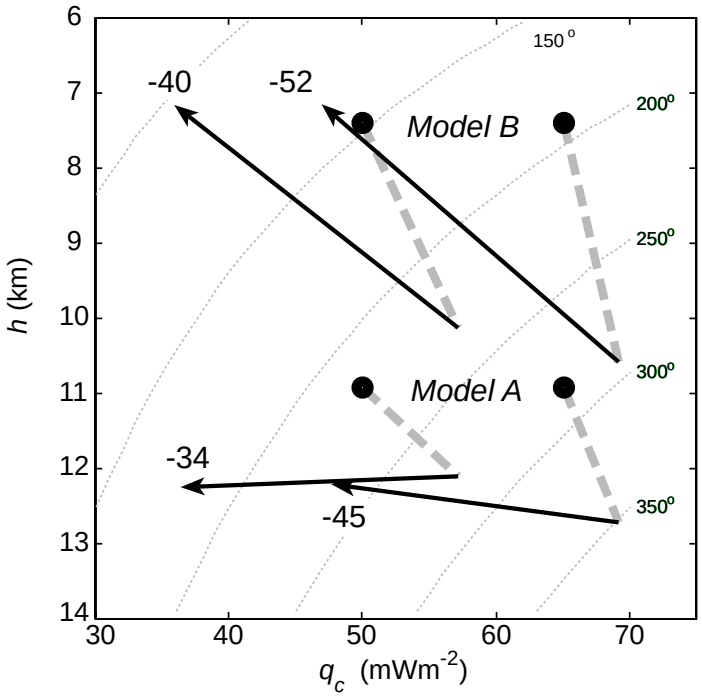


**Figure 4.8** $h$-$q_c$ paths appropriate to the sequence of events associated with extension and basin formation (i.e., the Leichardt, Myally and Mount Isa Rift Events) and the crustal thickening and erosion during the Isan Orogeny. Rifting and basin formation sufficient to generate a 7 km thick basin following all long-term subsidence is indicated by the dashed lines. Crustal shortening followed by erosion sufficient to generate ~ 13 km of denudation is shown by the solid lines. Two different initial geometries of heat producing elements are considered. Model A corresponds to the distribution shown in Figure 4.5a. Model B corresponds to the distribution shown in Figure 4.5b. Initial values of $h$-$q_c$ prior to deformation are indicated by the bullets. Deformation is considered to be homogeneous at the crustal scale. Contour intervals at 50°C show the values of $T'_{qc}$ appropriate to a given set of $h$-$q_c$ values (see also Chapter Three for further discussion of $h$-$q_c$ mappings).

thick sedimentary pile (a minimum estimate of sediment thickness in the LRFT from Australian Geological Survey Organization unpublished data; P. Southgate pers. comm., 1999), the increases in $h$ and $q_c$ will lead to long-term increases in $T'_{qc}$ in excess of 50°C.

Crustal shortening and erosion also change the distribution of heat sources within the crust. As crustal thickening normally results in erosion of the uppermost crust, its effect on both $h$ and $q_c$ is dependent on the distribution of heat production prior to deformation. As illustrated in Chapter Three of this thesis, for a differentiated crust in which heat production is concentrated in the upper crust, crustal thickening followed by erosion will lead to a long-term reduction in both $h$ and $q_c$. The solid lines in Figure 4.8 show the effect of deformation that homogeneously thickens the crust by 130% followed by erosion that returns crust to its present thickness of ~ 40 km (i.e., a deformation sufficient to generate average erosional levels of about 13 km, consistent with known geobarometry, e.g., Rubenach, 1992). In all cases modelled in Figure 4.8, the reduction in $q_c$ due to erosion leads to long-term reductions in $T'_{qc}$ of in excess of 100°C. Figure 4.8 shows that the successive imposition of crustal extension (with associated basin formation) followed by crustal thickening (with erosion) leads to long-term cooling, with the magnitude of this cooling dependent on the initial distribution of heat producing elements as well as the deformation parameters. For parameters considered appropriate to the evolution of the MII through the successive rifting events beginning with the Leichhardt event, through to the denudation following the Isan Orogeny, I estimate a long-term reduction of $T'_{qc}$ of ~ 35-50°C (Figure 4.8). Note also that in order to preserve a crust with a current complement of heat producing elements of ~ 50 $mWm^{-2}$, it is likely that the heat production distribution in the crust prior to the various tectonic events was of the order of ~ 65 $mWm^{-2}$.

## 4.6 Implications for polyphase tectonism in the Proterozoic

The geological record of the MII shows a protracted tectonic evolution spanning more than 300 million years. This history records episodic magmatism and deformation. Deposition of thick sedimentary sequences, and deep levels of erosional denudation, followed periods of extensional and convergent deformation respectively. This Chapter has attempted to show how this tectonic activity has shaped the distribution of heat producing elements inferred from analysis of present-day surface heat flow-heat production data. While the distribution of heat producing elements prior to the onset of tectonic activity cannot be rigorously constrained, it is clear that the tectonic evolution has produced progressive differentiation of heat producing elements, leading to the long-term cooling of the deep crust. The principal mechanism for this differentiation appears to have been the generation and segregation of granites from the deep crust, although significant changes in the parameters that define the heat production distribution can be attributed to crustal deformation and the associated surficial responses of sedimentation and erosion. Assuming that the initial crust was essentially undifferentiated, as seems to be required in order to produce the enriched granites of the MII, then the crustal differentiation associated with granite magmatism was sufficient to cool the lower crust by at least 200°C. Much of this differentiation is attributed to the volumetrically most abundant pulse of magmatism during the Barramundi Orogeny, however the subsequent periods of magmatism during the pre-Isan rifting events and following the Isan Orogeny, are also significant, and locally may have contributed in excess of 100°C cooling of the deep crust. Redistribution of heat producing elements during deformation associated with the Isan Orogeny, and subsequent erosional denudation is responsible for a further ~ 100°C cooling of the deep crust. In contrast,

rifting and basin-formation during the Leichardt, Myally and Mount Isa rift events is estimated to have lead to a long-term lower crustal heating of the order of 50°C (Figure 4.8).

The recognition that the tectonic record of the MII lead to the progressive cooling of the deep crust has profound implications for our understanding of its mechanical evolution. The strength of the continental lithosphere is known to be strongly temperature sensitive with Moho temperature providing a useful proxy for the strength (Sonder and England, 1986). As shown in Chapter Three of this thesis, a change in $h$-$q_c$ parameters sufficient to generate a 200°C reduction in Moho temperature, would equate with an eight-fold increase in the strength of the lithosphere or, alternatively, three orders of magnitude decrease in the rate of deformation that would apply to lithosphere subject to a tectonic load capable of localising permanent deformation (see also Sandiford et al., in press). These considerations provide important new insights into the long-term tectonic record of the MII. In particular, they suggest that the tectonic record is one of progressive strengthening. The long-term cooling and strengthening trend was locally countered by the role of subsidence during basin formation which, through burial of heat producing elements in the existing crust and the accumulation of more heat production in insulating sediments, helped to localise subsequent contractional deformation.

Interpreting the tectonic history of the Mount Isa region by understanding the feedback between tectonic processes and crustal strength allows some important controls on terrane reactivation and cratonization to be recognized. In particular, within any terrane the mechanical properties, and hence propensity for reactivation, are a function of the abundance and distribution of heat producing elements within the crust. Furthermore, the redistribution of heat producing elements during ongoing tectonism is capable of radically altering the mechanical response to subsequent events. Since cratonization implies that the cumulative lithospheric strength exceeds any likely applied tectonic force, it is favoured by processes that progressively concentrate heat sources in the upper crust. These observations suggest that the protracted history of magmatism and deformation at Mount Isa resulted from long-term crustal weakening due to the presence of anomalous concentrations of heat producing elements deep in the crust. In turn both magmatism and deformation, which are very sensitive to lower crustal thermal regimes, lead to the strengthening, and ultimately to the stabilization, of the crust through the progressive redistribution of heat producing elements to shallower levels and the removal of heat production through erosion.

# Chapter Five

# High-temperature, low-pressure metamorphism at Mount Isa, Queensland

The processes driving high temperature metamorphism at low to intermediate pressure have been the subject of many studies, and are fundamental to our understanding of crustal behaviour. Because crustal heat generation rates are normally considered to be too low to promote heating, such metamorphism is generally regarded as a consequence of the transient advection of heat from depth during magma ascent (De Yoreo et al., 1991; Karlstrom and Williams, 1995). However, it has become increasingly clear that such metamorphism is not always transient (Hodges et al., 1994; Williams et al., 1995). A notable example is in the vicinity of the Sybella Batholith in the western Mount Isa Inlier, Queensland, (Figure 5.1), where Mesoproterozoic metamorphism culminated in peak conditions of ~ 600°C and ~ 4 kbar (Rubenach, 1992), reflecting average upper crustal thermal gradients of ~ 40°Ckm$^{-1}$. Despite an apparent spatial association between metamorphic grade and the Sybella Batholith, there is an ~ 130 million year delay between granite intrusion and peak regional metamorphism (Connors and Page, 1995). Moreover, $^{40}Ar/^{39}Ar$ mineral closure ages suggest that elevated geothermal gradients were sustained for greater than 100 million years (Perkins et al., 1999). These data prohibit a primary role for advective heat transfer during granite emplacement and raise concerns about (1) what source provided thermal energy to drive metamorphism and (2) why there is a spatial association between the batholith and the metamorphic isograds (Figure 5.1).

This Chapter shows that the generation of steep upper crustal thermal gradients can be attributed to burial of high heat-producing granites beneath an insulating cover sequence during a prolonged period of rift-related subsidence. I begin this Chapter with an analysis of the setting and nature of metamorphism in the Western Fold Belt, and then present a compilation of heat flow,

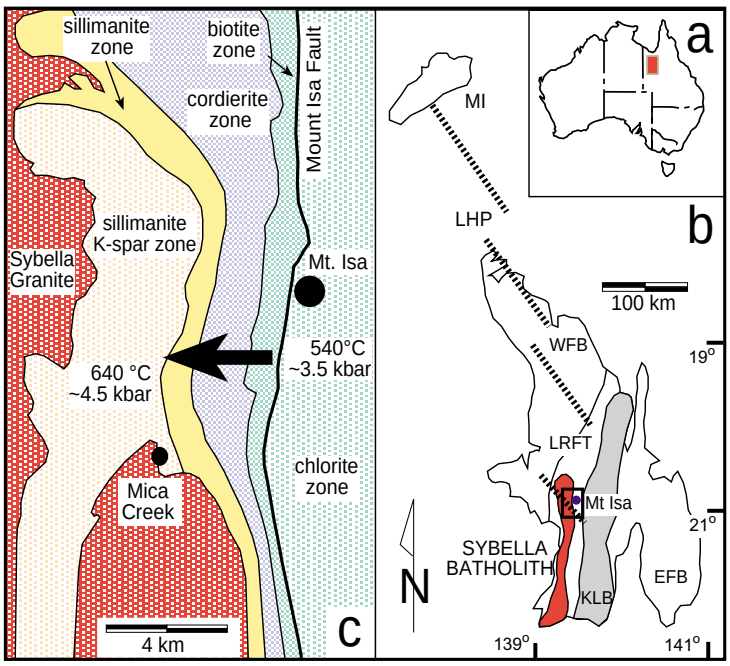


**Figure 5.1 (a)** Location of Mount Isa Inlier in north-west Queensland, Australia. **(b)** Structural domains of Mount Isa area (after Blake and Stewart, 1992), and section lines used for construction of Figure 5.2. WFB = Western fold belt (including Leichhardt River fault trough); KLB = Kalkadoon-Leichhardt fold belt; EFB = Eastern fold belt; MI = Murphy inlier, and LHP = Lawn Hill platform. **(c)** Isograd structure around the northeastern Sybella batholith, immediately west of Mount Isa city (area is indicated by small square in **b**) (from Rubenach, 1992).

heat production, and thermal conductivity data in order to constrain thermal regimes at the onset of the Isan Orogeny. This analysis forms the basis for a discussion of the origins of high-temperature metamorphism in this and other Proterozoic terranes.

## 5.1 The Sybella Batholith and the Isan Orogeny in the Western Fold Belt

The Sybella Batholith was emplaced into the Leichhardt River Fault Trough, a tectonic subdivision of the Western Fold Belt, at a depth of only a few kilometres during a rifting event at *ca.* 1660 Ma (O'Dea et al., 1997a). As outlined in the previous Chapter, the Sybella Batholith is estimated to be ~ 3 km thick at the time of emplacement. It was subsequently buried beneath the Isa Basin, a sedimentary succession ~ 13 km thick (Scott et al., 1999) (Figure 5.2). Although only ~ 5 km of this sedimentary cover is preserved in the Leichhardt River Fault Trough, correlative sections south of the Murphy inlier (Figure 5.1) and in the Eastern Fold Belt imply the presence of a temporally equivalent pre-orogenic basin throughout the Western Fold Belt (e.g., Southgate et al., 2000). The subsidence history was terminated by the Isan Orogeny (Blake and Stewart, 1992), during which contractional deformation was partitioned strongly into the Leichhardt River Fault Trough, the deepest portion of the pre-orogenic basin.

Isan Orogeny metamorphism in the Western Fold Belt is defined by regionally extensive intermediate to high temperature and low to intermediate pressure assemblages and elevated field gradients (Rubenach, 1992). Counterclockwise pressure-temperature paths show prograde heating through the andalusite field. Peak metamorphism is dated, by U-Pb zircon methods on a locally derived partial melt, at 1532 ± 7 Ma (Connors and Page, 1995). Mineral textures, including retrograde kyanite, indicate an isobaric or slightly decompressional cooling history (Rubenach, 1992). The absence of pressure sensitive assemblages does not allow a precise cooling path to be constrained; however, $^{40}Ar/^{39}Ar$ muscovite ages at Mica Creek (Figure 5.1) suggest cooling rates of ~1.5°CMa$^{-1}$ in the period from peak metamorphism to *ca.* 1400 Ma (Perkins et al., 1999).

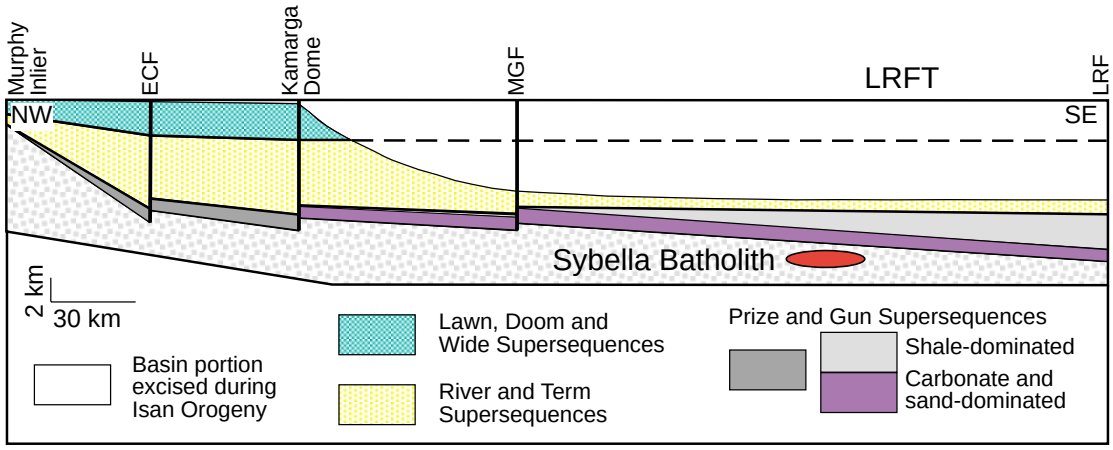


**Figure 5.2** Composite geometry of Isa basin immediately prior to Isan orogeny (*ca.* 1530 Ma) compiled using seismic and outcrop data by Deborah Scott (Australian Geological Survey Organization). Section constructed oblique to strike, northwest-southeast from Murphy inlier to Western fold belt-Kalkadoon-Leichhardt fold belt boundary; individual section localities are shown in Figure 5.1. Supersequence terminology is from Scott et al., (1999) and Southgate (2000). Thicknesses at Mount Gordon (MGF) and in Leichhardt River fault trough are minimum estimates, based on preserved thicknesses at Kamarga dome. Basin width includes estimate of the subsequent orogenic shortening. Sequences deepen and fine to south and east and in Leichhardt River Fault Trough the River and Term and Lawn, Doom and Wide supersequences are inferred to be 70-80% fine-grained clastics. Most dramatic basin inversion, and consequently most eroded part of basin, is area in easternmost Leichhardt River Fault Trough which contained the thickest sequence of pre-orogenic sediments. ECF = Elizabeth Creek Fault, LRF = Leichhardt River Fault.

On a regional scale, isograds cut across the north-plunging Sybella Batholith with greenschist facies assemblages in the north and upper amphibolite assemblages in the south. In the Mica Creek area isograds are parallel to the Mount Isa fault and its equivalents and displacements of ~ 1.5 km (Drummond et al., 1998) across these faults contribute to extraordinary metamorphic field gradients of ~ 50°Ckm$^{-1}$ (Figure 5.1). No significant syn-metamorphic mafic or felsic bodies have been identified at depth (Drummond et al., 1998) or in outcrop, and peak metamorphism is thought to have occurred during regional shortening that followed an extended period of post-rift subsidence, associated with deposition of the upper Mount Isa Group (O'Dea et al., 1997a).

## 5.2 Modern heat flow-heat production relations in the Western Mount Isa Inlier

Evaluation of the causes of metamorphism requires an assessment of the thermal structure of the lithosphere prior to metamorphism. This can be aided by analysis of modern-day heat flow-heat production relations and the thermal conductivity structure of the crust. As presented in the previous Chapter, the Mount Isa Inlier is characterized by elevated heat flow which can be demonstrably associated with elevated heat production in the modern Mount Isa crust. Much of this heat production is localized in discrete levels near the present surface. As suggested in the previous Chapter, at the regional scale the crust at Mount Isa must contribute as least 50 mWm$^{-2}$ to the observed surface heat flow, an assertion supported by calculated heat production values. This chapter is concerned with more local controls on lithospheric thermal regimes in Western Mount Isa Inlier.

Detailed airborne radiometric data (Figure 5.3) mean that variations in surface heat production in this area can be well constrained. Average heat production in the Sybella Batholith is ~ 5 μWm$^{-3}$ and in some individual stocks is as high as 10 μWm$^{-3}$ (Table 5.1, Figure 5.3). Seismic data (Drummond et al., 1998, Figure 5.3) show that beneath the Sybella Batholith the Big Toby granite forms a sheet ~ 5 km thick which has heat production ~ 3.5 μWm$^{-3}$ (Table 5.1). The fundamental importance of these values is highlighted by the fact that, based on the thickness estimates, the Sybella and Big Toby granites contribute more than 30 mWm$^{-2}$ to the modern surface heat flow in their own right and that in the middle Proterozoic, this contribution would have been ~ 30% greater. Average heat production in the remaining ~30 km of crust of only 1 μWm$^{-3}$ would account for the observed surface heat flow.

**Table 5.1** *Summary of geochemistry and heat production, Western Mount Isa Inlier*

| *Lithology* | *U (ppm)* | *Th (ppm)* | *$K_2O$ (wt%)* | *Q (μWm$^{-3}$)* | *Q* (μWm$^{-3}$)* |
|---|---|---|---|---|---|
| **Sybella Batholith** | | | | | |
| Main phase *(31)* | 8 | 35 | 5.07 | **5.12** | 6.86 |
| Beta-qz phase *(14)* | 8 | 33 | 5.38 | **5.01** | 6.77 |
| Microgranite *(12)* | 12 | 54 | 5.81 | **7.62** | 10.00 |
| **Big Toby Granite** *(4)* | 5 | 19 | 3.61 | **3.03** | 4.16 |
| **Sedimentary cover** | | | | | |
| Sandstones and conglomerates *(288)* | 2 | 8 | 2.00 | **1.39** | 1.82 |
| Siltstones and shales *(317)* | 6 | 18 | 4.30 | **3.37** | 3.82 |
| Carbonates *(1176)* | 2 | 3 | 1.50 | **0.75** | 1.31 |

Note: *Q* = present heat production; *Q** = heat production at time of peak metamorphism (~1550Ma). The number in parentheses is the number of samples analysed.

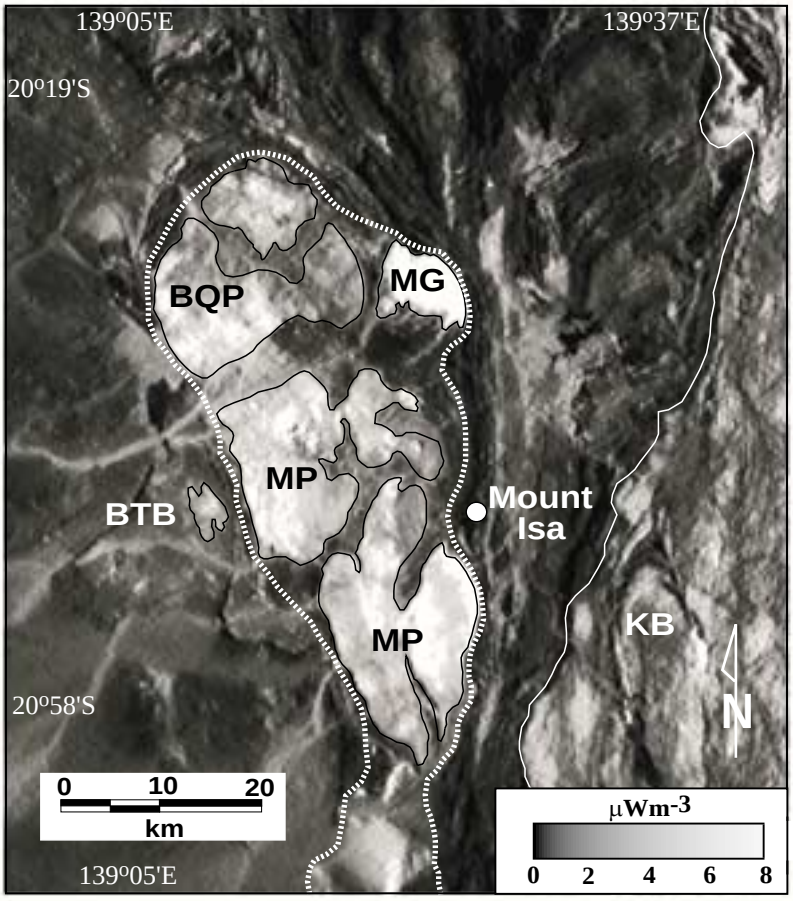


**Figure 5.3** Heat production of northern Sybella batholith ($\mu Wm^{-3}$) around time of peak metamorphism. Heat production values are calculated from calibrated radiometric data provided by MIM Exploration (Brisbane). All values above 8 $\mu Wm^{-3}$ (to a maximum of ~ 16 $\mu Wm^{-3}$) are shown in white. Approximate outcrop extents of Sybella batholith are shown and include MG = microgranite phase; BQP = beta-quartz phase; MP = main phase. BTB represents the small area of outcropping Big Toby Granite. The Kalkadoon batholith (KB) to east also shows elevated heat production (see also Chapter Two).

## 5.3 Thermal regimes at the onset of Isan metamorphism

From the point of view of the metamorphic evolution, it is useful to consider the thermal regimes that would result from such heat production distributions at the onset of the Isan Orogeny, following accumulation of the Isa Superbasin. Given that the Isa Superbasin accumulated over an interval of about 130 million years preceding the Isan Orogeny (Figure 5.2) it is likely that the lithosphere was close to conductive thermal equilibrium. Assuming heat conduction is only in the vertical direction, the temperature at any depth, $z$, reflects the heat flow at that depth, $q_z$, contributed by deeper sources, as well as the thermal conductivity, $k_s$, and heat production, $H_s$, of the overlying sequence. Assuming that the thermal properties of the overlying sequence are largely independent of depth, then the temperature at depth $z$ can be approximated by:

$$T_z \sim \frac{z}{k_s} * \left( q_z + \frac{H_s z}{2} \right) \qquad (5.1)$$

.

By the onset of the Isan Orogeny the Sybella Batholith was buried beneath ~ 13 km of Mount Isa Group sedimentary rocks and several kilometres of older sedimentary rocks and volcanics. This implies that the metamorphic pressures recorded in the vicinity of the Sybella Batholith (~ 4 kbar; Rubenach, 1992) are largely explicable in terms of burial during sedimentation, with some additional contribution due to crustal thickening during deformation. The present day surface heat flow provides insight into the magnitude of $q_z$, although it may differ because (1) radioactive decay has caused a reduction in the concentration of heat sources by ~ 30% since *ca.* 1500 Ma; (2) the heat flow contributed from the mantle, $q_m$, may have changed; and (3) the Isan orogeny has increased the

total heat production of the crustal columns due to crustal shortening of ~ 30%-40%. Points 1 and 3 cancel, at least to the first order, and it seems unlikely that at the onset of the Isan orogeny $q_m$ could have been much lower than the modern day values. Therefore I consider that in the Western Fold Belt the present surface heat flow $q_s$ (~ 80 $mWm^{-2}$) provides a conservative estimate for $q_z$ ($z$ = 15 km) at the onset of the Isan Orogeny.

The temperature at depth $z$ is strongly dependent on the thermal properties of the overlying sequence. Table 5.2 shows thermal conductivity data for the main sequences of the Isa Superbasin. The average thermal conductivity estimate of ~ 2.6 $Wm^{-1}K^{-1}$ was obtained by weighting the thermal conductivities of each sequence by relative thickness. This relatively low value reflects the dominance of fine-grained clastic sediments. The thermal conductivity of recent and diagenetic sediments is as much as 25%-50% lower than their lithified equivalents due to the effects of porosity, elevated temperature, and water saturation (Periera et al., 1986). The samples analysed here from lithified sequences therefore provide an upper bound on the conductivity of the sediments following deposition. The weighted average using data from unlithified equivalents is 1.4 $Wm^{-1}K^{-1}$ (Table 5.2). Given that significant diagenetic alteration already occurred during progressive burial, the thermal conductivity at the onset of the Isan orogeny is likely to have been between the lithified and unlithified estimates. Consequently, a likely range of thermal conductivities ~ 12%-25% lower than the weighted average lithified values is adopted (i.e., 2.0-2.3 $Wm^{-1}K^{-1}$). Geochemical data (Table 5.1) and calibrated airborne radiometric data (Figure 5.3) constrain heat production for the preserved components of the sedimentary cover to be ~ 2-3 $\mu Wm^{-3}$ at the time of metamorphism.

**Table 5.2** *Average Thermal conductivity, Isa Basin*

| *Sequence and Lithology* | *Estimated thickness (km)* | *Estimated thickness (%)* | *Conductivity ($Wm^{-1}K^{-1}$)* ***Case 1**** | *Conductivity ($Wm^{-1}K^{-1}$)* ***Case 2*** † | *Heat production ($\mu Wm^{-3}$)* |
|---|---|---|---|---|---|
| P&G Shale | 2.8 | 21.6 | 2.3 | 1.20 | 3.37 |
| P&G Carbonate | 0.4 | 2.9 | 3.0 | 1.77 | 0.75 |
| P&G Sand | 0.6 | 4.3 | 3.5 | 2.00 | 1.39 |
| R&T Shale | 4.8 | 36.8 | 2.3 | 1.20 | 3.37 |
| R&T Sand | 1.2 | 9.2 | 3.5 | 2.00 | 1.39 |
| L,D&W Shale | 2.0 | 15.2 | 2.3 | 1.20 | 3.37 |
| L,D&W Sand | 1.3 | 10.1 | 3.5 | 2.00 | 1.39 |
| **Total/Average** | **13.05** | **100** | **2.6** | **1.4**§ | **2.8**§ |

*Note:* Measured thermal conductivity data for Case 1 are from samples within the currently accepted lithological framework. Where a Supersequence contains more than one type of each lithological unit, preference, in calculating an approximate supersequence average, is given to the freshest sample of each lithology. Supersequence terminology is from Scott et al. (1999) and Southgate (2000). P&G, Prize and Gun, R&T, River and Term, and L,D&W, Lawn, Term and Wide, see also Figure 5.2.

* Case 1 - measurements on lithified (and in some cases metamorphosed) outcrop or drillcore samples at 25°C using a standard divided-bar apparatus; the maximum thermal conductivity of the pre-orogenic basin.

† Case 2 uses recent sedimentary thermal conductivities (Periera et al., 1986).

§ Average thermal conductivity and heat production values are a weighted average based on proportional vertical thickness by lithology. Heat production values are taken from Table 5.1.

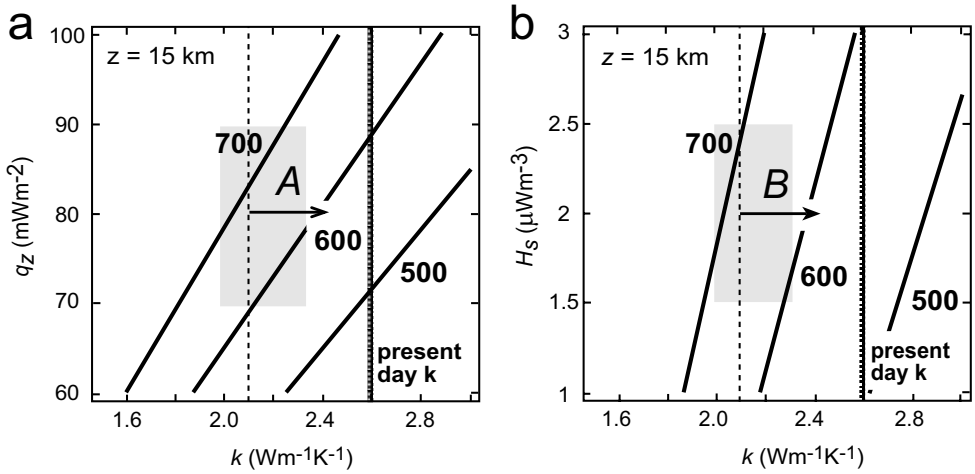


**Figure 5.4** Dependence of crustal temperatures at $z$ = 15 km on thermal conductivity of upper sedimentary sequence, $k$, and **(a)** integrated crustal heat flow, $q_z$ and **(b)** additional heat production in sedimentary pile, $H_s$. Shaded region is that area defined by known constraints on each parameter at time of metamorphism; present-day thermal conductivity is shown at 2.6 Wm$^{-1}$K$^{-1}$. Arrows *A* and *B*, show temperature reduction due to 15% increase in average thermal conductivity of basin, from ~ 2.1 to 2.4 Wm$^{-1}$K$^{-1}$, illustrating possibility of mid-crustal cooling associated only with diagenesis of sedimentary cover.

Figure 5.4 shows predicted temperatures at 15 km as a function of $H_S$, $k_S$ and $q_Z$. High temperatures and high geothermal gradients are favoured by high $H_S$ and low $k_S$, and enhanced by crustal thickening during deformation. On the basis of constraints outlined, plausible temperatures are in the range ~ 550-700°C and imply that the accumulation of the Isa basin was sufficient to generate the thermal and baric conditions appropriate to the ensuing metamorphism.

## 5.4 Discussion

Thermal regimes developed beneath basins are dependent on the heat production of the basement as well as the thermal conductivity of the overlying sedimentary succession. For the western Mount Isa Inlier, field gradients (when the throw on known faults is considered) and recorded peak metamorphic conditions are compatible with the thermal gradients expected to result from the accumulation of thick insulating sequences of the Isa Superbasin above basement that contributes ~ 80 mWm$^{-2}$ (including $q_m$). Such high geothermal gradients are likely to occur wherever such conditions are met and the data from Mount Isa imply that any understanding of the thermal energy budgets of high-temperature metamorphic terranes, regardless of tectonic setting, warrants detailed understanding of variations of heat production and thermal conductivity parameters at the crustal scale.

This interpretation raises the important question of what terminated the metamorphism. At Mount Isa, metamorphic recrystallization is clearly associated with the Isan Orogeny, which represents a major basin-inversion event during which contractional deformation was localized in the deepest and hottest parts of the basin. This Chapter has shown that the association between basin inversion and thermal regimes is not fortuitous, but reflects long-term thermal weakening of the lithosphere attendant with basin development on a radioactive basement. However, what causes the cooling that terminates metamorphism and, more particularly, the near-isobaric cooling that is interpreted to have occurred in the western Mount Isa Inlier? Ultimately, basin inversion during the Isan Orogeny lead to the unroofing of the high-heat-producing granites from beneath the Isa Basin. In

a manner analogous to the mechanism we have proposed during basin accumulation, this unroofing must ultimately cause dramatic cooling. However, the origin of the near-isobaric cooling remains enigmatic. One intriguing possibility is suggested by the role played by the thermal conductivity of the overlying sediment. The conductivity of a thick sedimentary pile will show both depth and time dependence. The time dependence will inevitably lead to an increase in thermal conductivity (at a given temperature) as diagenesis proceeds, while the depth dependence means that the bulk conductivity of the sedimentary succession is sensitive to the shallowest and most insulating sections. Either the progressive diagenesis of this uppermost section or its removal during progressive basin inversion would be expected to lead to significant cooling of the deeper lithosphere with relatively minimal pressure changes. For the Isa Basin, removal of 2 km of sediment with thermal conductivity significantly below the average basin value would lead to cooling of ~ 100°C with a corresponding pressure decrease of only ~ 0.5 kbar, unresolvable using modern geobarometric techniques. Similarly, an increase in the bulk conductivity of the entire sedimentary column of 15% would induce cooling of ~ 80°C (Figure 5.4). In either case, cooling would be more than sufficient to account for the observed post-peak pressure-temperature record and suggests that the time scales of cooling recorded by the $^{40}Ar/^{39}Ar$ data reflect either (1) the denudation that follows basin inversion or (2) the evolution of thermal conductivity in a deforming sedimentary basin.

# Chapter Six

# Tectonic reactivation and the localization of intraplate deformation: An example from Mount Painter, South Australia

Plate tectonics teaches that location is the paramount determinant in tectonic processes. In plate tectonics almost everything depends on position relative to active plate margins, with variations in tectonic style reflecting variations in the nature, and relative velocities, of the interacting plates. Nevertheless, the distribution of active deformation in the continents highlights the fact that proximity to active plate boundaries cannot be the sole determinant in shaping the tectonic response. For example, the heterogeneous partitioning of deformation in central Asia requires substantial variation in the mechanical properties of the Asian lithosphere (e.g., Neil and Houseman, 1997). The recognition of such heterogeneity raises critical questions such as what is the spatial and temporal amplitude of the mechanical variation in the continental lithosphere, what controls the spatial variations in mechanical response, and how does the mechanical response of lithosphere change as a function of tectonic activity?

Thermal regime is one of the most likely factors contributing to spatial and temporal variations in the mechanical response of the lithosphere (e.g., England, 1987; Sonder and England, 1986; Zhou and Sandiford, 1992). As outlined in Part One of this thesis, the characteristic thermal regime of continental lithosphere is constrained by the global heat flow dataset (Pollack et al., 1993). This dataset suggests that approximately one half to two thirds of the average surface heat flow (~ 65 $mWm^{-2}$) is due to heat production within the lithosphere, with the remainder due to heat supplied by convective processes from beneath the lithosphere. The same dataset also points to substantial regional variations in heat flow, as discussed in Chapter Two. For example, heat flow data from South Australia point to enrichment in heat producing elements possibly by as much as a factor of two relative to normal continental crust (e.g., Neumann et al., 2000). One of the most extraordinary parts of this anomalous heat flow region in South Australia is at Mount Painter in the northern Flinders Ranges. In the Mount Painter province Mesoproterozoic gneissic complexes of the Mount Painter and Mount Babbage basement are exposed over a 100 km by 30 km wide zone and have an area-averaged heat production of ~ 16 $\mu Wm^{-3}$, more than three times the upper crustal average. Some individual granite stocks have heat production significantly above this average (Table 6.1). For example, the Yerila granite in the Mount Babbage inlier has heat production of 62 $\mu Wm^{-3}$, while the Hot Springs Gneiss in the Mount Painter inlier has an average heat production of 41 $\mu Wm^{-3}$. In the Mount Painter inlier the Box Bore granite, Mount Neill granite and the Terrapinna granite have heat production of 22 $\mu Wm^{-3}$, 11 $\mu Wm^{-3}$ and 7 $\mu Wm^{-3}$ respectively (all values are modern heat production rates, summarized from Neumann et al., 2000). Such extreme heat production values are consistent with the present day heat flow of 120 $mWm^{-2}$, and suggest that crustal sources contribute at least 70 $mWm^{-2}$, and possibly up to 100 $mWm^{-2}$, to the surface heat flow in this region.

Despite apparently being located well within the continental interior from at least the

**Table 6.1** *Summary of geochemistry and heat production, Mount Painter inlier*

| *Lithology* | *Area ($km^2$)* | *U (ppm)* | *Th (ppm)* | *$K_2O$ (wt%)* | *Q ($\mu Wm^{-3}$)* |
|---|---|---|---|---|---|
| Mount Neill Granite; Pepegoona Porphyry (60) | 189 | 21 | 74 | 3.57 | **11.3** |
| Hot Springs Gneiss (42) | 22 | 75 | 288 | 4.17 | **41.0** |
| Box Bore Granite (30) | 40 | 44 | 131 | 6.37 | **21.6** |
| Yerila Granite (28) | 30 | 116 | 423 | 5.66 | **61.6** |
| Wattleowie Granite (27) | 18 | 6 | 33 | 5.78 | **4.5** |
| Terrapinna Granite (29) | 99 | 10 | 58 | 5.24 | **7.2** |
| Petermorra Volcanics (7) | 13 | 13 | 35 | 6.50 | **6.7** |
| ***Average** granites, granite gneisses, felsic volcanics* | **411** | **29** | **110** | **4.62** | **16.1** |
| Mesoproterozoic metasediments (9) | | 2.3 | 16.2 | 3.25 | **2.09** |
| Adelaidean cover sequence (14) | | 3.4 | 12.7 | 5.28 | **2.33** |

Note: *Q* = present heat production. The number in parentheses is the number of samples analysed. A full listing of the heat production data for Mesoproterozoic metasediments and the Adelaidean cover sequence is given in Appendix A. The Mesoproterozoic metasediments include the Freeling Heights Quartzite and Yagdlin Phyllite. Calculation of the average heat production of the Mesoproterozoic granites by area given in Appendix A, Table A.8

Granite data from Neumann et al., (2000); data for Mesoproterozoic sediments from Neumann, (2001), Schaefer, (1993) and Neumann, (1996); data for Adelaidean cover sequence from O'Halloran, (1992).

Mesoproterozoic to the present day, this extraordinary province records a long, complex, and ongoing record of deformation involving basin formation and inversion (e.g., Sandiford et al., 1998a; Paul et al., 1999). Modern thermochronological methods allow detailed reconstruction of thermal histories, which can be used to help understand the links between thermal regime and tectonic activity. In this chapter I first present K / Ar and $^{40}Ar/^{39}Ar$ data which allow the thermochronological record of the Mount Painter region to be constrained. This chapter continues to discuss the controls on tectonic reactivation in continental interiors with the results presented here providing evidence that thermally modulated variations in lithospheric strength may control the distribution of intraplate deformation at the continental scale.

## 6.1. Geologic Setting

The Adelaide Fold Belt in South Australia comprises deformed Neoproterozoic and Cambrian sediments of the Adelaide geosyncline (e.g., Preiss, 1987) overlying a Palaeoproterozoic and Mesoproterozoic crystalline basement. The fold belt is subdivided into four main structural domains, the southern Adelaide Fold-Thrust Belt, the Nackara Arc, the central Flinders Ranges, and the Northern Flinders Ranges (Figure 6.1). The Mount Painter province, which comprises the Mount Painter and Mount Babbage Inliers, forms the northernmost basement of the Adelaide Fold Belt system in the Northern Flinders Ranges (Figure 6.1). The eastern margin of the Northern Flinders Ranges coincides with the Paralana Fault, along which the Mount Painter province is thrust over the adjacent Curnamona Craton. The western margin of the northern Flinders Ranges is marked by the Norwest Fault. To the north of the ranges lie the Palaeozoic Warburton, Cooper and Eromanga basins, which are overlain by Mesozoic and Cainozoic sediments of the Lake Eyre Basin (Figure 6.1).

In the Mount Painter province the Mount Painter and Mount Babbage inliers consist of metasediments that were deposited and metamorphosed at high grade conditions during the Palaeoproterozoic (Teale, 1993), and subsequently intruded by Mesoproterozoic granitoids, and

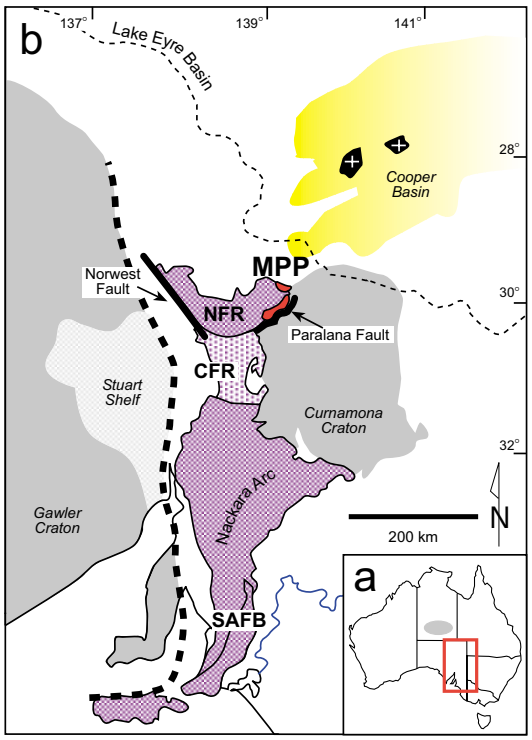


**Figure 6.1** (**a**) location of the Adelaide Fold Belt within South Australia (red box). Area of central Australia affected by the Permo-Carboniferous Alice Springs Orogeny (ASO) shown as grey stipple. (**b**) Structural framework of northern and central South Australia. The region shown in purple is the Adelaide Fold Belt. This region can be divided into 4 distinct structural domains: the Southern Adelaide Fold-Thrust Belt (SAFB), the Nackara Arc, the Central Flinders Ranges (CFR) and the Northern Flinders Ranges (NFR). The location of the Mount Painter Province (MPP) within the NFR region is shown in red. The MPP forms one of the basement inliers within the Adelaide Fold Belt, the others occurring in the SAFB and along the southern margin of the Curnamona Craton. Also shown are the inferred extents of the Proterozoic Curnamona and Gawler Cratons, the late Carboniferous-Triassic Cooper Basin and the Late Palaeocene-Holocene Lake Eyre Basin. The Warburton Basin, which underlies the Cooper Basin, is intruded by *ca.* 300 Ma granites (dark shading with crosses).

overlain by Mesoproterozoic sediments and volcanics. These Palaeoproterozoic and Mesoproterozoic units are overlain by a ~ 7-12 km thick Neoproterozoic sedimentary sequence forming part of the Adelaide geosyncline (Figure 6.2). This sedimentary cover was deposited between about 830 and 550 Ma (Preiss, 1987; Preiss, 2000) during a sequence of rift-related subsidence events. Subsequent Palaeozoic deformation and metamorphism affected both the basement and the cover.

In the Southern Adelaide Fold Belt (Figure 6.1), U-Pb zircon data from syn- and post-kinematic granites constrain deformation and metamorphism of the Adelaidean cover sequence to between 515 and 490 Ma (e.g., Jenkins and Sandiford, 1992; Foden et al., 1999), an event termed the Delamerian Orogeny. Tectonism throughout the remainder of the Adelaide Fold Belt, including at Mount Painter, is also ascribed to Delamerian times, largely on the basis of a similarity in structural style and a pre-deformational depositional record which everywhere terminates at about the same time in the Early Cambrian (e.g., Jenkins and Sandiford, 1992) (time scale from Young and Laurie, 1996, used throughout). In the Mount Painter region however, we can only be certain that the deformation occurred subsequent to ~ 550 Ma, the approximate depositional age of the youngest deformed sediments overlying the basement.

The Palaeozoic deformation is typically thick-skinned, basement involved, and is characterized by the propagation of large amplitude, basement-cored upright folds which plunge gently to the southwest. In the southwestern part of the Mount Painter inlier the basement/cover unconformity is folded on the regional scale by the Yankaninna Anticline (e.g., Sandiford et al., 1998a) (Figure 6.3), with total shortening estimated at ~ 20% (Paul et al., 1999). Metamorphic assemblages in both the cover and the basement indicate that the main fabric formed at high-temperature low-pressure conditions. Isograds in the lower part of the cover succession are essentially concordant with the basement unconformity (Figure 6.3b), defining an unusual style of "unconformity related contact metamorphism" (Mildren and Sandiford, 1995; Sandiford et al., 1998a). These isograds are marked by the progressive appearance of scapolite, tremolite, cordierite and diopside. The occurrence of cordierite-anthophyllite and diopside-bearing rocks immediately above the basement-cover

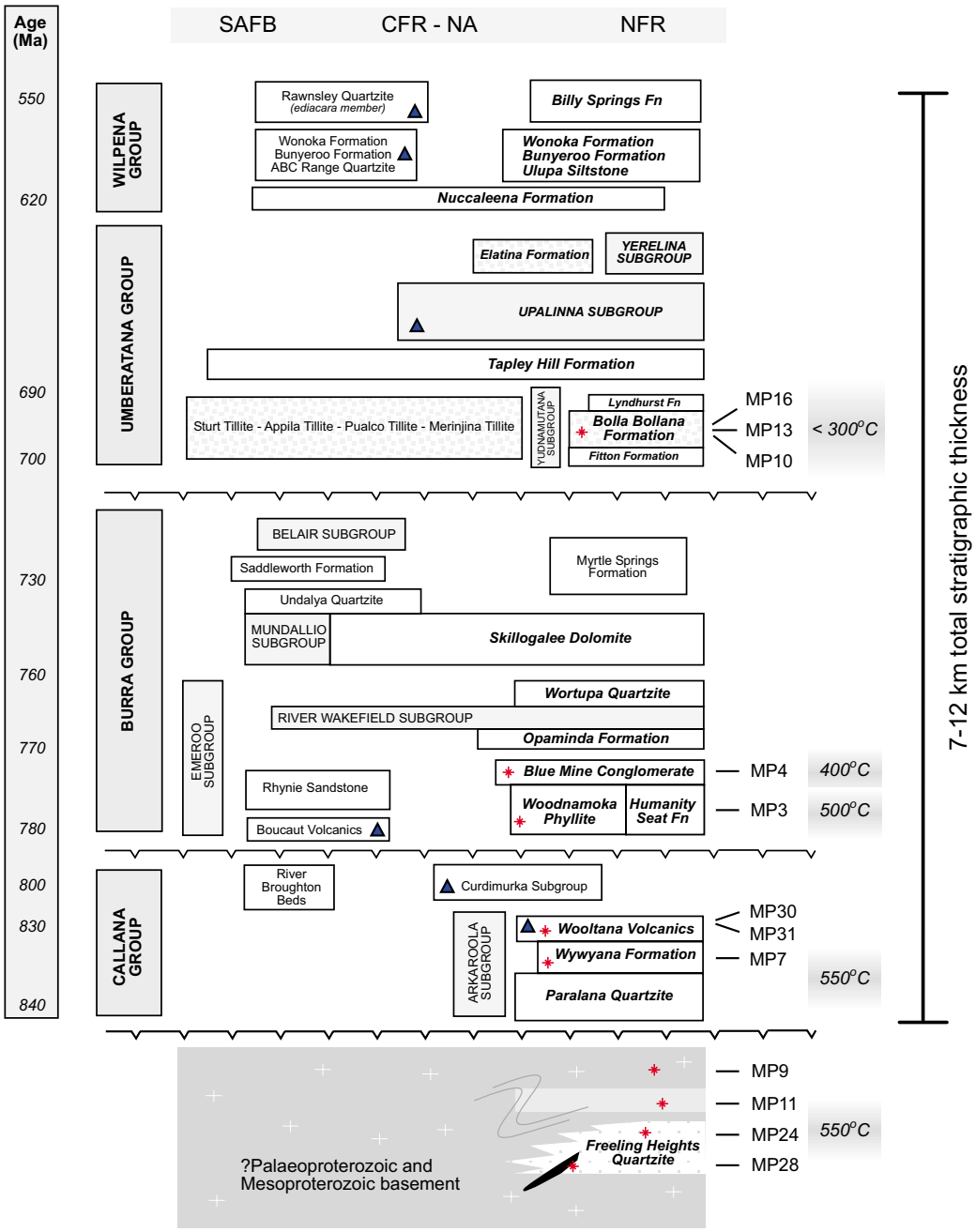


**Figure 6.2** Generalized stratigraphic relationships for the Adelaidean cover sequence in the Southern Adelaide Fold Belt (SAFB), Central Flinders Ranges and Nackara Arc (CFR-NA) and Northern Flinders Ranges (NFR). Italicised units outcrop in the Mount Painter province. Stratigraphic units denoted with an asterisk were sampled for potassium-argon analysis, with sample numbers listed to show relative stratigraphic position. Samples from the Palaeozoic intrusives are not shown. Estimated peak Palaeozoic (?Delamerian) metamorphic temperatures are indicated for each of the main sample groups. Units denoted with a triangle have been subject to age determinations and are used to construct the approximate chronological framework shown. Age data are largely SHRIMP U-Pb ages from zircons within cross cutting dykes or interleaved tuffs. Age data summarized from Preiss (2000). There has only been one age determination on units which outcrop at Mount Painter, so stratigraphic equivalence with units in the SAFB and CFR-NA is used to constrain the time of deposition in most cases. Stratigraphic relations adapted from Preiss (1993) and Preiss (2000). The major unconformities are shown by toothed lines.

unconformity suggests peak metamorphic temperatures of at least 500°C. Pressures at the unconformity are estimated to be ~ 3 kbar from the widespread association of cordierite-biotite-muscovite, equating to a depth of ~ 12 km assuming an average density of 2500 $kgm^{-3}$ for the covering sediments. These data imply an average upper-crustal thermal gradient of ~ 40°$Ckm^{-1}$ (Sandiford et al., 1998a). There is no evidence that the sequence has been buried to depths significantly greater than the ~ 12 km recorded by the prograde mineral assemblages. In view of the relatively mild tectonic shortening

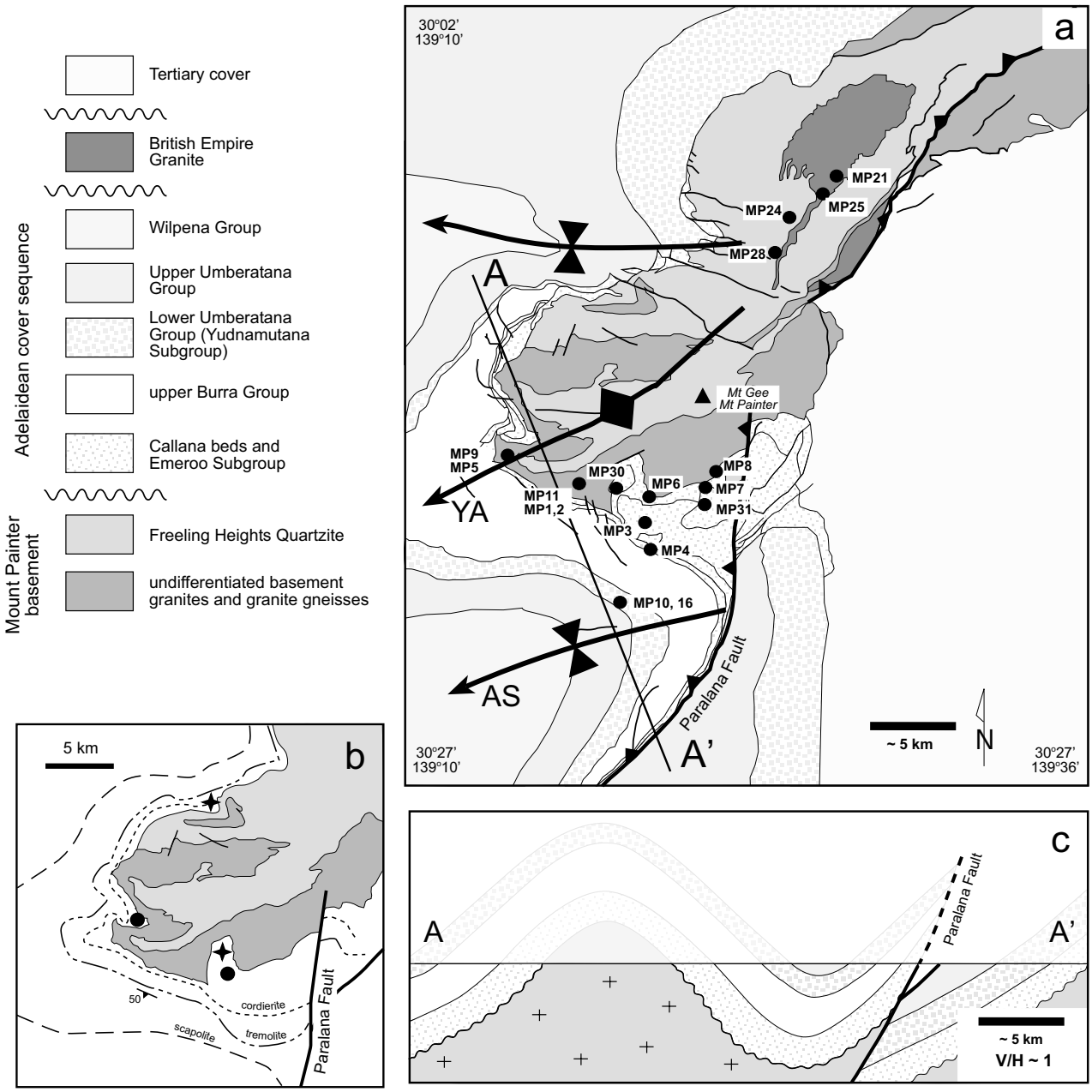


**Figure 6.3** Structural, stratigraphic and metamorphic summary for the Mount Painter Inlier **(a)** Geology of the southern Mount Painter Inlier showing sample locations. Geology modified from Coats et al. (1969) and shown by stratigraphic group only; YA = Yankannina Anticline, AS = Arkaroola Syncline (Paul et al., 1999). **(b)** Section of map from (a) illustrating the concordance of metamorphic isograds with the basement-cover unconformity. Each isograd represents the first appearance of each mineral**,** in the direction of increasing grade. Circles show diopside localities, stars show location of cordierite-anthophyllite assemblages. **(c)** schematic cross-section through the southern Mount Painter inlier illustrating general structural style. Section is drawn at approximately the same scale as map view, with no vertical exaggeration. Structural style and geometry based on measured regional cross-sections from Paul et al. (1999).

estimated by Paul et al. (1999), and evidence that the cover sequence is approximately 10 km thick, the principal contribution to burial appears to have been the accumulation of sediments through a succession of Neoproterozoic rift-sag cycles commencing at *ca*. 830 Ma (Paul et al., 1999).

While the timing of the Palaeozoic deformation and metamorphism can be loosely constrained to be younger than 550 Ma, the cause of this metamorphism is less clear. Available data suggests that there are no mafic intrusives post-dating the Wooltana Volcanics (whose extrusion marks the base of the Adelaidean sequence) and although there are a number of small Palaeozoic pegmatoidal bodies, as outlined below, these are considered to be a consequence rather than a cause of the

metamorphism. Of these, most form small plugs or dykes less than ~ 50 m in diameter and only one, the British Empire Granite, covers a significant area (Figure 6.3a). This body is a heterogeneous, peraluminous granite occurring near the structurally deepest part of the basement in which layering is parallel to that in the surrounding partly migmatitic Proterozoic rocks (Neumann, 1996). It exhibits complex interfingering and gradational contacts with the enclosing sediments, which suggests that it was derived locally.

The absence of evidence for any voluminous high-temperature synmetamorphic intrusions suggests that the commonly accepted paradigms for high temperature-low pressure metamorphism (e.g., De Yoreo et al., 1991; Karlstrom and Williams, 1995) do not apply in this case. However, the Proterozoic basement units in the Mount Painter Inlier are extraordinarily enriched in the heat producing elements (as outlined above and in Chapter Two) contributing at least 70 $mWm^{-2}$ and as much as 100 $mWm^{-2}$ to the surface heat flow. In a model that accounts for both metamorphic pressures and known sediment thicknesses, Sandiford et al. (1998a) suggested that the metamorphic conditions may primarily reflect the burial of high-heat producing Proterozoic basement beneath the Adelaidean cover sequence; a similar model to that outlined for the western Mount Isa Inlier in Chapter Five of this thesis. A significant problem with generating temperatures of ~ 500°C at ~ 12 km depth by conduction is the prevention of wholesale melting of the lower crust. Sandiford et al. (1998a) argued that at Mount Painter the only way that lower crustal temperatures could have been keep sufficiently low to prevent such melting was if mantle heat flow was extremely low, as might be expected following a period of extended thermal subsidence. Thus, they made the unconventional hypothesis that elevated upper crustal thermal regimes recorded during Early Palaeozoic metamorphism were attained as a direct consequence of processes that cooled the deeper parts of the lithosphere. A first order prediction of this conductive model is that temperature and depth are correlated, and only when the rocks are exhumed should they be cooled.

Although the Mount Painter Inlier has suffered an extended history of tectonic activity, being intermittently active from the Palaeoproterozoic through until at least the early Cambrian, a number of lines of evidence suggest that significant tectonic activity continued after this time in both the Mount Painter region and in adjacent crustal blocks. Whole-rock Rb-Sr isotopic ages of *ca.* 450-350 Ma for basement granites and gneisses (e.g., Neumann, 1996; Schaefer, 1993) and K/Ar age determinations on 6 biotite separates from the Yerila Granite, in the Mount Babbage inlier, of around 400 Ma (Webb, 1976) suggest that the Mount Painter rocks remained above about 300°C for a considerable time following the Delamerian Orogeny. The timing of the final exhumation is constrained by *ca.* 260-175 Ma apatite fission track ages (Foster et al., 1994). The northern part of the inlier is partly overlain unconformably by the Early Cretaceous Parabarana Sandstone, implying surface exposure by this time. The Mount Painter province is also characterized by ongoing tectonic activity, manifest by modern seismicity and juvenile topography (e.g., Sprigg, 1946; Callen and Telford, 1976). In the Warburton-Cooper Basin to the north, *ca.* 298 and 323 Ma granitoids (Gatehouse et al., 1995) are indicative of crustal disturbances extending toward central Australia where Carboniferous intraplate tectonism and magmatism is well known (e.g., Dunlap and Teyssier, 1995).

## 6.2 K/Ar and $^{40}Ar/^{39}Ar$ Analysis

At very high temperatures all the radiogenic argon ($^{40}Ar^*$) produced by decay of $^{40}K$ is expected to be lost continuously from a crystal lattice by volume diffusion. As a mineral cools it will reach

a temperature below which argon diffusion is negligible, so that the argon daughter product accumulates quantitatively. A K / Ar age or a $^{40}Ar/^{39}Ar$ total fusion age essentially records the time since closure of the mineral to argon diffusion. In general there is a restricted temperature interval for each mineral over which it passes from no accumulation to full accumulation of radiogenic argon. Dodson (1973) defined a closure temperature ($T_c$) corresponding to the apparent temperature at which the mineral becomes closed to diffusive loss. Common potassium-bearing minerals have a large range of closure temperature with respect to argon accumulation. Thus, hornblende has a $T_c$ of ~ 500°C (Harrison, 1981); muscovite has an estimated $T_c$ of ~ 400°C (Hames and Bowring, 1994), biotite a $T_c$ of ~ 300°C, (Harrison et al., 1985) and K-feldspar appears to exhibit a range of closure temperatures from about 350°C to 150°C (Lovera et al., 1989). Analysis of a number of different minerals from a particular region by the K / Ar and $^{40}Ar/^{39}Ar$ techniques allows a cooling history to be elucidated because of the different closure temperatures, and this is the approach followed here.

Slow cooling of a mineral can result in the development of radiogenic argon concentration gradients, especially adjacent to grain boundaries. Step heating of a sample that has previously been irradiated in a nuclear reactor to produce $^{39}Ar$ from $^{39}K$ (see McDougall and Harrison, 1999), may reveal variations in the $^{40}Ar^*/^{39}Ar$ ratio, which is proportional to age, if the mineral remains stable during at least part of the heating experiment. Results generally are shown as an age spectrum, a plot of age of each step against the cumulative proportion of argon released. Early workers proposed criteria for the identification of a plateau in an age spectrum (see McDougall and Harrison 1999, for discussion). Here the term plateau is used for that part of an age spectrum where the ages of consecutive steps are within $2\sigma$ of one another and together comprise at least 50% of the gas release. In this section I also apply the term “plateau-like” to part of an age spectrum which does not quite meet these criteria, mainly due to the presence of one or two discordant steps within a sequence of otherwise consecutive steps, which together comprise more than 50% of the gas release.

In this study, conventional K / Ar age measurements were performed on mineral separates from 19 samples from both Mesoproterozoic, or older, basement rocks and the overlying Neoproterozoic Adelaidean cover sequence (Table 6.2, locations shown in Figures 6.2 and 6.3a). The initial K / Ar study of hornblende, muscovite, biotite and K-feldspar was undertaken in part to guide the choice of samples for subsequent $^{40}Ar/^{39}Ar$ analyses. Petrological and thermal constraints on samples and the analytical methods employed are summarized in Appendix B.

### 6.2.1 Hornblendes

Three hornblende mineral separates, from samples MP30, MP31 and MP28, were analysed using the K / Ar technique. Sample MP30 is a hornblende, plagioclase and actinolite bearing metabasalt from the Wooltana Volcanics (Figure 6.2) adjacent to the basement-cover unconformity. This sample yields an apparent K / Ar age of 395 ± 4 Ma (Table 6.3). Sample MP31, also from the Wooltana Volcanics and containing both hornblende and epidote, yields an apparent age of 436 ± 5 Ma. Hornblende from sample MP28, an amphibolite dyke intruding basement rocks of the Freeling Heights Quartzite in the central Mount Painter inlier (Neumann, 1996), yields an age of 423 ± 6 Ma.

**Table 6.2** *Sample location and description*

| *Sample* | *mu* | *bt* | *K-spar* | *hbde* | *Lithology* | *Unit* | *Easting* | *Northing* | *Distance from u/c (km)* | *Description* |
|---|---|---|---|---|---|---|---|---|---|---|
| MP21 | # | | # | | British Empire Granite | PG | 350370 | 6666840 | - 2.0 | Coarse leucogranite, plag, muscovite, qz and microcline bearing |
| MP25 | # | # | | | British Empire Granite | PG | 349240 | 6665870 | - 2.0 | Coarse grained, plag, mu, bt and qz bearing granodiorite, associated with BEG |
| MP24 | *x* | *x* | *x* | | Freeling Heights Quartzite | MB | 347250 | 6663400 | - 2.0 | Strongly foliated and recrystallized quartzite, foliation defined by mu and bt |
| MP28 | | | | # | Amphibolite | MB | 346550 | 6661900 | - 2.0 | Recrystallized hornblende, bt amphibolite |
| MP11 | *x* | *x* | | | Metasediment | MB | 335164 | 6649213 | - 0.5 | Metasedimentary enclave within MB, strongly foliated and crenulated, foliation defined by mu and bt |
| MP2 | | *x* | | | Nooldoonooldoona pegmatite | MB | 335200 | 6649600 | - 0.5 | Metasomatized margin of local pegmatite; monomineralic, foliated biotite aggregate |
| MP9 | # | *x* | *x* | | Foliated Gneiss | MB | 331125 | 6650867 | - 0.2 | foliated mu, bt gneiss |
| MP5 | *x* | | | | Arkaroola pegmatite | PG | 330937 | 6650837 | -0.2 | Deformed, coarse grained Kspar, mu pegmatite |
| MP8 | # | | # | | Arkaroola Pegmatite | PG | 341924 | 6649759 | 0 | Megacrystic Kspar, mu, qz, tourmaline pegmatite |
| MP1 | | *x* | *x* | | Nooldoonooldoona pegmatite | PG | 335200 | 6649600 | + 0.5 | Local Kspar pegmatite |
| MP6 | # | | *x* | | Arkaroola pegmatite | PG | 339617 | 6648145 | + 0.5 | Coarse, relatively undeformed Kspar, mu and diopside bearing pegmatite |
| MP30 | | | | # | Wooltana Volcanics | ACS | 337550 | 6649000 | + 0.5 | Hornblende, plagioclase metabasalt |
| MP7 | | *x* | | | Local biotite schist | ACS | 341934 | 6649855 | + 0.5 | Monomineralic biotite schist, associated with andalusite bearing schist |
| MP31 | | | | # | Wooltana Volcanics | ACS | 342550 | 6648750 | + 0.6 | Hornblende, epidote metabasalt |
| MP3 | *x* | *x* | | | Woodnamoka Phyllite | ACS | 340250 | 6646550 | + 1.75 | Fine grained sandy schist |
| MP4 | | | *x* | | Blue Mine Conglomerate | ACS | 340050 | 6645550 | + 2.0 | K-feldspar clast in arkosic conglomerate |
| MP10 | | | *x* | | Bolla Bollana Formation | ACS | 337500 | 6643340 | + 3.0 | Granite clast within glacial Tillite |
| MP13 | | | # | | Bolla Bollana Formation | ACS | 337491 | 6642838 | + 3.0 | Granite clast within glacial Tillite |
| MP16 | | | *x* | | Bolla Bollana Formation | ACS | 337648 | 6642345 | + 3.0 | Porphyritic volcanic clast within glacial Tillite |

*Note:* Sample locations are given in Australian Map Grid (1984), Zone 54; plag = plagioclase; mu = muscovite; bt = biotite; qz = quartz; Kspar = K-feldspar
MB = Mesoproterozoic Mount Painter Basement; ACS = Neoproterozoic Adelaidean Cover Sequence; PG = Palaeozoic granite/pegmatite
Distances are quoted above (denoted positive) and below (denoted negative) the basement-cover unconformity; Field sample numbers given in Appendix B
Mineral separates denoted by an *x* were analysed by both K/Ar and $^{40}Ar/^{39}Ar$ methods; separates denoted by a # were analysed by the K/Ar method only

**Table 6.3** *Results of K-Ar isotopic analyses*

| Sample # | Lithology | Unit | Mineral | K (wt %) | Rad $^{40}Ar^*$ ($10^{-9}$ mol/g) | 100 $^{40}Ar^*$ / Total $^{40}Ar$ | Calculated age (My $\pm 1\sigma$) |
|---|---|---|---|---|---|---|---|
| MP21 | British Empire Granite | PG | K-feldspar | 12.46, 12.55 | 8.354 | 96.9 | 349.2 ± 2.8 |
| | | | muscovite | 8.827, 8.837 | 6.767 | 98.5 | 395.1 ± 3.1 |
| MP25 | British Empire Granite | PG | biotite | 7.395, 7.421 | 5.211 | 77.2 | 365.8 ± 3.0 |
| | | | muscovite | 8.845, 8.812 | 6.546 | 76.9 | 383.6 ± 3.0 |
| MP24 | Freeling Heights Quartzite | MB | K-feldspar | 12.51, 12.49 | 7.688 | 97.7 | 323.7 ± 2.5 |
| | | | biotite | 7.933, 7.950 | 5.219 | 82.5 | 343.9 ± 2.7 |
| | | | muscovite | 8.914, 8.964 | 6.492 | 94.3 | 376.5 ± 3.2 |
| MP28 | Amphibolite | MB | hornblende | 0.451, 0.458 | 0.375 | 95.9 | 422.5 ± 6.1 |
| MP9 | Basement gneiss | MB | K-feldspar | 11.92, 11.92 | 7.767 | 93.6 | 341.3 ± 2.6 |
| | | | biotite | 8.325, 8.269 | 6.421 | 84.1 | 398.7 ± 3.2 |
| | | | muscovite | 9.056, 8.979 | 6.921 | 98.4 | 395.7 ± 3.1 |
| MP11 | Basement metasediment | MB | muscovite | 8.479, 8.417 | 6.490 | 79.7 | 396.1 ± 3.2 |
| | | | biotite | 8.490, 8.538 | 6.306 | 99.1 | 383.3 ± 3.2 |
| MP8 | Arkaroola Pegmatite | PG | K-feldspar | 11.21, 11.36 | 6.944 | 88.2 | 323.9 ± 2.6 |
| | | | muscovite | 9.069, 8.955 | 6.286 | 97.0 | 363.0 ± 2.9 |
| MP5 | Arkaroola Pegmatite | PG | K-feldspar | 11.08, 11.07 | 6.886 | 86.2 | 327.0 ± 3.9 |
| | | | muscovite | 8.983, 8.954 | 6.789 | 88.1 | 390.9 ± 3.0 |
| MP1 | Local pegmatite | PG | K-feldspar | 13.33, 13.39 | 8.207 | 96.1 | 323.4 ± 2.5 |
| MP2 | Biotite schist | MB | biotite | 8.248, 8.319 | 5.909 | 96.6 | 370.5 ± 2.9 |
| MP6 | Arkaroola Pegmatite | PG | K-feldspar | 12.67, 12.66 | 8.079 | 93.4 | 334.6 ± 2.8 |
| | | | muscovite | 9.070, 9.063 | 6.296 | 88.2 | 361.6 ± 2.8 |
| MP30 | Wooltana Volcanics | ACS | hornblende | 0.294, 0.294 | 0.2254 | 91.3 | 395.3 ± 4.2 |
| MP31 | Wooltana Volcanics | ACS | hornblende | 0.312, 0.313 | 0.2666 | 51.8 | 435.5 ± 5.1 |
| MP7 | Biotite Schist | ACS | biotite | 8.336, 8.321 | 6.086 | 88.7 | 378.6 ± 3.0 |
| MP3 | Woodnamoka Phyllite | ACS | biotite | 8.071, 8.153 | 6.062 | 79.9 | 386.3 ± 3.1 |
| | | | muscovite | 8.382, 8.287 | 6.606 | 95.8 | 407.3 ± 3.2 |
| MP4 | Blue Mine Conglomerate | ACS | K-feldspar | 12.33, 12.34 | 8.712 | 66.6 | 367.2 ± 2.9 |
| MP10 | Bolla Bollana Formation | ACS | K-feldspar | 11.67, 11.62 | 8.749 | 90.0 | 388.3 ± 3.1 |
| MP13 | Bolla Bollana Formation | ACS | K-feldspar | 10.06 (x = 4) | 11.77 | 97.1 | 573.3 ± 6.1 |
| MP16 | Bolla Bollana Formation | ACS | K-feldspar | 8.572, 8.535 | 5.912 | 92.2 | 360.1 ± 3.0 |

*Note:* An age determination was made on each of two separate aliquots of argon from each sample. As these duplicate analyses were in good agreement, only one analysis is listed here. A complete listing is given in Appendix B

### 6.2.2 Muscovites and biotites

Potassium-argon results for both muscovite and biotite separates from metasediments and granite gneisses reveal a wide range of ages between 361 Ma and 407 Ma and 343 Ma and 398 Ma, respectively (Table 6.3). The apparent ages are mostly younger than the hornblende K / Ar data and they show that samples experienced significant argon loss after Delamerian orogenesis. Where both muscovite and biotite have been analysed, muscovite ages are equal to or older than biotite ages (Table 6.3), which is consistent with accepted notions about mica closure temperatures (e.g, McDougall and Harrison, 1999); however results from sample MP9 are an exception, discussed in more detail below.

Step-heating experiments were performed on 4 of the 9 muscovite samples in the K / Ar study, and 6 of the 7 biotite samples (Table 6.4). In general there is close agreement between integrated $^{40}Ar / ^{39}Ar$ total gas ages and K / Ar ages (Table 6.4). Isochron analysis did not give any additional useful information, as the samples are highly radiogenic.

Biotite samples (with the exception of MP24) show flat plateau segments, in many cases for more than 90% of the gas release. Age spectra for muscovite samples show similar plateau features,

**Table 6.4** *Summary of muscovite and biotite K-Ar and $^{40}Ar/^{39}Ar$ data*

| *Sample* | *Mineral* | *K-Ar age (Ma ±1σ)* | *Integrated total fusion $^{40}Ar/^{39}Ar$ age (Ma ±1σ)* | *Plateau age (Ma ±1σ)* |
|---|---|---|---|---|
| MP24 | muscovite | 376.1 ± 3.2 | 374.8 ± 2.0 | 375.4 ± 1.9 |
| MP11 | muscovite | 396.1 ± 3.2 | 389.9 ± 2.6 | 390.8 ± 2.4 |
| MP5 | muscovite | 390.9 ± 3.0 | 391.8 ± 2.0 | 392.8 ± 1.8 |
| MP3 | muscovite | 407.3 ± 3.2 | 402.9 ± 2.0 | 403.6 ± 1.6 |
| MP24 | biotite | 343.9 ± 2.9 | 350.9 ± 2.9 | - |
| MP11 | biotite | 383.3 ± 3.2 | 379.8 ± 2.0 | 380.5 ± 1.7 |
| MP9 | biotite | 398.7 ± 3.2 | 395.9 ± 2.0 | 401.0 ± 1.4 |
| MP2 | biotite | 371.2 ± 3.0 | 363.8 ± 1.7 | 365.3 ± 1.5 |
| MP7 | biotite | 378.3 ± 3.0 | 373.7 ± 1.7 | 373.5 ± 1.6 |
| MP3 | biotite | 386.3 ± 3.1 | 381.2 ± 2.2 | 386.2 ± 1.8 |

again for 80%-90% of the gas release (Figure 4). Total gas and plateau ages for muscovite samples show remarkable consistency with stratigraphic and structural position, increasing in age towards the top of the metamorphic pile (374.4 ± 1.9 Ma, 390.8 ± 2.4 Ma, 392.8 ± 1.8 Ma, 403.6 ± 1.6 Ma). The youngest ages found are those from the core of the basement anticline in the British Empire area, whereas the oldest apparent ages are from the highest parts of the cover sequence which were sampled. A similar trend is seen amongst the biotite samples; however, in this case sample MP2 is anomalously young for its structural position, whereas sample MP9 is anomalously old. Results from both samples are discussed in the section following.

**Sample MP24 (Freeling Heights Quartzite, Mount Painter basement)** Muscovite and biotite from sample MP24 yield K / Ar apparent ages of 376 ± 3 Ma and 344 ± 4 Ma respectively. This muscovite age is in close agreement with a $^{40}Ar/^{39}Ar$ integrated total gas age of 375 ± 2 Ma, whereas the K / Ar biotite age is slightly younger than the integrated $^{40}Ar/^{39}Ar$ total gas age of 351 ± 3 Ma. The age spectrum of biotite MP24 is strongly disturbed and unusual when compared to the other samples (Figure 6.4). Ages in the spectrum increase steadily for the first 70% of the gas release, before falling by around 40 Ma. The apparent age then climbs steadily again for the remaining steps. No plateau or plateau-like age is achieved. Inspection of the mineral separate reveals the existence of two populations of biotite, as indicated by green and brown colours. The brown biotite makes up about 10% of the mineral separate and it is possible that it may be more retentive of its argon than the green biotite, and that the hump shape of the age spectrum may be the result of differential release of argon from the biotites during step heating. The age spectrum for this sample is reminiscent of the age spectra for mixed mica populations described by Wijbrans and McDougall (1988).

**Sample MP11 (metasediment, Mount Painter basement)** Both muscovite and biotite were separated and analysed from sample MP11. The K / Ar ages are 396 ± 3 Ma and 383 ± 3 Ma, respectively, while $^{40}Ar/^{39}Ar$ integrated total gas ages are 390 ± 3 Ma and 380 ± 3 Ma, respectively. In this case the K / Ar and $^{40}Ar/^{39}Ar$ results are in agreement. The age spectrum for the biotite is flat throughout the gas release, yielding a plateau age of 381 ± 2 Ma. The age spectrum for the muscovite is not as flat, exhibiting a range of ages from 382 Ma in the third step to 400 Ma in the last step. The plateau age for this sample is 391 ± 2 Ma.

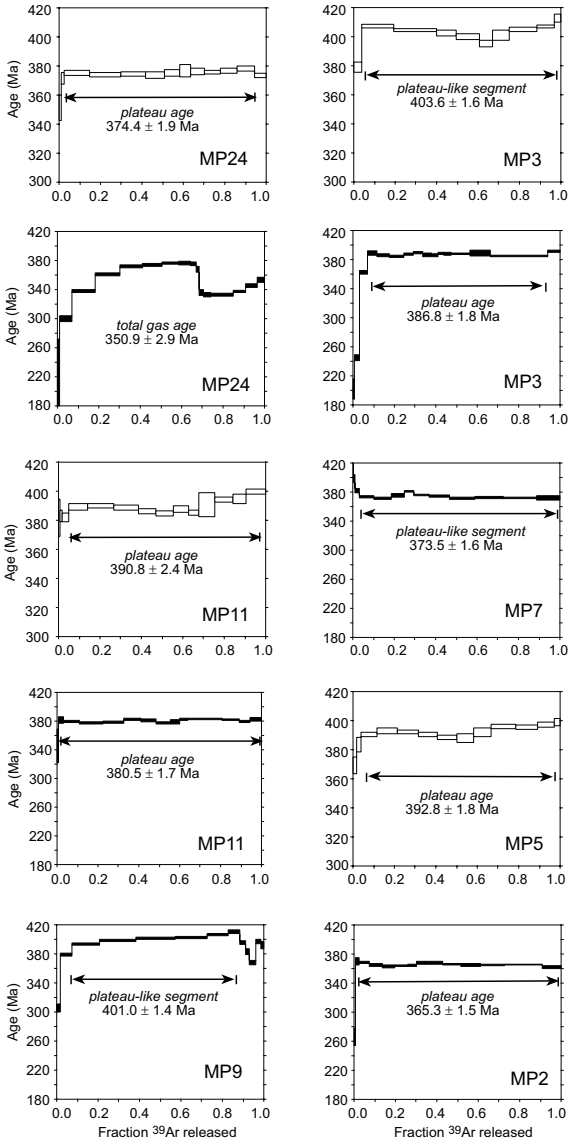


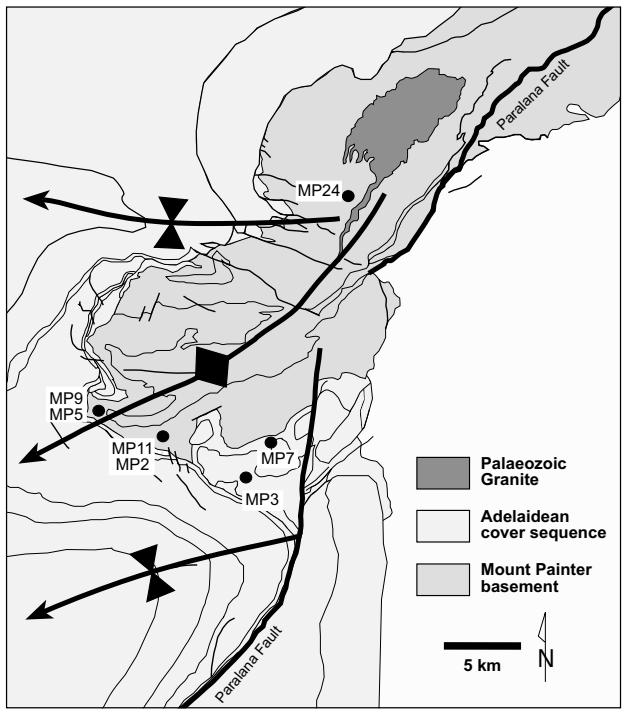


**Figure 6.4** Summary of $^{40}Ar/^{39}Ar$ age spectra for both biotite (filled spectra) and muscovite (unfilled spectra). Sample locations are shown with lithostratigraphy delineated as either Mount Painter basement or Adelaidean cover sequence only. To facilitate ready comparison, all muscovite age spectra are plotted to the same scale (with age range from 300-420 Ma) and likewise all biotite spectra are plotted to the same scale (with age range from 180-420 Ma).

**Samples MP9 and MP5 (granite gneiss and pegmatite, Mount Painter basement)** Both muscovite and biotite from sample MP9 were analysed using the K / Ar method; however, only the biotite mineral separate was subjected to $^{40}Ar/^{39}Ar$ analysis. These minerals yield the oldest apparent ages of all the basement samples analysed, with K / Ar ages of 395 ± 3 Ma and 399 ± 3 Ma respectively for the muscovite and biotite separates. The $^{40}Ar/^{39}Ar$ integrated total gas age for the biotite is 396 ± 2 Ma. For muscovite from the adjacent sample MP5, a pegmatite, the $^{40}Ar/^{39}Ar$ integrated total gas age is 392 ± 2 Ma. Together these data are unusual as the muscovites from both sample MP9 and adjacent MP5 are slightly younger than coexisting biotite. These samples are the only ones amongst those in the present study to exhibit this inverted age relationship. The data may indicate that biotite MP9 is contaminated by excess argon. The possibility that biotite in MP9 is unusually magnesium rich, giving it a closure temperature more like that of muscovite, is unlikely since it does not exhibit the optical characteristics of phlogopite. The age spectrum from biotite MP9 is also disturbed and shows a similar, but not as pronounced pattern to that observed in biotite MP24. In this case the apparent age rises steadily for the first 85% of the gas release, before decreasing and then increasing again in the remaining steps (Figure 6.4). The age spectrum for MP5 muscovite is nearly flat, with ages ranging from 384 Ma in the second step to 400 Ma in the last step with a plateau age of 393 ± 2 Ma.

**Sample MP2 (biotite selvedge from pegmatite)** Sample MP2 is a monomineralic biotite selvedge adjacent to a K-feldspar pegmatite which is probably Palaeozoic in age. The age spectrum for biotite MP2 is remarkably flat, allowing a plateau age of 365 ± 2 Ma to be defined over more than 95% of the gas release. This age, along with the integrated $^{40}Ar/^{39}Ar$ total gas age of 364 ± 2 Ma, is slightly younger than the K/Ar age of 371 ± 3 Ma. Sample MP2 is considerably younger than other biotite samples from equivalent structural positions (Tables 6.3, 6.4) and this may be the result of high temperature fluid circulation associated with the intrusion of the adjacent pegmatite. This hypothesis is supported by the unusually young ages recorded by nearby K-feldspar MP1, as discussed below.

**Sample MP7 (biotite schist, Adelaidean cover sequence)** Biotite from sample MP7 shows good agreement between the measured K/Ar age (378 ± 3 Ma) and the $^{40}Ar/^{39}Ar$ integrated total gas age (374 ± 2 Ma). It is characterized by a well defined plateau of age 374 ± 2 Ma.

**Sample MP3 (Woodnamoka Phyllite, Adelaidean cover sequence)** Both biotite and muscovite analysed from sample MP3 record the oldest ages of all those micas analysed, a result consistent with the fact that these samples are from the highest stratigraphic unit sampled for mica analysis. For biotite, the K/Ar age (386 ± 3 Ma) and $^{40}Ar/^{39}Ar$ integrated total gas age (381 ± 2 Ma) are in good agreement. A similar result is seen for muscovite MP3, with a K/Ar age of 407 ± 3 Ma and a $^{40}Ar/^{39}Ar$ integrated total gas age of 403 ± 2 Ma. These minerals yield well defined plateau ages for around 90% of the gas release (Figure 6.4), of 404 ± 2 Ma for muscovite and 387 ± 2 Ma for biotite.

### 6.2.3 K-feldspars

Twelve K-feldspar samples were analysed by the K/Ar method, and 7 of these samples were also subjected to $^{40}Ar/^{39}Ar$ step heating experiments. The K/Ar data reveal a wide spread in apparent age (Table 6.3) ranging between 323 Ma and 573 Ma. The youngest samples, which cluster in age around 325-335 Ma, are from pegmatites which are thought to have intruded during Palaeozoic metamorphism and deformation. The oldest apparent ages are recorded by K-feldspars of the Blue Mine Conglomerate and Bolla Bollana Formation – the highest stratigraphic units sampled. These ages cluster in the range 360-380 Ma with the exception of K-feldspar MP13 from the Bolla Bollana Formation, which gives an age of 573 ± 6 Ma. The agreement between K/Ar apparent ages and $^{40}Ar/^{39}Ar$ integrated total gas ages is close (Table 6.5); however, in several cases (samples MP24, MP4 and MP10) the K/Ar ages are 8-20 Ma younger than the integrated $^{40}Ar/^{39}Ar$ total gas ages. These younger apparent ages are possibly the result of incomplete argon extraction during the K/Ar age measurement.

The $^{40}Ar/^{39}Ar$ age spectra for all the K-feldspar samples (Figure 6.5) show some remarkably similar features. Samples are generally characterized by monotonically increasing age spectra, with some variations, with the steepest age gradients occurring over the first 20% of the gas release. In particular the similarity of the age of early released gas, which is ~ 250-320 Ma in all cases, is noted. The spectra for all samples, regardless of stratigraphic or structural position, rise to ages between 330 and 450 Ma, indicating that the K-feldspars experienced significant argon loss subsequent to the Delamerian Orogeny. Those samples which are not expected to have retained a Proterozoic pre-history and which have clearly suffered high temperature metamorphism show a remarkably narrow range of plateau ages. For samples MP1, MP6 and MP9, these plateau-like ages are all ~ 330 Ma.

**Table 6.5** *Summary of K-feldspar K-Ar and $^{40}Ar/^{39}Ar$ data*

| *Sample* | *K-Ar age (Ma ± 1σ)* | *Integrated total fusion $^{40}Ar/^{39}Ar$ age (Ma ± 1σ)* |
|---|---|---|
| MP24 | 323.7 ± 2.5 | 335.8 ± 1.5 |
| MP9 | 341.8 ± 2.7 | 338.2 ± 1.4 |
| MP1 | 323.3 ± 2.5 | 322.3 ± 1.4 |
| MP6 | 334.4 ± 3.1 | 330.0 ± 1.7 |
| MP4 | 367.2 ± 2.9 | 375.1 ± 2.0 |
| MP10 | 388.2 ± 3.1 | 408.2 ± 1.7 |
| MP16 | 359.3 ± 3.0 | 357.7 ± 1.9 |

Samples MP4, MP10 and MP16 show slightly more complicated age spectra. In all cases these samples show evidence for the presence of excess argon in the early released gas. Correction for chlorine-related excess argon was attempted for all three samples, following the method of Harrison et al. (1993) but this was generally not successful, owing to low total production of $^{38}Ar_{Cl}$ in the samples.

The K-feldspar age spectra have been interpreted using the multiple-diffusion-domain (MDD) method described by Lovera et al. (1989) and Richter et al. (1991). In this way we interpret the results in terms of cooling through a closure temperature range of approximately 350-150°C, the typical closure temperature window of K-feldspar if simple diffusion theory is applicable. The principal assumption of the MDD method is that the loss of argon is a thermally activated diffusion process which can be described by the Arrhenius equation. The method also assumes that the loss or retention of radiogenic argon is from a number of non-interacting diffusion domains of simple geometry, but of variable size. For any given sample, the greater the range in diffusion domain sizes the larger the closure temperature window to argon loss will be.

In these models a single activation energy and a slab geometry are assumed in order to calculate, via the method of Lovera et al. (1989), the distribution of diffusion domain length scales (volume fraction and effective size). The calculated domain distribution was then inverted to yield temperature-time histories, again following Lovera et al. (1989). Lovera et al. (1997) have provided detailed justification for this procedure and reiterate that step heating of K-feldspars commonly reveals dramatic age gradients which cannot be produced by closure of a single domain to argon loss. The MDD solutions were calculated from Arrhenius data using the time, temperature and fraction of $^{39}Ar$ released during the laboratory step-heating experiments (see Appendix B for further details). Fitting of the thermal histories involved a trial-and-error approach in which preferred Temperature-time paths were calculated by inputting trial thermal histories and minimizing the differences between the laboratory and modelled age spectra by iteration.

### 6.2.4 Multiple Diffusion Domain Analysis of K-feldspars

Results of MDD modelling are shown in Figure 6.5 and summarized in Table 6.6, where the diffusion coefficient, relative volume fraction of each domain and relative domain size are listed. If the laboratory heating schedules are applied to the model solutions in Table 6.6 the model gas release history is almost identical to that obtained during the experiment (note agreement between modelled and measured in Figure 6.5). Above about 1150°C, which for the Mount Painter samples corresponds typically to 80%-100% of the gas release, the samples melted and so further comparison of the laboratory and model data cannot be made. The laboratory and model data are also presented in Figure 6.6 in the form of Arrhenius and $\log r/r_o$ plots which allow comparison of the MDD solutions and the laboratory degassing data. The laboratory and model Arrhenius data are well matched and

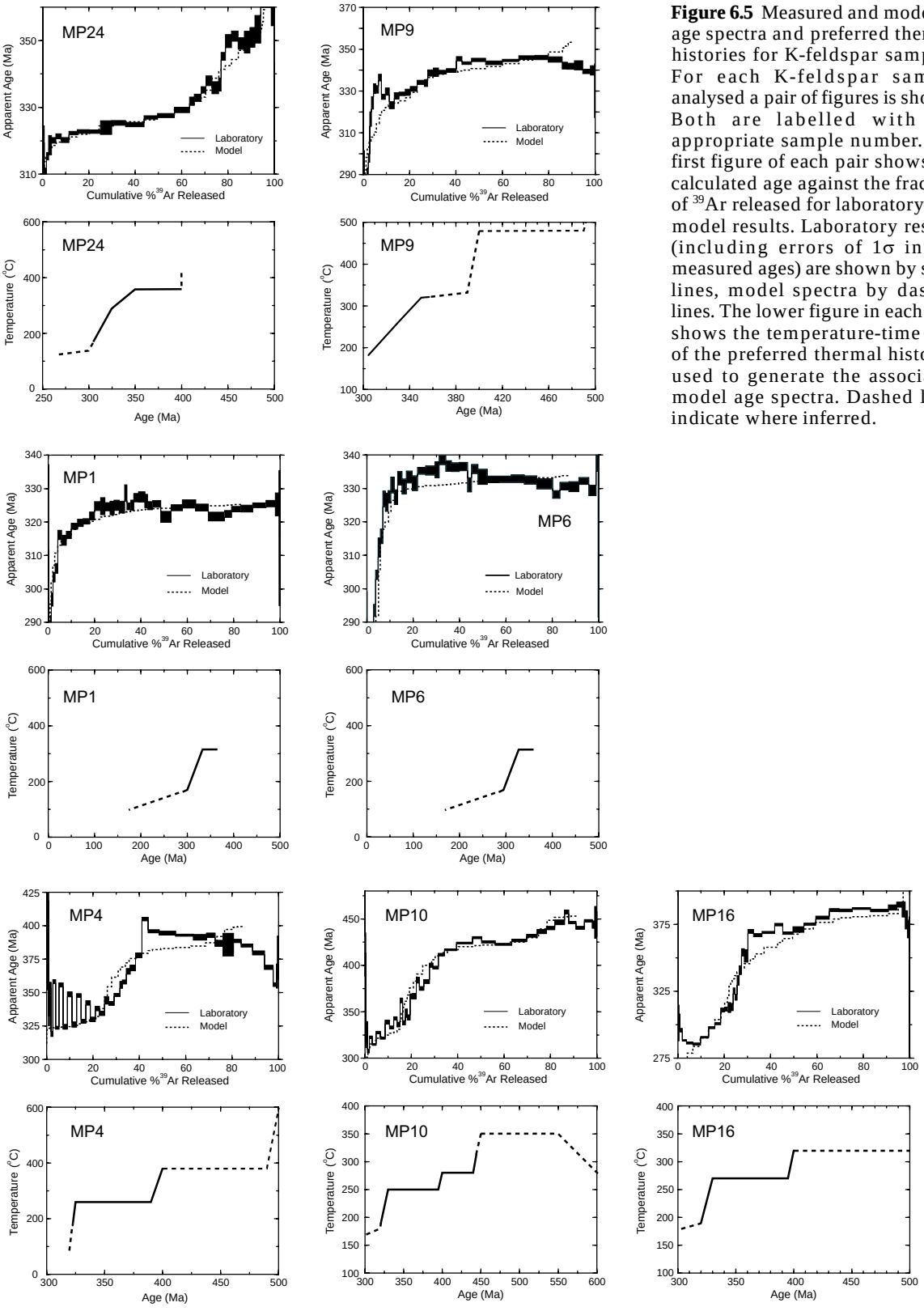


**Figure 6.5** Measured and modelled age spectra and preferred thermal histories for K-feldspar samples. For each K-feldspar sample analysed a pair of figures is shown. Both are labelled with the appropriate sample number. The first figure of each pair shows the calculated age against the fraction of $^{39}$Ar released for laboratory and model results. Laboratory results (including errors of 1σ in the measured ages) are shown by solid lines, model spectra by dashed lines. The lower figure in each pair shows the temperature-time plot of the preferred thermal histories used to generate the associated model age spectra. Dashed lines indicate where inferred.

the laboratory age spectra are able to be modelled using two end-member types of thermal histories: (1) continuous cooling and (2) thermal spikes; these two cases are thermally indistinguishable. For the Mount Painter samples a continuous cooling history, monotonically decreasing in temperature subsequent to Delamerian age metamorphism is preferred. Note that the K-feldspar thermal models are strictly applicable only for ages less than the maximum age recorded by each sample, and in all but one case these ages are < 400 Ma. As this is also the time of final hornblende closure, it seems unlikely that any significant thermal pulses occurred from this time until the present. The MP1 and

**Table 6.6** *Summary of domain size distributions for MDD modelling*

| Domain | Log Do, $cm^2s^{-1}$ | Volume Fraction | Domain Size (Relative) |
|---|---|---|---|
| *MP24 K-feldspar, Ea = 50.8 kcal/mol* | | | |
| 1 | 6.590 | 0.09085 | 0.00744 |
| 2 | 5.483 | 0.09334 | 0.02662 |
| 3 | 5.479 | 0.22392 | 0.02673 |
| 4 | 4.811 | 0.23098 | 0.05767 |
| 5 | 3.876 | 0.11587 | 0.16930 |
| 6 | 3.152 | 0.12770 | 0.38974 |
| 7 | 2.383 | 0.02228 | 0.94412 |
| 8 | 2.333 | 0.09506 | 1.00000 |
| *MP9 K-feldspar, Ea = 44.2 kcal/mol* | | | |
| 1 | 6.208 | 0.03057 | 0.00312 |
| 2 | 4.328 | 0.11149 | 0.02723 |
| 3 | 2.766 | 0.11008 | 0.16442 |
| 4 | 2.377 | 0.28358 | 0.25724 |
| 5 | 2.052 | 0.09280 | 0.37405 |
| 6 | 1.590 | 0.18839 | 0.63671 |
| 7 | 1.509 | 0.06575 | 0.69874 |
| 8 | 1.198 | 0.11734 | 1.00000 |
| *MP4 K-feldspar, Ea = 46.0 kcal/mol* | | | |
| 1 | 6.447 | 0.08810 | 0.00244 |
| 2 | 5.059 | 0.11218 | 0.01206 |
| 3 | 2.769 | 0.26864 | 0.16856 |
| 4 | 2.751 | 0.18867 | 0.17197 |
| 5 | 1.610 | 0.13244 | 0.64017 |
| 6 | 1.222 | 0.20996 | 1.00000 |
| *MP10 K-feldspar, Ea = 47.4 kcal/mol* | | | |
| 1 | 8.179 | 0.00870 | 0.00054 |
| 2 | 7.528 | 0.05558 | 0.00114 |
| 3 | 6.660 | 0.07347 | 0.00311 |
| 4 | 3.195 | 0.36358 | 0.16765 |
| 5 | 3.183 | 0.16095 | 0.17005 |
| 6 | 2.055 | 0.15591 | 0.62323 |
| 7 | 1.888 | 0.07329 | 0.75543 |
| 8 | 1.644 | 0.10852 | 1.00000 |
| *MP16 K-feldspar, Ea = 47.1 kcal/mol* | | | |
| 1 | 8.304 | 0.06874 | 0.00068 |
| 2 | 7.628 | 0.08909 | 0.00148 |
| 3 | 6.978 | 0.04717 | 0.00312 |
| 4 | 3.917 | 0.10099 | 0.10574 |
| 5 | 3.136 | 0.21418 | 0.25984 |
| 6 | 3.135 | 0.18763 | 0.26017 |
| 7 | 3.133 | 0.18564 | 0.26073 |
| 8 | 3.042 | 0.06291 | 0.28951 |
| 9 | 1.966 | 0.04364 | 1.00000 |
| *MP1 K-feldspar, Ea = 46.1 kcal/mol* | | | |
| 1 | 6.879 | 0.01636 | 0.00182 |
| 2 | 5.941 | 0.08418 | 0.00535 |
| 3 | 5.093 | 0.09713 | 0.01421 |
| 4 | 4.332 | 0.07210 | 0.03407 |
| 5 | 2.604 | 0.23105 | 0.24941 |
| 6 | 1.594 | 0.20141 | 0.79774 |
| 7 | 1.570 | 0.14432 | 0.82033 |
| 8 | 1.495 | 0.08339 | 0.89333 |
| 9 | 1.397 | 0.07006 | 1.00000 |
| *MP6 K-feldspar, Ea = 47.1 kcal/mol* | | | |
| 1 | 7.654 | 0.03504 | 0.00027 |
| 2 | 6.306 | 0.03499 | 0.00127 |
| 3 | 4.926 | 0.05078 | 0.00620 |
| 4 | 3.990 | 0.15724 | 0.01823 |
| 5 | 3.042 | 0.14838 | 0.05429 |
| 6 | 2.343 | 0.11531 | 0.12136 |
| 6 | 2.191 | 0.22231 | 0.14465 |
| 8 | 1.769 | 0.15329 | 0.23522 |
| 9 | 0.5115 | 0.08266 | 1.00000 |

*Ea* = activation energy

MP6 pegmatites, however, may have intruded as late as 360 Ma, so no prehistory is imposed on these samples (i.e., ages older than the maximum age of the samples are not modelled).

The MDD solutions have either six, eight or nine domains (Table 6.6). The resultant thermal models are insensitive to the number of domains; however, using fewer than 5 or 6 domains results in much poorer fits. Note in Table 6.6 that $D_0$ values for some domains are nearly identical, and that these pairs of domains can be combined without any loss of fit. The activation energies listed in Table 6.6 were calculated using the linear low-temperature portions of the Arrhenius data, typically the first six to eight points. As outlined by Lovera et al. (1997) the usual approach is to find the highest activation energy and use this for the modelling. For the Mount Painter samples estimated activation energies range from 44.2 to 50.8 kcal / mol (Table 6.6).

### 6.2.5 Thermal modelling of K-feldspar data

In developing the K-feldspar thermal models the first constraint is provided by the K / Ar ages from hornblende samples, as discussed above. Assuming that the closure temperature of hornblende to argon loss is 450°C (Harrison, 1981), we suggest that rocks from both the basement and cover sequences underwent a period of rapid cooling from temperatures of at least 450°C at around 400 Ma, the time of final hornblende closure. Given that K-feldspars are significantly less retentive of their argon, all the K-feldspars, with the possible exception of those high in the cover sequence, should have been completely outgassed of any previously accumulated radiogenic argon at ~ 400 Ma.

The best-fit thermal models show remarkable similarities (Figure 6.5). The general style of thermal evolution is common for all samples, regardless of structural or stratigraphic position. Good model fits for all samples are consistent with a period of rapid cooling at ~ 400 Ma, followed by a period of isothermal residence between ~ 390 and 330-325 Ma. A second

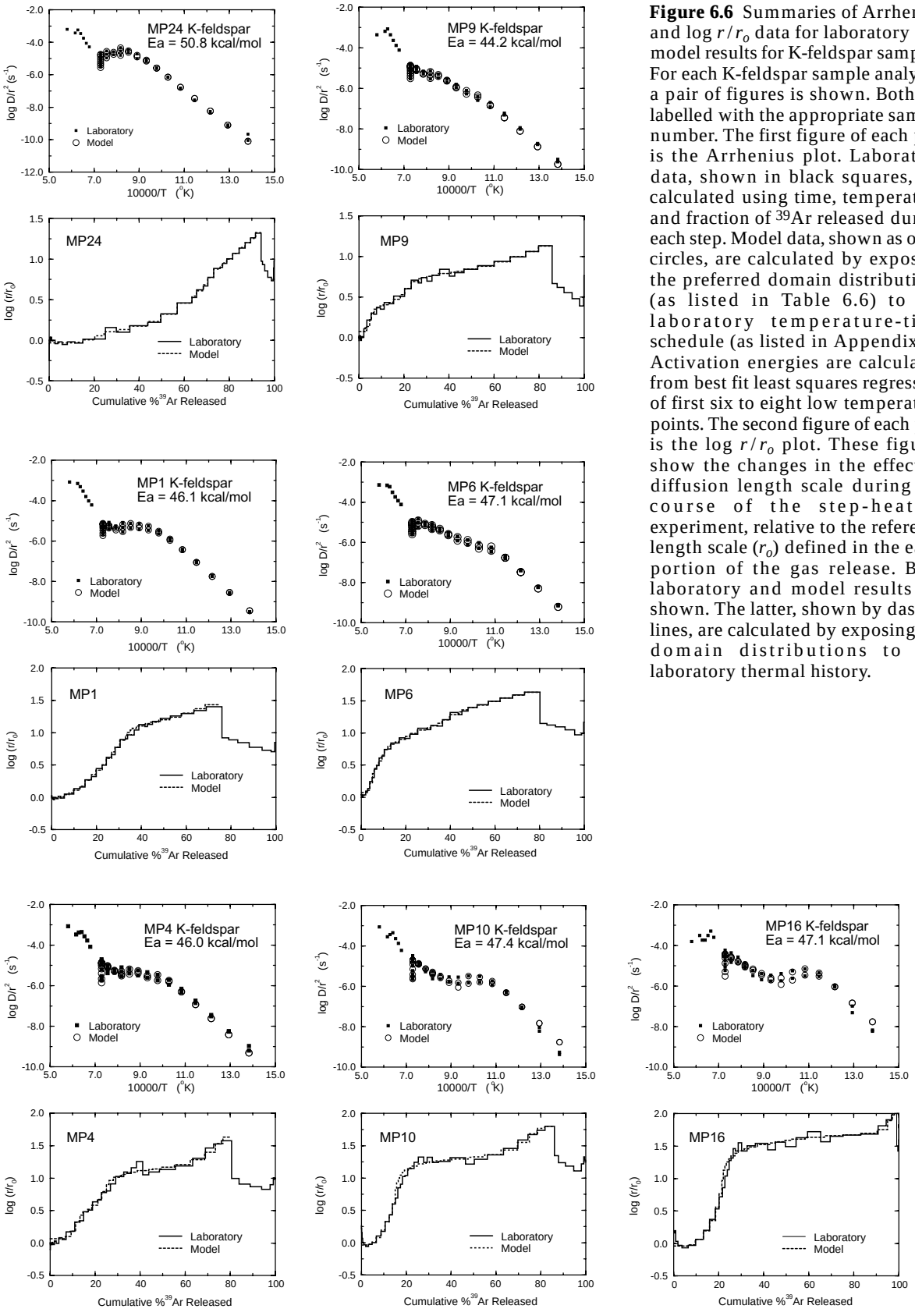


**Figure 6.6** Summaries of Arrhenius and log $r/r_o$ data for laboratory and model results for K-feldspar samples. For each K-feldspar sample analysed a pair of figures is shown. Both are labelled with the appropriate sample number. The first figure of each pair is the Arrhenius plot. Laboratory data, shown in black squares, are calculated using time, temperature and fraction of $^{39}$Ar released during each step. Model data, shown as open circles, are calculated by exposing the preferred domain distributions (as listed in Table 6.6) to the laboratory temperature-time schedule (as listed in Appendix B). Activation energies are calculated from best fit least squares regression of first six to eight low temperature points. The second figure of each pair is the log $r/r_o$ plot. These figures show the changes in the effective diffusion length scale during the course of the step-heating experiment, relative to the reference length scale ($r_o$) defined in the early portion of the gas release. Both laboratory and model results are shown. The latter, shown by dashed lines, are calculated by exposing the domain distributions to the laboratory thermal history.

period of rapid cooling at ~ 325 Ma is required by all samples to facilitate the closure of the smallest diffusion domains. In the following discussion the thermal models are described in detail for each group of K-feldspar samples, i.e., basement samples, samples from presumed Palaeozoic intrusives and samples from the cover sequence. The purpose of this discussion is to describe the times and temperatures at which changes in cooling rate are observed. These models, along with the K/Ar

and $^{40}Ar/^{39}Ar$ age measurements from micas and amphiboles, allow a generalised model for the tectonic evolution of the Mount Painter region to be developed.

**Samples MP24 and MP9 (Mount Painter basement)**

Potassium feldspar samples MP24 and MP9 yield similar thermal histories, despite differences in their age spectra. Apparent ages in the range 250-340 Ma are recorded by sample MP9, whereas sample MP24 records higher apparent ages in the range 305-380 Ma. This result is unexpected because sample MP24 is from a deeper structural and stratigraphic position and so might be expected to have experienced higher temperatures for longer periods and thus record younger apparent ages. The hump-shape of the age spectrum from 5%-15% gas release for sample MP9 suggests that the sample may contain minor excess argon, and this portion of the age spectrum cannot be fitted. Although these samples do not record ages older than 380 Ma, and both are consistent with a period of rapid cooling at ~ 400 Ma, neither model bears on this issue directly. However, good model fits are obtained for a period of isothermal residence between around 380 Ma and 350 Ma. Unlike the other samples studied here, samples MP24 and MP9 suggest monotonic cooling throughout the period 350-300 Ma. Sample MP9 cools from about 320°C at 350 Ma, whereas sample MP24 cools from 350°C. The latter result is consistent with the deeper structural and stratigraphic position of sample MP24. These samples start to cool ~ 25 Ma before the samples from the cover sequence.

**Samples MP4, MP10 and MP16 (Adelaidean cover sequence)**

K-feldspars MP10 and MP16, were both sampled from boulder clasts within the Bolla Bollana Formation, a glacial tillite deposited *ca.* 700 Ma. Sample MP10 is from a granitic clast, whereas MP16 is from a volcanic clast. Both K-feldspar samples show pronounced monotonically rising age spectra. The age spectrum of sample MP10 suggests that it started to accumulate argon before 440 Ma, with final closure of the smallest diffusion domains not occurring until around 310 Ma. The 440 Ma apparent ages are significantly older than the K/Ar ages recorded in the amphiboles. This is not surprising as this sample is of very low metamorphic grade and probably did not experience temperatures greater than about 350-300°C at any time since deposition, whereas the amphiboles are from structurally deeper locations which experienced higher temperatures. Consequently, it is not surprising that the sample retains a signature that is older than K-feldspars in the basement. According to the model, final closure took place during a rapid cooling event starting ~ 330 Ma. The age spectrum of K-feldspar MP16 is similar to that of sample MP10, but younger apparent ages are recorded. This sample did not begin to retain argon until ~ 390 Ma, and even though the youngest domains closed at ~ 290 Ma, this model also indicates rapid cooling starting at about 330 Ma. In addition, results for MP10 and MP16 are both consistent with an isothermal period between about 395 Ma and 330 Ma, at temperatures of 250°C and 270°C, respectively.

K-feldspar MP4 is strongly contaminated with excess argon in the first 25% of gas release, but as with both MP10 and MP16, the thermal model indicates a rapid cooling event at about 330 Ma. The latter portion of the age spectrum rises to 400 Ma, which is also consistent with an isothermal period between 390 Ma and 330 Ma, at a temperature of ~ 260°C. The cause of the marked decrease in ages in the last few steps is not known, but it is possible that portions of the sample were recrystallized at the time the excess argon was incorporated (~ 325 Ma), and that some of this young material retained its argon until melting.

The results lend strong support for a period of rapid cooling at ~ 400 Ma followed by a period of isothermal residence between about 395 and 330 Ma. During this period all three samples remained at very similar temperatures between 270°C and 250°C. Rapid cooling to around 180°C at 330 Ma provides good model fits, and this is also consistent with the results for the other K-feldspars studied, particularly samples MP1 and MP6 (see below).

**Samples MP1 and MP6 (pegmatites)**

Samples from these presumed Palaeozoic intrusives show remarkable plateau segments, with age gradients evident only for the first 10%-20% of the gas release. For about 85% of the gas released from sample MP6 the apparent ages are in the range 330-335 Ma, and the apparent ages decrease to a minimum of ~ 265 Ma, indicating final closure to argon loss at this time. A very similar age spectrum was obtained for sample MP1, where the 'plateau' age is ~ 320-325 Ma and the youngest apparent age is ~ 280 Ma. The lack of apparent ages older than 330 Ma raises important questions about the intrusion age of these rocks. Potassium-argon ages of muscovites from these and other Paleozoic pegmatites (samples MP8, MP5, and MP6) are 363 ± 3 Ma, 389 ± 3 Ma, and 361± 3 Ma, respectively, indicating that emplacement occurred earlier than the apparent ages recorded by the K-feldspars.

Good model fits for the age spectra of K-feldspars MP6 and MP1 are consistent with very rapid cooling from temperatures > 350°C at ~ 330 Ma, but it is cautioned that these are the highest model temperatures of any of the K-feldspars. Both samples cool at 7.6°CMa$^{-1}$ between 325 and 300 Ma. Between the time of intrusion (~ 400 Ma?) and rapid cooling at 325 Ma we speculate that these rocks remained isothermal at a temperature higher than 350°C. Very rapid cooling to temperatures ~ 210°C is required to facilitate closure of all but the smallest diffusion domains at ~ 325 Ma.

### 6.2.6 Interpretation of hornblende, muscovite and biotite data

Potassium-argon ages of the Mount Painter hornblendes suggest that the rocks were at temperatures > 450°C until at least ~ 400 Ma. At about this time the rocks must have cooled considerably in order that the hornblendes were finally closed to argon loss, as indicated by the cluster of mica ages within a few million years of 400 Ma. The hornblende data indicates that either (1) peak metamorphic conditions were attained during the Delamerian Orogeny and that the rocks remained above 500°C for at least 100 Ma after this event, or (2) that shortly after Delamerian peak metamorphism the rocks cooled into the partial retention zone for argon in hornblendes, and remained essentially isothermal at ~ 450-500°C (temperature range from simple diffusive loss modelling using the kinetic data of Harrison (1981) until the 400 Ma cooling event. The second interpretation is preferred for two reasons. First, the metamorphic assemblages in the Mount Painter area indicate Delamerian temperatures greater than 500°C, and the range of hornblende K / Ar ages, spanning some 30 million years, suggests that they closed during very slow cooling (essentially isothermal?). Second, there is no evidence that the range of hornblende ages may have been caused by reheating. The magnitude of cooling at ~ 400 Ma has been assessed, below, through analysis of argon loss in muscovites and biotites in the interval from ~ 400 Ma to 330 Ma.

Mica plateau ages are often interpreted to represent the time of closure to argon diffusion. As noted earlier, this temperature is typically thought to be ~ 350°C for muscovite (e.g., Robbins,

1972, Dodson and McClelland-Brown, 1985) and ~ 300°C for biotite (Harrison et al., 1985); however, these closure temperatures may vary by as much as 100°C depending on the characteristic diffusion length scale, the activation energy and the cooling rate (Hames and Bowring, 1994). Although the simple closure temperature model is commonly used in the interpretation of mica age data, Dunlap (2000) has shown that if the micas have experienced a long period of residence at near isothermal temperatures slightly below the closure temperature then they are likely to have experienced significant argon loss.

On first inspection the flat age spectra that characterize both muscovite and biotite samples from Mount Painter suggest that the samples experienced relatively rapid cooling through the closure temperature followed by limited post-crystallization resetting. However, given that the apparent lack of age gradients across the crystals may be a result of homogenization arising from dehydration and structural breakdown of the micas during the step-heating experiment and that the best-fit thermal histories for the K-feldspar samples reveal a period of isothermal residence between 390 and 325 Ma, it seems appropriate to evaluate the possible contribution of the partial argon loss effect identified by Dunlap (2000).

In order to do this each sample has been modelled using the method of Lister and Baldwin (1996). For each sample a T-t path consistent with hornblende and K-feldspar age data was chosen as a template for the mica modelling. The Lister and Baldwin (1996) finite difference algorithm requires that the minerals were completely outgassed prior to being subjected to the model thermal history. In order to ensure this the generic thermal history commenced at very high temperatures (~ 700°C) at 505 Ma. From this time until 500 Ma rapid cooling to 475°C is imposed, followed by isothermal residence at this temperature until 400 Ma. At this time a second period of rapid cooling is imposed, required for the closure of hornblende. This was followed by a second isothermal period between 395 Ma and 330 Ma. The final portion of the thermal history consisted of rapid cooling, between 330 Ma and 325 Ma and this was well constrained by the results of the MDD modelling of the K-feldspar data. To test the hypothesis of Dunlap (2000) the temperature of the 395 to 330 Ma isothermal period was varied with the resultant effect on apparent $^{40}Ar/^{39}Ar$ age noted. For muscovite, diffusion parameters of Hames and Bowring (1994) were used, and diffusion domain size was varied with grain size of the mineral separate. For biotite samples, experimental data (Harrison et al., 1985) were used and the diffusion domain size was assigned the average of the grain size of the mineral separate.

This modelling revealed two important results. First, partial argon loss does not appear to have affected the muscovite samples. Apparent $^{40}Ar/^{39}Ar$ plateau ages cannot be replicated by varying the temperature of the isothermal period, and it is concluded that the muscovite ages reflect simple closure to diffusive argon loss during rapid cooling at ~ 400 Ma. This conclusion seems valid as many muscovite samples from the basement (MP24, MP9, MP11) and from certain pegmatite samples (MP21, MP5) record K/Ar and integrated $^{40}Ar/^{39}Ar$ ages within error of the hornblende ages. On this basis it seems likely that the rocks must have cooled from above the hornblende closure temperature to below the muscovite closure temperature at around 400 Ma – a temperature drop of around 150°C. The older plateau age of muscovite MP3 ($403 \pm 2$ Ma) reflects the lower metamorphic grade to which samples from the Adelaidean sequence were subjected. The younger ages of muscovites MP8 and MP6 may reflect the young intrusive age of their host pegmatites (Figure 6.5).

The second point is that partial argon loss does seem to have significantly affected many biotite samples, with modelling showing that minor variations in the temperature of the isothermal period allow all biotite $^{40}Ar/^{39}Ar$ plateau ages to be replicated. Given that the closure temperature of biotite is lower than that of muscovite and that the best-fit K-feldspar thermal models place the isothermal residence variably between 350-250°C it seems possible that partial argon loss in biotite, but not in coexisting muscovite, may have occurred. This conclusion is also consistent with the wide spread in apparent ages observed for biotite samples not associated with Palaeozoic intrusives. The implications of these results are discussed in Section 6.3.2.

## 6.3 Model for the tectonic evolution of the Mount Painter province

Thermal models reconciling hornblende, mica and K-feldspar age data allow temperature-time paths to be constructed for the rocks at Mount Painter. These thermal models reveal three important periods of the post-Delamerian thermal history including (1) rapid cooling from around 475°C between 400 Ma and 395 Ma; (2) a period of ~ 70 Ma during which the terrane was essentially isothermal; and (3) a second period of rapid cooling at ~ 330-325 Ma (Figure 6.7). An interval of very slow cooling or near isothermal residence is likely to have followed the Delamerian Orogeny at around 500 Ma. The evolution of the MPP and adjacent crustal blocks is summarized in a series of schematic cross sections in Figure 6.9.

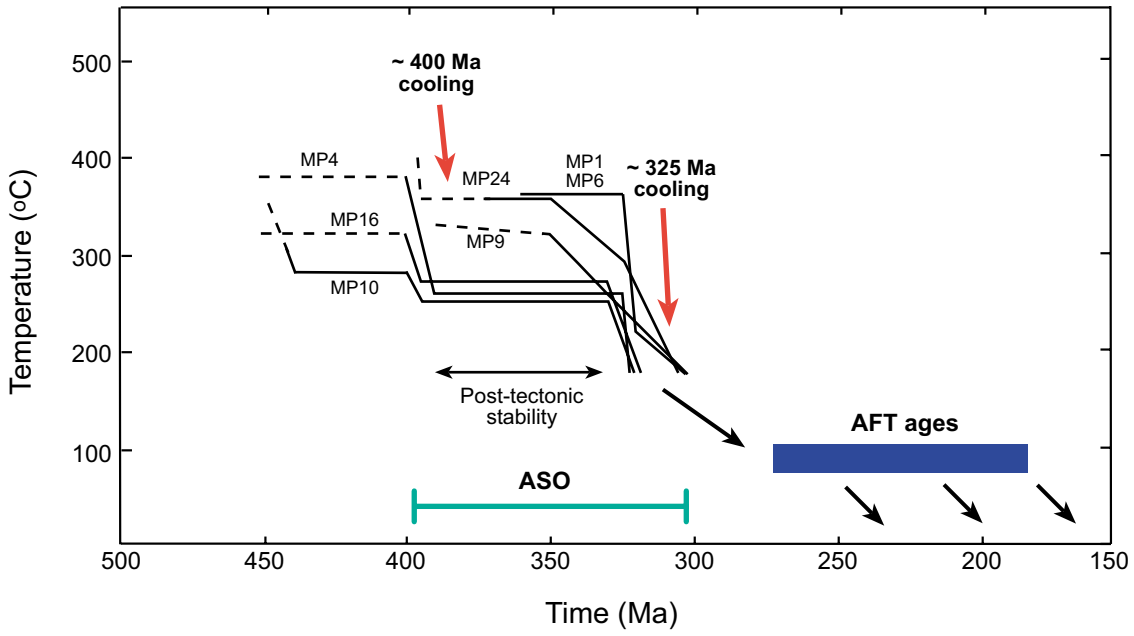


**Figure 6.7** Temperature-time paths for the post-Delamerian history of Mount Painter rocks from various stratigraphic/structural levels. This figure summarizes the results of hornblende K-Ar age determinations, mica K/Ar and $^{40}Ar/^{39}Ar$ data and multiple-diffusion-domain thermal modelling of K-feldspar $^{40}Ar/^{39}Ar$ data. A period of rapid cooling may have followed the Delamerian orogeny at ~ 500 Ma, but our models only bear directly on two subsequent periods of cooling, the first at ~ 400 Ma and the second at ~ 325 Ma. These latter two cooling episodes are separated by an isothermal period, corresponding to a period of post-tectonic stability. Cooling at ~ 400 Ma is associated with an average temperature drop of ~ 130°C for samples from the basement, and ~ 65°C for samples from the cover sequence. Cooling at ~ 325 Ma is associated with an average temperature drop of ~ 100°C for cover samples whereas samples from the basement cooled by ~ 150°C over the interval between 350 Ma and 330 Ma. Pegmatite samples cooled by at least 175°C in the interval 325-300 Ma. The amount of cooling during the 325 Ma episode is well constrained by the model fits for the K-feldspar samples, as discussed in the text. The cooling at ~ 400 Ma is constrained by K/Ar ages from hornblende and muscovite samples. Also shown is the age range of AFT data reported by Foster et al. (1994), and the duration of the Alice Springs Orogeny throughout central Australia (Dunlap and Teyssier, 1995).

### 6.3.1 Delamerian orogenesis and ~ 400 Ma cooling

Hornblende and muscovite apparent ages (Tables 6.3 and 6.4) constrain a period of rapid cooling from a temperature of around 475°C in the interval between 400 and 395 Ma. Data from K-feldspars are also consistent with such a cooling episode, although ages of around 400 Ma are recorded only by samples in the uppermost cover sequence. The K-feldspar models provide a constraint on the amount of cooling in this interval, and suggest that samples from the cover sequence cooled by around 65°C, and basement samples by 130°C.

As outlined above, metamorphic evidence suggests that the main fabric (which is axial to the regional mesoscale folds) formed at temperatures in excess of 500°C, implying that the deformation leading to the gross structuring of the Mount Painter region must also have occurred at temperatures > 500°C. As hornblende apparent ages are in the range 436 to 395 Ma, the regional scale folding and metamorphism must have occurred prior to 395 Ma. In the absence of higher temperature geochronological data, the current data cannot help to constrain the precise timing and duration of peak metamorphism; however, two possibilities can be suggested. First, peak metamorphism may have occurred during the Delamerian Orogeny (*ca.* 500 Ma) and was followed by slow cooling throughout the period 500-400 Ma, the latter resulting in the partial resetting of hornblende. Second, peak metamorphism may not have occurred until just prior to 436 Ma, the age of the oldest hornblende sample. In light of the regional deformational framework, however, the first hypothesis outlined above is preferred.

As noted earlier, in the absence of a likely source of magmatic heat Sandiford et al. (1998a) suggest that the elevated thermal gradients of ~ 40°Ckm$^{-1}$ that were associated with peak metamorphism (whether it be Delamerian or slightly younger) simply reflect the burial of the high heat producing Mount Painter basement units beneath the Adelaidean sedimentary cover. If this model is correct, then the presence of such a steady state thermal source allows the amount of exhumation associated with cooling to be constrained, at least to the first order. The thermal models outlined above suggest that the Mount Painter basement rocks cooled by at least 150°C at ~ 400 Ma. For steady-state thermal gradients of around 40°Ckm$^{-1}$, this magnitude cooling implies around 3-4 km of denudation.

### 6.3.2 Post-tectonic stability ~ 395-330 Ma

Following rapid cooling around 400-395 Ma, K-feldspar thermal models, for both basement and cover samples, are consistent with a period of post-tectonic stability between around 395 and 330 Ma. As outlined above, the apparent ages of biotite samples seem to have been affected by partial argon loss during this isothermal (or near isothermal) period. Because the mesoscale structuring of the Mount Painter region had taken place prior to 395 Ma, the variations in isothermal temperature required to replicate the biotite apparent ages represent the lateral thermal gradient along a projected north-south section through the Yankannina Anticline and Arkaroola Syncline at this time (Figure 6.3). Figure 6.8 shows these estimated palaeotemperatures, plotted as a function of distance from the basement-cover unconformity. What is clear from these results is that samples in the basement were isothermal at significantly higher temperatures than samples higher in the cover sequence, revealing a lateral thermal gradient of 7.3°Ckm$^{-1}$. This result is supported by the modelled temperatures of the K-feldspar samples, which, if included with the biotite estimates, yield a

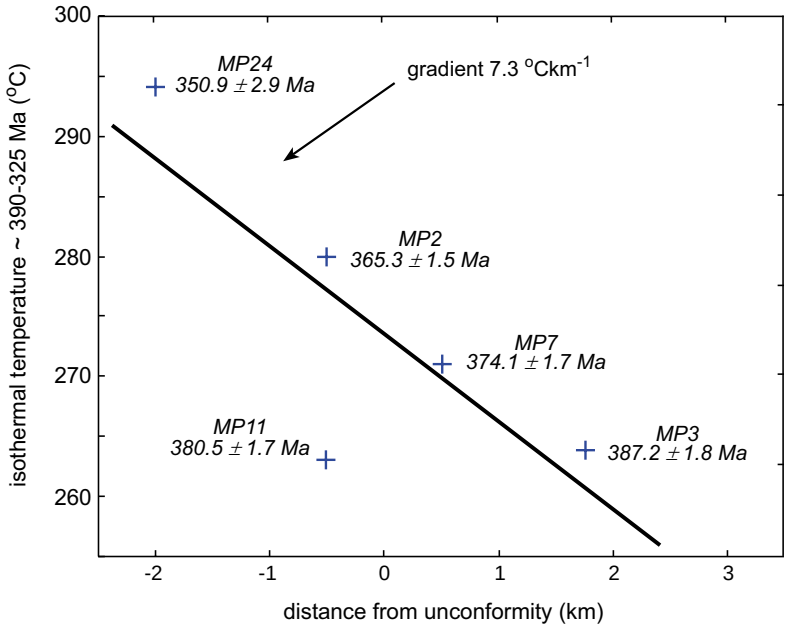


**Figure 6.8** Plot of reconstructed palaeotemperature as a function of distance from the basement-cover unconformity. As shown in Figure 5 the K-feldspar models suggest that the rocks remained essentially isothermal in the period following rapid cooling ~ 400 Ma and prior to cooling ~ 350 Ma. For comparison, we estimated the isothermal temperature required to match the $^{40}Ar/^{39}Ar$ plateau ages of biotite samples using a finite difference algorithm for diffusion from an infinite cylinder. We used diffusion parameters suggested in the literature (Harrison et al., 1985) and averaged the model isothermal temperature calculated for a diffusion domain radius of 150 microns (c.f., Harrison et al., 1985), and for the maximum sieve size of each mineral separate. These data show that samples within and nearby the Mount Painter basement units are hotter than samples higher in the cover sequence, suggesting either (1) a lateral gradient was maintained across the basement cover unconformity in the period 395-350 Ma, or (2) that subsequent deformation associated with cooling ~ 350-325 Ma resulted in differential uplift of the basement block with respect to the overlying cover sequence. The former hypothesis is consistent with models of the heat refraction which would result from juxtaposition of the high heat producing Mount Painter basement and the Adelaidean cover sequence within the Arkaroola Anticline and Yankannina Syncline (Mildren and Sandiford, 1995). Distance of samples from the basement-cover unconformity is listed in Table 6.2. Plateau ages are listed below each sample number. The line shown is the best-fit regression line, calculated using standard least-squares methods. The slope of 7.3°Ckm$^{-1}$ approximates the gradient across the basement-cover unconformity.

combined lateral gradient of 6.9°Ckm$^{-1}$.

The presence of such a lateral gradient is intriguing and may be the result of (1) minor differential uplift during slight tilting or tightening of the regional folds during the uplift associated with subsequent cooling at 325 Ma, or (2) the lateral refraction of heat resulting from the juxtaposition of the high heat producing Mount Painter basement with the low heat production cover sequence. Mildren and Sandiford (1995) have modelled the second scenario and show that the presence of high heat production Mount Painter basement adjacent to sediments with low heat production results in significant heat refraction, yielding lateral gradients of the order of 5-10°Ckm$^{-1}$. This modelling suggests that the observed thermal gradient is largely explicable in terms of heat refraction from the relatively conductive, high-heat producing basement rocks, and so it seems unlikely that subsequent exhumation at around 330 Ma resulted in additional growth of the regional folds.

### 6.3.3 ~ 330-325 Ma cooling

The K-feldspar thermal modelling reveals a second period of rapid cooling (~ 4-8°C Ma$^{-1}$) commencing between 330 and 325 Ma. During this interval basement rocks cooled by at least 150°C and samples from the cover sequence cooled by around 100°C. Based on the thermal arguments outlined above, this cooling is likely to have been associated with a further 3 km of denudation. Pegmatite samples cooled by at least 175°C in the interval between 325 Ma and 300 Ma.

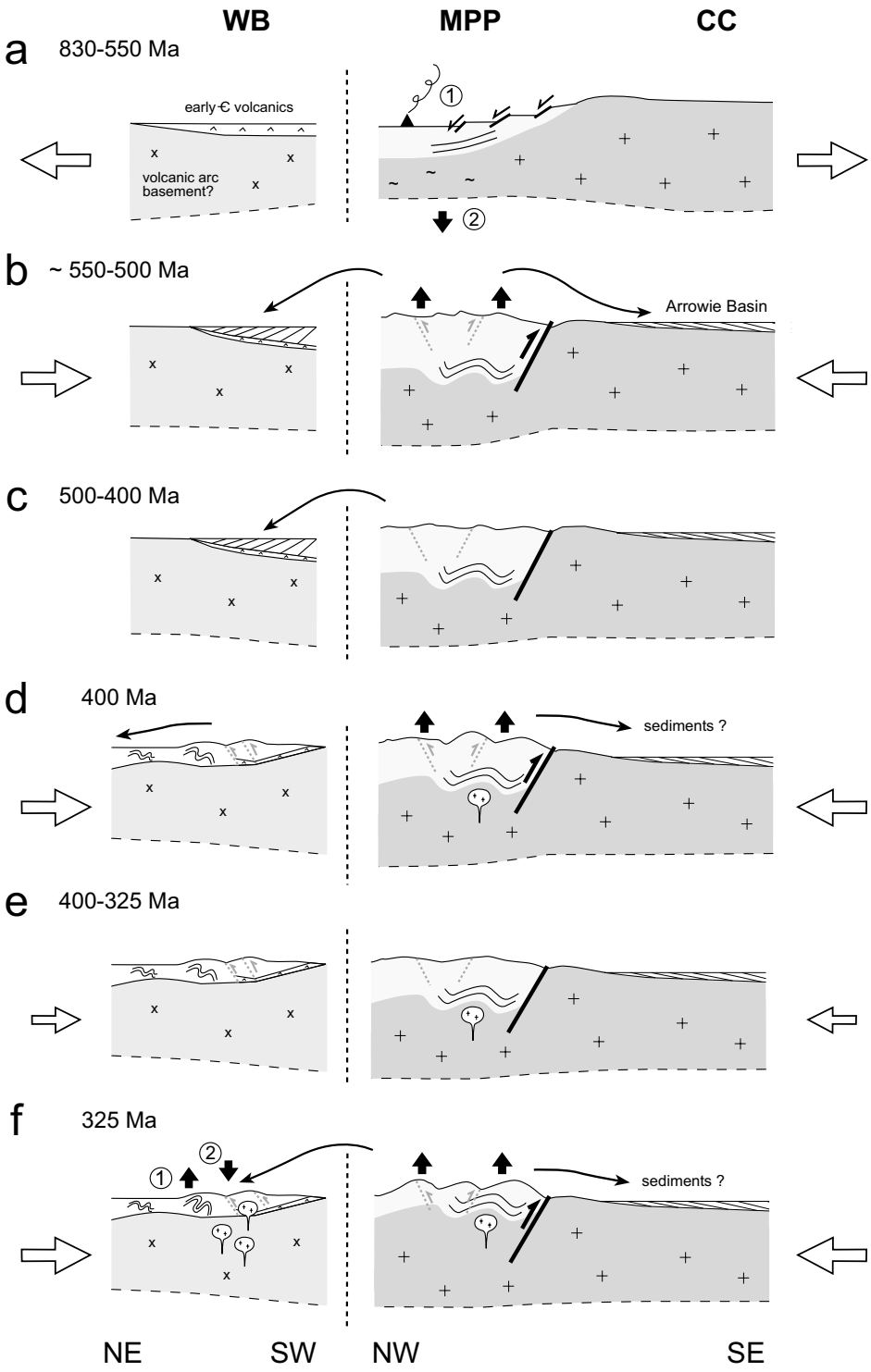


**Figure 6.9** NE-SW and NW-SE schematic cross sections showing the Neoproterozoic to Carboniferous development of the Mount Painter province (MPP) and adjacent crustal blocks (the Warburton Basin, WB, to the north and the Curnamona Craton, CC, to the south-east). The approximate modern crustal thickness is ~ 38 km (Collins, 1991). Sediments in the Warburton and Arrowie basins are not shown to scale. Arrows represent inferred tectonic stresses, with size indicating relative magnitude. The Paralana Fault is shown as a thick black line, the other faults in the central portion of the figure shown as thinner lines are inferred structures. The nature of the basement beneath the Warburton Basin is unclear, but it is likely a volcanic arc (Gatehouse, 1986). **(a)** the interval between 830 and 550 Ma represents deposition of the Adelaidean sedimentary cover during (1) dominantly rift and sag phase subsidence (830-690 Ma) and (2) dominantly sag phase subsidence. **(b)** Prior to the Delamerian orogeny at 500 Ma, Cambrian aged sediments were shed to the Warburton Basin in the north and the Arrowie Basin to the south. Uplift of the MPP during the Delamerian orogeny was gradual and largely driven by isostatic rebound. Sedimentation in the Arrowie Basin ceased at the time of the Delamerian orogeny. **(c)** The interval between 500 and 400 Ma is characterised by very slow post-Delamerian isostatic uplift, with continued sedimentation in the Warburton Basin; sediments were presumably transported south via large fluvial systems as there are no Ordovician sediments south or south-east of the MPP. During this period the MPP rocks cooled very slowly. **(d)** Represents initial uplift of the MPP during the earliest ASO, and the intrusion of the British Empire granite and numerous locally derived pegmatites into the middle crust. The MPP was inferred to have been exhumed by at least 3 km in this interval and the Warburton Basin was deformed under strong compression with folding and thrusting seen throughout the Cambrian and Ordovician sediments. **(e)** The period between 400 and 325 Ma represents post-ASO isostatic rebound of the MPP. The region must have been under mild compressive stress, as further deformation is recorded in the Warburton Basin. **(f)** the final stage of late Palaeozoic evolution involved the exhumation of the MPP by a further 3 km. Sediments in the Warburton basin continued to be deformed during this period, with the generation and emplacement of the Big Lake granite suite followed by (1) rapid uplift. Immediately following this uplift the Warburton Basin region became extensional again (2), with late Carboniferous sediments deposited directly over the granites. The Curnamona Craton remained essentially stable, in terms of vertical movements, throughout the Palaeozoic history. Evolution of Warburton and Arrowie Basins summarized from Gravestock (1995).

## 6.4 Discussion

The new argon age data presented here constrain two periods of post-Delamerian cooling, occurring at ~ 400 Ma and ~ 330-325 Ma. The age of these cooling events correlate well with the 400-300 Ma Alice Springs Orogeny (ASO), an intraplate tectonic event known throughout central Australia (e.g., Collins and Teyssier, 1989; Shaw et al., 1992; Dunlap et al., 1995). Consequently the cooling observed at Mount Painter is attributed to uplift associated with the ASO.

The ASO in central Australia exhibits many of the hallmarks of a classic orogeny; these include crustal penetrative thrust systems, large-scale nappe complexes, regional metamorphism and resetting of mineral isotopic systems on a regional scale. Unlike most plate margin orogens there is no significant granite plutonism in the Alice Springs Orogen, although localised abundant pegmatite formation supports the notion of limited crustal melting. Metamorphic assemblages developed during the ASO range from sub-greenschist to amphibolite facies (Dunlap et al., 1995). Denudation following Alice Springs deformation in central Australia has resulted in up to 20 km of exhumation which has brought the Proterozoic crystalline rocks of the Arunta Block up from beneath a thick (up to ~ 8 km) cover sequence of Neoproterozoic and Early Phanerozoic sediments forming part of the Centralian Superbasin (e.g., Korsch and Kennard, 1991).

Although the central Australian region records the most dramatic evidence for exhumation, deformation and metamorphism during the Alice Springs Orogeny, this event is also recorded in other parts of Australia. In particular, it is seen quite dramatically in the development of the Fitzroy Trough in the northwest of the continent (e.g., Willcox, 1996). Additionally, apatite fission track ages from a number of Proterozoic metamorphic terranes surrounding the central Australian region imply that Alice Springs-aged tectonism was also associated with mild denudation at the scale of the continent. Examples include the Mount Isa Inlier (Spikings et al., 1997) and the Broken Hill region (Hartley et al., 1998). In the latter case, $^{40}Ar/^{39}Ar$ and apatite fission track analyses reveal Alice Springs aged movement along major regional shear zones. Alice Springs aged tectonism is also recorded in the Darling River Lineament system in northwestern New South Wales, where one of three phases of Phanerozoic cooling, ~ 420-380 Ma, is attributed to this event (O'Sullivan et al., 1998). Locally, Gibson and Stüwe (2000) use apatite fission track data to constrain the exhumation history of the southern Adelaide Fold Belt, and suggest that in most areas the terrane cooled from temperatures > 120°C in the interval 300-270 Ma. Gibson and Stüwe (2000) attribute this cooling to the terminal ASO. Similar AFT ages of 350-200 Ma were obtained for basement rocks of the Curnamona Craton adjacent to the central Adelaide Fold Belt by Mitchell et al. (1998).

Although the published AFT data summarized above suggest that the ASO was associated with minor denudation in the southern Adelaide Fold Belt and adjacent crustal blocks, the argon data described here provide the first evidence to suggest that the ASO was associated with significant deformation anywhere in the Adelaide Fold Belt system.

As the argon data suggest that the ASO was responsible for at least 300-400°C of cooling at Mount Painter in two pulses at 400 Ma and ~ 330 Ma, it is likely to have been associated with significant tectonic activity in this region at this time. This conclusion is supported by a number of observations. Idnurm and Heinrich (1993) have reconstructed palaeomagnetic poles for uraniferous breccias in the Mount Gee and Mount Painter regions (Figure 6.3). These data indicate that the rocks have been magnetized twice, both times during the Permo-Carboniferous. Idnurm and Heinrich

(1993) note that these reconstructed poles are similar to those published from central Australia, which are generally related to the ASO (e.g., Li et al., 1989), and provide evidence for a hydrothermal fluid flow event through the Mount Painter rocks at this time.

Further evidence is provided by the occurrence of granites in the nearby Warburton Basin (a thin Early Cambrian to Ordovician Basin underlying the Cooper Basin; Figure 1) which have been dated, by SHRIMP analyses on zircons, at 323 ± 5 Ma and 298 ± 4 Ma (Gatehouse et al., 1995). Sun (1997) associates the intrusion of these granites with the first of three major periods of Phanerozoic deformation in the basin. The first event, associated with the ASO, resulted in the intrusion of the granite bodies and the propagation of regional scale thrust faults and large fold structures; the latter resulting in significant internal deformation within the basin. These granites are overlain directly by a thin but continuous sequence of late Carboniferous clastic sediments (Parker, 1993; Sun, 1997) implying that in the interval between 325 and 300 Ma the Warburton Basin area must have been characterized by elevated geothermal regimes followed by a period of very rapid uplift in order to unroof these plutons. Erosion of adjacent highlands is also required to provide a source for the dominantly clastic sediments which fill the basin.

The significance of the recognition of Alice Springs aged deformation at Mount Painter is two fold: (1) it helps constrain the long-term history of the Mount Painter crust, allowing a lengthy history of tectonic reactivation, from the Mesoproterozoic through until the present day, to be recognized; and (2) it dramatically extends the realm of significant Alice Springs aged deformation (e.g., Collins and Teyssier, 1989; Shaw et al., 1992; Dunlap and Teyssier, 1995) to the continental-scale.

As highlighted in the introduction to this chapter, these points help us understand important questions concerning the factors controlling the distribution of intraplate deformation in the Australian continent. In particular, why did the Mount Painter region suffer much more intense deformation during the ASO than other regions of the Adelaide Fold Belt, or other regions of adjacent Proterozoic crust? What processes controlled the long history of tectonic reactivation, both pre and post-ASO, which is recorded at Mount Painter? And why has this region suffered repeated tectonic reactivation when other terranes which share a similar history of crustal growth, for example the Mount Isa Inlier, achieved tectonic stability much earlier? The tectonic reactivation in this area during the ASO appears to be a consequence of two factors. First, the thermochronological data presented here show that through most of the Palaeozoic, the Mount Painter region was characterized by elevated thermal gradients, almost certainly due to the extraordinary concentrations of heat producing elements in the Mount Painter basement rocks. These thermal gradients resulted in the Mount Painter basement being above ~ 300°C from the Delamerian orogeny (~ 500 Ma) through to ~ 330 Ma, even though for much of this time it was probably at depths significantly shallower than 10 km. The existence of anomalous upper crustal thermal gradients over such long periods of time must reflect conditions appropriate to near steady-state conductive geotherms and implies that unusual geothermal conditions extended well down into the lithosphere. Elevated conductive geotherms are expected to equate with dramatic lithospheric weakening, and it is proposed that the localization of Palaeozoic intraplate deformation required to produce the two cooling events documented here, is a primary response to thermally modulated variations in the strength of the Australian continental lithosphere. Second, it is suggested that the bounding Paralana Fault is linked to a regional scale system of faults to the north that have controlled ASO age deformation not only

in the Warburton Basin and central Australia, but also in the Mount Painter region. This fault system probably penetrates into the lithospheric mantle and is a persistent zone of weakness that is still active today (as indicated by the seismic activity and young topography of the region). In particular, the juvenile topography that is clearly seen on aerial photographs of the Mount Painter region suggests this fault system is still effecting exhumation.

# Chapter Seven

# Discussion

The models and examples discussed in this thesis confirm that radiogenic heating, due to the decay of anomalous concentrations of heat producing elements within the crust, plays a significant role in modulating crustal thermal regimes and total lithospheric strength. High concentrations of crustal heat sources, such as found through much of the Proterozoic of Australia, lead to anomalous thermal regimes that are particularly sensitive to the way in which the heat sources are distributed. Indeed, a prime aim of this thesis has been to illustrate the role played by the vertical redistribution of heat producing elements in modulating thermal regimes.

These observations have important implications for crustal evolution on both a regional scale and on the scale of individual terranes. For example, this thesis has shown that radiogenic heating provides a plausible mechanism for generating high temperature-low pressure metamorphic conditions in a number of settings where the origins of such metamorphism has remained enigmatic. Furthermore, the thermal weakening associated with the presence of high concentrations of radiogenic heat sources within the crust may help to localize deformation and magmatism, particularly in intraplate settings.

On geological timescales of several 100 Ma or more, the redistribution of heat producing elements through ongoing tectonic processing of the lithosphere is likely to exert a profound control on its tectonic response, largely because the primary tectonic processes which effect the redistribution of heat sources are themselves temperature dependent. This interdependence suggests the existence of an important feedback system, which may help to explain the ordering of heat production in the lithosphere evident from analysis of the global heat flow dataset. This thesis has shown that in Australian Proterozoic terranes, where the complement of heat producing elements in the crust, $q_c$, is around twice the modern global average, this feedback system has had a significant impact on the long-term crustal evolution. In general Australian Proterozoic terranes are characterized by lengthy tectonic histories which reflect the progressive redistribution of heat producing elements into the upper crust, largely through magmatism, but also through the coupling of deformation and surface processes. Reducing either $h$, $q_c$, or both, leads to long-term deep crustal cooling and an increase in total lithospheric strength. Both processes can lead to effective cratonization, and indeed are probably essential for cratonization. Until $q_c$ and $h$ have been reduced sufficiently to minimize the thermal and mechanical impacts of the crustal heat sources, the crust will remain susceptible to applied tectonic loads, potentially suffering frequent and episodic tectonic reactivation. These results therefore provide a means for understanding lengthy histories of tectonic activity recorded in many terranes, particularly in intraplate settings. In addition to the observations summarized here, this model also has profound implications for our understanding of the long-term evolution of the Australian Proterozoic crust, particularly the factors which control the distribution of deformation, and our understanding of fundamental processes such as crustal differentiation. Aspects of these problems are addressed in the following discussion.

## 7.1 Plate tectonics and the Australian Proterozoic crust

The controls on crustal evolution and tectonism have long been the subject of considerable interest. While tectonic processes on the modern Earth are generally well understood in terms of conventional plate tectonic paradigms, the evolution of the early Earth is less well understood. During the early Archaean, higher heat productivity (by a factor of around 3), coupled with higher mantle heat flow, would have meant that the lithosphere was significantly weakened and unstable in a mechanical sense. Kröner (1991) suggested that such lithosphere would have prohibited the existence of rigid plates and that the characteristic high geothermal gradient regimes must have favoured global hot-spot activity, vertical magmatic accretion and semi-continuous tectonic activity rather than conventional plate-plate interactions. This, or similar models, has been accepted by many workers (e.g., Fyfe, 1973; Goodwin, 1981; Windley, 1995; Choukroune et al., 1997; Chardon et al., 1998; Hamilton, 1998; Bailey, 1999) but is still subject to ongoing debate by those who suggest that the continental crust had already achieved stability by this time (e.g., Bickle, 1978; Nisbet and Fowler, 1983; Campbell and Jarvis, 1984; Martin, 1986; Jackson et al., 1994; Mints, 1999).

As noted by Lenardic and Moresi (1999) stable continental cratons are defined as parts of the lithosphere that have attained stability, such that the lithospheric strength is significantly greater than the intraplate stress level, and which has not experienced major tectonic disruptions over a timescale of around one billion years. Precambrian terranes are often cratons, and the development of such cratons from lithosphere which must have been initially unstable is fundamental for understanding many aspects of the long-term evolution of the crust. Lenardic and Moresi (1999) showed that the chemical buoyancy of the subcratonic lithospheric roots cannot account for the stability of the cratons, and that the cratons themselves must be inherently strong. Several models have been proposed to account for the origin of this inherent strength. One factor is the secular decline in heat production which has caused significant reductions in $q_c$ (by a factor of two since 2.5 Ga and by a factor of three since 3.5 Ga) meaning that such crust became progressively cooler and stronger with time. Many workers also suggest that cratonization occurred progressively as a result of a combination of processes including (1) extensive continental underplating (e.g., Kröner, 1991), (2) volatile loss in the subcrustal mantle lithosphere (e.g., Pollack, 1986) and (3) large scale magmatic extraction (e.g., Kröner, 1984).

The origins of stable cratons are clearly related to tectonic processes occurring in both the Archaean and Proterozoic, however there is considerable ongoing debate about these issues (e.g., Kerr, 1978; Hargraves, 1981; Windley, 1981). In general terms the trend to effective cratonization, by whatever means, is thought to have lead to the onset of rigid plate behaviour around the late Archaean and early Palaeoproterozoic. At this time much of the continental crust is thought to have been stable, with deformation occurring principally in weak plate boundary zones due to plate-plate interactions. Kröner (1991) suggests that the voluminous crust formation event at around 2.1-1.9 Ga provided the first real evidence for modern plate tectonic style processes, as typified by the presence of arc-type granites, ophiolites and blueschist assemblages in terranes including the Canadian Trans-Hudson Orogen and the Svecofennian Orogen in Finland.

As alluded to in Chapter Four of this thesis, however, Proterozoic crustal evolution in many terranes seems to be characterized by semi-continuous tectonic activity spanning several hundreds of millions of years. Such prolonged and episodic tectonism is difficult to reconcile with commonly held perceptions about typical plate-tectonic cycles, and seems to indicate that many regions of

crust took an appreciable time to become cratonized. Nonetheless, the popularity of the uniformitarian view that "the present is the key to the past" (e.g., Kitts, 1963; Windley, 1993) has meant that dynamic plate-tectonic models of Proterozoic crustal evolution have prevailed, particularly in North America, Europe and Africa. This view, promoted by Talbot (1973), Condie (1986), Hoffman (1980, 1989, 1991), Kröner (1991), Ellis (1992) and Windley (1993) amongst others, suggests that Proterozoic crust evolved as a consequence of plate tectonic processes similar to, if not the same as, those which characterize the modern Earth. Although this model is undoubtedly appropriate in some terranes, for example the evolution of the 1100 Ma Grenville Orogen in North America (e.g., Baer, 1981), the 2100–1800 Ma Wopmay Orogen in northwest Canada (e.g., Hoffman, 1980; Hoffman and Bowring, 1984) and the 1800-1600 Ma Svecofennian belt in Finland (e.g., Nironen, 1997), the application of a plate-tectonic model to all Proterozoic crust is still highly speculative.

In recent times, this dynamic plate-tectonic model has been advocated for the evolution of Australian Proterozoic crust by Myers (1990) and Myers et al., (1996). These workers proposed that the three main Proterozoic cratons, the North, West and South Australian cratons evolved separately as microplate fragments before being assembled into the Rodinian supercontinent between 1300 and 1100 Ma. From this time tectonism in Australian Proterozoic terranes was thought to be largely intracratonic.

In contrast to the dynamic model, Rutland (1973, 1976), Gee (1979) and Etheridge et al., (1987) promoted a stabilist view of crustal evolution in Australian Proterozoic terranes. This stabilist model, which is based on the existence of a single raft of crust in which all tectonic and magmatic activity was intracratonic, stems largely from the synthesis of observations about the timing, duration and geometry of tectonic activity in many different Australian Proterozoic terranes. Together these observations suggest significant differences between Australian Proterozoic orogenic belts and many Archaean and Phanerozoic orogenic belts; in particular the absence of evidence for subducted oceanic lithosphere. Indeed, as summarized by Hancock and Rutland (1984) "... it has frequently been noted that Proterozoic fold belts lack the 'earmarks of subduction' associated with operation of the Wilson cycle," with this observation possibly indicating "... real differences between Proterozoic and Phanerozoic orogeny" (e.g., Rutland, 1973; Kröner, 1977). Moreover, as noted by Wyborn et al., (1992) many Australian Proterozoic granites have isotopic and geochemical signatures which are significantly different from both Archaean granites and most modern island arc granites associated with subduction.

These differences motivate a more detailed discussion of the factors which controlled Proterozoic tectonics in the Australian context. Although it is probably true that certain aspects of both the stabilist and dynamic models were valid, the observations outlined in this thesis suggest that rather than reconciling whether tectonic activity in Australian Proterozoic crust is strictly "plate-tectonic" (the dynamic view) or strictly "intraplate" (the stabilist view), it may prove more rewarding to view this activity in terms of the factors which control the long-term thermomechanical stability of the crust. Indeed such an approach has proven useful in understanding the distribution of active deformation in modern continental interiors remote from plate boundaries, such as central Asia. Although active deformation in Central Asia is clearly forced by plate tectonic processes associated with the India-Asia collision, the style and heterogeneous distribution of deformation also reflects the inherent mechanical properties of the Asian lithosphere (Neil and Houseman, 1997). In particular, Neil and Houseman (1997) have shown that the distribution of deformation over very large domains

in the Tian Shan, more than 1000 km from the plate boundary, is a result of the inherent strength contrasts between the Tian Shan and the adjacent Tarim Basin, through which plate boundary stresses are transferred.

This observation regarding the distribution of active deformation in the modern continents highlights the fact that proximity to active plate boundaries is not the sole determinant in shaping the tectonic response, a conclusion which I suggest is relevant to the evolution of Australian Proterozoic terranes. Available geochemical and isotopic data from many Australian Proterozoic terranes suggests that a significant proportion of the anomalous crustal heat production was scavenged from lower crustal sources. If this was so, then the early Proterozoic crust must have been characterized by much higher values of $h$, and probably also significantly higher $q_c$. As outlined earlier, such a configuration would have greatly increased lower crustal thermal regimes and meant that the Australian Proterozoic lithosphere was significantly weaker than the modern lithosphere. For example, for an average mantle heat flow of 20 $mWm^{-2}$, if heat sources which contribute 80 $mWm^{-2}$ to the surface heat flow had been concentrated in the deep crust (i.e., high $h$), Moho temperatures would have been of the order of 900°C meaning that the lithosphere was less than 100 km thick and weakened (by a factor of at least 2-3) when compared to differentiated, low $h$ crust.

This observation implies very real differences in the thermal and mechanical behaviour of the early Australian Proterozoic crust when compared to the modern crust. In particular, by virtue of its inherent weakness the Australian Proterozoic crust probably did not require significant tectonic forcing in order to deform, and must have been sensitive to even mild applied forces. These observations imply that the distribution of Proterozoic deformation in the Australian continent may have been controlled more by the intrinsic properties of the lithosphere than the nature of the tectonic forces. Indeed, the inherent weakness of the Australian Proterozoic continental lithosphere implies that it may be difficult to recognize the way in which plate tectonic processes impacted on its evolution. This interpretation provides a cautionary note to strictly plate tectonic interpretations such as those of Myers (1990) and Myers et al., (1996).

In light of the observations outlined here, I suggest that the redistribution of heat sources within the crust as a consequence of tectonic feedback represents an additional model for crustal evolution. I suggest that this style of evolution, which leads to a progressive reduction in both $h$ and $q_c$, represents the transition between a style of “soft-plate” deformation which persisted throughout the Australian Proterozoic crust during the Palaeoproterozoic and Mesoproterozoic, and the modern Phanerozoic style where this crust appears to be strong, rigid and craton-like and where deformation occurs principally at plate boundary zones. The immediate corollary of this model is that the onset of rigid plate behaviour in the Australian continent was probably diachronous, with the lower heat production terranes in Western Australia achieving a stable craton-like state significantly earlier than higher heat producing Proterozoic terranes within the CAHFP.

The presence of thin and thermally weakened lithosphere also has important consequences for the types of magmatism and deformation expected in Australian Proterozoic crust. First, characteristic high geothermal gradient regimes imply that most felsic igneous rocks would have been generated as a result of largely crustal melting at relatively shallow depths. This prediction is supported by available geochemical and isotopic data from Australian Proterozoic granites and felsic volcanics. These data suggest that most Proterozoic granites (in the range 1870-1500 Ma) are

I-type, Sr-depleted and Y-undepleted; a geochemical signature which indicates a source region in which plagioclase, but not garnet, was stable (Wyborn et al., 1992). Furthermore, available Nd isotopic constraints (Wyborn et al., 1992; Wyborn, 1998; Wyborn et al., 1998b) suggest that most of these granites have experienced a significant crustal prehistory and were derived from melting of crust rather than mantle sources. Both sets of observations support the assertion that high geothermal gradient regimes persisted throughout Australian Proterozoic crust during the Palaeoproterozoic and Mesoproterozoic.

Second, a thin and thermally weakened lithosphere is unlikely to have been able to support significant topography. This observation is broadly consistent with the predominance of low-pressure metamorphic assemblages throughout many Australian Proterozoic metamorphic belts. The inability of the Proterozoic lithosphere to support large mountain belts must have meant that the total supply and redistribution of sediments through erosion was significantly limited. Intriguingly, this prediction is consistent with available carbon isotopic data which suggests that throughout much of the Palaeoproterozoic and Mesoproterozoic the isotope ratio of $^{13}C$ and $^{12}C$ (expressed as $^{13}C$ ‰ PDB) shows very little secular variation, averaging around 0 ‰ (Des Marais et al., 1992; Veizer et al., 1992; Buick et al., 1995; Knoll et al., 1995; Braiser and Lindsay, 1998; Lindsay and Braiser, 2000). These data contrast sharply with the spectacular carbon isotopic excursions seen subsequently in the Neoproterozoic and Cambrian (e.g., Schopf and Klein, 1992) and earlier in the Palaeoproterozoic (e.g., Schopf and Klein, 1992; Karhu and Holland, 1996). Because the values of $^{13}C$ are determined by the relative rates of burial of $^{13}C$ and $^{12}C$ (e.g., Hayes, 1983; Holser, 1997), these data allow predictions to be made about the nature geodynamic activity during this Proterozoic interval. Generally positive $^{13}C$ excursions indicate increased burial of organic matter, while negative excursions indicate significant weathering and erosion of organic-rich rocks (e.g., Hayes, 1983; Holser, 1997). Consequently, Braiser and Lindsay (1998) concluded that a $^{13}C$ value of around 0 ‰ indicated that much of the Earth was covered by low-lying cratons or was characterized by reduced crustal activity and weathering, suggesting that the 2.0 and 1.0 Ga interval was one of prolonged stability in terms of global crustal dynamics. This suggestion lends credence to the model of a thermally weakened Proterozoic crust characterized by dominantly vertical accretion and by low average topography.

## 7.2 Thermo-mechanical controls on the differentiation of the continental crust

Analysis of surface heat flow and surface heat production data as well as heat production distributions in obliquely exposed terranes clearly indicate that the continents are strongly differentiated with respect to heat producing elements. Table 7.1 shows the average values of the parameters $h_r$ and $q_r$ from variously aged heat flow provinces where the linear heat flow-heat production relationship applies. $q_r$ is the reduced heat flow and, together with surface heat flow, $q_s$, provides a minimum bound on $q_c$ (= $q_s$-$q_r$) because $q_r$ overestimates $q_m$ (e.g., Jaupart, 1983; Vasseur and Singh, 1986). As outlined earlier in this thesis, the parameter $h_r$ represents the characteristic length scale for heat production in the lithosphere, however it is not strictly equivalent to the effective depth of the heat production, $h$, used in this thesis. Nonetheless, these data show that heat sources in regions of Proterozoic and Phanerozoic continental crust contribute around 30 $mWm^{-2}$ to the observed surface heat flow, with this heat production largely concentrated within the upper 10 or so kilometres of the crust (e.g., Lachenbruch, 1968; Birch et al., 1968; Taylor and McLennan, 1985). Archaean terranes

**Table 7.1** *Estimates of the parameters $h_r$ and $q_r$ from terranes of various ages*

| *Age of last tectonothermal event* | $q_r$ ($mWm^{-2}$) | $q_c$ ($mWm^{-2}$) | $h_r$ (km) |
|---|---|---|---|
| Archaean | 25.5 ± 0.7 | 13.7 ± 1.7 | **6.9** ± **1.7** |
| Proterozoic | 29.5 ± 10 | 24.2 ± 9.0 | **10.1** ± **3.6** |
| Palaeozoic | 25.5 ± 3.5 | 28.5 ± 10 | **11.6** ± **6.2** |
| Cenozoic-Mesozoic | 44.5 ± 17 | 24.3 ± 6.6 | **9.5** ± **3.7** |
| Average all terranes | 33.3 ± 14 | 24.3 ± 6.6 | **9.4** ± **3.5** |

Data from a compilation by Taylor and McLennan (1985); modified from Vitorello and Pollack, 1980, and Morgan, 1984). Values of $q_C$ are minimum estimates as $q_r$ overestimates $q_m$ (e.g., Jaupart, 1983; Vasseur and Singh, 1986)

are characterized by similar values of $q_r$, but somewhat lower values of $h_r$.

Two intriguing questions arise from these observations. The first question relates to our understanding of the mechanisms that have caused the crust to become differentiated in the heat producing elements; and the second, perhaps more intriguing question, is why, with the exception of the Australian Proterozoic crust and most Archaean terranes, there are indications of a relatively uniform pattern of differentiation amongst the heat production distributions? Indeed, as noted by Oxburgh (1980) " … it is difficult to see how a well ordered regional distribution of heat sources could come about."

Clearly the lithospheric complement of heat production must ultimately relate to processes of primary crustal accretion, and the conventional wisdom is that the character of heat production distributions in the crust is a primary feature of crustal growth. Moreover, because of the lithophile nature of the heat producing elements it is to be expected that they will be progressively concentrated into the upper crust, due to the buoyancy driven segregation of felsic melts from more mafic residuum during magmatic dominated crustal growth. Nevertheless, no compelling argument has yet emerged as to why magmatic dominated crustal growth processes should lead to the characteristic length scale and absolute abundance of heat producing elements inferred from heat flow data.

The temperature sensitivity of lithospheric rheology, however, implies that the parameters which are related to lithospheric thermal regimes, $q_c$, $h$, $z_l$ (lithospheric thickness), and $q_m$, are intimately related. Thus, high $q_c$ crust can be stabilized only if those heat sources are concentrated in the uppermost crust (low $h$) and the region is characterized by the development of a thick mantle, which has the effect of reducing $q_m$ and increasing $z_l$. The observation that Archaean terranes seem to be characterized by somewhat smaller length scales is consistent with this notion. As outlined earlier the secular decline of heat production and mantle heat flow implies that at the time of their formation, these terranes were characterized by high values of $q_c$, meaning that they required significantly lower length scales to be effectively stabilized.

These observations have important implications for the way in which crustal differentiation is viewed, and for understanding the origins of characteristic heat source distributions. Although a reduction in the length scale, $h$, is most readily effected by magmatic differentiation, this thesis has shown that the gross chemical and structural architecture of the continents also reflects complex

tectonic reworking in zones of continental deformation, both at plate boundaries (e.g., continental collisions), and in intraplate settings. In these settings heat producing elements are redistributed as a direct consequence of deformation as well as through related processes, such as erosion, that follow as the isostatic consequence of the deformation. The redistribution of heat producing elements into the upper crust as a result of these processes effects changes in $h$ and $q_c$ and will, over time, result in a significant long-term increase in lithospheric strength. Tectonic activity and the redistribution of heat producing elements will continue until the thermo-mechanical impacts of the heat sources have been minimized. From this viewpoint, it is not surprising that many regions of stable continental crust are characterized by very similar heat producing element distributions, as it is only once the heat sources have been redistributed into the uppermost crust or removed by erosion that the lithospheric strength will begin to exceed the normal amplitude in the tectonic stress levels experienced by continental interiors (a requirement for cratonic behaviour). Consequently, the characteristic modern crustal heat source distribution may be viewed as one that represents a thermomechanical state (for some characteristic mantle heat flow and crustal thickness) in which the continental lithosphere begins to lose its ability to respond to imposed forcing. Such crust becomes "craton-like" and is characterized by the values of $h$ and $q_c$ which effect this stability.

In summary, this thesis has been concerned with the possible role of crustal processes in modulating the long-term evolution of the continents. While not wishing to deny the importance of mantle processes, the observations outlined in this thesis have shown that the redistribution of crustal heat sources impacts significantly on the stability of cratonic lithosphere. Together with the secular decline in heat production and mantle heat flow, this model helps to account for the progressive differentiation and cratonization of the continental lithosphere. In particular, as this model is based on insights from Australian Proterozoic terranes it contributes significantly to our understanding of the long-term evolution of these regions of crust. Australian Proterozoic crust remains anomalous in so much as the available evidence suggests that the higher values of $q_c$ in these terranes are not compensated by significantly lower $h$. This observation suggests that Proterozoic Australia is only partly cratonized, and is consistent with the record of ongoing tectonic reactivation and Phanerozoic reworking in these regions of crust (e.g., the reworking of the central Australian crust during the 300-400 Ma Alice Springs Orogeny). I suggest that this ongoing tectonic reworking reflects the inherent weakness of high $q_c$ crust, and means that the heat production distribution in many Australian Proterozoic terranes is still being episodically modified.

## 7.3 Future Work

Although the results presented in this thesis provide significant new insights into the long-term behaviour of the continental crust, and have important bearing on models of crustal growth and tectonism, the potential exists for further work on various aspects of these problems.

In particular, although this thesis has focussed on the effects of radiogenic heating in Australian Proterozoic terranes, where average heat production rates are extreme, radiogenic heating may have also played a role in the thermal evolution of many other terranes, of both differing age and contrasting geological histories. It is possible that the Australian Proterozoic terranes simply provide one of the best examples of an anomalous heat source distribution, largely because they are characterized by low levels of average denudation which has meant that much of the crustal

complement of heat sources has been preserved within the upper crust. This possibility is supported by data from the Musgrave Inlier where average levels of denudation are much greater (~ 20 km), and average crustal heat generation rates are significantly lower (~ 2.7 $\mu Wm^{-3}$) than those which characterize many other Australian Proterozoic terranes. These data may suggest that in this terrane much of the available crustal heat production has already been removed through erosion and raise the possibility that if all the Proterozoic terranes within the CAHFP had suffered similar amounts of denudation, then the extraordinary nature of crustal thermal regimes in this region may not have been recognized. These observations suggest that the potential effects of radiogenic heating in other terranes need to be assessed. Central to this investigation is the need to:

- Develop a greater understanding of the variations in the total complement and distribution of crustal heat sources, largely through an increase in the density of heat flow determinations in regions where the heat flow field is not well known.
- Identify the origins of the high heat producing granites, with a view to establishing whether their petrogenesis was the result of an anomalous mantle source region or an unusual enrichment process.

Answers to these questions should provide insights into whether or not the tectonic feedback system described here may have also impacted upon the long-term evolution of other regions of continental crust. For example, if the origin of the anomalous heat producing granites can be attributed to an anomalous source region, and if the Australian terranes formed part of an ancient pre-Rodinian supercontinent at the time of enrichment (e.g., Powell, 2000) it is possible that high heat producing granites may have also intruded contiguous terranes elsewhere (e.g., the Mojave and Yavapi terranes in the South Western United States, and Proterozoic terranes in northwestern Canada; e.g., Burrett and Berry, 2000). An evaluation of this possibility may be aided by modern metamorphic and thermochronological methods, which could potentially provide insights into the role of crustal heat sources in terranes where much of the crustal complement of heat sources has since been removed by erosion. This is particularly the case for discriminating potential metamorphic heat sources, as transient and steady state thermal models make very different predictions about post-metamorphic cooling rates which can be readily assessed by modern thermochronological methods.

The models of crustal evolution developed in this thesis should also be applicable to a wide range of problems relating to Archaean tectonics. In particular, this view seems to be consistent with the observation that Archaean cratons are generally characterized by both lower average heat flow and considerably lower values of $h$ than most younger terranes. Moreover, because heat production rates were significantly higher during the Earth's early history (at least twice the modern day rate at around 3 Ga) the average Archaean $q_c$ may have been as high as 50 $mWm^{-2}$ meaning that the lithosphere was significantly unstable. The models shown here suggest that one way that such crust may have become stable was through the redistribution of heat sources into the upper crust, resulting in a reduction in the characteristic length scale, $h$. Although the application of this model to Archaean terranes would require further work, it may help to account for some of the characteristic properties of Archaean terranes, including the 'dome and basin' geometry in which the uppermost crust is dominated by large batholithic granite complexes (e.g., Sandiford and McLaren, in press).

Another important issue relates to the potential role of heat producing elements during transient tectonic processes. This thesis has been concerned only with the impacts of radiogenic

heating on steady-state thermal regimes and it is important to develop this work further by evaluating the potential role of radiogenic heating in dynamic settings, and on much shorter time scales when transient thermal effects are also very important. Such an approach may contribute to ongoing debate regarding the origins of anomalous crustal thermal regimes in orogenic settings where the relative contributions of crustal, mantle and magmatic heat sources are often unclear.

As a final point, it may also be important to evaluate the way in which high heat producing granites impact upon fluid circulation. Because upper crustal thermal gradients are influenced by the presence of long-lived quasi-steady state heat sources, the presence of high concentrations of heat sources in the upper crust has considerable implications for the generation and long-term circulation of hydrothermal fluids and the leaching of metals; processes essential for the formation of a large variety of ore deposits.

# References


Andrews, S.J. 1998. Stratigraphy and depositional setting of the upper McNamara Group, Lawn Hills region, Northwest Queensland. *In*: Williams, P.J., (*ed.*), Metallogeny of the McArthur River-Mount-Isa-Cloncurry minerals province. *Economic Geology*, 93, p. 1132-1152.

Ashwal, L.D., Morgan, P., Kelley, S.A. and Percival, J.A. 1987. Heat production in an Archaean crustal profile and implications for heat flow and mobilization of heat-producing elements. *Earth and Planetary Science Letters*, 85, p. 439-450.

Baer, A.J. 1981. A Grenvillian model of Proterozoic plate tectonics. *In*: Kröner A. (*ed.*), *Precambrian Plate Tectonics*. Elsevier, Amsterdam, p. 353-385.

Bailey, R.C. 1999. Gravity-driven continental overflow and Archaean tectonics. *Nature*, 398, p. 413-415.

Bea, F., Montero, P. and Molina, J.F. 1999. Mafic precursors, peraluminous granitoids, and late lamprophyres in the Avila Batholith: A model for the generation of Variscan Batholiths in Iberia. *Journal of Geology*, 107, p. 399-419.

Beaumont, C., Fullsack, P. and Hamilton, J. 1994. Styles of crustal deformation in compressional orogens caused by subduction of the underlying lithosphere. *In*: Clowes R. M., and Green, A.G. (*eds.*), Seismic reflection probing of the continents and their margins. *Tectonophysics*, 232, p. 119-132.

Beck, A.E. 1957. A steady state method for the rapid measurement of thermal conductivity of rocks. *Journal of Scientific Instruments*, 34, p. 186-189.

Beck, A.E., Anglin, F.M. and Sass, J.H. 1971. Analysis of heat flow data – in situ thermal conductivity measurements. *Canadian Journal of Earth Sciences*, 8, p. 1-19.

Belperio, A.P. 1995. (*compiler*) The Quaternary. *In*: Drexel, J.F. and Preiss, W.V. (*eds.*), The Geology of South Australia, Volume 2, The Phanerozoic. *South Australian Geological Survey*, *Bulletin*, 54, p. 219-280.

Benfield, A.E. 1939. Terrestrial heat flow in Great Britain. *Proceedings of the Royal Society of London*, 173, p. 428-450.

Benfield, A.E. 1947. A heat-flow value for a well in California. *American Journal of Science*, 245, p. 1-18.

Betts, P.G., Lister, G.S. and O'Dea, M.G. 1998. Asymmetric extension of the Middle Proterozoic lithosphere, Mount Isa terrane, Queensland, Australia. *Tectonophysics*, 296, p. 293-316.

Bickle, M.J. 1978. Heat loss from the Earth: Constraint on Archean tectonics from the relationships between geothermal gradients and the rate of plate production. *Earth and Planetary Science Letters*, 40, p. 301-315.

Birch, A.F. 1950. Flow of heat in the Front Range, Colorado. *Geological Society of America Bulletin*, 61, p. 567-630.

Birch, A.F. 1954. The present state of geothermal investigations. *Geophysics*, 19, p. 645-659.

Birch, F. and Clark, H. 1940. The thermal conductivity of rocks and its dependence upon temperature and composition. *American Journal of Science*, 238, p. 529-558.

Birch, A.F., Roy, R.F. and Decker, E.R. 1968. Heat flow and thermal history in New England and New York. *In*: White, W. and Zen, E. (*eds.*), *Studies of Appalachian Geology: Northern and Maritime*. Interscience, New York, USA, p. 437-451.

Black, P.R. and Braile, L.W. 1982. $P_n$ velocity and cooling of the continental lithosphere. *Journal of Geophysical Research*, 87, p. 10557-10568.

Blackwell, D.D. 1978. Heat flow and energy loss in the western US. *In*: Smith, R.B. and Eaton, G.P. (*eds.*), Cenozoic Tectonics and Regional Geophysics of the Western Cordillera. *Geological Society of America Memoir*, 152, p. 175-208.

Blackwell, D.D. and Steele, J.L. 1989. Thermal conductivity of sedimentary rocks; measurement and significance. *In*: Naeser, N.D. and McCulloh, T.H. (*eds.*), *Thermal history of sedimentary basins; methods and case histories*, p. 13-36.

Blake, D.H. 1987. Geology of the Mount Isa Inlier and environs, Queensland and Northern Territory. *Bureau of Mineral Resources Geology and Geophysics*, *Bulletin*, 225, pp. 83.

Blake, D.H. and Stewart, A.J. 1992. Stratigraphic and tectonic framework, Mount Isa Inlier. *In*: Stewart, A.J. and Blake, D.H. (*eds.*), Detailed Studies of the Mount Isa Inlier. *Australian Geological Survey Bulletin*, 243, p. 1-13.

Bodorkos, S., Oliver, N.H.S. and Cawood, P.A. 1999. The thermal evolution of the Halls Creek orogen, northern Australia. *Australian Journal of Earth Sciences*, 43, p. 453-465.

Brace, W.F. and Kohlstedt, D.L. 1980. Limits on lithospheric stress imposed by laboratory experiments. *Journal of Geophysical Research*, 85, 11, p. 6248-6252.

Brasier, M.D. and Lindsay, J.F. 1998. A billion years of environmental stability and the emergence of eukaryotes: New data from northern Australia. *Geology*, 26, p. 555-558.

Brigaud, F. and Vasseur, G. 1989. Mineralogy, porosity and fluid control on thermal conductivity of sedimentary rocks. *Geophysical Journal of the Royal Astronomical Society*, 98, p. 525-542.

Buick, R., De Marais, D.J. and Knoll, A.H. 1995. Stable isotope compositions of carbonates from the Mesoproterozoic Bangemall Group, northwestern Australia. *Chemical Geology*, 123, p. 153-171.

Bullard, E.C. 1939. Heat flow in South Africa. *Proceedings of the Royal Society of London*, 173, p. 474-502.

Burrett, C. and Berry, R. 2000. Proterozoic Australia-Western United States (AUSWUS) fit between Laurentia and Australia. *Geology*, 28, p. 103-106.

Byerlee, J.D. 1978. Friction in rocks. *Pure and Applied Geophysics*, 116, p. 615-626.

Callen, R.A. and Telford, R.H. 1976. New late Cainozoic rock units and depositional environments, Lake Frome area, South Australia. *Royal Society of South Australia Transactions*, 100, p. 125-167.

Campbell, I.H. and Jarvis, G.T. 1984. Mantle convection and early crustal evolution. *Precambrian Research*, 26, p. 15-56.

Carter, N.L. and Tsenn, M.C. 1987. Flow properties of continental lithosphere. *Tectonophysics*, 136, p. 27-63.

Cermak, V. and Rybach, L. 1989. Vertical distribution of heat production in the continental crust. *Tectonophysics*, 159, p. 217-230.

Chamberlain, C.P. and Sonder, L.J. 1990. Heat producing elements and the thermal and baric patterns of metamorphic belts. *Science*, 250, p. 763-769.

Chapman, D.S. and Furlong, K.P. 1977. Continental heat flow - age relationships. *Eos, Transactions of the American Geophysical Union*, 58, 12, p. 1240.

Chapman, D.S. and Pollack, H.N. 1975. Global heat flow; a new look. *Earth and Planetary Science Letters*, 28, p. 23-32.

Chardon, D., Choukroune, P. and Jayananda, M. 1998. Sinking of the Dharwar Basin (South India); implications for Archaean tectonics. *Precambrian Research*, 91, p. 15-39.

Chopra, P.N. and Paterson, M.S. 1981. The experimental deformation of dunite. *Tectonophysics*, 78, p. 453-473.

Chopra, P.N. and Paterson, M.S. 1984. The role of water in the deformation of dunite. *Journal of Geophysical Research*, 89, p. 7861-7876.

Choukroune, P., Chardon, D., Calvert, A.J. and Bouhallier, H. 1997. Archaean crustal growth and tectonic processes; a comparison of the Superior Province, Canada, and the Dharwar Craton, India. *In*: Burg, J.P. and Ford, M. (*eds.*), *Orogeny through Time. Geological Society of London Special Publications*, 121, p. 63-98.

Clark, S.P. 1966. Thermal conductivity. *In*: Clark, S.P. (*ed.*), Handbook of Physical constants (revised edition). *Geological Society of America Memoir*, 91, p. 459-482.

Coats, R.P., Horwitz, R.C., Crawford, A.R., Campana, B. and Thatcher, D. 1969. Mount Painter Province, 1:125 000 Geological Map, Geological Survey of South Australia.

Coblentz, D., Richardson, R.M. and Sandiford, M. 1994. On the gravitational potential of the Earth's lithosphere. *Tectonics*, 13, p. 929-945.

Collins, C.D.N. 1991. The nature of the crust-mantle boundary under Australia from seismic evidence. *Geological Society of Australia Special Publications*, 17, p. 67-80.

Collins, W.J. and Teyssier, C. 1989. Crustal scale ductile fault systems in the Arunta Inlier, central Australia. *Tectonophysics*, 158, p. 49-66.

Condie, K.C. 1986. Origin and early growth rate of continents. *Precambrian Research*, 11, p. 261-278.

Connors, K.A. and Page, R.W. 1995. Relationships between magmatism and deformation in the western Mount Isa Inlier, Australia. *Precambrian Research*, 71, p. 131-153.

Coster, H.P. 1947. Terrestrial heat flow in Persia. *Geophysical Journal of the Royal Astronomical Society*, 5, p. 131-145.

Cull, J.P. 1974. Thermal conductivity probes for rapid measurements in rock. *Journal of Physics E, Scientific Instruments*, 7, p. 1-4.

Cull, J.P. 1982. An appraisal of Australian heat-flow data. *Bureau of Mineral Resources Journal of Australian Geology and Geophysics*, 7, p. 11-21.

Cull, J.P. and Conley, D. 1983. Geothermal gradients and heat flow in Australian sedimentary basins. *Bureau of Mineral Resources Journal of Australian Geology and Geophysics*, 8, p. 329-337.

Cull, J.P. and Denham, D. 1979. Regional variations in Australian heat flow. *Bureau of Mineral Resources Journal of Australian Geology and Geophysics*, 4, p. 1-13.

Cull, J.P. and Sparksman, G.F. 1977. Measurements of surface heat flow. *Bureau of Mineral Resources Record*, 1977/39, pp. 17.

Dallmeyer, R.D. and Keppie, J.D. 1993. $^{40}Ar/^{39}Ar$ mineral ages from the southern Cape Breton Highlands and Creignish Hills, Cape Breton Island, Canada: Evidence for a polyphase tectonothermal evolution. *Journal of Geology*, 101, p. 467-482.

Dalrymple, G.B. and Lanphere, M.A. 1969. *Potassium-Argon dating: Principles, techniques and applications to geochronology*. Freeman and Company, San Francisco, USA, pp. 258.

Daly, R.A. 1947. The Vredefort ring-structure of South Africa. *Journal of Geology*, 69, p. 499-516.

Davies, G. 1980. Review of oceanic and global heat flow estimates. *Reviews of Geophysics*, 18, p. 718-722.

De Yoreo, J.J., Lux, D.L. and Guidotti, C.V. 1991. Thermal modelling in low-pressure/high temperature metamorphic belts. *Tectonophysics*, 188 p. 209-238.

Derrick, G.M., Wilson, I.H. and Sweet, I.P. 1980. The Quilalar and Surprise Creek formations: new Proterozoic units from the Mount Isa Inlier; their regional sedimentology and application to regional

correlation. *Bureau of Mineral Resources Journal of Australian Geology and Geophysics*, 5, p. 215-223.

Des Marais, D.J., Strauss, H., Summons, R.E. and Hayes, J.M. 1992. Carbon isotopic evidence for the stepwise oxidation of the Proterozoic environment. *Nature*, 359, p. 605-609.

Dodson, M.H. 1973. Closure temperature in cooling geochronological and petrological systems. *Contributions to Mineralogy and Petrology*, 40, p. 259-274.

Dodson, M.H. and McClelland-Brown, E. 1985. Isotopic and palaeomagnetic evidence for rates of cooling, uplift and erosion. *Geological Society of London Memoir*, 10, p. 315-325.

Dovenyi, P. and Horvath, F. 1988. A review of temperature, thermal conductivity and heat flow data for the Pannonian Basin. *In*: Royden, L.H. and Horvath, F. (*eds*.), The Pannonian Basin: a study in basin evolution. *American Association of Petroleum Geologists Memoir*, 45, p. 195-233.

Drummond, B.J. 1988. A review of crust / upper mantle structure in the Precambrian areas of Australia and implications for Precambrian crustal evolution. *Precambrian Research*, 40 / 41, p. 101-116.

Drummond, B. J., Goleby, B. R., Goncharov, A. G., Wyborn, L. A. I., Collins, C. D. N. and MacCready, T. 1998. Crustal-scale structures in the Proterozoic Mount Isa inlier of north Australia: Their seismic response and influence on mineralisation. *Tectonophysics*, 288, p. 43-56.

Dunlap, W.J. 2000. Natures diffusion experiment: The cooling-rate cooling-age correlation. *Geology*, 28, p. 139-142.

Dunlap, W.J. and Teyssier, C. 1995. Palaeozoic deformation and isotopic disturbance in the southeastern Arunta Block, central Australia. *Precambrian Research*, 71, p. 229-250.

Dunlap, W.J., Teyssier, C., McDougall, I. and Baldwin, S. 1995. Thermal and structural evolution of the intracratonic Arltunga Nappe Complex, Central Australia. *Tectonics*, 14, p. 1182-1204.

Durrance, E.M. 1986. *Radioactivity in geology: principles and applications*. Halstead Press, New York, USA, pp. 441.

Elburg, M.A., Bons, P.D., Dougherty-Page, J., Janka, C.E., Neumann, N.L. and Schaefer, B.F. Age and metasomatic alteration of the Mount Neill Granite at Nooldoonooldoona Waterhole, Mount Painter inlier, South Australia. Submitted to *Australian Journal of Earth Sciences*, December 2000.

Ellis, D.J. 1992. Precambrian tectonics and the physicochemical evolution of the continental crust: II, Lithosphere delamination and ensialic orogeny. *Precambrian Research*, 55, p. 507-524.

England, P.C. 1983. Constraints on extension of continental lithosphere. *Journal of Geophysical Research*, 88, p. 1145-1152.

England, P.C. 1987. Diffuse continental deformation; length scales, rates and metamorphic evolution. *Philosophical Transactions of the Royal Society of London*, 321, p. 3-22.

England, P.C. and Thompson, A.B. 1984. Pressure-Temperature-Time paths of regional metamorphism I. Heat transfer during the evolution of regions of thickened continental crust. *Journal of Petrology*, 25, p. 894-928.

England, P.C. and Thompson, A.B. 1986. Sone thermal and tectonic models for crustal melting in continental collision zones. *In*: Coward, M.P. and Ries, A.C. (*eds*.), Collision Tectonics. *Geological Society of London Special Publications*, 19, p. 83-94.

England, P.C., Oxburgh, E.R. and Richardson, S.W. 1980. Heat refraction and heat production in and around granite plutons in north-east England. *Geophysical Journal of the Royal Astronomical Society*, 62, p. 439-455.

Eriksson, K.A., Simpson, E.L. and Jackson, M.J. 1993. Stratigraphic evolution of a Proterozoic syn-rift to post-rift basin: constraints on the nature of lithospheric extension in the Mount Isa Inlier, Australia. *In*: Frostick L.E. and Steel R.J. (*eds*.), Tectonic controls and signatures in sedimentary successions. *International Association of Sedimentologists Special Publications*, 20, p. 203-221.

Etheridge M.A., Rutland R.W.R. and Wyborn L.A.I. 1987. Orogenesis and Tectonic process in the Early to Middle Proterozoic of Northern Australia. *In*: Kröner A. (*ed*.), Precambrian Lithospheric Evolution. *American Geophysical Union Geodynamic Series*, 17, p.131-147.

Foden, J., Sandiford, M., Dougherty-Page, J. and Williams, I. 1999. Geochemistry and geochronology of the Rathjen gneiss; implications for the early tectonic evolution of the Delamerian Orogen. *Australian Journal of Earth Sciences*, 46, p. 377-389.

Foster, D.A., Murphy, J.M. and Gleadow, A.J.W. 1994. Middle Tertiary hydrothermal activity and uplift of the northern Flinders Ranges, South Australia: Insights from apatite fission-track thermochronology. *Australian Journal of Earth Sciences*, 41, p. 11-17.

Fountain, D.M., Salisbury, M.H. and Furlong, K.P. 1987. Heat production and thermal conductivity of rocks from the Pikwitonei-Sachigo continental cross section, central Manitoba: Implications for the thermal structure of Archaean crust. *Canadian Journal of Earth Sciences*, 24, p. 1583-1594.

Fowler, C.M.R. 1990. *The solid earth: an introduction to global geophysics*. Cambridge University Press, New York, pp. 472.

Furlong, K.P, Spakman, W. and Wortel, R. 1995. Thermal structure of the continental lithosphere; constraints from seismic tomography. *Tectonophysics*, 244, p. 107-117.

Fyfe, W.S. 1973. The generation of batholiths. *Tectonophysics*, 17, p. 273-283.

Gallagher, K. 1987. Thermal conductivity of

sedimentary and basement rocks from the Eromanga and Cooper Basins, South Australia. *Exploration Geophysics*, 18, p. 381-392.

Gallagher, K. 1990. Some strategies for estimating present day heat flow from exploration wells, with examples. *Exploration Geophysics*, 21, p. 145-159.

Galson, D.A., Wilson, N.P., Scharli, U. and Rybach, L. 1987. A comparison of the divided-bar and QTM methods of measuring thermal conductivity. *Geothermics*, 16, p. 215-226.

Gatehouse, C.G. 1986. The geology of the Warburton Basin in South Australia. *Australian Journal of Earth Sciences*, 33, p. 161-180.

Gatehouse, C.G., Fanning, C.M. and Flint, R.B. 1995. Geochronology of the Big Lake Suite, Warburton Basin, northeastern South Australia. *Geological Survey of South Australia, Quarterly Geological Notes*, 128, p. 8-16.

Gee, R.D. 1979. Structure and tectonic style of the Western Australian shield. *Tectonophysics*, 58, p. 327-369.

Gerdes, A., Worner, G. and Henk, A. 2000. Post-collisional granite generation and HT-LP metamorphism by radiogenic heating: The Variscan South Bohemian Batholith. *Journal of the Geological Society of London*, 157, p. 57-587.

Gibson, H.J. and Stüwe, K. 2000. Multiphase cooling and exhumation of the southern Adelaide Fold Belt: constraints from apatite fission track data. *Basin Research*, 12, p. 31-45.

Goncharov, A.G., Collins, C.D.N, Goleby B.R., Drummond, B.J. and MacCready, T. 1996. The Mount Isa geodynamic transect, Implications of the seismic refraction model. *Australian Geological Survey Organization Research Newsletter*, 24, p. 9-10.

Goncharov, A.G., Lizinsky, M.D., Collins, C.D.N., Kalnin, K.A., Fomin, T.N., Drummond, B.J., Goleby, B.R. and Platonenkova, L.N. 1998. Intra-crustal 'seismic isostasy' in the Baltic Shield and Australian Precambrian cratons from deep seismic profiles and the Kola Superdeep bore hole data. *In*: Braun, J., Dooley, J.C., Goleby, B.R., Van der Hilst, R.D. and Klootwijk, C.T. (*eds.*), Structure and Evolution of the Australian Continent. *American Geophysical Union Geodynamic Series*, 26, p. 119-138.

Goodwin, A.M. 1981. Archaean plates and greenstone belts. *In*: Kröner, A. (*ed.*), *Precambrian Plate Tectonics.* Elsevier Scientific Publishing, Amsterdam, Netherlands, p. 105-135.

Gorter, J.D. 1984. Source potential of the Horn Valley Siltstone, Amadeus Basin. *Australian Petroleum Exploration Association Journal*, 24, p. 66-90.

Gravestock, D.I. 1995. (*compiler*) The early and middle Palaeozoic. *In*: Drexel, J.F. and Preiss, W.V. (*eds.*), The Geology of South Australia, Volume 2, The Phanerozoic. *South Australian Geological Survey, Bulletin*, 54, p. 3-61.

Griffiths, C.M., Brereton, N.R., Beausillon, R. and Castillo, D. 1992. Thermal conductivity prediction from petrophysical data: a case study. *In*: Hurst, A., Griffiths, C.M. and Worthington, P.F. (*eds.*), *Geological Applications of Wireline Logs II. Geological Society of London Special Publications*, 65, p 299-315.

Haenel, R., Rybach, L. and Stegena, L. 1988. (*eds.*) *Handbook of terrestrial heat-flow density determination; with guidelines and recommendations of the International Heat Flow Commission*. Kluwer academic publishers, Dordrecht, Netherlands, pp. 486.

Hames, W.E. and Bowring, S.A. 1994. An empirical evaluation of the argon diffusion geometry in muscovite. *Earth and Planetary Science Letters*, 124, p. 161-169.

Hamilton, W.B. 1998. Archean magmatism and deformation were not products of plate tectonics. *Precambrian Research*, 91, p. 143-179.

Hancock, S.L. and Rutland, R.W.R. 1984. Tectonics of an early Proterozoic geosuture; the Halls Creek orogenic subprovince, northern Australia. *In*: Kröner, A. and Zwart, H.J. (*eds.*), Precambrian crustal evolution. *Journal of Geodynamics*, 1, p. 387-432.

Hand, M., Slater, K., McLaren, S.N. and Sandiford, M. 1999. Heat production rates in Australian Proterozoic terranes. *Geological Society of Australia, Abstracts*, 54, p. 35.

Hansen, F.D. and Carter, N.L. 1983. Semibrittle creep of dry and wet Westerly granite at 1000 MPa. *United States Symposium on Rock Mechanics*, 24th, Texas A & M University, College Station, Texas, p. 429-447.

Hargraves, R.B. 1981. Precambrian tectonic style: A liberal uniformitarian interpretation. *In*: Kröner, A. (*ed.*), *Precambrian Plate Tectonics*. Elsevier Scientific Publishing, Amsterdam, Netherlands, p. 21-56.

Harrison, T.M. 1981. Diffusion of $^{40}$Ar in hornblende. *Contributions to Mineralogy and Petrology*, 78, p. 324-331.

Harrison, T.M., Duncan, I. and McDougall, I. 1985. Diffusion of $^{40}$Ar in biotite; temperature, pressure and compositional effects. *Geochimica et Cosmochimica Acta*, 49, p. 2461-2468.

Harrison, T.M., Heizler, M.T. and Lovera, O.M. 1993. In vacuo crushing experiments and K-feldspar thermochronometry. *Earth and Planetary Science Letters*, 117, p. 169-180.

Hart, R.J., Nicolaysen, L.O. and Gale, N.H. 1981. Radioelement concentrations in the deep profile through Precambrian basement of the Vredefort Structure. *Journal of Geophysical Research*, 86, 11, p. 10639-10652.

Hartley, M. J., Foster, D. A. and Gray, D. R. 1998. The Significance of younger thermal events in the Willyama Inliers: Using $^{40}$Ar/$^{39}$Ar Thermochronology. *Geological Society of Australia, Abstracts*, 52, p. 19-20.

Hayes, J.M. 1983. Geochemical evidence bearing on

the origin of aerobiosis: a speculative hypothesis. *In*: Schopf, J.W. (*ed.*), *Earth's earliest biosphere: Its origins and evolution*. Princeton University Press, Princeton, New Jersey, USA. p. 291-301.

Hawkesworth, C.J. 1974. Vertical distribution of heat production in the basement of the Eastern Alps. *Nature*, 249, p. 435-436.

Hodges, K.V., Hames, W.E. and Bowring, S.A. 1994. $^{40}Ar/^{39}Ar$ age gradients in micas from a high-temperature-low-pressure metamorphic terrain, evidence for very slow cooling and implications for the interpretation of age spectra. *Geology*, 22, p. 55-58.

Hoffman, P.F. 1980. Wopmay Orogen: A Wilson cycle of early Proterozoic age in the northwest of the Canadian Shield. *In*: Strangway, D.W. (*ed.*), The continental crust and its mineral deposits. *Geological Association of Canada Special Papers*, 20, p. 523-549.

Hoffman, P.F. 1989. Speculations on Laurentia's first gigayear (2.0 to 1.0 Ga). *Geology*, 17, p. 135-138.

Hoffman, P.F. 1991. Did the breakout of Laurentia turn Gondwanaland inside-out? *Science*, 252, p. 1409-1412.

Hoffman, P.F. and Bowring, S.A. 1984. Short-lived 1.9 Ga continental margin and its destruction, Wopmay orogen, northwest Canada. *Geology*, 12, p. 68-72.

Holser, W.T. 1997. Geochemical events documented in inorganic carbon isotopes. *Palaeogeography, Palaeoclimatology and Palaeoecology*, 132, p. 173-182.

Horai, K. and Shankland, T.J. 1987. Thermal conductivity of rocks and minerals. *Methods of Experimental Physics*, 24, p. 271-302.

Houseman, G.A., McKenzie, D.P. and Molnar, P. 1981. Convective instability of a thickened boundary layer and its relevance for the thermal evolution of continental convergent belts. *Journal of Geophysical Research*, 86, p. 6115-6132.

Houseman, G.A., Cull, J.P., Muir, P.M. and Paterson, H.L. 1989. Geothermal signatures and uranium ore deposits on the Stuart Shelf of South Australia. *Geophysics*, 54, p. 158-170.

Howard, L.E. and Sass, J.H. 1964. Terrestrial heat flow in Australia. *Journal of Geophysical Research*, 69, p. 1617-1626.

Huerta, A.D., Royden, L.H. and Hodges, K.V. 1998. The thermal structure of collisional orogens as a response to accretion, erosion and radiogenic heating. *Journal of Geophysical Research*, 103, p. 15287-15302.

Huerta, A.D., Royden, L.H. and Hodges, K.V. 1999. The effects of accretion, erosion and radiogenic on the metamorphic evolution of collisional orogens. *Journal of Metamorphic Geology*, 17, p. 349-366.

Hyndman, R.D. 1967. Heat flow in Queensland and Northern Territory, Australia. *Journal of Geophysical Research*, 72, p. 527-537.

Hyndman, R.D. and Lewis, T.J. 1999. Geophysical consequences of the Cordillera-Craton thermal transition in southwestern Canada. *Tectonophysics*, 306, p. 397-422.

Hyndman, R.D. and Sass, J.H. 1966. Geothermal measurements at Mount Isa, Queensland. *Journal of Geophysical Research*, 71, p. 587-601.

Idnurm, M. and Heinrich, C.A. 1993. A palaeomagnetic study of hydrothermal activity and uranium mineralization at Mount Painter, South Australia. *Australian Journal of Earth Sciences*, 40, p. 87-101.

Jackson, S.L., Fyon, J.A. and Corfu, F. 1994. Review of Archean supracrustal assemblages of the southern Abitibi greenstone belt in Ontario, Canada; products of microplate interaction within a large-scale plate-tectonic setting. *Precambrian Research*, 65, p. 183-205.

Jaupart, C. 1983. Horizontal heat transfer due to radioactivity contrasts: causes and consequences of the linear heat flow relation. *Geophysical Journal of the Royal Astronomical Society*, 75, p. 411-435.

Jaupart, C. and Mareschal, J.C. 1999. The thermal structure and thickness of continental roots. *Lithos*, 48, p. 93-114.

Jenkins, R.J.F. and Sandiford, M. 1992. Observations on the tectonic evolution of the southern Adelaide fold belt. *Tectonophysics*, 214, p. 27-36.

Johnson, G.I. 1980. The geology of the Mount Babbage inlier, northern Mount Painter province, South Australia – a petrological, geochemical and geochronological study. B.Sc (Hons) thesis (unpublished), University of Adelaide, Australia, pp. 23

Kalsbeek, F. 1995. Geochemistry, tectonic setting, and poly-orogenic history of Palaeoproterozoic basement rocks from the Caledonian fold belt of North-East Greenland. *Precambrian Research*, 72, p. 301-315.

Kamo, S.L., Reimold, W.U., Krogh, T.E. and Colliston, W.P. 1996. A 2.023 Ga age for the Vredefort impact event and a first report of shock metamorphosed zircons in pseudotachylitic breccias and granophyre. *Earth and Planetary Science Letters*, 144, p. 369-387.

Karhu, J.A. and Holland, H.D. 1996. Carbon isotopes and the rise of atmospheric oxygen. *Geology*, 24, p. 867-870.

Karlstrom, K.E. and Williams, M.J. 1995. A case for simultaneous deformation, metamorphism and plutonism: An example from Proterozoic rocks in central Arizona. *Journal of Structural Geology*, 17, p. 59-81.

Kennett, B.L.N. and Van der Hilst, R.D. 1996. Using a synthetic continental array in Australia to study the Earth's interior. *Journal of Physics of the Earth*, 44, p. 669-674.

Kerr, R.A. 1978. Precambrian tectonics: Is the present the key to the past? *Science*, 199, p. 505-522.

Ketcham, R.A. 1996. The distribution of heat-

producing elements in the upper mantle and middle crust of southern and western central Arizona, evidence from the core complexes. *Journal of Geophysical Research*, 101, p. 13611-13632.

Kirby, S.H. and Kronenberg, A.K. 1987. Rheology of the lithosphere; selected topics. *Reviews of Geophysics*, 25, p. 1219-1244.

Kitts, D.B. 1963. The theory of geology. *In*: Albritton C.G. (*ed.*), *The Fabric of Geology.* Addison Wesley, Reading, Massachusetts, USA, p. 49-68.

Knoll, A.H., Kaufman, A.J. and Semikhatov, M.A. 1995. The carbon-isotopic composition of Proterozoic carbonates: Riphean successions from north-western Siberia (Anabar Massif, Turukhansk Uplift). *American Journal of Science*, 295, p. 823-850.

Korsch, R.J. and Kennard, L.M. 1991. (*eds.*) Geological and geophysical studies in the Amadeus Basin, central Australia. *Bureau of Mineral Resources Geology and Geophysics Bulletin*, 236, pp. 594.

Koyaguchi, T. and Kaneko, K. 1999. A two-stage thermal evolution model of magmas in continental crust. *Journal of Petrology*, 40, p. 241-254.

Kröner, A. 1977. Precambrian mobile belts of southern and eastern Africa – ancient sutures or sites of ensialic mobility? A case for crustal evolution towards plate tectonics. *Tectonophysics*, 40, p. 101-135.

Kröner, A. 1984. Evolution, growth and stabilization of the Precambrian lithosphere. *Physics and Chemistry of the Earth*, 15, p. 69-106.

Kröner, A. 1991. Tectonic evolution in the Archaean and Proterozoic. *Tectonophysics*, 187, p. 393-410.

Lachenbruch, A.H. 1957. A probe for measurement of thermal conductivity of frozen soils in place. *Transactions of the American Geophysical Union*, 38, p. 691-697.

Lachenbruch, A.H. 1968. Preliminary geothermal model of the Sierra Nevada. *Journal of Geophysical Research*, 73, p. 6977-6989.

Lachenbruch, A.H. 1970. Crustal temperature and heat production: implications of the linear heat-flow relation. *Journal of Geophysical Research*, 75, p. 3291-3300.

Lachenbruch, A.H. and Bunker, C.M. 1971. Vertical gradients of heat production in the continental crust, 2: some estimates from borehole data. *Journal of Geophysical Research*, 76, p. 3852-3860.

Lachenbruch, A.H., Sass, J.H. and Morgan, P. 1994. Thermal regime of the southern Basin and Range Province: 2. Implications of heat flow for regional extension and metamorphic core complexes. *Journal of Geophysical Research*, 99, p. 22121-22133.

Lambert, I.B. and Heier, K.S. 1967. The vertical distribution of uranium, thorium and potassium in the continental crust. *Geochimica et Cosmochimica Acta*, 31, p. 377-390.

Lambert, I.B. and Heier, K.S. 1968. Geochemical investigations of deep-seated rocks in the Australian shield. *Lithos*, 1, p. 30-53.

Lathrop, A.S., Blum, J.D. and Chamberlain, C.P. 1994. Isotopic evidence for closed-system anatexis at midcrustal levels: An example from the Acadian Appalachians of New England. *Journal of Geophysical Research*, 99, p. 9453-9468.

Lenardic, A. and Moresi, L.-N. 1999. Some thoughts on the stability of cratonic lithosphere: Effects of buoyancy and viscosity. *Journal of Geophysical Research*, 104, p. 12747-12758.

Lerche, I. 1991. Temperature dependence of thermal conductivity and its impact on assessments of heat flux. *Pure and Applied Geophysics*, 136, p. 191-200.

Lewis, T.J. and Hyndman, R.D. 1999. High heat flow along the SNORCLE transect. *In*: Cook, F. and Erdmer, P. (*compilers*). Slave-Northern Cordillera Lithospheric Evolution (SNORCLE) Transect and Cordilleran Tectonics Workshop Meeting, University of Calgary, *Lithoprobe Report*, 69, p. 83-84.

Li, Z.X., Powell, C.McA. and Schmidt, P.W. 1989. Syn-deformational remanent magnetization of the Mount Eclipse Sandstone, Central Australia. *Geophysical Journal International*, 99, p. 205-222.

Lilley, F.E.M., Sloane, M.N. and Sass, J.H. 1978. A compilation of Australian heat flow measurements. *Journal of the Geological Society of Australia*, 24, p. 439-445.

Lindsay, J.F. and Brasier, M.D. 2000. A carbon isotope reference curve for *ca.* 1700-1575 Ma McArthur and Mount Isa Basins, Northern Australia. *Precambrian Research*, 99, p. 271-308.

Lister, G.S. and Baldwin, S.L. 1996. Modelling the effect of arbitrary P-T-t histories on argon diffusion in minerals using the MacArgon program for the Apple Macintosh. *Tectonophysics*, 253, p. 83-109.

Liu, L. and Zoback, M.D. 1997. Lithospheric strength and intraplate seismicity in the New Madrid seismic zone. *Tectonics*, 16, p. 585-595.

Loosveld, R.J.H. and Etheridge, M.A. 1990. A model for low-pressure facies metamorphism during crustal thickening. *Journal of Metamorphic Geology*, 8, p. 257-267.

Lovera, O.M., Richter, F.M. and Harrison, T.M. 1989. The $^{40}Ar/^{39}Ar$ thermochronometry for slowly cooled samples having a distribution of diffusion domain sizes. *Journal of Geophysical Research*, 94, p. 17917-17935.

Lovera, O.M., Grove, M., Harrison, T.M. and Mahon, K.I. 1997. Systematic analysis of K-feldspar $^{40}Ar/^{39}Ar$ step heating results: I, Significance of activation energy determinations. *Geochimica et Cosmochimica Acta*, 61, p. 3171-3192.

Majorowicz, J.A. 1996. Anomalous heat flow regime in the western margin of the North American craton. *Journal of Geodynamics*, 21, p. 123-140.

Martin, H. 1986. Effect of steeper Archean geothermal gradient on geochemistry of subduction-zone

magmas. *Geology*, 14, p. 753-756.

McCready, T. 1997. Geologic interpretation of the Mount Isa Deep Seismic Transect. PhD thesis (unpublished), Monash University, Australia, pp. 322.

McCulloch, M.T. 1987. Sm-Nd isotopic constraints on the evolution of Precambrian crust in the Australian continent. *American Geophysical Union Geodynamic Series*, 17, p. 115-130.

McDougall, I. and Harrison, T.M. 1999. *Geochronology and thermochronology by the $^{40}Ar/^{39}Ar$ method*, 2nd edition. Oxford University Press, New York, pp. 269.

McDougall, I. and Roksandic, Z. 1974. Total fusion $^{40}Ar/^{39}Ar$ ages using HIFAR reactor. *Journal of the Geological Society of Australia*, 21, p. 81-89.

McDougall, I. and Schmincke, H.U. 1977. Geochronology of Gran Canaria, Canary Islands; age of shield building volcanism and other magmatic phases. *Bulletin of Volcanology*, 40, p. 57-77.

McKenzie, D. 1989. Some remarks on the movement of small melt fractions in the mantle. *Earth and Planetary Science Letters*, 95, p. 53-72.

McLaren, S.N. and Sandiford, M. (in press) Long-term thermal consequences of tectonic activity at Mount Isa, Australia: Implications for polyphase tectonism in the Proterozoic. In: Miller, J.A., Buick, I.S., Hand, M. and Holdsworth, R.E. (*eds*), *Continental Reworking and Reactivation, Geological Society of London Special Publications*.

McLaren, S.N., Sandiford, M. and Hand, M. 1999. High radiogenic heat-producing granites and metamorphism – An example from the Mount Isa Inlier, Australia. *Geology*, 27, p. 679-682.

McLennan, S.M. and Taylor, S.R. 1996. Heat flow and the chemical composition of continental crust. *Journal of Geology*, 104, p. 369-377.

Middleton, M.F. 1993. A transient method of measuring the thermal properties of rocks. *Geophysics*, 58, p. 357-365.

Mildren, S. and Sandiford, M. 1995. A heat refraction mechanism for low-P metamorphism in the northern Flinders Ranges, South Australia. *Australian Journal of Earth Sciences*, 42, p. 241-247.

Mints, M.V. 1999. Lithospheric state parameters and plate tectonics in the Archean. *Geotectonics*, 33, p. 462-473.

Mitchell, M.M., Kohn, B.P. and Foster, D.A. 1998. Post-orogenic cooling history of eastern South Australia from apatite fission track thermochronology. *In*: Van den haute, P. and De Corte, F. (*eds.*), *Advances in Fission-track Geochronology*, p. 207-224.

Molnar, P. 1992. Brace-Goetze strength profiles; The partitioning of strike-slip and thrust faulting at zones of oblique convergence, and the stress-heat flow paradox of the San Andreas Fault. *In*: Evans, B. and Wong, T. (*eds.*), *Fault Mechanics and Transport Properties of Rocks*, p. 435-459.

Morgan, P. 1984. The thermal structure and thermal evolution of the continental lithosphere. *In*: Pollack, H.N. and Murthy, V.R. (*eds.*), Structure and evolution of the continental lithosphere. *Physics and Chemistry of the Earth*, 15, p. 107-185.

Myers, J.S. 1990. Precambrian tectonic evolution of part of Gondwana, southwestern Australia. *Geology*, 18, p. 537-540.

Myers, J.S., Shaw, R.D. and Tyler, I.M. 1996. Tectonic evolution of Proterozoic Australia. *Tectonics*, 15, p. 1431-1446.

Neil, E.A. and Houseman, G.A. 1997. Geodynamics of the Tarim Basin and the Tian Shan in central Asia. *Tectonics*, 16, p. 571-584.

Neil, E.A. and Houseman, G.A. 1999. Rayleigh-Taylor instability of the upper mantle and its role in intraplate orogeny. *Geophysical Journal International*, 138, p. 89-107.

Neumann, N.L. 1996. Isotopic and geochemical characteristics of the British Empire Granite as indicators of magma provenance and processes of melt generation in the Mount Painter Inlier, South Australia. B.Sc (Hons) thesis (unpublished), The University of Adelaide, Australia, pp. 38.

Neumann, N.L. 2001. Geochemical and isotopic characteristics of South Australian Proterozoic granites: Implications for the origin and evolution of high heat producing terranes. PhD thesis (unpublished), The University of Adelaide, Australia.

Neumann, N.L., Sandiford, M. and Foden, J. 2000. Regional geochemistry and continental heat flow: Implications for the origin of the South Australian heat flow anomaly. *Earth and Planetary Science Letters*, 183, p. 107-120.

Newmark, R.L., Kasameyer, P.W. and Younker, L.W. 1988. Shallow drilling in the Salton Sea region: The thermal anomaly. *Journal of Geophysical Research*, 93, p. 13005-13024.

Newstead, G. and Beck, A. 1953. Borehole temperature measuring equipment and the geothermal flux in Tasmania. *Australian Journal of Physics*, 6, p. 480-489.

Nicolaysen, L.O., Hart, R.J. and Gale, N.H. 1981. The Vredefort radioelement profile extended to supracrustal strata at Carletonville, with implications for continental heat flow. *Journal of Geophysical Research*, 86, 11, p. 10653-10661.

Nironen, M. 1997. The Svecofennian Orogen; a tectonic model. *Precambrian Research*, 86, p. 21-44.

Nisbet, E.G. and Fowler, C.M.R. 1983. Model for Archean plate tectonics. *Geology*, 11, p. 376-379.

Nyblade, A.A. and Pollack, H.N. 1993. A global analysis of heat flow from Precambrian terrains: Implications for the thermal structure of Archaean and Proterozoic lithosphere. *Journal of Geophysical Research*, 98, p. 12207-12218.

O'Dea, M.G., Lister, G.S., Betts, P.G. and Pound, K.S. 1997a. A shortened intraplate rift system in the Proterozoic Mount Isa terrane, northwest Queensland, Australia. *Tectonics*, 16, p. 425-441.

O'Dea, M.G., Lister, G.S., MacCready, T., Betts, P.G., Oliver, N.H.S., Pound, K.S., Huang, W. and Valenta, R.K. 1997b. Geodynamic evolution of the Proterozoic Mount Isa terrain. *In*: Burg, J.P. and Ford, M. (*eds.*), Orogeny through Time. *Geological Society of London Special Publications*, 121, p. 99-122.

O'Halloran, G. 1992. The evolution of provenance and depositional processes during early Adelaidean sedimentation: a sedimentological and Nd isotopic investigation. B.Sc (Hons) thesis (unpublished), The University of Adelaide, Australia, pp. 55.

O'Reilly, S.Y. and Griffin, W.L. 1985. A xenolith-derived geotherm for southeastern Australia and its geophysical implications. *Tectonophysics*, 111, p. 41-64.

O'Sullivan, P.B., Kohn, B.P. and Mitchell, M.M. 1998. Phanerozoic reactivation along a fundamental Proterozoic crustal fault, the Darling River Lineament, Australia; constraints from apatite fission track thermochronology. *Earth and Planetary Science Letters*, 164, p. 451-465.

Oxburgh, E.R. 1980. Heat flow and magma genesis. *In*: Hargraves, R.B. (*ed.*), *Physics of magmatic processes*. Princeton University Press, Princeton, New Jersey, USA, p. 161-200.

Page, R.W. 1983. Chronology of magmatism, skarn formation and uranium mineralization, Mary Kathleen, Queensland, Australia. *Economic Geology*, 78, p. 838-853.

Page, R.W. and Sun, S-s. 1998. Aspects of geochronology and crustal evolution in the Eastern Fold Belt, Mount Isa Inlier. *Australian Journal of Earth Sciences*, 45, p. 343-361.

Page, R.W. and Sweet, I.P. 1998. Geochronology of basin phases in the western Mount Isa Inlier, and correlation with the McArthur Basin. *Australian Journal of Earth Sciences*, 45, p. 219-232.

Page, R.W. and Williams, I.S. 1988. Age of the Barramundi Orogeny in northern Australia by means of ion microprobe and conventional U-Pb zircon studies. *Precambrian Research*, 40 / 41, p. 21-36.

Page, R.W., Sun, S-s. and Carr, G. 1994. Proterozoic sediment-hosted lead-zinc-silver deposits in northern Australia – U-Pb zircon and Pb isotopic studies (abstract). *Australian Journal of Earth Sciences*, 37, p. 334-335.

Parker, A.J. 1993. Geological Framework. *In*: Drexel, J.F., Preiss, W.V. and Parker, A.J. (*eds.*), The Geology of South Australia, Volume 1, The Precambrian. *South Australian Geological Survey, Bulletin*, 54, p. 9-31.

Paterson, M.S. 1987. Problems in the extrapolation of laboratory rheological data. *Tectonophysics*, 133, p. 33-43.

Paul, E.G. 1998. The geometry and controls on basement-involved deformation in the Adelaide Fold Belt, South Australia. PhD thesis (unpublished), The University of Adelaide, Australia, pp. 228.

Paul, E.G., Flöttmann, T. and Sandiford, M. 1999. Structural geometry and controls on basement-involved deformation in the northern Flinders Ranges, Adelaide fold belt, South Australia. *Australian Journal of Earth Sciences*, 46, p. 343-354.

Pearson, P.J., Holcombe, R.J. and Page, R.W. 1992. Syn-kinematic emplacement of the Middle Proterozoic Wonga Batholith into a mid-crustal extensional shear zone, Mount Isa Inlier, Queensland, Australia. *In*: Stewart, A.J. and Blake, D.H. (*eds.*), Detailed Studies of the Mount Isa Inlier. *Australian Geological Survey Bulletin*, 243, p. 289-238.

Periera, E.B., Hamza, V.M., Furtado, V. and Adams, J.A.S. 1986. U, Th and K content, heat production and thermal conductivity of Sao Paulo, Brazil, continental shelf sediments: a reconnaissance work. *Chemical Geology*, 58, p. 217-226.

Perkins, C., Heinrich, C. A. and Wyborn, L. A. I. 1999. $^{40}Ar/^{39}Ar$ geochronology of Cu mineralization and regional alteration, Mount Isa, Australia. *Economic Geology*, 94, p. 23-35.

Pinet, C. and Jaupart, C. 1987. The vertical distribution of radiogenic heat production in the Precambrian crust of Norway and Sweden; geothermal implications. *Geophysical Research Letters*, 14, p. 260-263.

Pollack, H.N. 1986. Cratonization and thermal evolution of the mantle. *Earth and Planetary Science Letters*, 80, p. 175-182.

Pollack, H.N., Hurter, S.J. and Johnson, J.R. 1993. Heat flow from the Earth's interior: Analysis of the global data set. *Reviews of Geophysics*, 31, p. 267-280.

Powell, C.McA. 2000. 2000 Mawson Lecture: The search for supercontinents. *In*: Skilbeck, C.G. and Hubble, T.C.T. (*eds.*), Understanding Planet Earth: Searching for a sustainable future. Abstracts of the 15th Australian Geological Convention, University of Technology, Sydney, NSW, Australia. July 3-7. *Geological Society of Australia, Abstracts*, 59, p. 398.

Preiss, W.V. 1987. (*compiler*) The Adelaide Geosyncline: late Proterozoic stratigraphy, sedimentation, palaeontology and tectonics. *Geological Survey of South Australia, Bulletin*, 53, pp. 438.

Preiss, W.V. 1993. The Neoproterozoic. *In*: Drexel, J.F., Preiss, W.V. and Parker, A.J. (*eds.*) The Geology of South Australia, Volume 1, The Precambrian. *South Australian Geological Survey, Bulletin*, 54, p. 171-196.

Preiss, W.V. 2000. The Adelaide Geosyncline of South Australia and its significance in Neoproterozoic continental reconstruction. *Precambrian Research*, 100, p. 21-63.

Ratcliffe, E.H. 1959. Thermal conductivities of fused and crystalline quartz. *British Journal of Applied Physics*, 10, p. 22-25.

Ratcliffe, E.H. 1960. The thermal conductivities of ocean sediments. *Journal of Geophysical Research*, 65, p. 1535-1541.

Reinhardt, J. 1992. Proterozoic low-pressure / high-temperature metamorphism and anti-clockwise P-T-t paths for the Hazeldene area, Mount Isa Inlier, Queensland, Australia. *Journal of Metamorphic Geology*, 10, p. 333-346.

Renne, P.R., Swisher, C.C., Deino, A.L., Karner, D.B., Owens, T.L. and DePaolo, D.J. 1998. Intercalibration of standards, absolute ages and uncertainties in $^{40}Ar/^{39}Ar$ dating. *Chemical Geology*, 145, p. 117-152.

Richardson, S. W. and Oxburgh, E.R. 1978. Heat flow, radiogenic heat production and crustal temperatures in England and Wales. *Journal of the Geological Society of London*, 135, p. 323-337.

Richter, F.M., Lovera, O.M., Harrison, T.M. and Copeland, P. 1991. Tibetan tectonics from $^{40}Ar/^{39}Ar$ analysis of a single K-feldspar sample. *Earth and Planetary Science Letters*, 105, p. 266-278.

Robbins, G.A. 1972. Radiogenic argon diffusion in muscovite under hydrothermal conditions. M.Sc. thesis (unpublished), Brown University, Providence, USA.

Roy, R.F., Blackwell, D.D. and Birch, F. 1968. Heat generation of plutonic rocks and continental heat flow provinces. *Earth and Planetary Science Letters*, 5, p. 1-12.

Rubenach, M.J. 1992. Proterozoic low-pressure / high-temperature metamorphism and anti-clockwise P-T-t paths for the Hazeldene area, Mount Isa Inlier, Queensland, Australia. *Journal of Metamorphic Geology*, 10, p. 333-346.

Rutherford, E. and Soddy, F. 1903. Radioactive change. *Philosophical Magazine, Series 6*, 5, p. 576-591.

Rutland, R.W.R. 1973. Tectonic evolution of the continental crust in Australia. *In*: Tarling, D.H. and Runcorn, S.K. (*eds.*), *Continental drift, sea floor spreading and plate tectonics: Implications for the Earth Sciences*. Academic Press, San Diego, USA, p. 1003-1025.

Rutland, R.W.R. 1976. Orogenic evolution of Australia. *Earth Science Reviews*, 12, p. 161-196.

Saltus, R.W. and Thompson, G.A. 1995. Why is it downhill from Tonopah to Las Vegas? A case for mantle plume support of the high northern Basin and Range. *Tectonics*, 14, p. 1235-1244.

Sandiford, M. 1999. Mechanics of Basin Inversion. *Tectonophysics*, 305, p. 109-120.

Sandiford, M. and Hand, M. 1998a. Australian Proterozoic high-temperature, low-pressure metamorphism in the conductive limit. In: Treloar, P.J. and O'Brien, P.J. (*eds*), *What drives metamorphism and metamorphic reactions?, Geological Society of London Special Publications*, 138, p. 109-120.

Sandiford, M. and Hand, M. 1998b. Controls on the locus of Phanerozoic intraplate deformation in central Australia. *Earth and Planetary Science Letters*, 162, p. 97-110.

Sandiford, M. and McLaren, S.N. (in press) Thermo-mechanical controls on heat production distributions and the long-term evolution of the continents. *In*: Brown, M. and Rushmer, T. (*eds.*), *Evolution and differentiation of the continental crust*. Cambridge University Press, California, USA.

Sandiford, M. and Powell, R. 1991. Some remarks on high-T / low-P metamorphism in convergent orogens. *Journal of Metamorphic Geology*, 9, p. 333-340.

Sandiford, M., Hand, M. and McLaren, S.N. 1998a. High geothermal gradient metamorphism during thermal subsidence. *Earth and Planetary Science Letters*, 163, p. 149-165.

Sandiford, M., Paul, E.G. and Flöttmann, T. 1998b. Sedimentary thickness variations and deformation intensity during basin inversion in the Flinders Ranges, South Australia. *Journal of Structural Geology*, 20, p. 1721-1731.

Sandiford, M., Hand, M. and McLaren, S.N. (in press) Tectonic feedback, intraplate orogeny and the geochemical structure of the crust: a central Australian perspective. *In*: Miller, J.A., Buick, I.S., Hand, M. and Holdsworth, R.E. (*eds.*), *Continental Reworking and Reactivation, Geological Society of London Special Publications*.

Sass, J.H. 1964. Heat flow values from eastern Australia. *Journal of Geophysical Research*, 69, p. 3889-3893.

Sass, J.H. and Lachenbruch, A.H. 1979. Thermal regime of the Australian continental crust. *In*: McElhinny, M.W. (*ed.*), *The Earth – its origin, structure and evolution*. Academic Press, London, UK, p. 301-351.

Sass, J.H. and Le Marne, A.E. 1963. Heat flow at Broken Hill, New South Wales. *Geophysical Journal of the Royal Astronomical Society*, 7, p. 477-489.

Sass, J.H., Jaeger, J.C. and Munroe, R.J. 1976. Heat flow and near surface radioactivity in the Australian continental crust. *United States Geological Survey, Open File Report*, 76-250.

Sass, J.H., Stone, C. and Munroe, R.J. 1984. Thermal conductivity determinations on solid rock – A comparison between a steady-state divided-bar apparatus and a commercial transient line-source device. *Journal of Volcanology and Geothermal Research*, 20, p. 145-153.

Sass, J.H., Lachenbruch, A.H., Galanis, S.P., Morgan, P., Preist, S.S., Moses, T.H. and Munroe, R.J. 1994. Thermal regime of the southern Basin and Range Province: 1. Heat flow data from Arizona and the Mojave Desert of California and Nevada. *Journal of Geophysical Research*, 99, p. 22093, 22119.

Schaefer, B.F. 1993. Isotopic and geochemical

constraints on Proterozoic crustal growth from the Mount Painter Inlier, B.Sc (Hons) thesis (unpublished), The University of Adelaide, Australia, pp. 29.

Scharli, U. and Rybach, L. 1984. On the thermal conductivity of low-porosity crystalline rocks. *Tectonophysics*, 103, p. 307-313.

Schneider, R.V., Roy, R.F. and Smith, A.R. 1987. Investigations and interpretations of the vertical distribution of U, Th and K; South Africa and Canada. *Geophysical Research Letters*, 14, p. 264-267.

Schopf, J.W. and Klein, C., 1992. (*eds.*). *The Proterozoic biosphere – A multi-disciplinary study.* Cambridge University Press, Cambridge, United Kingdom, pp. 1348.

Sclater, J.G., Jaupart, C. and Galson, D. 1980. The heat flow through oceanic and continental crust and the heat loss of the Earth. *Reviews of Geophysics and Space Physics*, 18, p. 269-311.

Scott, D.L., Bradshaw, B.B. and Tarlowski, C.T. 1999. The tectonostratigraphic history of the northern Lawn Hill Platform, Australia: An integrated intracontinental basin analysis. *Tectonophysics*, 300, p. 329-358.

Scrimgeour, I. and Close, D. 1999. Regional high-pressure metamorphism during intracratonic deformation; the Petermann Orogeny, central Australia. *Journal of Metamorphic Geology*, 17, p. 557-572.

Sekiguchi, K. 1984. A method for determining terrestrial heat flow in oil basin areas. *Tectonophysics*, 103, p. 67-79.

Shaw, H.R. 1970. Earth tides, global heat flow and tectonics. *Science*, 168, p. 1084-1087.

Shaw, R.D., Zeitler, P.K., McDougall, I. and Tingate, P.R. 1992. The Palaeozoic history of an unusual intracratonic thrust belt in central Australia based on $^{40}Ar/^{39}Ar$, K/Ar and fission track dating. *Journal of the Geological Society of London*, 149, p. 937-954.

Silver, L.T. and Chappell, B.W. 1988. The Peninsular Ranges Batholith: an insight into the evolution of the Cordilleran batholiths of southwestern North America. *Transactions of the Royal Society of Edinburgh Earth Sciences*, 79, p. 105-121.

Singh, R.N. and Negi, J.G. 1980. On the estimation of the vertical distribution of radiogenic heat production in the crust. *Geophysical Journal of the Royal Astronomical Society*, 62, p. 221-224.

Smith, P.B. 1992. The alteration history of the late Proterozoic Wooltana Volcanics of the Mount Painter province, South Australia. B.Sc (Hons) thesis (unpublished), The University of Adelaide, Australia, pp. 26.

Somerville, M., Wyborn, D., Chopra, P.N., Rahman, S.S., Estrella, D. and Van der Meulen, T., 1994. Hot dry rocks feasibility study, *ERDC Report* 94/243, pp. 133.

Sonder, L. and England, P.C. 1986. Vertical averages of rheology of the continental lithospheric; relation to thin sheet parameters. *Earth and Planetary Science Letters*, 77, 81-90.

Southgate, P.N. 2000. (*ed.*), Carpentaria-Mount Isa Zinc Belt: basement framework, chronostratigraphy and geodynamic evolution of Proterozoic successions. *Australian Journal of Earth Sciences*, 47, p. 337-657.

Southgate, P.N., Bradshaw, B.E., Domagala, J., Jackson, M.J., Idnurm, M., Krassay, A.A., Page, R.W., Sami, T.T., Scott, D.L., Lindsay, J.F., McConachie, B.A. and Tarlowski, C. 2000. Chronostratigraphic basin framework for Palaeoproterozoic rocks (1730-1575 Ma) in northern Australia and implications for base-metal mineralization. *Australian Journal of Earth Sciences*, 47, p. 461-483.

Spikings, R.A., Foster, D.A. and Kohn, B.P. 1997. Phanerozoic denudation history of the Mount Isa Inlier, Northern Australia: A record of the response of a Proterozoic mobile belt to intraplate tectonics. *International Geology Review*, 39, p. 107-124.

Spray, J.G., Kelley, S.P. and Reimold, W.U. 1995. Laser probe $^{40}Ar/^{39}Ar$ dating of coesite and stishovite bearing pseudotachlytes and the age of the Vredefort impact event. *Meteoritics*, 30, p. 335-343.

Sprigg, R.C. 1946. Reconnaissance geological survey of portion of the western escarpment of the Mount Lofty Ranges. *Royal Society of South Australia Transactions*, 70, p. 313-347.

Steiger, R. and Jäger, E. 1977. Subcommission on geochronology: Convention on the use of decay constants in geo- and cosmochronology. *Earth and Planetary Science Letters*, 36, p. 359-362.

Sun, X. 1997. Structural style of the Warburton Basin and control in the Cooper and Eromanga Basins, South Australia. *Exploration Geophysics*, 28, p. 333-339.

Sutherland, F.L., Raynor, L.R. and Pogson, R.E. 1994. Spinel to garnet lherzolite transition in relation to high temperature palaeogeotherms, eastern Australia. *Australian Journal of Earth Sciences*, 41, p. 205-220.

Talbot, C.J. 1973. A plate tectonic model for the Archaean crust. *Philosophical Transactions of the Royal Society of London*, 173, p. 413-427.

Taylor, S.R. and McLennan, S.M. 1985. *The continental crust: its composition and evolution*. Blackwell Scientific Publications, Oxford, United Kingdon, pp. 312.

Teale, G.S. 1993. The Mount Painter and Mount Babbage Inliers. *In*: Drexel, J.F., Preiss, W.V. and Parker, A.J. (*eds.*), The Geology of South Australia, Volume 1, The Precambrian. *South Australian Geological Survey, Bulletin*, 54, p. 93-100.

Tetley, N., McDougall, I. and Heydegger, H.R. 1980. Thermal neutron interferences in the $^{40}Ar/^{39}Ar$ dating technique. *Journal of Geophysical Research*, 85, p. 7201-7205.

Thornton, G.D. 1980. Geology, geochemistry and

geochronology of the eastern Babbage Block, Mount Painter Province, South Australia. B.Sc (Hons) thesis (unpublished), The University of Adelaide, Australia, pp. 25.

Tokarev, V., Sandiford, M. and Gostin, V. 1999. Landscape evolution in the Mount Lofty Ranges: implications for regolith development. *In*: Taylor, G. and Pain, C. (*eds*.), *Regolith '98: new approaches to an old continent*, p. 131-139.

Turcotte, D.L. and Oxburgh, E.R. 1972. Statistical thermodynamic model for the distribution of crustal heat sources. *Science*, 176, p. 1021-1022.

Turcotte, D.L. and Schubert, G. 1982. *Geodynamics: Applications of continuum physics to geological problems*. John Wiley & Sons, Inc., New York, USA, pp. 450.

Van der Held, E.F.M., Hardebol, J. and Kalshoven, J. 1953. On the measurement of the thermal conductivity of liquids by a non-stationary method. *Physica*, 19, p. 208-216.

Van der Hilst, R.D., Kennett, B.L.N., Christie, D. and Grant, L. 1994. SKIPPY mobile broad-band arrays to study the seismic structure of the lithosphere and mantle beneath Australia. *Eos, Transactions of the American Geophysical Union*, 75, p. 177-181.

Vasseur, G. and Nouri, Y. 1980. Trend of heat flow in France: Relation with deep structures. *Tectonophysics*, 65, p. 209-223.

Vasseur, G. and Singh, R.N. 1986. The effects of random horizontal variations in the radiogenic heat source distribution and its relationship with heat flow. *Journal of Geophysical Research*, 91, p. 10397-10404.

Veizer, J., Plumb, K.A., Clayton, R.N., Hinton, R.W. and Grotzinger, J.P. 1992. Geochemistry of Precambrian carbonates, V. Late Palaeoproterozoic seawater. *Geochimica et Cosmochimica Acta*, 56, p. 2487-2501.

Verdoya, M., Pasquale, V., Chiozzi, P. and Kukkonen, I.T. 1998. Radiogenic heat production in the Variscan crust: new determinations and distribution models in Corsica (northwest Mediterranean). *Tectonophysics*, 291, p. 63-75.

Vitorello, I. and Pollack, H.N. 1980. On the variation of continental heat flow with age and the thermal evolution of continents. *Journal of Geophysical Research*, 85, p. 983-995.

Von Herzen, R. and Maxwell, A.E. 1959. The measurement of thermal conductivity of deep-sea sediments by a needle-probe method. *Journal of Geophysical Research*, 64, p. 1557-1563.

Webb, A.W.. 1976. Geochronology. *In*: Radke, F. and Webb, A.W. (*eds*.), *Geochronology of the eastern basement rocks*, Amdel progress reports 9 and 10, South Australian Department of Mines and Energy, Open File Envelope, 2136 (unpublished).

Wells, A.T. and Moss, F.J. 1983. The Ngalia Basin, Northern Territory: Stratigraphy and structure. *Bureau of Mineral Resources Geology and Geophysics Bulletin*, 212, pp. 88.

Wickham, S.M. and Oxburgh, E.R. 1985. Continental rifts as a setting for regional metamorphism. *Nature*, 318, p. 330-333.

Wijbrans, J.R. and McDougall, I. 1988. Metamorphic evolution of the Attic Cycladic metamorphic belt on Naxos (Cyclades, Greece) utilizing $^{40}Ar/^{39}Ar$ age spectrum measurements. *Journal of Metamorphic Geology*, 6, p. 571-594.

Willcox, J.B. 1996. Critical tectonic events in the development of the North West Shelf. *Geological Society of Australia, Abstracts*, 41, p. 473.

Williams, D.L. and von Herzen, R.P. 1974. Heat loss from the Earth: New estimate. *Geology*, 2, p. 327-328.

Williams, I.S., Buick, I.S. and Cartwright, I. 1995. An extended episode of early Mesoproterozoic metamorphic fluid flow in the Reynolds Range, central Australia. *Journal of Metamorphic Geology*, 14, p.29-47.

Wilks, K.R. and Carter, N.L. 1990. Rheology of some continental lower crustal rocks. *In*: Fountain, D.M. and Boriani, A. (*eds*.), The Nature of the Lower Continental Crust. *Tectonophysics*, 182, p. 57-77.

Windley, B.F. 1981. Precambrian rocks in the light of the plate-tectonic concept. *In*: Kröner, A. (*ed*.), *Precambrian Plate Tectonics*. Elsevier Scientific Publishing, Amsterdam, p. 1-20.

Windley, B.F. 1993. Uniformitarianism today: plate tectonics is the key to the past? *Journal of the Geological Society of London*, 150, p. 7-19.

Windley, B.F. 1995. *The evolving continents*. Wiley Publishers, London, pp. 526.

Wingate, M.T.D., Campbell, I.H., Compston, W. and Gibson, G.M. 1998. Ion-probe U-Pb ages for Neoproterozoic basaltic magmatism in south-central Australia and implications for the breakup of Rodinia. *Precambrian Research*, 87, p. 135-159.

Wronski, E.B. 1977. Two heat flow values for Tasmania. *Geophysical Journal of the Royal Astronomical Society*, 48, p. 131-133.

Wyborn, L.A.I. 1988. Petrology, geochemistry and origin of a major Australian 1880-1849 Ma felsic volcano-plutonic suite: A model for intracontinental felsic magma generation. *Precambrian Research*, 40/41, p. 37-60.

Wyborn, L.A.I. 1998. Younger *ca.* 1500 Ma granites of the Williams and Naraku Batholiths, Cloncurry district, eastern Mount Isa Inlier: geochemistry, origin, metallogenic significance and exploration indicators. *Australian Journal of Earth Sciences*, 45, p. 397-411.

Wyborn, L.A.I., Page, R.W. and Parker, A.J. 1987. Geochemical and geochronological signatures in Australian Proterozoic igneous rocks. *In*: Pharaoh, T.C., Beckinsale, R.D. and Rickard, D.T. (*eds*.), *Geochemistry and mineralization of Proterozoic volcanic suites*. *Geological Society of London Special Publications*, 33, p. 377-394.

Wyborn, L.A.I., Page, R.W. and McCulloch, M.T. 1988. Petrology, geochronology and isotope geochemistry of the post-1820 Ma granites of the Mount Isa Inlier; mechanisms for the generation of Proterozoic anorogenic granites. *Precambrian Research*, 40 / 41. p. 509-541.

Wyborn, L.A.I., Wyborn, D., Warren, R.G. and Drummond, B.J. 1992. Proterozoic granite types in Australia: implications for lower crust composition, structure and evolution. *Transactions of the Royal Society of Edinburgh Earth Sciences*, 83, p. 201-209.

Wyborn, L.A.I., Goleby, B., Drummond, B. and Gallagher, R. 1996. The Mount Isa Geodynamic transect – a 2.5-dimensional metallogenic GIS analysis. *Australian Geological Survey Organization Research Newsletter*, 24, p. 10-12.

Wyborn L.A.I., Budd, A.R. and Bastrakova, I.V. 1998a. The metallogenic potential of Australian Proterozoic granites, Granite GIS (Partial Release) CD ROM, Australian Geological Survey Organization, Canberra, Australia.

Wyborn, L.A.I., Bastrakova, I.V. and Budd, A.R. 1998b. Australian Proterozoic granites – characteristics, sources and possible mechanisms for derivation and emplacement. *Australian Geological Survey Organization Record*, 1998 / 33, p. 47-49.

Young, G.C. and Laurie, J.R. 1996. (*eds.*), *An Australian Phanerozoic timescale*. Oxford University Press, Melbourne, Australia, pp. 279.

Zhou, S. and Sandiford, M. 1992. On the stability of isostatically compensated mountain belts. *Journal of Geophysical Research*, 97, p. 14207-14221.

Zielhaus, A. and Van der Hilst, R.D. 1996. Upper-mantle shear velocity beneath eastern Australia from inversion of waveforms from Skippy portable arrays. *Geophysical Journal International*, 127, p. 1-16.

Zierfuss, H. 1969. Heat conductivity of some carbonate rocks and clayey sandstones. *American Association of Petroleum Geologists, Bulletin*, 53, p. 251-260.

# Appendix A

# Thermal property measurements: Heat production, heat flow and thermal conductivity in Australian Proterozoic terranes

## A.1 Heat Production

On geological time scales only 3 elements, and in particular 4 isotopes, $^{238}U$, $^{235}U$, $^{232}Th$ and $^{40}K$, occur in sufficient abundance to contribute to the lithospheric thermal budget. As shown by Rutherford and Soddy (1903) the rate of decay of a radioactive substance is exponential, with the activity at any time proportional to the number of radioactive atoms present. This relation can be expressed in the form:

$$N = N_o \exp(-\lambda t) \tag{A.1}$$

where $N$ is the number of radioactive atoms present at time $t$, $N_o$ is the number of radioactive atoms present at time $t_o$, some time in the past, and  is the constant of proportionality termed the decay constant. As decay rates and modern heat generation rates are known for each of the radioactive isotopes (Table A.1), the heat generated by a particular lithology can be quantified based on the total abundance of these elements, according to the following equations:

$$H_U = C_o^U H^U = C_o^U \; 9.71 \times 10^{-5} \tag{A.2}$$

$$H_{Th} = C_o^{Th} H^{Th} = C_o^{Th} \; 2.69 \times 10^{-5} \tag{A.3}$$

$$H_K = C_o^K H^K = 0.000128 \, C_o^K \; 3.58 \times 10^{-9} \tag{A.4}$$

The total heat production of a particular unit is given by the sum,

$$H = H_U + H_{Th} + H_K \tag{A.5}$$

The equation listed for heat production from Uranium is based on the bulk heat generation rate for both isotopes $^{238}U$ and $^{235}U$, based on the relative proportions of these isotopes which comprise all natural Uranium (Turcotte and Schubert, 1982). Because the radiogenic isotope of Potassium, $^{40}K$, comprises only 0.0128% of all potassium, this factor must be included in Equation A.4. All naturally occurring Thorium and Uranium is radiogenic. Heat production is given in units of $Wm^{-3}$ (volumetric heat production). As noted in Chapter Two of this thesis, the typical concentrations of radiogenic elements within the Earth commonly have heat production rates of the order of 0-5 $\mu Wm^{-3}$.

The total abundance of the heat producing elements is generally measured by X-ray fluorescence on powdered whole rock samples. Alternatively, concentrations may be taken from well calibrated airborne radiometric data (as shown for the Sybella Batholith in Chapter Five of this thesis). The conversion from total counts U, Th and K to elemental concentrations (and consequently to heat production) was possible in the Sybella case only because calibration pads were present

***Table A.1*** *Heat generation rates and half-lives of the heat producing radioactive isotopes*

| *Isotope* | *Heat generation rate ($Wkg^{-1}$)* | *Half life, $t_{1/2}$ (years)* |
|---|---|---|
| $^{238}U$ | $9.37 \times 10^{-5}$ | $4.47 \times 10^{9}$ |
| $^{235}U$ | $5.69 \times 10^{-4}$ | $7.04 \times 10^{8}$ |
| U | $9.71 \times 10^{-5}$ | |
| $^{232}Th$ | $2.69 \times 10^{-5}$ | $1.40 \times 10^{10}$ |
| $^{40}K$ | $2.79 \times 10^{-5}$ | $1.25 \times 10^{9}$ |
| K | $3.58 \times 10^{-9}$ | |

within the survey area. This meant that accurate calibration of the survey equipment could be performed at the beginning and end of each run. Surveys could also be calibrated by detailed hand-held spectrometer traverses (e.g., Hand et al., 1999).

Because the decay rates and half-lives of each of the radiogenic isotopes are known, the mean heat production rate of a given lithology can be related to the present-day heat production. The concentration $C$ of a radioactive isotope at time $t$ is related to the present concentration $C_o$ and the half-life, $t_{1/2}$ by the equation:

$$C = C_o \exp\left(\frac{t \ln 2}{t_{1/2}}\right) \tag{A.6}$$

Consequently the heat production for some time, $t$, in the past is given by:

$$H = C_o^U H^U \exp\left(\frac{t \ln 2}{t_{1/2}^{U^{238}}}\right) + C_o^{Th} H^{Th} \exp\left(\frac{t \ln 2}{t_{1/2}^{Th^{232}}}\right) + 0.000128\, C_o^K H^K \exp\left(\frac{t \ln 2}{t_{1/2}^{K^{40}}}\right) \tag{A.7}$$

However, such calculations are valid only if the system can be considered to be closed with respect to U, Th and K.

In the following series of tables I present average heat production data by area for granites of the major Australian Proterozoic inliers. Granite groupings are based on Supersuite terminology from Wyborn et al., (1998a) and contrast with the chronological grouping of granites given in Table 2.2. In all cases the concentrations of the heat producing elements have been determined using X-ray fluorescence. Note that in all tables average heat production is listed for the modern day, based on present abundances of the heat producing elements. As noted in the text, average heat production in the Proterozoic would have been around 20-30% higher than the values listed in these tables. The percentage area occupied by each major granite group is an estimate only based on the accurate outcrop area of each granite (from Wyborn et al., 1998a) and an estimated area of the entire inlier. Estimates of the total area of each inlier are likely to overestimate the area of outcrop, so the values shown in these tables are likely to be a minimum estimate of the percentage of granite *vs.* the total outcrop area.

***Table A.2*** *Heat Production in granites, granite gneisses and felsic volcanics: Arnhem Land*

| *Granite Suite* | *Age Range* | *Type* | *Area of outcrop ($km^2$)* | *U (ppm)* | *Th (ppm)* | *K (wt%)* | *Th:U* | *Average Q ($\mu Wm^{-3}$)* |
|---|---|---|---|---|---|---|---|---|
| Fagan Supersuite | 1717 – 1707 | I | 368 | 3.7 | 39.5 | 7.38 | 10.6 | **4.56** |
| Bickerton Suite | 1814 | I | 15 | 4.5 | 32.7 | 3.11 | 7.3 | **3.85** |
| Giddy Suite | ~ 1835 | I | 359 | 5.0 | 36.8 | 5.96 | 7.4 | **4.55** |
| Bradshaw Suite | ~ 1875 – 1845 | S | 565 | 5.2 | 24.6 | 4.43 | 4.8 | **3.57** |
| ***TOTAL*** | | | **1307** | **4.7** | **31.9** | **5.63** | | **4.08** |

***Table A.3*** *Heat Production in granites, granite gneisses and felsic volcanics: Arunta Inlier*

| *Granite Suite* | *Age Range* | *Type* | *Area of outcrop ($km^2$)* | *U (ppm)* | *Th (ppm)* | *K (wt%)* | *Th:U* | *Average Q ($\mu Wm^{-3}$)* |
|---|---|---|---|---|---|---|---|---|
| Alarinjela Suite | ~ 1713 | I | 290 | 9.4 | 29.3 | 5.12 | 6.7 | **3.76** |
| Ali Curung Suite | ~ 1713 | I | 262 | 8.0 | 33.4 | 4.58 | 4.2 | **4.97** |
| Barrow Creek Suite | ~ 1713 | S | 244 | 12.4 | 31.8 | 4.99 | 2.6 | **6.04** |
| Carrington Granite Suite | ~ 1780 | | 429 | 6.1 | 39.0 | 4.24 | 6.4 | **4.84** |
| Entia Suite | ~ 1770 | I | 539 | 1.3 | 6.5 | 3.90 | 5.2 | **1.18** |
| Haverson Suite | ~ 1820 | | 945 | 7.3 | 38.7 | 5.25 | 5.3 | **5.24** |
| Iwupataka Complex | ~ 1615 – 1600 | I | 628 | 4.6 | 25.7 | 4.51 | 5.6 | **3.50** |
| Jennings Suite | ~ 1770 | I | 1153 | 2.2 | 22.0 | 4.15 | 9.9 | **2.58** |
| Jervois Suite | ~ 1770 | I | 880 | 2.7 | 19.0 | 4.12 | 6.9 | **2.50** |
| Jinka Suite | ~ 1713 | I | 1205 | 16.9 | 89.0 | 5.60 | 5.3 | **11.43** |
| Madderns Yard Suite | ~ 1680 – 1650 | I | 4001 | 2.2 | 20.2 | 3.03 | 9.3 | **2.32** |
| Mount Webb Suite | ~ 1615 – 1480 | I | 5623 | 10.0 | 39.7 | 4.46 | 4.0 | **5.92** |
| Mount Zeil Suite | 1760 | I | 108 | 1.8 | 13.8 | 4.58 | 7.6 | **1.92** |
| Napperby Suite | ~ 1780 – 1775 | I | 6041 | 10.3 | 60.7 | 5.30 | 5.9 | **7.61** |
| Narwietooma Suite | 1880 | I | 1448 | 1.7 | 9.0 | 3.36 | 5.2 | **1.43** |
| Southwark Granitic Suite | ~ 1570 | I | 1996 | 7.7 | 51.1 | 5.00 | 6.6 | **6.22** |
| Ungrouped | | I | 1401 | 5.0 | 40.4 | 4.11 | 8.0 | **4.65** |
| ***TOTAL*** | | | **27233** | **7.2** | **40.1** | **4.46** | | **5.24** |

***Table A.4*** *Heat Production in granites, granite gneisses and felsic volcanics: Broken Hill - Olary region*

| *Granite Suite* | *Age Range* | *Type* | *Area of outcrop ($km^2$)* | *U (ppm)* | *Th (ppm)* | *K (wt%)* | *Th:U* | *Average Q ($\mu Wm^{-3}$)* |
|---|---|---|---|---|---|---|---|---|
| 1590 Suite | ~ 1590 | I | 450 | 5.7 | 36.3 | 4.52 | 6.4 | **4.56** |
| Potosi Suite | 1700 – 1670 | S | 459 | 2.1 | 25.2 | 3.10 | 11.9 | **2.68** |
| Himalaya Suite | 1710 – 1700 | I | 911 | 5.2 | 11.1 | 1.26 | 2.1 | **2.28** |
| Redan Suite | 1820 | I | 99 | 3.4 | 8.4 | 0.67 | 2.5 | **1.56** |
| ***TOTAL*** | | | **1920** | **4.5** | **20.2** | **2.44** | | **2.88** |

***Table A.5*** *Heat Production in granites, granite gneisses and felsic volcanics: Gawler Province*

| *Granite Suite* | *Age Range* | *Type* | *Area of outcrop ($km^2$)* | *U (ppm)* | *Th (ppm)* | *K (wt%)* | *Th:U* | *Average Q ($\mu Wm^{-3}$)* |
|---|---|---|---|---|---|---|---|---|
| Hiltaba Supersuite | 1590 – 1580 | I | 19419 | 7.4 | 32.6 | 4.98 | 4.4 | **4.79** |
| St. Peters Suite | 1620 – 1615 | I | 73 | 4.2 | 12.4 | 3.28 | 3.0 | **2.31** |
| Younger Lincoln S/Suite | 1755 – 1655 | I | 496 | 10.6 | 37.9 | 4.28 | 3.6 | **5.93** |
| Minbrie Gneiss | 1800 | I | 899 | 4.6 | 36.9 | 5.27 | 7.0 | **4.51** |
| ***TOTAL*** | | | **20888** | **7.4** | **32.8** | **4.94** | | **4.79** |

***Table A.6*** *Heat Production in granites, granite gneisses and felsic volcanics: Georgetown Inlier*

| *Granite Suite* | *Age Range* | *Type* | *Area of outcrop ($km^2$)* | *U (ppm)* | *Th (ppm)* | *K (wt%)* | *Th:U* | *Average Q ($\mu Wm^{-3}$)* |
|---|---|---|---|---|---|---|---|---|
| Esmeralda Supersuite | 1560 – 1550 | I | 4664 | 10.5 | 28.8 | 5.08 | 2.8 | **5.34** |
| Forest Home Supersuite | 1550 | I | 31 | 1.3 | 2.4 | 2.00 | 1.9 | **0.70** |
| Forsayth Supersuite | 1550 – 1540 | S | 1681 | 6.7 | 31.1 | 4.59 | 4.6 | **4.46** |
| Lighthouse Suite | 1560 | I | 36 | 1.8 | 6.2 | 3.99 | 3.5 | **1.29** |
| ***TOTAL*** | | | **6411** | **9.4** | **29.1** | **4.93** | | **5.06** |

***Table A.7*** *Heat Production in granites, granite gneisses and felsic volcanics: Kimberley Province*

| *Granite Suite* | *Age Range* | *Type* | *Area of outcrop ($km^2$)* | *U (ppm)* | *Th (ppm)* | *K (wt%)* | *Th:U* | *Average Q ($\mu Wm^{-3}$)* |
|---|---|---|---|---|---|---|---|---|
| Butchers Gully Suite | 1860 | | 100 | 6.1 | 46.6 | 5.58 | 7.6 | **5.50** |
| Dougalls Suite | 1850 | I | 44 | 1.2 | 5.0 | 1.18 | 4.3 | **0.78** |
| Koongie Park Suite | 1845 | I | 58 | 3.7 | 16.6 | 2.88 | 4.5 | **2.45** |
| Paperbark Suite | 1862 – 1852 | I | 9189 | 5.2 | 20.5 | 4.50 | 3.9 | **3.28** |
| Sally Downs Supersuite | 1827 – 1819 | I | 2502 | 3.3 | 18.7 | 3.41 | 5.7 | **2.55** |
| Sophie Downs Suite | ~ 1912 | I | 65 | 2.2 | 16.8 | 5.10 | 7.7 | **2.29** |
| San Sou Suite | 1800 – 1790 | I | 91 | 12.1 | 25.5 | 4.97 | 2.1 | **5.51** |
| Ungrouped | 1863 – 1850 | I | 24 | 2.0 | 9.2 | 3.22 | 4.6 | **1.51** |
| ***TOTAL*** | | | **12073** | **4.8** | **20.2** | **4.26** | | **3.15** |

*Note*: The Kimberley Province includes the Halls Creek and King Leopold Orogens

***Table A.8*** *Heat Production in granites, granite gneisses and felsic volcanics: Mount Isa Inlier*

| *Granite Suite* | *Age Range* | *Type* | *Area of outcrop ($km^2$)* | *U (ppm)* | *Th (ppm)* | *K (wt%)* | *Th:U* | *Average Q ($\mu Wm^{-3}$)* |
|---|---|---|---|---|---|---|---|---|
| Argylla Suite | 1790 – 1780 | I | 1815 | 6.2 | 28.8 | 5.28 | 4.7 | **4.21** |
| Big Toby Suite | | I | 20 | 1.2 | 8.7 | 4.10 | 7.4 | **1.33** |
| Burstall Suite | 1745 – 1740 | I | 199 | 8.0 | 45.1 | 5.07 | 5.6 | **5.86** |
| Cowie Suite | 1500 | | 15 | 17.4 | 76.2 | 4.52 | 4.4 | **10.54** |
| Fiery Supersuite | 1725 – 1698 | I | 537 | 4.8 | 27.4 | 8.85 | 5.7 | **4.09** |
| Kalkadoon Supersuite | 1860 – 1820 | I | 3478 | 4.4 | 25.0 | 4.46 | 5.7 | **3.40** |
| Nicholson Suite | 1850 | I | 1208 | 8.0 | 27.1 | 5.44 | 3.4 | **4.59** |
| Sybella Suite | 1678 – 1655 | I | 1098 | 7.1 | 37.6 | 5.26 | 5.3 | **5.09** |
| Tommy Creek Suite | 1762 – 1625 | I | 250 | 5.7 | 31.6 | 4.14 | 5.5 | **4.19** |
| Ungrouped | | | 120 | 6.9 | 24.7 | 3.93 | 3.6 | **3.99** |
| Williams Supersuite | 1520 – 1493 | I | 1864 | 13.4 | 55.5 | 3.90 | 4.1 | **7.93** |
| Wonga Suite | 1760 – 1740 | I | 332 | 9.4 | 53.1 | 5.39 | 5.6 | **6.84** |
| ***TOTAL*** | | | **10935** | **7.2** | **33.9** | **4.93** | | **4.82** |

***Table A.9*** *Heat Production in granites, granite gneisses and felsic volcanics: Mount Painter Province*

| *Granite Suite* | *Age Range* | *Type* | *Area of outcrop ($km^2$)* | *U (ppm)* | *Th (ppm)* | *K (wt%)* | *Th:U* | *Average Q ($\mu Wm^{-3}$)* |
|---|---|---|---|---|---|---|---|---|
| Terrapinna granite | 1557 | I | 99 | 10 | 58 | 5.2 | | **7.20** |
| Yerila granite | 1556 | I | 30 | 116 | 423 | 5.7 | | **61.6** |
| Hot Springs Gneiss | 1560 | I | 22 | 75 | 288 | 4.2 | | **41.0** |
| Petermorra Volcanics | 1560 | I | 13 | 10 | 35 | 6.5 | | **6.7** |
| Box Bore granite | 1560 | I | 40 | 44 | 131 | 6.4 | | **21.6** |
| Wattleowie granite | 1560 | I | 18 | 6 | 33 | 5.8 | | **4.5** |
| Mount Neill granite | 1570 | I | 189 | 21 | 74 | 3.6 | | **11.3** |
| ***TOTAL*** | | | **411** | **29** | **110** | **4.62** | | **16.13** |

*Note:* Data compiled from Neumann et al., (2000)

***Table A.10*** *Heat Production in granites, granite gneisses and felsic volcanics: Musgrave Inlier*

| *Granite Suite* | *Age Range* | *Type* | *Area of outcrop ($km^2$)* | *U (ppm)* | *Th (ppm)* | *K (wt%)* | *Th:U* | *Average Q ($\mu Wm^{-3}$)* |
|---|---|---|---|---|---|---|---|---|
| Kulgera Suite | 1190 – 1150 | I | 3639 | 1.5 | 22.8 | 4.26 | 14.9 | **2.47** |
| Winburn Suite | 1078 | I | 1783 | 5.8 | 41.8 | 4.66 | 7.3 | **5.00** |
| Ungrouped | 1190 – 1150 | I | 77 | 0.7 | 18.8 | 4.04 | 28.1 | **3.00** |
| ***TOTAL*** | | | **5499** | **1.3** | **21.8** | **4.19** | | **2.68** |

***Table A.11*** *Heat Production in granites, granite gneisses and felsic volcanics: Pine Creek Inlier*

| *Granite Suite* | *Age Range* | *Type* | *Area of outcrop ($km^2$)* | *U (ppm)* | *Th (ppm)* | *K (wt%)* | *Th:U* | *Average Q ($\mu Wm^{-3}$)* |
|---|---|---|---|---|---|---|---|---|
| Allia Suite | 1845 – 1760 | S | 415 | 5.7 | 17.2 | 4.32 | 3.0 | **3.15** |
| Cullen Supersuite | 1860 – 1775 | I | 3160 | 10.1 | 39.4 | 4.98 | 3.9 | **5.99** |
| El Sherana Supersuite | 1870 – 1850 | | 72 | 14.1 | 42.3 | 2.40 | 3.0 | **6.99** |
| Gerowie Suite | 1890 – 1885 | I | 1173 | 4.9 | 23.5 | 3.27 | 4.8 | **3.30** |
| Jim Jim Suite | 1863 – 1760 | I | 2234 | 7.7 | 34.1 | 5.09 | 4.5 | **4.98** |
| Nimbuwah Suite | ~ 1870 | I | 1109 | 2.8 | 22.7 | 3.68 | 8.1 | **2.73** |
| Wagait Suite | ~ 1850 | I | 333 | 6.7 | 25.8 | 4.77 | 3.9 | **6.64** |
| Ungrouped | ~ 1825 | | 29 | 10.0 | 49.0 | 4.72 | 4.9 | **4.08** |
| ***TOTAL*** | | | **8626** | **7.5** | **32.1** | **4.55** | | **4.73** |

***Table A.12*** *Heat Production in granites, granite gneisses and felsic volcanics: Tanami Inlier*

| *Granite Suite* | *Age Range* | *Type* | *Area of outcrop ($km^2$)* | *U (ppm)* | *Th (ppm)* | *K (wt%)* | *Th:U* | *Average Q ($\mu Wm^{-3}$)* |
|---|---|---|---|---|---|---|---|---|
| Browns Range Suite | ~ 1820 | I | 6 | 2.1 | 3.3 | 2.20 | 1.6 | **1.00** |
| The Granites Supersuite | 1824 – 1795 | I | 784 | 11.7 | 31.0 | 5.20 | 2.6 | **5.82** |
| ***TOTAL*** | | | **790** | **11.7** | **30.7** | **5.19** | | **5.79** |

***Table A.13*** *Heat Production in granites, granite gneisses and felsic volcanics: Tennant Creek Inlier*

| *Granite Suite* | *Age* | *Type* | *Area of outcrop ($km^2$)* | *U (ppm)* | *Th (ppm)* | *K (wt%)* | *Th:U* | *Average Q ($\mu Wm^{-3}$)* |
|---|---|---|---|---|---|---|---|---|
| Devils Suite | 1720 - 1670 | I | 443 | 8.8 | 36.4 | 5.23 | 4.2 | **5.45** |
| Treasure Suite | ~ 1810 - 1820 | I | 1493 | 6.0 | 24.5 | 5.08 | 4.1 | **3.84** |
| Tennant Creek Suite | ~ 1840 - 1870 | I | 2195 | 5.5 | 23.5 | 4.60 | 4.2 | **3.60** |
| ***TOTAL*** | | | **4131** | **6.1** | **25.2** | **4.84** | **4.2** | **3.89** |

Granites within Proterozoic terranes outside the CAHFP are also characterized by elevated heat production rates. Tables A.14, A.15 and A.16 (following) show average heat production data for the Albany-Fraser, Gascoyne and Paterson Orogens in Western Australia. These data support the elevated heat production rates reported throughout terranes within the CAHFP and suggest that a time dependent process, or source, of enrichment was active during much of the Palaeo-Mesoproterozoic growth of the Australian continent.

***Table A.14*** *Heat Production in granites, granite gneisses and felsic volcanics: Albany Fraser Belt*

| *Granite Suite* | *Age Range* | *Type* | *Area of outcrop ($km^2$)* | *U (ppm)* | *Th (ppm)* | *K (wt%)* | *Th:U* | *Average Q ($\mu Wm^{-3}$)* |
|---|---|---|---|---|---|---|---|---|
| Mount Andrew Migmatite | 1670 | I | 297 | 3.3 | 13.4 | 4.03 | 4.1 | **2.23** |
| Porongurup Suite | 1330 – 1135 | I | 8079 | 3.9 | 35.4 | 4.53 | 9.0 | **4.04** |
| Ungrouped | 1692 – 1190 | I | 852 | 3.4 | 17.1 | 4.11 | 5.0 | **2.53** |
| ***TOTAL*** | | | **9229** | **3.9** | **33.0** | **4.48** | | **3.84** |

***Table A.15*** *Heat Production in granites, granite gneisses and felsic volcanics: Gascoyne Province*

| *Granite Suite* | *Age Range* | *Type* | *Area of outcrop ($km^2$)* | *U (ppm)* | *Th (ppm)* | *K (wt%)* | *Th:U* | *Average Q ($\mu Wm^{-3}$)* |
|---|---|---|---|---|---|---|---|---|
| Boolaloo Supersuite | 1680 | I | 326 | 3.2 | 16.7 | 3.48 | 5.2 | **2.39** |
| Chararoo Supersuite | 1800 | S | 1812 | 4.0 | 44.0 | 4.90 | 10.9 | **4.76** |
| Minnie Creek Supersuite | 1800 | I | 9656 | 2.6 | 29.9 | 4.12 | 11.7 | **3.24** |
| ***TOTAL*** | | | **11794** | **2.8** | **31.7** | **4.22** | | **3.45** |

***Table A.16*** *– Heat Production of granites, granite gneisses and felsic volcanics: Paterson Inlier*

| *Granite Suite* | *Age Range* | *Type* | *Area of outcrop ($km^2$)* | *U (ppm)* | *Th (ppm)* | *K (wt%)* | *Th:U* | *Average Q ($\mu Wm^{-3}$)* |
|---|---|---|---|---|---|---|---|---|
| O'Callaghans Supersuite | 630 – 615 | I | 75 | 12.3 | 45.9 | 4.65 | 3.7 | **7.01** |
| Krakatinny Supersuite | 1310 | I | 63 | 3.6 | 16.8 | 3.41 | 4.7 | **2.48** |
| Kalkan Supersuite | 1780 | I | 598 | 7.0 | 33.8 | 5.15 | 4.8 | **4.79** |
| ***TOTAL*** | | | **737** | **7.2** | **33.6** | **4.95** | | **4.82** |

## A.2 Heat flow in Australian Proterozoic terranes

Although considerable effort has been expended in the collection of surface heat flow data in many continental settings, particularly in the United States and Europe, the Australian heat flow field is defined by only ~ 120 data points. The first heat flow determination was made in Tasmania by Newstead and Beck in 1953, and from that time until the late 1970's heat flow determinations were made at 90 localities across the continent, lead largely by the pioneering work of J.C. Jaeger and J.H. Sass. These early data have been compiled in the review paper of Cull (1982) and only a handful of determinations have been published since (Houseman et al., 1989; Gallagher, 1990). As discussed in Chapter Two of this thesis, Sass and Lachenbruch (1979) divided the Australian heat flow field into three provinces: the Western, Central and Eastern provinces. This tripartite division is closely allied to tectonic age. The dominantly Archaean Western province has an average heat flow of 39 $\pm$ 8 $mWm^{-2}$, the dominantly Proterozoic Central province has an average heat flow of 82 $\pm$ 25 $mWm^{-2}$ and the dominantly Palaeozoic Eastern province has an average heat flow of 72 $\pm$ 27 $mWm^{-2}$. The average heat flow in the Central Australian Heat flow province (CAHFP) is anomalous when compared to global averages and is the result of the presence of anomalous concentrations of the heat producing elements within Proterozoic crust. This observation motivates an evaluation of the thermal effects of these anomalous heat sources. A summary of all the heat flow determinations within the CAHFP is presented in Table A.17.

In the steady-state, in the absence of erosion, tectonic deformation and groundwater circulation, surface heat flow provides a measure of the heat conducted through the outermost part of the lithosphere. Surface heat flow is therefore a function of two fundamentally sources: the heat produced from sources within the lithosphere, $q_c$, and the heat supplied to the base of the lithosphere by processes such as convection in the deeper mantle, $q_m$. The measurement of surface heat flow is based on Fouriers Law:

$$q = k.gradT \tag{A.8}$$

where $q$ is the heat flow per unit area, $gradT$ is the temperature gradient, and $k$ is the thermal conductivity of the rock in which the gradient is measured. In continental settings, surface heat flow is generally measured in boreholes at depths greater than 100 m (and preferably greater than 300 m; Cull, 1982) to avoid seasonal climatic effects. Cull (1982) noted that amongst the Australian heat flow dataset thermal conductivities were generally measured on core samples extracted from each borehole in which temperatures were measured. In most cases heat flow was generally calculated by combining average conductivities with a linear least-squares thermal gradient over the full length of the borehole.

Potential errors are associated with the collection of both thermal gradient and thermal conductivity data, and these errors may contribute to errors in the calculated surface heat flow. The quality of the borehole used for the heat flow determination may also contribute to erroneous surface heat flow measurements. The Australian heat flow dataset contains measurements from tunnels, mines, flowing bores and cased and uncased boreholes of various depths (Cull and Denham, 1979) and in each case the condition of the borehole and its physical environment impact on the quality of the heat flow measurement. Cull (1982) has estimated the relative quality of each heat flow determination in his compilation by evaluating these sources of error and these 'quality factors' are listed Table A.17. The three digits of the quality factor represent the quality of (1) the thermal gradient

data, (2) the thermal conductivity data, and (3) the borehole used for the heat flow measurement. Errors in thermal gradient data are principally related to the depth of the determination and the interval over which the gradient has been interpolated. Measurements at great depth (> 500 m) are assigned maximum weight (5) and intervals closer to the surface have lower weights. Weights are also reduced for detrimental factors such as groundwater flow or thermal refraction. The weights for thermal conductivity data are assigned the maximum value (5) where conductivity data are available at close intervals. Weights are reduced for other data and for measurements made using transient methods. The lowest weight of 1 is assigned where thermal conductivity is estimated. The attributes necessary for the highest rating of borehole conditions include a long equilibration period (> 6 months) the existence of a fluid medium, but no hydrological flow, flat topography and uniform stratigraphy. Ratings are reduced for the absence of each attribute. Cull (1982) considers a combined quality factor of at least 333 to constitute a “good” determination. Using these criteria, more than 60% of the heat flow measurements from the CAHFP can be considered to be “good” quality or better. This value increases to around 75% for the full Australian heat flow database.

***Table A.17*** *Heat flow measurements from the CAHFP (compiled from Cull, 1982, and more recent data)*

| *Locality* | *State* | *Latitude* | *Longitude* | *Quality (1)(2)(3)* | $q_s$ *($mWm^{-2}$)* | *Reference* |
|---|---|---|---|---|---|---|
| Broken Hill | NSW | 31.95 | 141.47 | 534 | 80 | Sass and Le Marne, 1963 |
| Tennant Creek | NT | 19.67 | 134.22 | 444 | 89 | Howard and Sass, 1964 |
| Rum Jungle | NT | 13.00 | 131.00 | 433 | 84 | Howard and Sass, 1964 |
| Alice Springs | NT | 23.92 | 133.97 | 434 | 62 | Hyndman, 1967 |
| McArthur | NT | 16.47 | 136.05 | 433 | 70 | Hyndman, 1967 |
| Freweena | NT | 19.2 | 135.10 | *123* | 75 | Hyndman, 1967 |
| Cattle Creek | NT | 20.02 | 137.83 | *332* | 48 | Hyndman, 1967 |
| Warrego | NT | 19.45 | 133.82 | 554 | 113 | Sass, Jaeger and Monroe, 1976 |
| Warrego | NT | 19.45 | 133.82 | *122* | 161 | Lilley, Sloane and Sass, 1978 |
| Batchelor | NT | 13.03 | 131.08 | 344 | 80 | Sass, Jaeger and Monroe, 1976 |
| Rover | NT | 20.08 | 133.67 | 443 | 100 | Lilley, Sloane and Sass, 1978 |
| Explorer | NT | 19.68 | 134.23 | 444 | 100 | Lilley, Sloane and Sass, 1978 |
| Tanami | NT | 19.97 | 129.70 | *122* | 34 | Cull and Denham, 1979 |
| Yuendumu | NT | 22.33 | 131.73 | 333 | 56 | Cull and Denham, 1979 |
| Jabiluka | NT | 12.05 | 132.89 | 444 | 86 | Cull, 1982 |
| Blockade | Qld | 20.58 | 140.00 | 344 | 74 | Hyndman and Sass, 1966 |
| Mount Isa | Qld | 20.74 | 139.45 | 554 | 82 | Hyndman and Sass, 1966 |
| Dugald River | Qld | 20.31 | 140.20 | 334 | 72 | Cull and Denham, 1979 |
| Mount Dore | Qld | 21.8 | 140.60 | 333 | 98 | Cull and Denham, 1979 |
| Mount Whelan | Qld | 23.32 | 138.87 | 444 | 80 | Cull, 1982 |
| Eromanga Basin | Qld | 27.79 | 140.18 | | 116 | Gallagher, 1990 |
| Georgetown | Qld | 17.95 | 143.42 | *233* | 77 | Cull, 1982 |
| Arbouin | Qld | 17.33 | 145.27 | 333 | 100 | Cull, 1982 |
| Balfes Creek | Qld | 20.33 | 145.85 | 443 | 77 | Cull and Denham, 1979 |
| Radium Hill | SA | 32.50 | 140.50 | 344 | 75 | Howard and Sass, 1964 |
| Kanmantoo | SA | 35.08 | 139.25 | 333 | 88 | Sass, 1964 |
| Whyalla | SA | 33.17 | 137.50 | 343 | 91 | Sass, 1964 |
| Bendigo St | SA | 33.20 | 139.47 | 344 | 64 | Sass, Jaeger and Monroe, 1976 |
| Carrieton | SA | 32.55 | 138.48 | 343 | 92 | Sass, Jaeger and Monroe, 1976 |
| Bute | SA | 33.93 | 137.97 | 434 | 87 | Lilley, Sloane and Sass, 1978 |
| Ediacara | SA | 30.60 | 138.12 | *222* | 96 | Sass, Jaeger and Monroe, 1976 |
| Iron Knob | SA | 32.72 | 137.13 | *220* | 109 | Sass, Jaeger and Monroe, 1976 |
| Kadina | SA | 33.97 | 137.75 | 444 | 101 | Sass, Jaeger and Monroe, 1976 |
| Maralinga | SA | 30.17 | 131.60 | *322* | 54 | Sass, Jaeger and Monroe, 1976 |
| Mootooroo | SA | 32.25 | 140.93 | 544 | 68 | Sass, Jaeger and Monroe, 1976 |
| Mount Mctagga | SA | 30.45 | 139.30 | *232* | 101 | Sass, Jaeger and Monroe, 1976 |
| Parabarabana | SA | 29.98 | 139.72 | *332* | 126 | Sass, Jaeger and Monroe, 1976 |
| Stockyard | SA | 34.77 | 138.80 | *243* | 88 | Sass, Jaeger and Monroe, 1976 |
| Wudinna | SA | 32.98 | 135.55 | 344 | 58 | Sass, Jaeger and Monroe, 1976 |
| Tarcoola | SA | 30.62 | 134.50 | 334 | 49 | Sass, Jaeger and Monroe, 1976 |
| Wokurna | SA | 33.72 | 138.12 | 555 | 91 | Lilley, Sloane and Sass, 1978 |
| Olympic Dam* | SA | 26.95 | 135.33 | | 125 | Houseman et al., 1989 |
| Andamooka* | SA | 30.45 | 137.16 | | 67 | Houseman et al., 1989 |
| Rosebery | TAS | 41.77 | 145.57 | *352* | 104 | Newstead and Beck, 1953 |
| Olga Ridge | TAS | 42.77 | 145.78 | *322* | 57 | Wronski, 1977 |
| Bililuna | WA | 19.51 | 127.64 | *122* | 52 | Cull and Denham, 1979 |
| Noonkanbah | WA | 18.11 | 124.82 | 333 | 67 | Cull and Denham, 1979 |
| Halls Creek | WA | 18.23 | 127.70 | *122* | 26 | Cull and Denham, 1979 |
| St George | WA | 18.69 | 125.14 | 333 | 65 | Cull and Denham, 1979 |
| ***Average*** | | | | | **81.9** | |

*Note:* Locations of the heat flow determinations at Andamooka and Olympic Dam were not given by Houseman et al., (1989) Locations listed here are estimated

## A.3 Thermal conductivity

As noted by Horai and Shankland (1987), at normal crustal temperatures the transfer of heat via conduction ordinarily occurs through the lattice vibrations of crystals composing the rock-forming minerals. The thermal conductivity of a rock is a measure of the relative efficiency of these lattice vibrations, and is defined as the coefficient of static heat transfer. A knowledge of the variations in thermal conductivity is essential for understanding lithospheric thermal regimes, for the accurate calculation of surface heat flow from borehole thermal gradient data, and particularly for the development of models of crustal thermal regimes. Indeed as noted by Blackwell and Steele in their review paper of 1989, "if the mean thermal conductivity cannot be accurately predicted, even the most sophisticated and appropriate modelling techniques ... may fail". However, despite the importance of thermal conductivity data to many aspects of lithospheric thermal studies, its' determination and impacts have received scant attention in most published studies. Indeed, thermal conductivity is probably the most poorly constrained of the three main thermal parameters. This is due in part to the often laborious analytical method required to measure thermal conductivity, and also because empirical studies have shown that the parameter varies considerably as a function of lithotype in any given upper crustal section.

By definition, thermal conductivity ($k$) is related to thermal diffusivity ($\alpha$, the coefficient of transient heat transfer) by the density ($\rho$) and heat capacity ($c$), thus:

$$k = \rho * c * \alpha \tag{A.9}$$

There are two methods by which thermal conductivity may be measured: (1) it may be measured directly using steady-state heat sources in a divided-bar apparatus (Birch and Clark, 1940; Birch, 1950; Beck, 1957; Ratcliffe, 1959), or (2) it may be estimated following direct determination of thermal diffusivity using transient heat sources, for example the needle probe (e.g., Von Herzen and Maxwell, 1959; Beck et al., 1971; Cull, 1974; Middleton, 1993) or Quick Thermal Meter (e.g., Sass et al., 1984; Galson et al., 1987) methods. Although these are the only two methods available for the determination of thermal conductivity, several interpretative techniques have been developed for the estimation of thermal conductivity using petrophysical logs (e.g., Griffiths et al., 1992).

All of the transient heat source techniques employ an infinitely long, continuous line source of heat (a needle probe) which also contains a temperature thermistor (Von Herzen and Maxwell, 1959). The temperature near the line source is measured as a function of time, and this data is used to calculate thermal conductivity. This method is widely applicable as accurate measurements can be made in a matter of minutes. Moreover, the relatively simple construction of the apparatus means that it may be used not only for solid rock samples, but also *in situ* in ocean sediments (e.g., Von Herzen and Maxwell, 1959), soils (e.g., Lachenbruch, 1957) and liquids (e.g., Van der Held et al., 1953).

Steady state methods are generally more widely available with the first divided-bar apparatus developed during the 1930's and 1940's (e.g., Birch and Clark, 1940). The steady state method is based on the principle of constant temperature difference, with samples stacked axially within the apparatus, with constant temperature maintained at each end (e.g., Beck, 1957; Cull and Sparksman, 1977). This configuration enables the thermal gradient to be determined across the sample, allowing the thermal conductivity to be determined (see further discussion below). This apparatus is generally

used only for the routine measurement of solid rock samples, and unconsolidated cuttings. However, sample preparation is often time-consuming and laborious and depending on conditions, it may take anywhere from 20 minutes (e.g., Beck, 1957) to more than an hour (e.g., Birch, 1950) for the apparatus to reach thermal equilibrium before a measurement can be made.

The primary advantage of the transient heat source methods is the ease and speed of sample preparation and measurement. However, thermal conductivity determinations made in this way are generally less accurate than those made using steady state methods, largely because significant assumptions are often made about the specific heat capacity (see Equation A.9). For a given sample measurements using transient heat sources will have an accuracy within 10% of the mean value (e.g., Galson et al., 1987) while those using steady state methods are generally accurate to within 2% (e.g., Cull and Sparksman, 1977).

### A.3.1 Controls on the variability of thermal conductivity

As noted by Clark (1966) a considerable body of data exists on the thermal conductivity of rocks and minerals at room temperature. Generally most rocks have thermal conductivities in the range 1.5-3.5 $Wm^{-1}K^{-1}$ (Table A.18). Sedimentary rocks seem to show the greatest variation in thermal conductivity, from around 1.5 $Wm^{-1}K^{-1}$ for marine sediments to around 5 $Wm^{-1}K^{-1}$ for dolomites. In contrast, igneous and metamorphic rocks generally fall in a narrower range between 2.5-3.5 $Wm^{-1}K^{-1}$, although quartzites are characterized by significantly higher thermal conductivity (around 6-7 $Wm^{-1}K^{-1}$). As noted by Brigaud and Vasseur (1989) there are five principal factors which determine the thermal conductivity of a mineral aggregate, *viz*, mineralogy (e.g., Zierfuss, 1969), porosity and pore fluid content (e.g., Ratcliffe, 1960), rock structure (stratification and clast morphology) and temperature (e.g., Birch and Clark, 1940; Dovenyi and Horvath, 1988; Lerche, 1991). In this section I describe the way in which each of these factors impact on the thermal conductivity of rocks.

***Table A.18*** *Average thermal conductivity by lithotype*

| *Lithology* | *k ($Wm^{-1}K^{-1}$)* |
|---|---|
| Granite | 3.25 |
| Granodiorite | 2.78 |
| Gneiss | 2.78 |
| Amphibolite | 2.90 |
| Serpentinized peridotite | 2.65 |
| Dolerite | 2.00 |
| Schist | 2.40 |
| Quartzite | 6.72 |
| Limestone | 2.56 |
| Marl | 1.47 |
| Dolomite | 4.99 (1.77) |
| Shale | 2.39 (1.20) |
| Sandstone | 1.97 (2.00) |
| Air | 0.0264 |
| Water (at 293 K) | 0.598 |

All data from averaged from a compilation by Clark (1966). Data in parentheses correspond to recent sedimentary rocks including dolomites, shales and sandstones taken from the ocean floor (Periera et al., 1986). The values of air and water are shown for comparison.

*Mineralogy*

The dependence of thermal conductivity on mineralogy is well recognised and has been subject of considerable study. Numerous thermal conductivity measurements have been made on mono-mineralic aggregates and much of this data has been compiled into datasets of standard values. For example, Brigaud and Vasseur (1989) list thermal conductivity values for many common

sedimentary minerals and Clark (1966) compiled thermal conductivity data for a range of sedimentary, igneous and metamorphic minerals. It is reasonable to expect that the thermal conductivity of a rock aggregate will be some volumetric average of the thermal conductivities of the constituent minerals, and the pore fluid (air in the case of dry-samples). In terms of sedimentary rocks, thermal conductivities of clay minerals are systematically lower than non-clay minerals (Table A.19) and the relative proportion of each exerts the primary mineralogical control on the average thermal conductivity of sedimentary rocks (Brigaud and Vasseur, 1989). These observations suggest that shales and siltstones will generally have lower thermal conductivity than sandstones or limestones of the same sequence (Table A.18).

***Table A.19*** *Thermal conductivity data for some common minerals and mono-mineralic aggregates*

| *Mineral* | *Conductivity* ($Wm^{-1}K^{-1}$) | *Mineral* | *Conductivity* ($Wm^{-1}K^{-1}$) |
|---|---|---|---|
| quartz | 7.7 | illite | 1.9 |
| calcite | 3.3 | smectite | 1.9 |
| dolomite | 5.3 | kaolinite | 2.6 |
| talc * | 3.0 | halite * | 5.9 |
| gypsum * | 1.3 | fluorite * | 4.0 |
| anhydrite | 6.3 | chlorite | 3.3 |
| serpentine* | 2.5 | hornblendite* | 2.8 |
| anorthosite* | 2.1 | garnet* | 3.6 |
| diopside* | 4.3 | pyroxenite* | 3.6 |

Note: Data labelled (*) from Clark, 1966. Other data from Brigaud and Vasseur, 1989

*Temperature*

The effect of temperature on the variability of thermal conductivity is less well understood and for this reason the potential variations in thermal conductivity with temperature are generally ignored in most thermal modelling studies. Under laboratory conditions thermal conductivity is generally measured at room temperature (~ 25°C) as this is generally the most convenient method of setting up the experimental apparatus. However, in many regions it is not unusual for down-hole temperatures of the order of 200-250°C to be reached at relatively shallow depths (e.g., Dovenyi and Horvath, 1988, for the Pannonian Basin; Gallagher, 1990, for the Cooper Basin). In many regions empirical relationships are used to describe the temperature dependence of thermal conductivity. One such relationship is that described by Lerche (1991):

$$k(T) = k_o\left(\frac{1+\alpha T_o}{1+\alpha T}\right) \qquad \text{(A.10)}$$

where, $k(T)$ is the thermal conductivity at temperature $T$ (in degrees Kelvin) and $k_o$ is the thermal conductivity of the same unit measured at a reference temperature of 300 K ($T_o$). $\alpha$ is a material coefficient which is positive for all sedimentary units except shales. Many specializations of this equation have been developed for different sedimentary basins (e.g., Sekiguchi, 1984, for basins in Japan). In general, thermal conductivity of an isotropic rock unit will decrease with increasing temperature. There are however some exceptions to this trend, including shales which show an increase in thermal conductivity of about 30% over a temperature range of 273-700 K (Lerche, 1991). An increase in thermal conductivity with temperature is also generally shown by materials which at lower temperatures are quite poor conductors, for example, feldspar aggregates and silica glass (Birch and Clark, 1940). Although such relationships between temperature and thermal conductivity are known, Lerche (1991) suggests that for typical sedimentary sequences which are dominated by silts and sandstones the effect of the temperature dependence of thermal conductivity is negligible until the sequence is at least around 10-20km in thickness. Examples of the way in which thermal

***Table A.20*** *Selected data on the variation in thermal conductivity with temperature*

| *Rock* | *Temperature (°C)* | *Conductivity ($Wm^{-1}K^{-1}$)* | *Rock* | *Temperature (°C)* | *Conductivity ($Wm^{-1}K^{-1}$)* |
|---|---|---|---|---|---|
| Granite | 0 | 6.66 | Dunite | 0 | 12.4 |
| | 50 | 6.25 | | 50 | 10.5 |
| | 100 | 5.90 | | 100 | 9.4 |
| | 200 | 5.50 | | 200 | 8.1 |
| Marble | 0 | 5.4 | Quartz | 0 | 13.1 |
| | 20 | 5.7 | sandstone | 100 | 10.3 |
| | 100 | 4.9 | | 200 | 8.7 |
| | 350 | 3.2 | | | |
| All data from a compilation by Clark (1966) | | | | | |

conductivity varies for a number of common rock types are given in Table A.20 (data from Clark, 1966).

*Porosity and pore fluids*

As noted above the thermal conductivity of any bulk rock aggregate will be some volumetric average of the thermal conductivity of the individual constituent mineral phases and of the fluid which fills any available pore space. Rock pore space can be filled with various kinds of fluid: air, water, saline water, oil or gas, which all have widely varying thermal conductivities. In particular, air has a thermal conductivity of $0.0264 Wm^{-1}K^{-1}$ which is significantly less than the conductivity of water (around $0.598\ Wm^{-1}K^{-1}$ and $0.61 Wm^{-1}K^{-1}$, Clark, 1966; Gallagher, 1987). This difference, even in rocks of very low porosity (1%-5%) can make a difference of up to 30% in the value of measured conductivity (e.g., Scharli and Rybach, 1984). This effect is quite significant given that the natural range of rock thermal conductivity is generally only around $1.5\text{-}3.5\ Wm^{-1}K^{-1}$. Generally thermal conductivity studies include sample measurements under both water and air saturated conditions.

*Rock Structure*

Thermal conductivity, for sedimentary and layered metamorphic rocks, is routinely measured perpendicular to bedding. However, as discussed by Brigaud and Vasseur (1989) there is significant directional variability of thermal conductivity in layered rocks. In general, thermal conductivity when measured parallel to layering is greater than the tkermal conductivity measured perpendicular to that layering. Other rock structures, such as fractures, also affect the measured thermal conductivity. Griffiths et al., (1992) show that fractures within a sample provide pathways for the preferential flow of heat and so measured thermal conductivity in strongly fractured rocks is significantly lower than the thermal conductivity of an equivalent unfractured sample.

### A.3.2 Thermal conductivity measurements: Analytical method

As part of this study, thermal conductivity measurements were made on sedimentary and metasedimentary rocks from the Mount Isa and Mount Painter regions. These determinations were made using steady state heat source methods in a standard divided-bar apparatus constructed at the University of Adelaide, Department of Geology and Geophysics by Mr. John Stanley. The configuration of this apparatus is very similar to that described by Cull and Sparksman (1977), and Birch (1950). The apparatus is illustrated in Figure A.1.

After field collection suitable samples were chosen for thermal conductivity analysis. Samples were first cut into blocks and then a core (25 mm in diameter) was drilled from each block. Cores were generally orientated perpendicular to layering, although for some samples a core was also taken parallel to layering to investigate the directional variability of sample thermal conductivity. After drilling, the core samples were cut and then ground (using a diamond lap) into small disks generally 10 mm in thickness. The ends of each disk were made as close to parallel as possible by the use of accurate caliper measurement.

The sample disc was then loaded axially into a stack within a vertical press. The sample was placed between two brass plates which each contained a ~ 2mm thick disc of the secondary standard "lexan" (Figure A.1). The lexan standards were used at each end of the stack to allow two separate determinations of heat flux to be made (Cull and Sparksman, 1977). Water, from thermostatically controlled baths, circulated across the top and the base of the stack to keep each brass plate at constant temperature, ~ 35°C at the top of the stack and ~ 25°C at the bottom of the stack. Thermocouples were inserted into the brass plates either side of the lexan both above and below the sample disc (Figure A.1). The thermocouples were used to monitor the temperatures through the stack in order that the thermal gradients across both the sample and the lexan standard could be determined. In the apparatus used in this study, chrome / alumel thermocouples were used, connected to a nanovoltmeter. Data was collected using a *Datataker 50* datalogger, connected directly to a PC. During the measurements, the stack was kept under a constant pressure of ~ 10 MPa

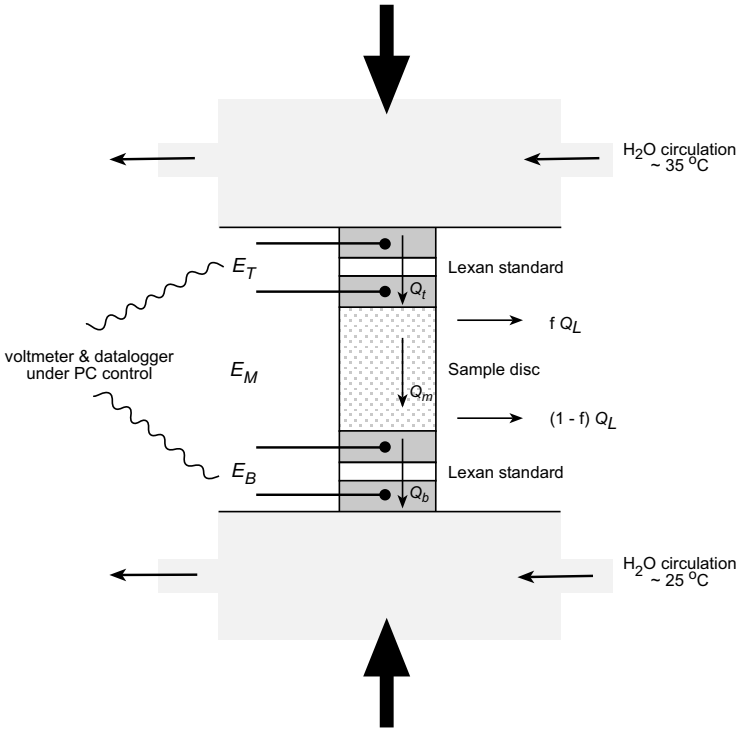


**Figure A.1** Schematic illustration of divided-bar apparatus used for thermal conductivity measurements, after Cull and Sparksman (1977).

through the use of a simple hydraulic pump and the sample stack was insulated using polystyrene shielding. Various pastes, including heat sink compounds, were trialed to provide a good thermal contact between the sample and the brass plates. On advice from Dr. Colin Williams (United States Geological Survey, Menlo Park, CA) and Dr. Ted Lilley (Research School of Earth Sciences, ANU) common household detergent was found to be the most satisfactory 'thermolyte' and the results shown in Tables A.21, A.22 and A.23 were all obtained using this configuration. Because all the surfaces had been polished flat and the stack was under pressure, contact resistance was assumed to be sufficiently small to be ignored (e.g., Cull and Sparksman, 1977).

If the system can be considered to be closed, the heat flow through the stack is constant and so Fouriers Law applies (Equation A.8). Consequently the thermal conductivity of the sample ($k_S$) will be given by:

$$k_S = \frac{k_R * \beta_R}{\beta_S} \tag{A.11}$$

where $k_R$ is the conductivity of the primary reference material, $\beta_S$ is the thermal gradient through the sample and $\beta_R$ is the thermal gradient through the secondary standard. Before making determinations on unknown samples, the system must first be calibrated using the primary standards: fused silica and crystalline quartz. If conduction through the apparatus were perfect, then this procedure would be straightforward. However, despite attempts to insulate the apparatus, there are generally significant losses of heat though the sides of the stack, and so in reality the heat flux through the three segments of the apparatus is more accurately described by the equations:

$$Q_M = Q_T - (f * Q_L) \tag{A.12}$$

$$\text{and,} \quad Q_M = Q_B + (1-f) * Q_L \tag{A.13}$$

where $Q_T$ is the heat flux through the top of the stack, $Q_M$ the heat flux through the sample space, $Q_B$ the heat flux through the bottom of the stack, $Q_L$ the total radial heat loss and $f$ the fraction of $Q_L$ lost in the top half of the stack. By eliminating $Q_L$ the equations can be reduced to :

$$Q_T = Q_M + f * (Q_T - Q_B) \tag{A.14}$$

In the divided bar apparatus, the change in temperature is given by the drop in voltage registered by the thermocouples across each junction and the thickness ($z$) of each segment. Because the stack is symmetric (Figure A.1) the thermal conductivity of the standard at the top and bottom of the stack will both be equal to the thermal conductivity of the lexan, thus: $k_T = k_B = k_L$. Likewise, the thickness of the standard at the top and bottom will also be equal, $z_T = z_B = z_L$. Equation A.14 above can then be reduced to the calibration equation, thus:

$$\left(\frac{Z_L}{k_L}\right) * \left(\frac{k_s * E_s}{z_s}\right) = E_T - f\left(E_T - E_B\right) \tag{A.15}$$

where $z_s$ is the thickness of the sample, $k_s$ is the thermal conductivity of the sample, $E_s$ is the voltage across the sample space, $E_T$ is the voltage across the top lexan standard and $E_B$ is the voltage across the bottom lexan standard. The factor $f$ has been determined to be 0.625 by Cull and Sparksman (1977). Calibration of the bar, generally by the use of one or more primary standards, is required to determine the thermal conductivity of the lexan standard, $k_L$. For work associated with this thesis,

the system was calibrated using both primary quartz and fused silica standards, first using standards loaned by Professor Jim Cull (Monash University) and a second set manufactured by Jung Precision Optics in Salisbury, South Australia. The thermal conductivity of the fused silica and crystalline quartz standards was taken from Ratcliffe (1959). The variation in the conductivity of the lexan standard provided an internal check on the variability of the apparatus. A total of 40 determinations over the period from November 1997 to May 1999 gave an average thermal conductivity for the secondary lexan standard of 0.16 $Wm^{-1}K^{-1}$.

Rearranging Equation A.15, the conductivity of an unknown sample ($k_s$) is given by:

$$k_s = \left(\frac{k_L}{8z_L}\right) * \left(\frac{3E_T + 5E_B}{E_s}\right) * z_s \qquad \text{(A.16)}$$

where for the apparatus used here, $z_L$ = 1.1 mm, and the thickness of the samples, $z_S$, was generally around 1 cm. Samples of this thickness are generally useful in decreasing the total thermal resistance and heat losses through the sides of the stack. In the following tables I list thermal conductivity data for samples from the Mount Isa and Mount Painter regions.

**Table A.21** *Sample descriptions and thermal conductivity data, Mount Isa Inlier (outcrop samples)*

| *Sample* | *Lithology* | *Location* | | *Description* | *Comments* | *Voltage readings* | | | *k sample** |
|---|---|---|---|---|---|---|---|---|---|
| | | *Easting* | *Northing* | | | $E_{top}$ | $E_{bottom}$ | $E_{sample}$ | |
| 98ISA01 | Judenan beds bt gneiss | 338750 | 7696400 | high grade biotite gneissic unit | 1 | 0.159 | 0.0782 | 0.13324 | **2.659** |
| | | | | | 2 | 0.1615 | 0.0789 | 0.1329 | **2.644** |
| | | | | | 3 | 0.1660 | 0.0797 | 0.1279 | **2.595** |
| 98ISA02 | Judenan beds mica qzte | 338750 | 7696400 | mica rich quartzite - much coarser than quartzites from further east, indicating steep metamorphic gradients across only 1-2 km. Possible replacement of sillimanite | 1 | 0.1780 | 0.0512 | 0.1528 | **4.595** |
| | | | | | 2 | 0.1754 | 0.0495 | 0.1452 | **4.575** |
| | | | | | 3 | 0.1864 | 0.0452 | 0.1397 | **5.062** |
| 98ISA03 | ECV pelitic schist | 336300 | 7701100 | mica schist (? possible replacement of cd) | | - | - | - | **-** |
| 98ISA04 | ECV amphibolite | 336900 | 7700825 | amphibolite | | 0.1454 | 0.1251 | 0.1091 | **1.427** |
| 98ISA05 | Sybella Batholith, main phase | 336100 | 7682650 | coarse grained porphyritic kspar and biotite granite | | - | - | - | **-** |
| 98ISA06 | ECV oa/hbde bearing schist | 333400 | 7681850 | high grade amphibolite, orthoamphibole bearing schist and hornblende bearing schist (sampled from a retrograde shear zone) | | - | - | - | **-** |
| 98ISA07 | ECV oa bearing mafic | 337550 | 7696850 | orthoamphibole bearing mafic | | - | - | - | **-** |
| 98ISA08 | Paradise Ck Fn, quartzite | 298250 | 7739050 | quartzite | 1 | 0.1694 | 0.0564 | 0.1439 | **3.957** |
| | | | | | 2 | 0.1713 | 0.0577 | 0.1435 | **3.839** |
| 98ISA09 | Gunpowder Ck Fn, sandy shale | 306900 | 7740050 | sandy shale | 1 | 0.138 | 0.136 | 0.1086 | **1.278** |
| | | | | | 2 | 0.142 | 0.1195 | 0.11266 | **1.494** |
| | | | | | 2 (Repeat) | 0.1420 | 0.1239 | 0.1116 | **1.442** |
| | | | | | WS | 0.1695 | 0.1016 | 0.1025 | **1.825** |
| 98ISA10 | Judenan Beds, Haslingden Gp | 308550 | 7739850 | quartzite | 1 | 0.18 | 0.0445 | 0.14817 | **5.225** |
| | | | | | 2 | 0.1785 | 0.0458 | 0.1485 | **5.076** |
| 98ISA11 | Carters Bore Rhyolite | 307600 | 7740000 | quartz-feldspar porphyry | | - | - | - | **-** |
| 98ISA13 | Corella Fn, scapolitic granofels | 381150 | 7710975 | scapolitic granofels | 1 | 0.1570 | 0.0920 | 0.1281 | **2.197** |
| | | | | | 2 | 0.1576 | 0.0894 | 0.1284 | **2.266** |
| 98ISA14 | Corella Fn, scapolitic granofels | 381650 | 7704050 | scapolitic granofels | | - | - | - | **-** |

**Table A.21** *continued ...*

| Sample | Lithology | Location | | Description | Comments | Voltage readings | | | k sample* |
|---|---|---|---|---|---|---|---|---|---|
| | | Easting | Northing | | | $E_{top}$ | $E_{bottom}$ | $E_{sample}$ | |
| 98ISA15 | Corella Fn, calc-silicate | 402650 | 7701200 | high grade calc-silicate from margin of Burstall Granite; amph + epidote + kspar | 1 | 0.1530 | 0.1106 | 0.1249 | **1.755** |
| | | | | | 2 | 0.1534 | 0.1031 | 0.1236 | **1.889** |
| 98ISA16 | Burstall Granite | 402100 | 7701650 | Deformed, coarse grained bt + plag + qz granite | | - | - | - | **-** |
| 98ISA17 | Breakaway Shale | 343200 | 7723500 | finely laminated purple and white dolomitic shale with relic pyrite crystals; weathered | 1 | 0.1325 | 0.1411 | 0.1054 | **1.136** |
| | | | | | 2 | 0.1284 | 0.1588 | 0.0986 | **1.005** |
| 98ISA18 | Breakaway Shale | 347250 | 7721050 | finely laminated white shale (weathered) | | 0.1476 | 0.1311 | 0.1022 | **1.323** |
| 98ISA18a | Urquhart Shale | 345650 | 7722650 | ferruginous white shale; relic pyrite | 1 | 0.1596 | 0.0890 | 0.1248 | **2.252** |
| | | | | | 2 | 0.1560 | 0.0921 | 0.1267 | **2.173** |
| 98ISA19 | ECV Lena Quartzite | 351600 | 7708100 | quartzite - well developed outcrop scale cleavage | | 0.1803 | 0.0533 | 0.1396 | **4.228** |
| 98ISA20 | Kalkadoon Batholith | 361450 | 7711900 | coarse to medium grained mafic from granite margin | | - | - | - | **-** |
| 98ISA21 | Lower Mount Guide Quartzite | 357400 | 7709175 | fine to medium arkosic sandstone, contains some relic kspar grains | | 0.1637 | 0.0787 | 0.1330 | **2.672** |
| 98ISA22 | Upper Mount Guide Quartzite | 352500 | 7710350 | feldspathic sandstone | 1 | 0.1743 | 0.0565 | 0.1435 | **3.992** |
| | | | | | 1 (WS) | 0.1734 | 0.0481 | 0.1462 | **4.729** |
| 98ISA23 | ECV Cromwell Metabasalt | 352050 | 7710050 | very fine grained mafic | 1 | 0.1689 | 0.0785 | 0.1371 | **2.761** |
| | | | | | 2 | 0.1593 | 0.0870 | 0.1257 | **2.313** |
| 98ISA24 | Native Bee Siltstone | 343250 | 7709150 | grey finely laminated and siltstone with well developed cleavage; possibly transitional facies from Breakaway Shale | | 0.1432 | 0.1287 | 0.1076 | **1.353** |
| 98ISA25 | Moondarra Siltstone | 343600 | 7703400 | very fine grained laminated grey siltstone | | - | - | - | **-** |
| 98ISA26 | Myally sub-group (undiff) | 344350 | 7697850 | siltstone, well bedded with good cleavage | | 0.1195 | 0.1696 | 0.0895 | **0.855** |
| 98ISA27 | ECV Cromwell Metabasalt | 346250 | 7693850 | fine grained amphibolite; very well developed cleavage | | 0.1619 | 0.0879 | 0.1296 | **2.344** |
| 98ISA28 | Mount Guide Quartzite | 349400 | 7691900 | feldspathic sandstone containing some epidote which may be a contact effect due to proximity of Leichhardt Volcanics (?) | | 0.1730 | 0.0648 | 0.1394 | **3.414** |
| 98ISA29 | Kalkadoon Batholith, main | 350650 | 7685400 | mafic from margin of Batholith | | - | - | - | **-** |

**Table A.21** *continued ...*

| *Sample* | *Lithology* | *Location* | | *Description* | *Comments* | *Voltage readings* | | | *k sample** |
|---|---|---|---|---|---|---|---|---|---|
| | | *Easting* | *Northing* | | | $E_{top}$ | $E_{bottom}$ | $E_{sample}$ | |
| 98ISA30 | Kalkadoon Batholith, main | 369300 | 7708400 | coarse qz, bt, plag, minor kspar leucogranite | | - | - | - | **-** |
| 98ISA31a,b,c | Ballara Quartize | 370650 | 7708450 | calcareous quartzite --> variable in outcrop | | 0.1520 | 0.1142 | 0.1200 | **1.681** |
| 98ISA32 | Corella Formation | 377950 | 7704050 | limestone and calcareous granofels, very fine grained containing some epidote (?) | | 0.1550 | 0.0956 | 0.1278 | **2.100** |
| 98ISA33 | Deighton Quartzite | 380100 | 7703800 | white sugary textured quartzite | | 0.1791 | 0.0541 | 0.1381 | **4.128** |
| 98ISA34 | Moondarra Siltstone | 347300 | 7717350 | well bedded, finely laminated silts, grey to brown; $S_o$ 086/22N | | 0.157 | 0.092 | 0.12832 | **2.195** |
| 98ISA35 | Basal Warrina Park Quartzite | 351600 | 7722450 | Silver-grey fine grained quartzite with some cleavage and joint development | | 0.1818 | 0.0408 | 0.1498 | **5.764** |
| 98ISA36,a | Warrina Park Quartzite | 349850 | 7722100 | ferruginous siltstone/sandstone, transitional quartzite from *Piw3* | quartzite | 0.1755 | 0.0563 | 0.1450 | **4.042** |
| | | | | | siltstone | 0.131 | 0.1555 | 0.0926 | **1.000** |
| | | | | | siltstone | 0.125 | 0.158 | 0.0976 | **0.993** |
| 98ISA37 | Warrina Park Quartzite | 350600 | 7722200 | basal ferruginous siltstones, very fine grained and finely laminated red-bed siltstones; some lighter Fe-poor bands | | 0.1471 | 0.1353 | 0.0946 | **1.229** |
| 98ISA38 | Breakaway Shale | 350050 | 7721400 | grey finely laminated shale/siltstone; very fine grained; well developed cleavage | | - | - | - | **-** |
| 98ISA39 | Moondarra Siltstone | 342200 | 7722300 | grey well cleaved siltstone, finely laminated, weathered | | - | - | - | **-** |
| 98ISA40 | Native Bee Siltstone, transitional | 342100 | 7718250 | pink-dark grey finely laminated dolomitic siltstones, very fine grained and containing some relic pyrite | 1 | 0.1566 | 0.0955 | 0.1280 | **2.113** |
| | | | | | 2 | 0.1520 | 0.0993 | 0.1232 | **1.942** |
| 98ISA41 | Urquhart Shale | 341900 | 7709800 | very weathered red-grey laminated shales, $S_o$ 175/57W | | 0.1164 | 0.1685 | 0.0922 | **0.852** |
| 98ISA42 | Kennedy Siltstone | 341000 | 7710250 | layered dolomitic siltstone (weathered), brown to grey laminations on 0.5-0.25cm scale; $S_o$ 180/67W | | - | - | - | **-** |
| 98ISA43 | Judenan Beds, Haslingden Gp | 340600 | 7710500 | pelitic schist; variable to fine grained quartzite containing bt (mainly in veinlets) and mu; well lineated and foliated schists ?possible relic sillimanite, $S_1$ 174/55W | | 0.1678 | 0.0798 | 0.1239 | **2.529** |

**Table A.21** *continued ...*

| *Sample* | *Lithology* | *Location* | | *Description* | *Comments* | *Voltage readings* | | | *k sample** |
|---|---|---|---|---|---|---|---|---|---|
| | | *Easting* | *Northing* | | | $E_{top}$ | $E_{bottom}$ | $E_{sample}$ | |
| 98ISA44 | Judenan Beds, Haslingden Gp | 339100 | 7709750 | feldspathic quartzite, weathered, pink-orange-white and sugary in texture | 1 | 0.1769 | 0.0505 | 0.1485 | **4.586** |
| | | | | | 2 | 0.1818 | 0.0478 | 0.1468 | **4.869** |
| 98ISA45 | Native Bee Siltstone | 339850 | 7695500 | sampled from adjacent to Mount Isa Fault but no evidence for metamorphic mineral growth - well cleaved and finely laminated grey siltstones | | 0.1139 | 0.1881 | 0.0805 | **0.720** |
| 98ISA46 | ECV quartzite sub-unit | 338850 | 7690300 | grey-silver sugary quartzite, epidote absent, ?some feldspar; weathered | | 0.1770 | 0.0458 | 0.1506 | **5.101** |
| 98ISA47 | ECV | 334550 | 7680400 | deformed, strongly foliated and lineated fine grained hbde + plag + epidote + oa amphibolite; also contains embayed orthoamphibole splays | | 0.152 | 0.1015 | 0.11785 | **1.873** |
| 98ISA48 | ? Native Bee Siltstone | 340600 | 7691700 | grey to dark grey very fine grained laminated siltstone | | - | - | - | **-** |
| 98ISA49 | ECV pelitic interbed | 325400 | 7684150 | retrogressed porphyroblastic mica (bt + mu) schist. Blasts pre-date foliation development as they are flattened and replaced by fabric forming bt + mu. Also later stage random bt on foliation plane | | - | - | - | **-** |
| 98ISA50 | May Downs Gneiss | 331100 | 7691500 | sillimanite schist within May Downs Gneiss. Fabric forming and also later post-kinematic randomly orientated sillimanite | | - | - | - | **-** |
| 98ISA51 | Mount Guide Quartzite | 335250 | 7700550 | sugary grey-silver quartzite with some micaceous interbeds. Sampled from close to the contact with a small amphibolite dyke | | 0.173 | 0.0658 | 0.13516 | **3.299** |
| 98ISA52 | Breakaway Shale | 341650 | 7723300 | weathered, grey-white cleaved siltstone; evidence of relic pyrite | | 0.149 | 0.1175 | 0.10809 | **1.521** |
| 98ISA53 | Surprise Creek Formation; siltstone | 363250 | 7721500 | grey laminated and heavily cleaved siltstones, contain possible mica growth | | 0.148 | 0.1203 | 0.11168 | **1.445** |
| 98ISA54 | Surprise Creek Formation; siltstone | 363000 | 7721050 | representative grey laminated siltstones - no obvious metamorphic mineral development. Some primary sedimentary features preserved | | 0.1317 | 0.1447 | 0.1042 | **1.135** |

**Table A.21** *continued ...*

| *Sample* | *Lithology* | *Location* | | *Description* | *Comments* | *Voltage readings* | | | *k sample** |
|---|---|---|---|---|---|---|---|---|---|
| | | *Easting* | *Northing* | | | $E_{top}$ | $E_{bottom}$ | $E_{sample}$ | |
| 98ISA55 | Surprise Creek Formation; quartzite | 362800 | 7720750 | scree but moderately fresh quartzite sample, typical silver, sugary textured quartzite | | 0.193 | 0.0506 | 0.12697 | **4.365** |
| 98ISA56 | Surprise Ck Formation; quartzite | 362400 | 7720500 | quartzite, heavily cleaved and fractured | | 0.157 | 0.0887 | 0.12635 | **2.256** |
| 98ISA-CLAST X,Y, MATRIX A | Warrina Park Quartzite, conglomerate | 349650 | 7708400 | Conglomerate at base of Warrina Park Quartzite, samples taken of 2 types of quartzite clasts and a powder sample of the qz + kspar gravelly arkosic matrix | Quartzite clast X | 0.1817 | 0.0436 | 0.1462 | **5.318** |
| 98ISA-SYC1,1a | ECV pelitic schist | 334300 | 7717300 | mica schist from old workings, contains retrogressed relic ?cd porphyroblasts which are now replaced by fabric forming ?bt + mu | | - | - | - | **-** |
| 98ISA-SYC2 | *(do)* Mafics | 335300 | 7717100 | "undeformed" or "igneous textured" mafics which are more likely recrystallised pre-metamorphic ECV mafics | | - | - | - | **-** |
| 98ISA-SYC3 | ECV pelitic schist | 336700 | 7717200 | magnetite-chlorite schist (some with relic orthoamphibole) from within the main fabric which wraps around the "undeformed" mafics. Possible cross-cutting SZ present | | - | - | - | **-** |
| 98ISA-SYC4 | *(do)* Mafics | 336400 | 7717300 | “undeformed igneous textured” mafic dyke which cross cuts the more amphibolitic (hornblende) rich mafics – need to look for metamorphic recrystallization textures | Thin Section | - | - | - | **-** |
| 98ISA-SYC5 | *(do)* Mafics | 336450 | 7717300 | recrystallized amphibolite | Thin Section | - | - | - | **-** |
| 98ISA-SYC6 | *(do)* Mafics | 336500 | 7717300 | sheared and well foliated amphibolite from boudin neck far east of SYC outcrop. Need to section to look for deformation textures associated with the macroscopic boudinage. | Thin Section | - | - | - | **-** |
| 98ISA-SYC7 | *(do)* Mafics | 336100 | 7717500 | recrystallized mafic, looks undeformed again but still from within the boudin core | Thin Section | - | - | - | **-** |
| 98ISA-SYC8 | (do) Mafics | 336500 | 7717500 | mafic from dyke which was mapped out and photographed, dyke is clearly folded into the regional fabric of the chl + mt retrogressed schists. Again looks undeformed and contains hornblende porphyroclasts? | Thin Section | - | - | - | **-** |

**Table A.21** *continued ...*

| *Sample* | *Lithology* | *Location* | | *Description* | *Comments* | *Voltage readings* | | | *k sample** |
|---|---|---|---|---|---|---|---|---|---|
| | | *Easting* | *Northing* | | | $E_{top}$ | $E_{bottom}$ | $E_{sample}$ | |
| 98ISA-KP1 | *(do4)* Mafics, Sybella microgranite | 330000 | 7722500 | contact between Sybella “microgranite” and *do4* dolerites – field relationships suggest the granite intruded into the mafics. Both lithologies look undeformed but must pre-date the deformation; absence of deformation likely to be the result of strain partitioning | | - | - | - | **-** |
| 98ISA-KP2 | *(do4)* Mafics | 330000 | 7722500 | representative sample of the mafics from near the Sybella contact, the two lithologies may be comagmatic or more likely the mafics are earlier and part of the ECV succession | Thin Section | - | - | - | **-** |
| 98ISAUG1 | Urquhart Shale | Mount Isa Mine | | Fresh sample of Urquhart shale from underground in the main Mount Isa Mine, finely laminated black shale containing abundant pyrite | | 0.1660 | 0.0783 | 0.1291 | **2.653** |
| | | | | | * | 0.1624 | 0.0791 | 0.1356 | **2.677** |
| | | | | | Parallel to $S_1$ | 0.1629 | 0.0689 | 0.1400 | **3.137** |

(1) All measurements unless otherwise indicated were made on air saturated sample cores. Measurements denoted by “WS” were taken on water saturated cores. All measurement taken on cores orientated perpendicular to the primary (sedimentary) layering unless otherwise indicated. Numbers in the Comments column indicate duplicate cores cut from the same sample. Comments indicate variations in run conditions, or sample orientation; parallel = parallel to bedding.

(2) Pressures were maintained at 10000 kPa (0.1 kbar) during the course of each thermal conductivity determination

(3) Some terminology (*do*, *do4* etc) taken from 1:100 000 scale “Mount Isa” geological map compiled between 1971 and 1975 by R.M. Hill and M. Little, published in 1978 by the Bureau of Mineral Resources, Canberra, ACT; ECV = Eastern Creek Volcanics

(4) Mineral abbreviations are as follows: oa = orthoamphibole; hbde = hornblende; chl = chlorite; mt = magnetite; bt = biotite; mu = muscovite; qz = quartz; cd = cordierite; kspar = K-feldspar; plag = plagioclase

**Table A.22** *Thermal conductivity data, Mount Isa Inlier (drill core samples)*

| *Sample* | *Lithology* | *Depth* | *Drillhole name* | *Comments* | *Voltage readings* | | | *k sample** |
|---|---|---|---|---|---|---|---|---|
| | | | | | $E_{top}$ | $E_{bottom}$ | $E_{sample}$ | |
| 98ISA-AU1 | Paradise Creek Formation | 256.7 | Buckley River BR069D | | 0.1754 | 0.0732 | 0.1328 | **2.957** |
| 98ISA-AU2 | Paradise Creek Formation | 256.5 | Buckley River BR069D | | 0.172 | 0.0694 | 0.1321 | **3.083** |
| 98ISA-AU3 | Paradise Creek Formation | 196.3 | Buckley River BR069D | | 0.1817 | 0.0641 | 0.1330 | **3.433** |
| 98ISA-AU4 | Paradise Creek Formation | 196.1 | Buckley River BR069D | | 0.1685 | 0.0658 | 0.1399 | **3.296** |
| 98ISA-AU5 | Paradise Creek Formation | 207.3 | Buckley River BR069D | | 0.1683 | 0.0769 | 0.1393 | **2.839** |
| 98ISA-AU6 | Paradise Creek Formation | 207.8 | Buckley River BR069D | | 0.1682 | 0.0695 | 0.1352 | **3.089** |
| 98ISA-AU7 | Paradise Creek Formation | 223.4 | Buckley River BR069D | | 0.1714 | 0.0686 | 0.1324 | **3.112** |
| 98ISA-AU8 | Paradise Creek Formation | 233.4 | Buckley River BR069D | | 0.1731 | 0.0605 | 0.1384 | **3.642** |
| 98ISA-AU9 | Paradise Creek Formation | 238.6 | Buckley River BR069D | | 0.1671 | 0.0714 | 0.1346 | **2.988** |
| 98ISA-AU10 | Paradise Creek Formation | 269.3 | Buckley River BR069D | | 0.1743 | 0.0600 | 0.1369 | **3.631** |
| 98ISA-AU11 | Paradise Creek Formation | 329.6 | Buckley River BR069D | | | | | |
| 98ISA-AU12 | Native Bee Siltstone | 336.9 | Hilton Deep Stratigraphic Hole 941007 HILTON Q541 WD1 | | 0.1623 | 0.0966 | 0.1197 | **2.027** |
| 98ISA-AU13 | Native Bee Siltstone | 334.7 | Hilton Deep Stratigraphic Hole 941007 HILTON Q541 WD1 | | 0.1649 | 0.0752 | 0.1369 | **2.850** |
| 98ISA-AU14 | Native Bee Siltstone | 703.9 | Hilton Deep Stratigraphic Hole 941007 HILTON Q541 WD1 | 1 | 0.1547 | 0.1039 | 0.1154 | **1.823** |
| | | | | 2 | 0.1546 | 0.0990 | 0.1250 | **2.000** |
| 98ISA-AU15 | Native Bee Siltstone | 715.5 | Hilton Deep Stratigraphic Hole 941007 HILTON Q541 WD1 | | 0.163 | 0.0834 | 0.1271 | **2.450** |
| 98ISA-AU16 | Native Bee Siltstone | 457.8 | Hilton Deep Stratigraphic Hole 941007 HILTON Q541 WD1 | | 0.167 | 0.0758 | 0.1377 | **2.854** |
| 98ISA-AU17 | Native Bee Siltstone | 461.7 | Hilton Deep Stratigraphic Hole 941007 HILTON Q541 WD1 | | 0.163 | 0.0826 | 0.128 | **2.485** |
| 98ISA-AU18 | Native Bee Siltstone | 588.6 | Hilton Deep Stratigraphic Hole 941007 HILTON Q541 WD1 | | 0.162 | 0.0833 | 0.1313 | **2.483** |

Access to core samples and drill logs courtesy of MIM Exploration, Mount Isa. Thanks are due to Rick Valenta, Richard Downs and Paul Jose for their assistance.

Details of sample and experimental configuration the same as shown in Table A.21

**Table A.23** *Sample descriptions and thermal conductivity data, Mount Painter Inlier (outcrop samples)*

| *Sample* | *Lithology* | *Location* | | *Description* | *Comments* | *Voltage readings* | | | *k sample** |
|---|---|---|---|---|---|---|---|---|---|
| | | *Easting* | *Northing* | | | $E_{top}$ | $E_{bottom}$ | $E_{sample}$ | |
| 97MTP01 | Quartzite of the Gunsight Prospect (Unit 3, volcanics, schist and quartzite) | | | very well bedded quartzite with kspar, diopside banding and fine heavy mineral lamellae, Unit is very ferruginous in o/c and directly overlies Mt. Neill Granite | | 0.1487 | 0.0991 | 0.1261 | **1.975** |
| 97MTP02 | sandstone | | | Sugary textured sandstone or low grade quartzite | | 0.1699 | 0.0517 | 0.1490 | **4.414** |
| 97MTP03 | Opaminda Formation | 341850 | 6638250 | Very fine grained dark grey siltstones with some small beds of coarser sands. Unit also contains minor interbeds of limestone and green shale. | | 0.1417 | 0.1153 | 0.1184 | **1.604** |
| 97MTP04 | Blue Mine Conglomerate | 341710 | 6637460 | feldspathic quartzite member of the Blue Mine Conglomerate, coarse grained to arkosic sandstone, blocky in o/c | | | | | |
| 97MTP05 | Tapley Hill/basal Balcanoona Formation | 341900 | 6637170 | hard, well cemented dolostone | 1 | 0.1671 | 0.0602 | 0.1451 | **3.703** |
| | | | | | 2 | 0.1688 | 0.0599 | 0.1429 | **3.705** |
| 97MTP05a | Tapley Hill/basal Balcanoona Formation | 341900 | 6637170 | silts of the Tapley Hill formation, thinly bedded very fine grained yellow and purple silts | 1 | 0.1441 | 0.1056 | 0.1231 | **1.804** |
| | | | | | 2 | 0.1447 | 0.1104 | 0.1184 | **1.690** |
| 97MTP06 | Balcanoona Formation | 343250 | 6638860 | dolomite of basal Balcanoona Formation, yellow dolomite which is overlain in o/c by purple/pink coloured dolomite | 1 | 0.1616 | 0.0680 | 0.1397 | **3.165** |
| | | | | | 2 | 0.1640 | 0.0651 | 0.1435 | **3.377** |
| 97MTP06a | Balcanoona Formation | 343650 | 6638950 | basal algal limestone unit of the Balcanoona Formation, unusual blue/grey limestone with considerable internal structure | | 0.1492 | 0.0966 | 0.1252 | **2.020** |
| 97MTP07 | Blue Mine Conglomerate | 343760 | 6641880 | dark blue/grey siltstone interbed within the Blue Mine Conglomerate | | 0.1459 | 0.1021 | 0.1236 | **1.881** |
| 97MTP08 | Balcanoona Formation | 344100 | 6642560 | basal dolomite of Balcanoona Formation (same unit as 97MTP06) Yellow/pink dolostone which contains late cross-cutting pink calcite veins | | 0.1687 | 0.0590 | 0.1436 | **3.773** |

**Table A.23** *continued ...*

| *Sample* | *Lithology* | *Location* | | *Description* | *Comments* | *Voltage readings* | | | *k sample** |
|---|---|---|---|---|---|---|---|---|---|
| | | *Easting* | *Northing* | | | $E_{top}$ | $E_{bottom}$ | $E_{sample}$ | |
| 97MTP09 | Tapley Hill Formation | 345100 | 6645490 | yellow and purple banded silts of the Tapley Hill Formation, very finely banded and cleaved | 1 | 0.1393 | 0.1190 | 0.1166 | **1.530** |
| | | | | | 2 | 0.1437 | 0.1062 | 0.1224 | **1.786** |
| 97MTP10 | Humanity Seat Formation | 345150 | 6646900 | medium grained heavy mineral laminated sandstones which may also contain purple/grey shale laminations | | 0.1666 | 0.0608 | 0.1428 | **3.628** |
| 97MTP11 | Wywyana Formation | 348190 | 6650900 | heavily ferruginized very fine grained dolomite or marble which appears similar to the basal dolomites of the Balcanoona Formation; unit is bounded south and north by NE trending faults | | 0.1728 | 0.0494 | 0.1477 | **4.622** |
| 97MTP12 | Wortupa Quartzite | 349400 | 6647150 | very coarse to medium grained quartzite, arkosic in places | | 0.1671 | 0.0566 | 0.1443 | **3.747** |
| 97MTP13 | Unnamed Member | 349570 | 6647130 | very finely banded feldspar rich purple siltstone; may be Opaminda Formation or a transitional facies of arkosic quartzite or Blue Mine Conglomerate | 1 | 0.1550 | 0.0949 | 0.1217 | **2.057** |
| | | | | | 1 (Repeat) | 0.1492 | 0.0964 | 0.1268 | **2.040** |
| | | | | | 1 (WS) | 0.1530 | 0.1040 | 0.1272 | **1.914** |
| | | | | | 2 | 0.1431 | 0.1063 | 0.1226 | **1.783** |
| 97MTP14 | Unnamed Member | 349100 | 6647270 | Arkosic unit from within the Unnamed formation; very gritty and feldspar rich, poorly sorted with distinct banding defined by varying feldspar content, texturally and mineralogically immature | | 0.1656 | 0.0690 | 0.1379 | **3.125** |
| 97MTP15 | Wortupa Quartzite | 343030 | 6640910 | quite feldspathic, very coarse grained and immature quartzite | | 0.1640 | 0.0621 | 0.1438 | **3.547** |
| 97MTP15a | Wortupa Quartzite | 343030 | 6640910 | occurs stratigraphically above the Wortupa and is possibly a transitional facies between the Wortupa and quartzites of the Unnamed unit, well sorted with less feldspar content | | 0.1682 | 0.0577 | 0.1450 | **3.876** |
| 97MTP16 | Opaminda Formation | 340100 | 6645350 | dark grey siltstones with minor green shale interbeds, very well laminated black grey/green siltstones, some gritty horizons | | 0.1337 | 0.1289 | 0.1119 | **1.339** |

**Table A.23** *continued ...*

| *Sample* | *Lithology* | *Location* | | *Description* | *Comments* | *Voltage readings* | | | *k sample** |
|---|---|---|---|---|---|---|---|---|---|
| | | *Easting* | *Northing* | | | $E_{top}$ | $E_{bottom}$ | $E_{sample}$ | |
| 97MTP17 | Skillogalee Dolomite or uppermost Unnamed unit | 342380 | 6641820 | weathered medium grained grey marble/dolomite poorly layered in o/c. O/c as discontinuous strike ridges | | 0.1700 | 0.0535 | 0.1469 | **4.233** |
| 97MTP18 | Skillogalee Dolomite | 342020 | 6642380 | very well cemented grey-white dolomite | 1 (parallel) | 0.1692 | 0.0512 | 0.1490 | **4.448** |
| | | | | | 2 | 0.1701 | 0.0515 | 0.1497 | **4.445** |
| 97MTP19 | Skillogalee Dolomite | 341640 | 6642940 | well layered, grey/yellow dolomite, very well cemented | 1 | 0.1676 | 0.0573 | 0.1444 | **3.887** |
| | | | | | 2 (parallel) | 0.1705 | 0.0531 | 0.1473 | **4.270** |
| 97MTP20 | Skillogalee Dolomite | 340700 | 6643730 | well layered brown-yellow dolomite, very different from the more massive, marble-like grey dolomites sampled earlier in the traverse | | 0.1535 | 0.0949 | 0.1259 | **2.087** |
| 97MTP21 | Un-named Unit | 340300 | 6644270 | grey finely laminated dolomitic siltstone; interlayered green shales | | 0.1431 | 0.1119 | 0.1178 | **1.654** |
| 97MTP22 | Opaminda Formation | 339570 | 6645480 | very finely laminated grey shales-siltstones occurring stratigraphically below the Blue Mine Conglomerate, possibly a silty interbed of the Conglomerate | | 0.1404 | 0.1118 | 0.1191 | 1.654 |
| 97MTP23 | Woodnamulka Phyllite | 340180 | 6646580 | bt-mu fine grained schist | | 0.1306 | 0.1377 | 0.1082 | **1.232** |
| 97MTP24 | sandstone interbed within Woodnulka Phyllite | 341040 | 6648070 | grey-white medium grained sandstone. This is likely a transitional sandstone facies into the Humanity Seat Formation. In places the unit is cross-bedded and contains conglomeratic interbeds | | 0.1621 | 0.0682 | 0.1400 | **3.161** |
| 97MTP25 | Opaminda Formation/Unnamed Unit | 338060 | 6645240 | black siltstone, which contains some interbedded sands grading to gritty horizons. Possibly a silt interbed of the Unnamed Unit | | 0.1614 | 0.0726 | 0.1391 | **2.956** |
| 97MTP26 | Paralana Quartzite | 343540 | 6649550 | white quartzite member of the Paralana Quartzite, sugary textured (slightly weathered). Sampled quite close to the sheared contact with basement porphyry | | 0.1698 | 0.0539 | 0.1469 | **4.198** |
| 97MTP27 | Paralana Quartzite | 343430 | 6649450 | pink Paralana quartzite (? due to K or Fe flow), quite crystalline and fresh | | 0.1727 | 0.0570 | 0.1456 | **3.891** |
| 97MTP28 | Paralana Quartzite | 343340 | 6649350 | gradational pink-white quartzite, quite crystalline and fresh | | 0.1727 | 0.0444 | 0.1512 | **5.219** |

Details of sample and experimental configuration the same as shown in Table A.21

# Appendix B
# Argon Thermochronology

Appendix B contains detail and results of argon thermochronological studies on samples from the Mount Painter Province, in northern South Australia (see Chapter Six for discussion). This work was undertaken in order to evaluate the thermal history of the rocks at Mount Painter, which are extraordinarily enriched in the heat producing elements. In this section I describe the thermal and petrological constraints on the samples analysed, describe the analytical procedures undertaken and present the argon thermochronological data in a series of tables. The results of this work have recently been prepared for publication in a manuscript entitled "Thermochronology of high heat producing crust at Mount Painter, South Australia: Implications for tectonic reactivation of continental interiors".

## B.1 Thermal and petrological constraints on samples

Below I describe each of the samples used in the argon thermochronological study, including petrological constraints which may bear on the thermal evolution of the minerals analysed. The sampling traverse, summarized in Table B.1 and shown in Figure 6.3, covers ~ 4-5 km of equivalent stratigraphic thickness. As outlined in Chapter Six, Mount Painter basement units consist of both Palaeoproterozoic granitic gneisses and Mesoproterozoic metasedimentary rocks and granitic gneisses. The latter are thought to have been intruded into and deposited upon the former after a period of Palaeoproterozoic metamorphism. Subsequently both Mesoproterozoic and Palaeoproterozoic rocks were deformed and metamorphosed, together with the Adelaidean cover sequence, during the Palaeozoic. The peak metamorphic conditions during this event are estimated at ~ 550°C and ~ 3-4 kbar.

### B.1.1 Samples from the Mount Painter basement

Sample MP9 (Figure 6.3), from the most southerly exposure of the Mount Painter basement, is a well foliated granitic gneiss consisting principally of biotite, muscovite, quartz, plagioclase and K-feldspar. The foliation is defined by aligned phyllosilicates, particularly coarse grained muscovite, within a recrystallized quartz matrix. The foliation wraps around coarse relic plagioclase-K-feldspar-quartz aggregates. In all cases K-feldspar appears to be early formed and is overgrown by polygonal plagioclase grains. Relic K-feldspar grains are also present within the recrystallized matrix material. Some large relic K-feldspar grains are perthitic, and with the exception of minor sericitic alteration along grain boundaries, are relatively clean and inclusion free. This sample underwent deformation at lower amphibolite facies conditions in the Palaeozoic; however, its protolith age and early tectonic history remain ambiguous. Correlations with units in the Nooldoonooldoona area suggest that it may be Mesoproterozoic in age (Elburg et al., submitted); however, it has also been described as part of the Palaeoproterozoic metavolcanic granitic suite by Teale (1993). Consequently it is possible that this sample may have also suffered high temperature (740-760°C and 4.5-5.5 kbar) metamorphism during the Palaeoproterozoic (Teale, 1993).

**Table B.1** *Sample location and description*

| *Sample* | *Field sample* | *mu* | *bt* | *K-spar* | *hbde* | *Lithology* | *Unit* | *Easting* | *Northing* | *Distance from u/c (km)* | *Description* |
|---|---|---|---|---|---|---|---|---|---|---|---|
| MP21 | 1086-MP1 | # | | # | | British Empire Granite | PG | 350370 | 6666840 | - 2.0 | Coarse leucogranite, plag, muscovite, qz and microcline bearing |
| MP25 | 1086-MP5 | # | # | | | British Empire Granite | PG | 349240 | 6665870 | - 2.0 | Coarse grained, plag, mu, bt and qz bearing granodiorite, associated with BEG |
| MP24 | 1086-NC4 | *x* | *x* | *x* | | Freeling Heights Quartzite | MB | 347250 | 6663400 | - 2.0 | Strongly foliated and recrystallized quartzite, foliation defined by mu and bt |
| MP28 | 1086-Pct | | | | # | Amphibolite | MB | 346550 | 6661900 | - 2.0 | Recrystallized hornblende, bt amphibolite |
| MP11 | Ndsed | *x* | *x* | | | Metasediment | MB | 335164 | 6649213 | - 0.5 | Metasedimentary enclave within MB, strongly foliated and crenulated, foliation defined by mu and bt |
| MP2 | AR2 | | *x* | | | Nooldoonooldoona pegmatite | MB | 335200 | 6649600 | - 0.5 | Metasomatized margin of local pegmatite; monomineralic, foliated biotite aggregate |
| MP9 | WDC2 | # | *x* | *x* | | Foliated Gneiss | MB | 331125 | 6650867 | - 0.2 | foliated mu, bt gneiss |
| MP5 | AR5 | *x* | | | | Arkaroola pegmatite | PG | 330937 | 6650837 | -0.2 | Deformed, coarse grained kspar, mu pegmatite |
| MP8 | Arkpeg | # | | # | | Arkaroola Pegmatite | PG | 341924 | 6649759 | 0 | Megacrystic kspar, mu, qz, tourmaline pegmatite |
| MP1 | AR1 | | *x* | *x* | | Nooldoonooldoona pegmatite | PG | 335200 | 6649600 | + 0.5 | Local kspar pegmatite |
| MP6 | AR6 | # | | *x* | | Arkaroola pegmatite | PG | 339617 | 6648145 | + 0.5 | Coarse, relatively undeformed kspar, mu and diopside bearing pegmatite |
| MP30 | 976-WP3 | | | | # | Wooltana Volcanics | ACS | 337550 | 6649000 | + 0.5 | Hornblende, plagioclase metabasalt |
| MP7 | btsed | | *x* | | | Local biotite schist | ACS | 341934 | 6649855 | + 0.5 | Monomineralic biotite schist, associated with andalusite bearing schist |
| MP31 | 976-C6B | | | | # | Wooltana Volcanics | ACS | 342550 | 6648750 | + 0.6 | Hornblende, epidote metabasalt |
| MP3 | WP2 | *x* | *x* | | | Woodnamoka Phyllite | ACS | 340250 | 6646550 | + 1.75 | Fine grained sandy schist |
| MP4 | BMC | | | *x* | | Blue Mine Conglomerate | ACS | 340050 | 6645550 | + 2.0 | K-feldspar clast in arkosic conglomerate |
| MP10 | AR10 | | | *x* | | Bolla Bollana Formation | ACS | 337500 | 6643340 | + 3.0 | Granite clast within glacial Tillite |
| MP13 | AR13 | | | # | | Bolla Bollana Formation | ACS | 337491 | 6642838 | + 3.0 | Granite clast within glacial Tillite |
| MP16 | AR16 | | | *x* | | Bolla Bollana Formation | ACS | 337648 | 6642345 | + 3.0 | Porphyritic volcanic clast within glacial Tillite |

*Note:* Sample locations are given in Australian Map Grid (1984), Zone 54

MB = Mesoproterozoic Mount Painter Basement; ACS = Neoproterozoic Adelaidean Cover Sequence; PG = Palaeozoic granite/pegmatite

Distances are quoted above (denoted positive) and below (denoted negative) the basement-cover unconformity

Mineral separates denoted by an *x* were analysed by both K/Ar and $^{40}Ar/^{39}Ar$ methods; separates denoted by a # were analysed by the K/Ar method only

Sample MP24 from the Mesoproterozoic Freeling Heights Quartzite, is a metamorphosed psammitic unit which has suffered extensive recrystallization and metamorphic mineral growth, presumably during the Delamerian Orogeny. A strong foliation is defined by both muscovite and biotite and also by the alignment of recrystallized quartz aggregates. It also contains minor late growth K-feldspar which appears as small, largely unaltered grains within the quartz-muscovite foliation. Most K-feldspar grains contain both fluid and mineral inclusions.

Sample MP11 is a metasedimentary / metavolcanic enclave within the Nooldoonooldoona Trondhjemite at Nooldoonooldoona Waterhole. This unit is strongly foliated with a pervasive schistosity defined by both biotite and muscovite which wraps around unusually large, and nearly circular quartz augen (3-6 mm). This lithology has been dated by Pb-Pb methods on zircon at ~ 1575 Ma (Elburg et al., submitted) and is therefore unlikely to have experienced any pre-Delamerian tectonic or metamorphic activity.

Sample MP28 is a fine grained strongly recrystallized hornblende, biotite, quartz amphibolite which contains minor plagioclase. This sample is taken from a metamorphosed mafic intrusion within the Freeling Heights Quartzite (Neumann, 1996). A strong foliation is defined by the alignment of coarse grained biotite and hornblende.

### B.1.2 Samples from the Neoproterozoic cover sequence

Samples MP30, MP31, MP7, MP3, MP4, MP10 and MP16 were taken from the Neoproterozoic Adelaidean cover sequence (Figure 6.3), and span an equivalent stratigraphic thickness of ~ 3 km. Little geochronological information is available for sediments in the Mount Painter region and age correlations are based largely on determinations made elsewhere on equivalent units (Figure 6.2).

Sample MP7 is a coarse biotite schist adjacent to the basement / cover contact in the vicinity of Radium Creek. Although it appears to form part of the lowermost Callana Group (Wywyana Formation) it is almost completely recrystallized and may be a metasomatized upthrust slice of basement material. Biotite crystals contain abundant monazite inclusions and are relatively clean, suffering minor alteration along grain boundaries only. This unit is associated with a coarse knobby andalusite schist, and, regardless of whether it is cover or basement rock, peak metamorphic temperatures are estimated to have been ~ 500-550°C.

Samples MP30 and MP31, studied previously by Smith (1992), were both taken from the Wooltana Volcanics. Sample MP30 is a metabasalt which consists of hornblende, plagioclase (andesine) and minor actinolite. Sample MP31 contains hornblende and epidote in approximately equal proportions. Both samples also contain accessory rutile and illite. These samples were taken from the extensive outcrops of Wooltana Volcanics adjacent to the basement-cover unconformity. The Wooltana Volcanics are thought to be equivalent to the extensive Gairdner Dyke Swarm; the latter have been dated by SHRIMP U-Pb methods (on baddeleyite) at 827 ± 6 Ma (Wingate et al., 1998).

Sample MP3 is a medium grained crenulated muscovite-biotite schist of the Woodnamoka Phyllite. This unit is laterally equivalent to the quartzitic Humanity Seat Formation and unconformably overlies the Wooltana Volcanics. Its stratigraphic age is estimated at ~ 780 Ma, based on the age of the Boucaut Volcanics which underlie lateral equivalents of this unit in the Nackara Arc (Figure 6.2;

Preiss, 2000). Peak metamorphic conditions are estimated at ~ 500°C based on the occurrence of cordierite and anthophyllite in the underlying Wywyana Formation. Sample MP3 contains fine grained muscovite and coarser grained biotite which together define the foliation; both minerals are largely unaltered.

Sample MP4 is from the Blue Mine Conglomerate, a coarse arkosic conglomerate containing abundant K-feldspar and quartz clasts. The matrix is defined by very-fine grained biotite growth within a fine recrystallized and dominantly silicic matrix. K-feldspar clasts exhibit a wide range of grain size from ~ 1 to 4 mm; most of the large (3-4 mm) clasts have a strong perthitic texture. All grains have suffered extensive sericitic alteration, and most contain abundant fluid inclusions and have undulose extinction. Clast K-feldspars dominate, although there is also minor finer grained (300-500 μm) K-feldspar present within the matrix. The latter contain abundant fluid inclusions and they are not as heavily altered as the larger grains. The Blue Mine Conglomerate is about 2 km stratigraphically above the basement-cover unconformity and metamorphic temperatures are estimated to have reached ~ 400°C during the Palaeozoic.

Samples MP10 and MP16 are K-feldspars from boulder clasts within the Bolla Bollana Formation (Figure 6.2, 6.3), a thick (~ 1500-2000 m) glacial tillite of Sturtian age (~ 700 Ma, e.g., Preiss, 1987; 2000). MP10 is taken from a large and remarkably clean coarse grained granitic clast containing muscovite, biotite and K-feldspar. The K-feldspars exhibit extensive sericitic alteration, principally along grain boundaries. Most grains are heavily fractured and also contain abundant fluid inclusions. The K-feldspar is dominantly microcline and is present as early formed relic igneous crystals and also as finer grains within the heavily altered and recrystallized quartz (+ minor muscovite, biotite and chlorite) matrix. Relic igneous textures are largely overprinted by alteration features. MP16 is taken from a volcanic clast, containing quartz, plagioclase and K-feldspar phenocrysts in a fine-grained and heavily altered silicic matrix. K-feldspar grains are large (100-600 μm), perthitic and may contain small plagioclase cores. Sericitic alteration occurs along fractures and grain boundaries. Given the depositional age of the Sturtian Tillite and the geology of the surrounding terranes, we suggest that these clasts are likely to have been derived from the underlying basement (e.g., Preiss, 1993) or from erosion of Mesoproterozoic granites and volcanics from the Gawler Craton to the west. The metamorphic grade of these units is lowest greenschist, with metamorphic temperatures not exceeding ~ 300-350°C. Consequently they may be expected to retain some pre-Delamerian signature.

### B.1.3 Samples from Palaeozoic Intrusives

As outlined earlier, the Mount Painter basement and Adelaidean cover rocks are intruded by a number of coarse pegmatites and megacrystic aluminous granites. These bodies are largely undeformed and are interpreted as local melts formed during Palaeozoic metamorphism. The largest of these bodies is the British Empire Granite, which intrudes the Mount Painter basement in the central Mount Painter Inlier (Figure 6.3), and which has been the subject of a detailed study by Neumann (1996). Although the emplacement age of this granite is not well constrained, Neumann (1996) constructed a three point isochron using whole-rock Rb-Sr isotopic measurements which yielded an age ~ 375 Ma. In this study two British Empire Granite samples, MP21 and MP25, have been analysed. Sample MP21 is a coarse grained muscovite granite. K-feldspar is dominantly

microcline and is largely unaltered, particularly when compared to the plagioclase grains which have suffered extensive sericitic alteration. Microcline forms interstitial masses around 100-200 μm in diameter between larger plagioclase / quartz aggregates. MP25 is granodioritic in composition and was sampled from the 'tail' like extension of the main British Empire Granite body (Figure 6.3). The sample contains very large quartz-plagioclase aggregates, with K-feldspar (dominantly microcline) forming unaltered interstitial grains. Both plagioclase and K-feldspar grains contain abundant quartz inclusions. Muscovite grains are around 50-100 μm in length and are unaltered. Biotite grains are of similar dimension and appear to be intergrown with the muscovite grains. They are largely unaltered, but do contain numerous monazite / zircon inclusions.

Samples MP1 and MP2 intrude basement rocks in the Nooldoonooldoona Waterhole region. Sample MP1 is a small (~ 1 m wide) essentially undeformed, monomineralic K-feldspar pegmatite. MP1 K-feldspar is perthitic on the hand sample scale, but shows no evidence for chemical alteration. Narrow (~ 0.5 m) biotite selvedges have formed along the metasomatized margins of this pegmatite, and sample MP2 was taken from these units. As well as abundant, very coarse grained biotite, this sample also contains coarse-grained (1-2 mm) tourmaline. Biotite grains have suffered extensive radiation damage due to abundant monazite inclusions, and are also mildly altered, principally along grain boundaries. As both units are essentially undeformed, they are interpreted to be melt products of Palaeozoic deformation.

Sample MP5 is a deformed pegmatite from the Wild Dog Creek region that intrudes ?Palaeoproterozoic granitic gneisses (see sample MP9) in the southern part of the inlier. It contains very coarse K-feldspar and muscovite, and is thought to be late syn- to post-tectonic with respect to the Palaeozoic deformation. K-feldspar crystals are perthitic in hand specimen and show evidence for extensive sericitic alteration on the microscale. Sample MP8 is a deformed megacrystic K-feldspar, muscovite, quartz and tourmaline pegmatite from the basement-cover contact in the Radium Creek region. Like sample MP5, MP8 K-feldspars are perthitic in hand specimen. At the microscale large K-feldspar crystals contain large irregularly shaped plagioclase inclusions. The K-feldspars have also suffered significant sericitic alteration, and some contain quartz filled micro-fractures.

Sample MP6 is also a coarse quartz, muscovite, K-feldspar and diopside-bearing pegmatite. It is essentially undeformed and intrudes basal Adelaidean calcsilicates (of the Wywyana Group) near Arkaroola Waterhole. K-feldspar crystals are coarse (2-8 cm), perthitic and altered principally along fracture planes. Small K-feldspar grains are also contained within large quartz crystals. This pegmatite is thought to be equivalent to or slightly younger than the pegmatite from Wild Dog Creek (sample MP5) and again may be a melt product related to Palaeozoic metamorphism.

## B.2 Analytical Procedure

Mineral separation was carried out using routine heavy liquid flotation, differential grain size reduction (rolling) and magnetic methods. All samples (listed in Table B.1) were concentrated to better than 99%, with the principal impurities being mineral and fluid inclusions. Most K-feldspars were sized between 125 and 180 μm using standard mesh sieves. Most micas were sized between 100 and 250 μm and hornblendes were sized between 180 and 250 μm (see Table B.2 for details of mesh sizes).

Conventional total fusion K / Ar analysis was performed prior to irradiation and $^{40}Ar/^{39}Ar$ analysis. All samples, for both phases of the analytical program, were analysed at the Research School of Earth Sciences at the Australian National University. Here I first describe the analytical method employed for K / Ar analysis, and then discuss the irradiation and analysis procedure for the $^{40}Ar/^{39}Ar$ method.

### B.2.1 K/Ar analytical method

Following mineral separation, the potassium concentration of each sample was measured using a standard instrumental flame photometry technique. As the first step in this process, samples were dissolved overnight at ~ 120°C in analytical grade 50% w / w hydrofluoric acid enabling silicon to be removed as $SiF_4$ through evaporation (Dalrymple and Lanphere, 1969). The resultant solution was diluted with a known quantity of Lithium solution (the internal standard) (e.g., McDougall and Schmincke, 1977). This solution was then analysed on an Instrumentation Laboratory IL 443 flame photometer. The concentration of K (wt %) was determined by comparison of the intensity of potassium radiation for the unknown samples with that of a series of known standard solutions of both higher and lower potassium concentrations. For materials containing > 1% $K_20$, potassium determinations by this method typically allow a precision of better than 1% to be obtained (Dalrymple and Lanphere, 1969). The accuracy of flame photometry measurements is comparable to other methods (such as isotope dilution) and generally depends on the accuracy of the standard solutions used.

For argon isotopic measurements, a separate aliquot of the sample was weighed into a molybdenum crucible and loaded into an ultra-high vacuum extraction line. At the Research School of Earth Sciences at the ANU, ultra-high vacuum on the K / Ar lines is maintained by a rotary pump and mercury diffusion pump system. After samples (and break-seal spike tubes) have been loaded into the line, it is baked at 150-240°C for around 12 hours to remove atmospheric contamination (largely adsorbed air and water vapour). The bake-out procedure also increases the pumping efficiency of the vacuum system. After baking was complete the extraction line was checked for leaks; generally pressures of less than $10^{-7}$ torr were achieved.

Samples were subsequently fused using an external induction radio-frequency generator. In general, biotite samples were fused at ~ 1200-1300°C for 20 minutes, muscovites at ~ 1300-1400°C for 30 minutes, K-feldspars at ~ 1700-1800°C for 45 minutes and hornblendes at ~ 1300°C for 30 minutes (Table B.3). The sample gas was collected on activated charcoal (at the temperature of boiling liquid nitrogen) during and after heating**,** and a $^{38}Ar$ spike was added after heating was finished. The gas was then exposed to a copper, copper oxide furnace (at 600°C) where hydrogen and hydrocarbons are oxidized and water so produced was absorbed onto a synthetic molecular

**Table B.2** *Mesh sizes of mineral separates*

| *Mineral* | *Sample* | *Mesh size* | *Micron size* |
|---|---|---|---|
| muscovite | MP24 | 60/120# | 125-250 |
| | MP9 | 60/120# | 125-250 |
| | MP11 | 60/120# | 125-250 |
| | MP8 | +120# | > 125 |
| | MP5 | 60/150# | 100-125 |
| | MP6 | 85/170# | 90-178 |
| | MP3 | 85/170# | 90-178 |
| biotite | MP24 | -60# | < 250 |
| | MP9 | +120# | > 125 |
| | MP11 | 60/120# | 125-250 |
| | MP2 | 60/120# | 125-250 |
| | MP7 | 60/120# | 125-250 |
| | MP3 | 36/60# | 250-422 |
| K-feldspar | MP24 | 60/120# | 125-250 |
| | MP9 | 60/100# | 125-150 |
| | MP8 | 60/85# | 125-178 |
| | MP5 | 60/120# | 125-250 |
| | MP1 | 60/85# | 125-178 |
| | MP6 | 60/85# | 125-178 |
| | MP4 | 60/85# | 125-178 |
| | MP10 | 60/85# | 125-178 |
| | MP13 | 60/150# | 100-125 |
| | MP16 | 60/100# | 125-150 |
| hornblende | MP30 | 60/85# | 125-178 |
| | MP31 | 60/85# | 125-178 |
| | MP28 | 60/85# | 125-178 |

**Table B.3** *K/Ar fusion data*

| *Mineral* | *Sample* | *T fusion (℃)* | *t fusion (minutes)* |
|---|---|---|---|
| muscovite | MP24 | 1450 | 30 |
| | MP9 | 1500 | 30 |
| | MP11 | 1430 | 30 |
| | MP8 | 1480 | 30 |
| | MP5 | 1500 | 30 |
| | MP6 | 1450 | 30 |
| | MP3 | 1500 | 30 |
| biotite | MP24 | 1500 | 20 |
| | MP9 | 1430 | 20 |
| | MP11 | 1440 | 20 |
| | MP2 | 1400 | 20 |
| | MP7 | 1500 | 20 |
| | MP3 | 1440 | 22 |
| K-feldspar | MP24 | 1750 | 50 |
| | MP9 | 1740 | 45 |
| | MP8 | 1720 | 45 |
| | MP5 | 1800 | 45 |
| | MP1 | 1650 | 45 |
| | MP6 | 1800 | 45 |
| | MP4 | 1700 | 45 |
| | MP10 | 1750 | 45 |
| | MP13 | 1750 | 45 |
| | MP16 | 1700 | 45 |
| hornblende | MP30 | 1300 | 30 |
| | MP31 | 1300 | 30 |
| | MP28 | 1300 | 30 |

sieve. The gas was then exposed to a titanium furnace (at 750°C) where all the reactive gases (such as $O_2$ and $N_2$) were removed. The purified argon was then transferred to an MS10 mass spectrometer for isotopic analysis.

In general two isotopic analyses were performed on different splits of each gas sample – an 'all-in' measurement, and a 'leak-in' measurement. In the latter an orifice correction had to be applied to account for mass fractionation. All measurements were performed with the mass spectrometer in the static mode. Mass discrimination and machine sensitivity were monitored using aliquots of pure air argon both before and after the unknown samples were measured. The results of all K / Ar analyses are listed in Table B.4.

**Table B.4** *Results of K/Ar isotopic analyses*

| *Sample #* | *Lithology* | *Mineral* | *K (wt %)* | *Rad $^{40}Ar^*$ ($10^{-9}$ mol/g)* | *100 $^{40}Ar^*$ / Total $^{40}Ar$* | *Calculated age σ (My ± 2 )* |
|---|---|---|---|---|---|---|
| MP21 | British Empire Granite | K-feldspar | 12.46, 12.55 | 8.354 | 96.9 | 349.2 ± 2.8 |
| | | | | 8.358 | 96.7 | 349.3 ± 2.8 |
| | | muscovite | 8.827, 8.837 | 6.767 | 98.5 | 395.1 ± 3.1 |
| | | | | 6.762 | 98.5 | 394.8 ± 3.1 |
| MP25 | British Empire Granodiorite | biotite | 7.395, 7.421 | 5.211 | 77.2 | 365.8 ± 3.0 |
| | | | | 5.190 | 76.9 | 364.7 ± 3.8 |
| | | muscovite | 8.845, 8.812 | 6.546 | 76.9 | 383.6 ± 3.0 |
| | | | | 6.543 | 76.9 | 383.5 ± 3.1 |
| MP24 | Freeling Heights Quartzite | K-feldspar | 12.51, 12.49 | 7.688 | 97.7 | 323.7 ± 2.5 |
| | | biotite | 7.933, 7.950 | 5.218 | 82.5 | 343.9 ± 2.9 |
| | | | | 5.219 | 82.5 | 343.9 ± 2.7 |
| | | muscovite | 8.914, 8.964 | 6.483 | 94.1 | 376.1 ± 3.2 |
| | | | | 6.492 | 94.3 | 376.5 ± 3.2 |
| MP28 | Amphibolite | hornblende | 0.451, 0.458 | 0.375 | 95.9 | 422.5 ± 6.1 |
| MP9 | Basement gneiss | K-feldspar | 11.92, 11.92 | 7.767 | 93.6 | 341.3 ± 2.6 |
| | | | | 7.792 | 93.9 | 342.3 ± 2.7 |
| | | biotite | 8.325, 8.269 | 6.421 | 84.1 | 398.7 ± 3.2 |
| | | | | 6.447 | 84.3 | 400.2 ± 3.2 |
| | | muscovite | 9.056, 8.979 | 6.921 | 98.4 | 395.7 ± 3.1 |
| | | | | 6.925 | 98.4 | 394.0 ± 3.2 |
| MP11 | Basement metasediment | muscovite | 8.479, 8.417 | 5.919 | 28.6 | 364.0 ± 3.5 |
| | | | | 5.912 | 28.7 | 364.1 ± 3.6 |
| | | muscovite (repeat) | 8.479, 8.417 | 6.490 | 79.7 | 396.1 ± 3.2 |
| | | | | 6.471 | 79.5 | 395.1 ± 3.2 |
| | | biotite | 8.490, 8.538 | 6.306 | 99.1 | 383.3 ± 3.2 |
| | | | | 6.315 | 99.2 | 383.8 ± 3.2 |
| MP8 | Arkaroola Pegmatite | K-feldspar | 11.21, 11.36 | 6.975 | 88.5 | 325.2 ± 3.9 |
| | | | | 6.944 | 88.2 | 323.9 ± 2.6 |
| | | muscovite | 9.069, 8.955 | 6.286 | 97.0 | 363.0 ± 2.9 |
| | | | | 6.294 | 97.1 | 363.5 ± 2.9 |
| MP5 | Arkaroola Pegmatite | K-feldspar | 11.08, 11.07 | 6.886 | 86.2 | 327.0 ± 3.9 |
| | | | | 6.869 | 85.9 | 326.2 ± 3.9 |
| | | muscovite | 8.983, 8.954 | 6.789 | 88.1 | 390.9 ± 3.0 |
| | | | | 6.725 | 87.8 | 387.6 ± 3.0 |
| MP1 | Local pegmatite | K-feldspar | 13.33, 13.39 | 8.207 | 96.1 | 323.4 ± 2.5 |
| | | | | 8.200 | 96.1 | 323.2 ± 2.6 |
| MP2 | Biotite schist | biotite | 8.248, 8.319 | 5.922 | 96.7 | 371.2 ± 3.0 |
| | | | | 5.909 | 96.6 | 370.5 ± 2.9 |
| MP6 | Arkaroola Pegmatite | K-feldspar | 12.67, 12.66 | 8.079 | 93.4 | 334.6 ± 2.8 |
| | | | | 8.069 | 93.3 | 334.3 ± 3.5 |
| | | muscovite | 9.070, 9.063 | 6.289 | 88.0 | 361.2 ± 2.8 |
| | | | | 6.296 | 88.2 | 361.6 ± 2.8 |
| MP30 | Wooltana Volcanics | hornblende | 0.294, 0.294 | 0.2254 | 91.3 | 361.6 ± 2.8 |
| MP31 | Wooltana Volcanics | hornblende | 0.312, 0.313 | 0.2666 | 51.8 | 435.5 ± 5.1 |
| MP7 | Biotite Schist | biotite | 8.336, 8.321 | 6.080 | 88.6 | 378.3 ± 3.0 |
| | | | | 6.086 | 88.7 | 378.6 ± 3.0 |
| MP3 | Woodnamoka Phyllite | biotite | 8.071, 8.153 | 6.062 | 79.9 | 386.3 ± 3.1 |
| | | | | 6.050 | 79.8 | 385.7 ± 3.3 |
| | | muscovite | 8.382, 8.288 | 6.606 | 95.8 | 407.3 ± 3.2 |
| | | | | 6.588 | 95.5 | 406.3 ± 3.2 |
| MP4 | Blue Mine Conglomerate | K-feldspar | 12.33, 12.34 | 8.711 | 66.5 | 367.2 ± 2.8 |
| | | | | 8.712 | 66.6 | 367.2 ± 2.9 |
| MP10 | Bolla Bollana Formation | K-feldspar | 11.67, 11.62 | 8.743 | 89.9 | 388.1 ± 3.1 |
| | | | | 8.749 | 90.0 | 388.3 ± 3.1 |
| MP13 | Bolla Bollana Formation | K-feldspar | 10.06 (x = 4) | 11.77 | 97.1 | 573.3 ± 6.1 |
| | | | | 11.77 | 97.1 | 573.3 ± 6.2 |
| MP16 | Bolla Bollana Formation | K-feldspar | 8.572, 8.535 | 5.912 | 92.2 | 360.1 ± 3.0 |
| | | | | 5.886 | 91.9 | 358.6 ± 3.0 |

### B.2.2 $^{40}Ar/^{39}Ar$ analytical method

Samples were irradiated for 504 hours in facilities X33 or X34 of the Australian Nuclear Science and Technology Organization HIFAR reactor, Lucas Heights, NSW. Samples were packed in aluminium cans with a number of splits of the fluence monitor biotite GA1550 (with K/Ar age, 98.79 Ma, McDougall and Roksandic, 1974; Renne et al., 1998; Table B.5, B.6). The sample can was inverted 180 three times during the irradiation to minimize the effect of the large neutron flux gradient along the length of the can. A cadmium liner was used to minimize interference from thermal neutrons. Irradiation time was chosen in order to achieve a $^{40}Ar^*/^{39}Ar_K$ ratio of ~ 20.

After irradiation, the samples were allowed to decay to safe radiation levels. Each sample was unpacked from its aluminium casing and transferred to plastic vials. All material was stored in Pb castles when not in use, and appropriate safety precautions (including the use of a lead apron, appropriate tools for sample manipulation and radiation monitoring badges) were taken. Samples were then weighed and wrapped in Sn foil ready to load into the argon extraction line. Sample weights were calculated to provide ~ 45 V $^{40}Ar^*$ for micas and ~ 120 V for K-feldspars (note mass spectrometer sensitivity below). Fluence monitors were weighed in triplicate (~ 0.6mg) and subject to total fusion in a VG Isotech MM1200 gas source mass spectrometer. The $^{40}Ar^*/^{39}Ar_K$ ratio was determined for each fluence monitor, and this enabled the determination of the irradiation parameter, *J*. Results of these analyses are shown in Table B.6 and Figure B.1, plotted as $^{40}Ar^*/^{39}Ar_K$ along the length of the irradiation can.

During step-heating experiments the temperature was monitored using a thermocouple at the base of a tantalum crucible within a double-vacuum resistance furnace. Temperatures were progressively increased over the course of the experiment, with temperatures and times of each step chosen to give an even gas release. The heating schedule for biotite samples commenced at 550°C and concluded at 1350°C. Muscovite samples were heated from 700°C to 1350°C. K-feldspar samples were subject to a series of 43 steps at temperatures between 450°C and 1450°C (including many duplicate or triplicate isothermal steps). The schedule of heating times and temperatures for each sample can be found in Table B.7 (muscovite samples), Table B.8 (biotite samples) and Tables B9-B15 (K-feldspar samples).

**Table B.5** *Fluence Monitor Data*

| *Fluence Monitor* | *Position in can (mm from top)* | *Packet label* | *Mass (mg)* | *$^{40}Ar^*/^{39}Ar_K$* | *$J$ (x $10^{-3}$) ($2\sigma$(x $10^{-5}$))* |
|---|---|---|---|---|---|
| F1 | 28.00 | B | 0.60 | 6.9351 | 8.0410 (2.44) |
| | | C | 0.57 | 6.9449 | 8.0297 (2.63) |
| F2 | 24.75 | D | 0.59 | 6.8951 | 8.0451 (2.40) |
| F3 | 20.50 | G | 0.58 | 6.9316 | 8.0877 (2.10) |
| F4 | 17.50 | K | 0.60 | 6.9289 | 8.0483 (2.13) |
| | | M | 0.61 | 6.9387 | 8.0391 (2.16) |
| F5 | 14.00 | N | 0.61 | 7.0439 | 7.9169 (1.90) |
| | | O | 0.56 | 7.0079 | 7.9575 (1.94) |
| F6 | 11.25 | R | 0.61 | 6.9955 | 7.9716 (3.21) |
| | | S | 0.59 | 7.5929 | 7.3445 (2.18) |
| F7 | 7.00 | U | 0.55 | 7.0375 | 7.9241 (2.42) |
| F8 | 3.75 | W | 0.56 | 6.9528 | 8.0206 (2.77) |
| | | Y | 0.60 | 6.9452 | 8.0293 (2.36) |

**Table B.6** *Sample irradiation parameters*

| *Sample* | *Mineral* | *Position in can (mm from top)* | *Mass (mg)* | *$^{40}Ar^*/^{39}Ar_K$ (interpolated)* |
|---|---|---|---|---|
| MP24 | K-feldspar | 26.50 | 1.26 | 6.9163 |
| | biotite | 9.50 | 0.59 | 7.0334 |
| | muscovite | 10.50 | 0.57 | 7.0302 |
| MP9 | K-feldspar | 25.50 | 1.24 | 6.9077 |
| | biotite | 7.75 | 0.50 | 7.0288 |
| | muscovite | 8.50 | 0.51 | 7.0326 |
| | muscovite | 5.25 | 0.50 | 6.9941 |
| | biotite | 6.00 | 0.52 | 7.0088 |
| MP5 | muscovite | 12.50 | 0.51 | 7.0147 |
| MP1 | K-feldspar | 21.50 | 1.21 | 6.9092 |
| | biotite | 11.75 | 0.54 | 7.0216 |
| MP6 | K-feldspar | 19.75 | 1.18 | 6.9240 |
| | biotite | 4.50 | 0.52 | 6.9759 |
| MP3 | biotite | 13.25 | 0.57 | 7.0064 |
| | muscovite | 15.00 | 0.60 | 6.9845 |
| MP4 | K-feldspar | 19.00 | 1.17 | 6.9321 |
| MP10 | K-feldspar | 18.25 | 1.19 | 6.9411 |
| MP16 | K-feldspar | 15.75 | 1.68 | 6.9743 |

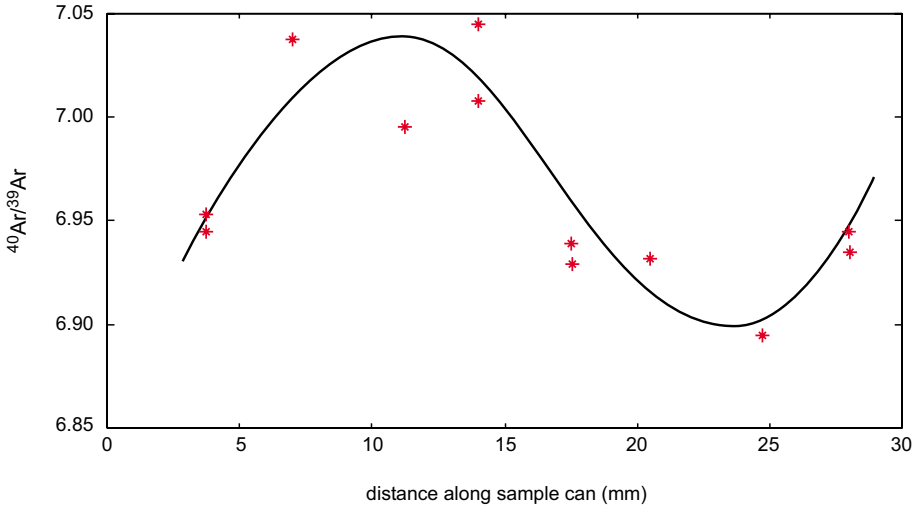


**Figure B.1** Plot of the variation in $^{40}Ar/^{39}Ar$ along the length of the sample irradiation can (ANU 56) Stars show measured $^{40}Ar/^{39}Ar$ values from fluence monitor samples.

After each temperature step, the gas released was exposed to Zr-Al getters to remove all active gases; gettering time in the vacuum line was generally ~ 10 minutes. Subsequently the purified argon was analysed in the mass spectrometer. For micas isotopic analysis was performed using a VG Isotech MM1200 gas source mass spectrometer, operated in the static mode. Ion beam measurements were made using an electron multiplier with sensitivity of $7.6 \times 10^{-15}$ mol/mV. For K-feldspars isotopic analysis was performed using a VG 3600 gas source mass spectrometer. Measurement was made using a Daly collector and photomultiplier with overall sensitivity of $3.5 \times 10^{-17}$ mol/mV. Corrections for argon produced by interactions of neutrons with K and Ca were made using standard correction factors (Tetley et al., 1980 and Dunlap, unpublished data). $^{40}K$ abundance and decay constants were taken from standard values recommended by the IUGS Subcommission on Geochronology (Steiger and Jäger, 1977).

**Table B.7** *$^{40}Ar/^{39}Ar$ Step Heating Data – Muscovites*

| Temp (°C) | $^{40}Ar/^{39}Ar$ | $^{37}Ar/^{39}Ar$ ($10^{-4}$) | $^{36}Ar/^{39}Ar$ ($10^{-3}$) | $^{39}Ar$ ($10^{-15}$ mol) | Cumulative $^{39}Ar$ (%) | $\%^{40}Ar^*$ | $^{40}Ar^*/^{39}Ar_K$ | Calculated Age (Ma) ± 1 s.d. |
|---|---|---|---|---|---|---|---|---|
| **MP24, Muscovite, 0.57 mg, J = 0.008006** | | | | | | | | |
| 700 | 35.36 | 367.3 | 28.75 | 3.196 | 1.1 | 75.9 | 26.85 | 351.2 ± 8.8 |
| 760 | 30.42 | 56.40 | 6.246 | 4.014 | 2.5 | 93.8 | 28.56 | 371.5 ± 3.8 |
| 815 | 29.64 | 0.4683 | 2.431 | 35.19 | 14.6 | 97.5 | 28.89 | 375.4 ± 1.7 |
| 830 | 28.96 | 0.3873 | 0.5848 | 42.58 | 29.2 | 99.3 | 28.77 | 374.0 ± 1.3 |
| 845 | 28.88 | 0.4776 | 0.1778 | 34.55 | 41.1 | 99.7 | 28.80 | 374.4 ± 1.4 |
| 860 | 28.89 | 0.6409 | 0.4018 | 25.76 | 49.9 | 99.5 | 28.74 | 373.7 ± 2.4 |
| 880 | 29.03 | 0.7958 | 0.3693 | 20.76 | 57.1 | 99.5 | 28.89 | 375.4 ± 2.3 |
| 910 | 29.04 | 1.078 | 0.0084 | 15.47 | 62.4 | 99.9 | 29.02 | 376.9 ± 4.1 |
| 965 | 29.03 | 0.8869 | 0.1977 | 18.83 | 68.8 | 99.7 | 28.95 | 376.1 ± 2.2 |
| 1000 | 29.07 | 0.7558 | 0.3974 | 22.11 | 76.4 | 99.5 | 28.92 | 375.7 ± 1.4 |
| 1025 | 29.13 | 0.7197 | 0.3292 | 23.30 | 84.4 | 99.6 | 29.00 | 376.7 ± 1.6 |
| 1050 | 29.26 | 0.7069 | 0.4056 | 23.75 | 92.6 | 99.5 | 29.12 | 378.1 ± 1.8 |
| 1080 | 29.08 | 1.026 | 1.042 | 16.37 | 98.2 | 98.8 | 28.75 | 373.7 ± 1.5 |
| 1350 | 32.85 | 3.246 | 16.50 | 5.178 | 100.0 | 85.1 | 27.96 | 364.4 ± 4.2 |
| *Totals* | | | | 291.1 | | | 28.84 | 374.8 ± 2.0 |
| Plateau Age = 375.4 ± 1.9 Ma | | | Conventional K/Ar age = 376.1 ± 3.2 Ma | | | | | |
| $\lambda_e = 5.543 \times 10^{-10}\ a^{-1}$ | | | Flux monitor, GA1550 Biotite, $^{40}Ar^*/^{39}Ar_K = 7.030$ | | | | | |
| **MP11, Muscovite, 0.50 mg, J = 0.008048** | | | | | | | | |
| 700 | 39.33 | 450.9 | 33.99 | 1.756 | 0.6 | 74.4 | 29.27 | 381.6 ± 13 |
| 760 | 31.63 | 144.6 | 7.494 | 3.727 | 1.8 | 92.9 | 29.40 | 383.1 ± 4.1 |
| 815 | 30.76 | 1.919 | 4.806 | 8.885 | 4.8 | 95.3 | 29.31 | 382.0 ± 3.1 |
| 835 | 30.45 | 0.6245 | 1.742 | 27.32 | 13.9 | 98.2 | 29.91 | 389.1 ± 2.3 |
| 850 | 30.27 | 0.4493 | 0.8594 | 37.99 | 26.5 | 99.1 | 29.99 | 390.0 ± 1.7 |
| 865 | 30.07 | 0.4682 | 0.4959 | 36.48 | 38.6 | 99.4 | 29.89 | 388.9 ± 1.7 |
| 880 | 29.88 | 0.6650 | 0.6327 | 25.70 | 47.2 | 99.3 | 29.66 | 386.2 ± 1.8 |
| 910 | 29.72 | 0.6858 | 0.4345 | 24.95 | 55.5 | 99.5 | 29.56 | 384.9 ± 1.8 |
| 965 | 29.91 | 0.7740 | 0.2476 | 22.12 | 62.8 | 99.7 | 29.80 | 387.9 ± 2.2 |
| 1000 | 29.90 | 1.161 | 0.9322 | 14.75 | 67.7 | 99.0 | 29.59 | 385.4 ± 1.9 |
| 1025 | 30.21 | 0.7401 | 0.4568 | 23.16 | 75.4 | 99.5 | 30.04 | 390.6 ± 8.2 |
| 1050 | 30.44 | 0.6568 | 0.2152 | 26.11 | 84.1 | 99.7 | 30.35 | 394.2 ± 1.9 |
| 1080 | 30.52 | 0.8667 | 0.3328 | 19.80 | 90.7 | 99.6 | 30.38 | 394.6 ± 3.3 |
| 1350 | 31.64 | 0.6144 | 2.716 | 27.96 | 100.0 | 97.4 | 30.81 | 399.6 ± 1.7 |
| *Totals* | | | | 300.7 | | | 29.98 | 389.9 ± 2.6 |
| Plateau Age = 390.8 ± 2.4 Ma | | | Conventional K/Ar age = 396.1 ± 3.2 Ma | | | | | |
| $\lambda_e = 5.543 \times 10^{-10}\ a^{-1}$ | | | Flux monitor, GA1550 Biotite, $^{40}Ar^*/^{39}Ar_K = 6.994$ | | | | | |

**Table B.7** *$^{40}Ar/^{39}Ar$ Step Heating Data – Muscovites ... continued*

| Temp (°C) | $^{40}Ar/^{39}Ar$ | $^{37}Ar/^{39}Ar$ ($10^{-4}$) | $^{36}Ar/^{39}Ar$ ($10^{-3}$) | $^{39}Ar$ ($10^{-15}$ mol) | Cumulative $^{39}Ar$ (%) | $\%^{40}Ar^*$ | $^{40}Ar^*/^{39}Ar_K$ | Calculated Age (Ma) ± 1 s.d. |
|---|---|---|---|---|---|---|---|---|
| **MP5, Muscovite, 0.51 mg, J = 0.008024** | | | | | | | | |
| 700 | 36.99 | 242.0 | 29.32 | 4.471 | 1.8 | 76.5 | 28.31 | 369.2 ± 5.7 |
| 760 | 33.79 | 69.35 | 14.39 | 4.865 | 3.8 | 87.3 | 29.52 | 383.5 ± 4.8 |
| 815 | 31.64 | 0.8492 | 5.108 | 19.03 | 11.6 | 95.1 | 30.11 | 390.4 ± 1.6 |
| 835 | 30.84 | 0.6852 | 1.607 | 23.60 | 21.2 | 98.4 | 30.34 | 393.1 ± 1.9 |
| 855 | 30.63 | 0.6451 | 1.117 | 25.08 | 31.5 | 98.8 | 30.27 | 392.3 ± 1.2 |
| 875 | 30.42 | 0.7250 | 0.8885 | 22.33 | 40.6 | 99.0 | 30.13 | 390.6 ± 1.5 |
| 910 | 30.24 | 0.7019 | 0.8575 | 23.08 | 50.0 | 99.1 | 29.95 | 388.6 ± 1.3 |
| 965 | 30.20 | 0.8130 | 0.8424 | 20.11 | 58.2 | 99.1 | 29.92 | 388.2 ± 3.0 |
| 1000 | 30.59 | 0.7942 | 1.030 | 20.60 | 66.6 | 98.9 | 30.26 | 392.1 ± 2.9 |
| 1025 | 30.83 | 0.5670 | 0.7042 | 28.87 | 78.4 | 99.2 | 30.60 | 396.1 ± 1.3 |
| 1045 | 30.72 | 0.6358 | 0.5454 | 25.78 | 88.9 | 99.4 | 30.53 | 395.4 ± 1.5 |
| 1070 | 30.87 | 0.8180 | 0.4943 | 20.05 | 97.1 | 99.4 | 30.70 | 397.3 ± 2.0 |
| 1110 | 31.91 | 2.476 | 3.501 | 6.627 | 99.8 | 96.7 | 30.86 | 399.1 ± 2.5 |
| 1350 | 81.31 | 33.62 | 216.8 | 0.4884 | 100.0 | 21.2 | 17.23 | 233.6 ± 63 |
| *Totals* | | | | 245.0 | | | 30.23 | 391.8 ± 2.0 |
| Plateau Age = 392.8 ± 1.8 Ma | | | Conventional K/Ar age = 390.9 ± 3.0 Ma | | | | | |
| $\lambda_e = 5.543 \times 10^{-10}\ a^{-1}$ | | | Flux monitor, GA1550 Biotite, $^{40}Ar^*/^{39}Ar_K = 7.015$ | | | | | |
| **MP3, Muscovite, 0.60 mg, J = 0.008059** | | | | | | | | |
| 750 | 32.30 | 46.46 | 10.95 | 10.06 | 3.7 | 89.9 | 29.02 | 379.1 ± 3.5 |
| 800 | 31.86 | 0.3821 | 1.408 | 41.46 | 19.1 | 98.6 | 31.41 | 407.1 ± 1.2 |
| 830 | 31.38 | 0.2826 | 0.5482 | 56.09 | 39.8 | 99.4 | 31.19 | 404.5 ± 1.0 |
| 845 | 31.19 | 0.6229 | 0.4780 | 25.46 | 49.2 | 99.5 | 31.02 | 402.5 ± 2.1 |
| 890 | 31.15 | 0.5279 | 1.119 | 30.06 | 60.3 | 98.9 | 30.80 | 400.0 ± 1.8 |
| 940 | 31.05 | 0.9287 | 2.147 | 17.10 | 66.7 | 97.9 | 30.39 | 395.2 ± 2.2 |
| 1000 | 31.10 | 0.7681 | 0.6109 | 20.87 | 74.4 | 99.3 | 30.90 | 401.2 ± 3.5 |
| 1040 | 31.41 | 0.4384 | 0.5485 | 36.61 | 87.9 | 99.4 | 31.23 | 404.9 ± 1.6 |
| 1060 | 31.76 | 0.7351 | 1.079 | 21.86 | 96.0 | 98.9 | 31.42 | 407.1 ± 1.0 |
| 1090 | 32.76 | 1.829 | 2.838 | 8.792 | 99.3 | 97.4 | 31.89 | 412.6 ± 2.7 |
| 1130 | 39.08 | 64.54 | 23.57 | 1.410 | 99.8 | 82.1 | 32.09 | 415.0 ± 14 |
| 1200 | 213.0 | 2196 | 580.6 | 0.07366 | 99.8 | 19.4 | 41.41 | 519.5 ± 286 |
| 1350 | 132.2 | 29.70 | 365.2 | 0.5424 | 100.0 | 18.4 | 24.27 | 322.3 ± 77 |
| *Totals* | | | | 270.34 | | | 31.05 | 402.9 ± 2.0 |
| Plateau Age = 403.6 ± 1.6 Ma | | | Conventional K/Ar age = 407.3 ± 3.2 Ma | | | | | |
| $\lambda_e = 5.543 \times 10^{-10}\ a^{-1}$ | | | Flux monitor, GA1550 Biotite, $^{40}Ar^*/^{39}Ar_K = 6.985$ | | | | | |

**Table B.8** *$^{40}Ar/^{39}Ar$ Step Heating Data – Biotites*

| Temp (°C) | $^{40}Ar/^{39}Ar$ | $^{37}Ar/^{39}Ar$ ($10^{-4}$) | $^{36}Ar/^{39}Ar$ ($10^{-3}$) | $^{39}Ar$ ($10^{-15}$ mol) | Cumulative $^{39}Ar$ (%) | $\%^{40}Ar^*$ | $^{40}Ar^*/^{39}Ar_K$ | Calculated Age (Ma) ± 1 s.d. |
|---|---|---|---|---|---|---|---|---|
| **MP24, Biotite, 0.59 mg, J = 0.008003** | | | | | | | | |
| 550 | 218.3 | 3.991 | 683.6 | 3.581 | 1.1 | 7.4 | 16.25 | 220.5 ± 51 |
| 650 | 40.61 | 0.7566 | 60.85 | 18.90 | 6.8 | 55.7 | 22.61 | 300.1 ± 4.0 |
| 680 | 32.26 | 0.3906 | 22.03 | 36.64 | 18.0 | 79.7 | 25.72 | 337.7 ± 2.0 |
| 700 | 30.25 | 0.3619 | 8.581 | 39.54 | 30.0 | 91.5 | 27.68 | 361.0 ± 2.0 |
| 715 | 30.01 | 0.4072 | 4.584 | 35.19 | 40.7 | 95.4 | 28.64 | 372.3 ± 2.0 |
| 730 | 29.72 | 0.4723 | 3.007 | 30.36 | 49.9 | 96.9 | 28.80 | 374.2 ± 1.9 |
| 750 | 29.90 | 0.5399 | 2.973 | 26.58 | 58.0 | 97.0 | 29.00 | 376.5 ± 1.2 |
| 770 | 29.88 | 0.7894 | 2.906 | 18.19 | 63.5 | 97.0 | 28.99 | 376.4 ± 2.2 |
| 790 | 30.34 | 1.464 | 4.761 | 9.814 | 66.5 | 95.3 | 28.91 | 375.4 ± 2.5 |
| 820 | 30.21 | 3.555 | 6.369 | 4.687 | 67.9 | 93.7 | 28.31 | 368.4 ± 3.9 |
| 870 | 28.48 | 2.242 | 9.776 | 6.419 | 69.9 | 89.8 | 25.57 | 335.8 ± 3.7 |
| 930 | 28.73 | 19.41 | 11.38 | 11.64 | 73.4 | 88.2 | 25.33 | 333.0 ± 2.7 |
| 1000 | 27.29 | 0.4173 | 6.631 | 34.82 | 84.0 | 92.7 | 25.30 | 332.6 ± 1.9 |
| 1030 | 28.11 | 4.760 | 7.973 | 20.03 | 90.1 | 91.5 | 25.73 | 337.8 ± 1.4 |
| 1070 | 28.90 | 3.145 | 8.498 | 18.58 | 95.7 | 91.2 | 26.37 | 345.4 ± 2.4 |
| 1150 | 32.10 | 1.340 | 17.01 | 10.87 | 99.0 | 84.3 | 27.04 | 353.5 ± 3.3 |
| 1350 | 83.68 | 18.75 | 210.0 | 3.162 | 100.0 | 25.8 | 21.62 | 287.9 ± 25 |
| *Totals* | | | | 329.0 | | | 26.83 | 350.9 ± 2.9 |
| | | | | Conventional K/Ar age = 343.9 ± 2.9 Ma | | | | |
| $\lambda_e = 5.543 \times 10^{-10}\ a^{-1}$ | | | | Fluence monitor, GA1550 Biotite, $^{40}Ar^*/^{39}Ar_K = 7.033$ | | | | |
| **MP11, Biotite, 0.52 mg, J = 0.008031** | | | | | | | | |
| 550 | 42.71 | 812.2 | 55.57 | 1.544 | 0.7 | 61.5 | 26.28 | 345.5 ± 23 |
| 650 | 31.28 | 39.06 | 6.491 | 5.617 | 3.1 | 93.8 | 29.33 | 381.6 ± 4.2 |
| 680 | 29.75 | 0.8407 | 1.912 | 18.14 | 10.8 | 98.0 | 29.16 | 379.5 ± 1.5 |
| 700 | 29.24 | 0.5643 | 0.9009 | 27.04 | 22.3 | 99.0 | 28.95 | 377.2 ± 1.5 |
| 715 | 29.26 | 0.6341 | 0.4855 | 24.08 | 32.6 | 99.4 | 29.09 | 378.8 ± 1.7 |
| 730 | 29.57 | 0.7745 | 0.5067 | 19.73 | 41.1 | 99.4 | 29.39 | 382.3 ± 1.4 |
| 750 | 29.36 | 0.9267 | 0.2157 | 16.64 | 48.2 | 99.7 | 29.27 | 380.9 ± 1.6 |
| 780 | 29.13 | 0.9267 | 0.4576 | 16.65 | 55.3 | 99.4 | 28.97 | 377.4 ± 1.9 |
| 830 | 29.51 | 1.485 | 1.288 | 10.40 | 59.7 | 98.6 | 29.11 | 379.0 ± 2.9 |
| 900 | 29.70 | 1.700 | 0.8692 | 9.091 | 63.6 | 99.0 | 29.41 | 382.6 ± 1.6 |
| 980 | 29.86 | 0.3925 | 1.236 | 39.39 | 80.4 | 98.7 | 29.45 | 383.0 ± 1.0 |
| 1010 | 29.75 | 0.8045 | 1.213 | 19.23 | 88.6 | 98.7 | 29.36 | 381.9 ± 1.3 |
| 1050 | 30.63 | 1.260 | 4.916 | 12.29 | 93.9 | 95.2 | 29.15 | 379.4 ± 1.9 |
| 1130 | 30.60 | 1.158 | 3.924 | 13.39 | 99.6 | 96.1 | 29.41 | 382.5 ± 2.4 |
| 1350 | 120.9 | 420.7 | 335.3 | 1.020 | 100.0 | 18.0 | 21.76 | 290.6 ± 41 |
| *Totals* | | | | 234.3 | | | 29.18 | 379.8 ± 2.0 |
| Plateau Age = 380.5 ± 1.7 Ma | | | | Conventional K/Ar age = 383.3 ± 3.2 Ma | | | | |
| $\lambda_e = 5.543 \times 10^{-10}\ a^{-1}$ | | | | Fluence monitor, GA1550 Biotite, $^{40}Ar^*/^{39}Ar_K = 7.009$ | | | | |

**Table B.8** *$^{40}Ar/^{39}Ar$ Step Heating Data – Biotites ... continued*

| Temp (°C) | $^{40}Ar/^{39}Ar$ | $^{37}Ar/^{39}Ar$ ($10^{-4}$) | $^{36}Ar/^{39}Ar$ ($10^{-3}$) | $^{39}Ar$ ($10^{-15}$ mol) | Cumulative $^{39}Ar$ (%) | $\%^{40}Ar^*$ | $^{40}Ar^*/^{39}Ar_K$ | Calculated Age (Ma) ± 1 s.d. |
|---|---|---|---|---|---|---|---|---|
| **MP9, Biotite, 0.50 mg, J = 0.008008** | | | | | | | | |
| 550 | 33.11 | 344.0 | 33.95 | 5.802 | 1.9 | 69.6 | 23.05 | 305.6 ± 5.3 |
| 650 | 32.78 | 0.8816 | 12.09 | 16.56 | 7.2 | 89.0 | 29.19 | 378.9 ± 2.2 |
| 680 | 31.19 | 0.3489 | 2.472 | 41.87 | 20.8 | 97.6 | 30.43 | 393.5 ± 1.1 |
| 700 | 31.19 | 0.2734 | 0.8902 | 53.48 | 38.0 | 99.1 | 30.89 | 398.8 ± 1.7 |
| 715 | 31.24 | 0.2499 | 0.3406 | 58.55 | 57.0 | 99.6 | 31.11 | 401.3 ± 1.4 |
| 730 | 31.33 | 0.3087 | 0.3169 | 47.43 | 72.3 | 99.6 | 31.21 | 402.5 ± 1.2 |
| 745 | 31.77 | 0.4687 | 0.4962 | 31.26 | 82.4 | 99.5 | 31.59 | 406.9 ± 1.5 |
| 760 | 32.09 | 0.8649 | 0.6348 | 16.95 | 87.9 | 99.3 | 31.88 | 410.2 ± 2.4 |
| 790 | 31.72 | 23.69 | 3.580 | 9.003 | 90.8 | 96.6 | 30.64 | 395.8 ± 2.6 |
| 850 | 31.70 | 39.73 | 7.288 | 5.892 | 92.7 | 93.1 | 29.52 | 382.8 ± 4.0 |
| 940 | 31.47 | 42.42 | 10.70 | 8.682 | 95.5 | 89.9 | 28.27 | 368.2 ± 2.9 |
| 1000 | 32.09 | 1.920 | 4.468 | 7.715 | 98.0 | 95.8 | 30.74 | 397.1 ± 2.7 |
| 1080 | 33.68 | 3.157 | 11.38 | 4.694 | 99.5 | 89.9 | 30.30 | 391.9 ± 4.9 |
| 1350 | 118.8 | 9.907 | 329.8 | 1.497 | 100.0 | 17.9 | 21.28 | 283.9 ± 46 |
| *Totals* | | | | 309.4 | | | 30.64 | 395.9 ± 2.0 |
| Plateau Age = 401.0 ± 1.4 Ma | | | | Conventional K/Ar age = 398.7 ± 3.2 Ma | | | | |
| $\lambda_e = 5.543 \times 10^{-10}\ a^{-1}$ | | | | Fluence monitor, GA1550 Biotite, $^{40}Ar^*/^{39}Ar_K = 7.029$ | | | | |
| **MP2, Biotite, 0.54 mg, J = 0.008016** | | | | | | | | |
| 550 | 30.61 | 1396 | 62.22 | 1.300 | 0.4 | 39.9 | 12.21 | 168.4 ± 21 |
| 650 | 27.29 | 251.0 | 25.21 | 2.813 | 1.3 | 72.6 | 19.82 | 266.0 ± 12 |
| 690 | 31.60 | 53.19 | 10.65 | 5.428 | 2.9 | 90.0 | 28.42 | 370.3 ± 5.2 |
| 735 | 29.39 | 8.643 | 3.672 | 15.84 | 7.8 | 96.2 | 28.29 | 368.7 ± 1.7 |
| 765 | 28.53 | 0.7426 | 1.875 | 20.05 | 13.9 | 98.0 | 27.96 | 364.8 ± 1.8 |
| 795 | 28.34 | 0.7700 | 1.713 | 19.35 | 19.9 | 98.1 | 27.81 | 363.0 ± 2.1 |
| 860 | 28.46 | 0.7320 | 1.852 | 20.37 | 26.1 | 98.0 | 27.88 | 363.9 ± 1.3 |
| 915 | 29.11 | 1.041 | 3.890 | 14.33 | 30.5 | 96.0 | 27.93 | 364.4 ± 1.9 |
| 960 | 29.16 | 1.146 | 3.055 | 13.03 | 34.5 | 96.8 | 28.22 | 368.0 ± 1.6 |
| 1010 | 28.81 | 0.5407 | 1.860 | 27.63 | 43.0 | 98.0 | 28.23 | 368.1 ± 1.8 |
| 1030 | 28.60 | 5.762 | 1.672 | 28.55 | 51.8 | 98.2 | 28.07 | 366.2 ± 1.2 |
| 1050 | 28.43 | 0.4916 | 1.425 | 30.43 | 61.1 | 98.4 | 27.97 | 365.0 ± 2.0 |
| 1080 | 28.45 | 0.3962 | 1.510 | 37.78 | 72.7 | 98.3 | 27.97 | 364.9 ± 1.2 |
| 1150 | 28.47 | 0.2536 | 1.427 | 59.08 | 90.8 | 98.4 | 28.02 | 365.6 ± 0.9 |
| 1350 | 32.20 | 0.5018 | 15.09 | 29.87 | 100.0 | 86.1 | 27.72 | 361.9 ± 1.6 |
| *Totals* | | | | 325.9 | | | 27.87 | 363.8 ± 1.7 |
| Plateau Age = 365.3 ± 1.5 Ma | | | | Conventional K/Ar age = 371.2 ± 3.0 Ma | | | | |
| $\lambda_e = 5.543 \times 10^{-10}\ a^{-1}$ | | | | Fluence monitor, GA1550 Biotite, $^{40}Ar^*/^{39}Ar_K = 7.022$ | | | | |

**Table B.8** *$^{40}Ar/^{39}Ar$ Step Heating Data – Biotites ... continued*

| Temp (°C) | $^{40}Ar/^{39}Ar$ | $^{37}Ar/^{39}Ar$ ($10^{-4}$) | $^{36}Ar/^{39}Ar$ ($10^{-3}$) | $^{39}Ar$ ($10^{-15}$ mol) | Cumulative $^{39}Ar$ (%) | $\%^{40}Ar^*$ | $^{40}Ar^*/^{39}Ar_K$ | Calculated Age (Ma) ± 1 s.d. |
|---|---|---|---|---|---|---|---|---|
| **MP7, Biotite, 0.52 mg, J = 0.008069** | | | | | | | | |
| 550 | 40.66 | 2761 | 95.38 | 0.6623 | 0.3 | 30.7 | 12.49 | 173.2 ± 26 |
| 650 | 42.89 | 1411 | 17.60 | 0.6967 | 0.5 | 87.8 | 37.69 | 479.0 ± 13 |
| 690 | 32.69 | 416.9 | 6.861 | 1.679 | 1.2 | 93.7 | 30.64 | 398.5 ± 5.1 |
| 740 | 30.26 | 2.518 | 3.413 | 6.180 | 3.6 | 96.6 | 29.22 | 382.0 ± 3.1 |
| 790 | 28.65 | 0.8928 | 0.3818 | 17.44 | 10.4 | 99.5 | 28.52 | 373.6 ± 1.4 |
| 850 | 28.48 | 0.7238 | 0.3612 | 21.72 | 18.8 | 99.5 | 28.35 | 371.7 ± 1.8 |
| 915 | 28.88 | 0.9924 | 0.6719 | 15.85 | 24.9 | 99.2 | 28.67 | 375.4 ± 2.5 |
| 965 | 29.31 | 1.294 | 0.4834 | 12.16 | 29.7 | 99.4 | 29.15 | 381.0 ± 1.2 |
| 1010 | 28.86 | 0.8145 | 0.3365 | 19.35 | 37.2 | 99.6 | 28.72 | 376.0 ± 1.4 |
| 1040 | 28.74 | 0.6395 | 0.3356 | 24.66 | 46.7 | 99.6 | 28.61 | 374.7 ± 1.4 |
| 1070 | 28.57 | 0.5033 | 0.5742 | 31.35 | 58.9 | 99.3 | 28.37 | 371.9 ± 1.4 |
| 1100 | 28.65 | 0.4413 | 0.5858 | 35.78 | 72.8 | 99.3 | 28.44 | 372.7 ± 1.5 |
| 1150 | 28.57 | 0.3816 | 0.5171 | 41.40 | 88.9 | 99.4 | 28.41 | 372.3 ± 1.0 |
| 1350 | 30.95 | 6.975 | 8.535 | 28.66 | 100.0 | 91.8 | 28.40 | 372.2 ± 2.8 |
| *Totals* | | | | 257.6 | | | 28.52 | 373.7 ± 1.7 |
| Plateau Age = 374.1 ± 1.7 Ma | | | | Conventional K/Ar age = 378.3 ± 3.0 Ma | | | | |
| $\lambda_e = 5.543 \times 10^{-10}\ a^{-1}$ | | | | Fluence monitor, GA1550 Biotite, $^{40}Ar^*/^{39}Ar_K = 6.976$ | | | | |
| **MP3, Biotite, 0.57 mg, J = 0.008034** | | | | | | | | |
| 550 | 42.89 | 343.0 | 95.15 | 1.485 | 0.6 | 34.4 | 14.75 | 202.0 ± 14 |
| 650 | 24.08 | 9.955 | 20.15 | 6.195 | 3.4 | 75.2 | 18.11 | 245.0 ± 4.2 |
| 680 | 30.05 | 11.18 | 7.855 | 8.166 | 7.0 | 92.2 | 27.70 | 362.5 ± 2.8 |
| 700 | 30.92 | 5.121 | 3.215 | 11.14 | 11.9 | 96.8 | 29.95 | 389.0 ± 2.5 |
| 715 | 30.50 | 0.9528 | 2.690 | 13.34 | 17.8 | 97.3 | 29.68 | 385.8 ± 2.1 |
| 730 | 30.27 | 0.7876 | 2.185 | 16.15 | 24.9 | 97.8 | 29.60 | 384.8 ± 1.3 |
| 745 | 30.63 | 1.169 | 2.618 | 10.89 | 29.7 | 97.4 | 29.85 | 387.8 ± 1.7 |
| 760 | 30.69 | 0.7806 | 2.292 | 10.78 | 33.8 | 97.7 | 29.98 | 389.3 ± 1.7 |
| 775 | 30.56 | 3.956 | 2.677 | 9.900 | 37.5 | 97.3 | 29.74 | 386.5 ± 3.0 |
| 790 | 30.76 | 19.44 | 3.511 | 6.691 | 40.0 | 96.5 | 29.70 | 386.0 ± 2.4 |
| 820 | 30.93 | 28.12 | 3.338 | 6.821 | 42.6 | 96.7 | 29.92 | 388.6 ± 1.5 |
| 860 | 30.90 | 7.248 | 3.416 | 8.247 | 45.7 | 96.6 | 29.85 | 387.8 ± 2.3 |
| 940 | 30.39 | 10.35 | 1.646 | 21.11 | 55.0 | 98.3 | 29.88 | 388.2 ± 1.3 |
| 1000 | 31.66 | 70.60 | 5.651 | 22.35 | 64.8 | 94.6 | 29.96 | 389.1 ± 4.1 |
| 1060 | 29.98 | 3.913 | 1.021 | 64.00 | 93.1 | 98.9 | 29.65 | 385.4 ± 1.0 |
| 1130 | 31.60 | 0.9126 | 4.739 | 14.18 | 99.4 | 95.5 | 30.17 | 391.6 ± 1.5 |
| 1350 | 129.0 | 9.062 | 354.1 | 1.429 | 100.0 | 18.9 | 24.39 | 322.8 ± 36 |
| *Totals* | | | | 232.9 | | | 29.29 | 381.0 ± 2.2 |
| Plateau Age = 387.2 ± 1.8 Ma | | | | Conventional K/Ar age = 386.3 ± 3.1 Ma | | | | |
| $\lambda_e = 5.543 \times 10^{-10}\ a^{-1}$ | | | | Fluence monitor, GA1550 Biotite, $^{40}Ar^*/^{39}Ar_K = 7.006$ | | | | |

**Table B.9** *$^{40}Ar/^{39}Ar$ Step Heating Data – K-feldspar, sample MP24*

| Temp (°C) | $^{40}Ar/^{39}Ar$ | $^{38}Ar/^{39}Ar$ ($10^{-2}$) | $^{37}Ar/^{39}Ar$ ($10^{-4}$) | $^{36}Ar/^{39}Ar$ ($10^{-3}$) | $^{39}Ar$ (mol) ($10^{-15}$) | Cumulative $^{39}Ar$ (%) | $^{40}Ar^*$ (%) | $^{40}Ar^*/^{39}Ar_K$ | Calculated Age (Ma) ± 1 s.d. | Cl/K ($10^{-5}$) |
|---|---|---|---|---|---|---|---|---|---|---|
| **MP24, K-feldspar, 1.26 mg, J = 0.008138** | | | | | | | | | | |
| 450 | 168.5 | 25.77 | 372.1 | 284.4 | 0.2053 | 0.1 | 50.1 | 84.50 | 944.2 ± 41 | 1120 |
| 450 | 111.0 | 18.48 | 7355 | 261.1 | 0.1105 | 0.1 | 30.5 | 33.90 | 439.6 ± 39 | 209 |
| 500 | 67.11 | 15.30 | 17.37 | 84.53 | 0.2107 | 0.1 | 62.8 | 42.12 | 531.8 ± 21 | 228 |
| 500 | 54.99 | 14.80 | 649.5 | 88.37 | 0.2915 | 0.2 | 52.5 | 28.86 | 380.6 ± 7.6 | 152 |
| 550 | 29.75 | 13.55 | 144.4 | 18.14 | 0.5459 | 0.3 | 81.9 | 24.36 | 326.3 ± 7.0 | 161 |
| 550 | 30.00 | 13.66 | 5.946 | 24.63 | 0.6909 | 0.5 | 75.7 | 22.70 | 305.8 ± 9.0 | 160 |
| 600 | 26.03 | 12.99 | 609.3 | 6.027 | 1.216 | 0.7 | 93.1 | 24.23 | 324.7 ± 2.6 | 118 |
| 600 | 25.70 | 12.82 | 67.42 | 8.597 | 1.625 | 1.1 | 90.0 | 23.14 | 311.2 ± 3.4 | 89 |
| 650 | 24.22 | 12.75 | 35.91 | 3.024 | 2.777 | 1.7 | 96.2 | 23.30 | 313.3 ± 1.1 | 93 |
| 650 | 25.01 | 12.75 | 46.19 | 4.346 | 4.038 | 2.6 | 94.8 | 23.69 | 318.1 ± 1.1 | 90 |
| 700 | 24.50 | 12.69 | 85.62 | 1.708 | 5.771 | 3.9 | 97.8 | 23.96 | 321.4 ± 2.9 | 88 |
| 700 | 24.71 | 12.48 | 122.4 | 2.069 | 8.238 | 5.8 | 97.4 | 24.08 | 322.9 ± 0.9 | 58 |
| 750 | 24.48 | 12.48 | 42.34 | 0.9109 | 10.36 | 8.1 | 98.8 | 24.18 | 324.1 ± 0.7 | 61 |
| 750 | 24.52 | 12.51 | 44.47 | 1.350 | 14.76 | 11.4 | 98.3 | 24.09 | 323.0 ± 0.7 | 65 |
| 800 | 24.41 | 12.46 | 0.2823 | 0.4199 | 16.07 | 15.0 | 99.4 | 24.26 | 325.0 ± 0.5 | 60 |
| 800 | 24.54 | 12.42 | 61.60 | 0.7397 | 22.67 | 20.1 | 99.0 | 24.30 | 325.5 ± 0.6 | 54 |
| 850 | 24.48 | 12.48 | 20.39 | 0.5228 | 21.71 | 25.0 | 99.3 | 24.29 | 325.5 ± 0.5 | 63 |
| 850* | 24.48 | 12.48 | 20.39 | 0.1847 | 21.71 | 29.9 | 99.7 | 24.39 | 326.7 ± 2.1* | 64 |
| 900 | 24.63 | 12.38 | 0.2930 | 0.3098 | 26.51 | 35.8 | 99.5 | 24.51 | 328.1 ± 0.7 | 50 |
| 900 | 24.68 | 12.37 | 0.2193 | 0.6208 | 35.47 | 43.8 | 99.1 | 24.47 | 327.6 ± 0.7 | 48 |
| 950 | 24.79 | 12.36 | 17.00 | 0.3938 | 25.93 | 49.6 | 99.4 | 24.65 | 329.8 ± 0.5 | 47 |
| 950 | 24.93 | 12.37 | 0.2428 | 0.7077 | 32.09 | 56.8 | 99.1 | 24.69 | 330.3 ± 0.6 | 48 |
| 950 | 25.21 | 12.46 | 10.58 | 1.207 | 29.28 | 63.4 | 98.5 | 24.83 | 332.1 ± 0.8 | 58 |
| 1000 | 25.41 | 12.57 | 1.182 | 1.147 | 9.295 | 65.5 | 98.6 | 25.05 | 334.7 ± 1.3 | 73 |
| 1000 | 25.57 | 12.52 | 317.6 | 1.380 | 13.12 | 68.4 | 98.3 | 25.13 | 335.7 ± 1.1 | 65 |
| 1050 | 25.75 | 12.64 | 335.2 | 1.329 | 8.917 | 70.4 | 98.4 | 25.33 | 338.1 ± 1.0 | 82 |
| 1050 | 26.20 | 12.56 | 0.9364 | 2.128 | 11.77 | 73.1 | 97.5 | 25.55 | 340.8 ± 1.5 | 69 |
| 1050 | 26.85 | 12.49 | 1.487 | 4.925 | 12.77 | 76.0 | 94.5 | 25.38 | 338.7 ± 1.8 | 53 |
| 1100 | 26.71 | 12.86 | 380.7 | 4.186 | 4.859 | 77.0 | 95.3 | 25.46 | 339.7 ± 2.0 | 104 |
| 1100 | 27.42 | 13.03 | 43.93 | 4.176 | 8.371 | 78.9 | 95.4 | 26.16 | 348.2 ± 1.2 | 127 |
| 1100 | 27.95 | 13.04 | 1.583 | 4.712 | 11.52 | 81.5 | 94.9 | 26.54 | 352.8 ± 2.0 | 128 |
| 1100 | 29.09 | 13.40 | 1.404 | 8.129 | 12.67 | 84.4 | 91.6 | 26.66 | 354.3 ± 1.5 | 167 |
| 1100 | 30.52 | 13.33 | 316.4 | 13.57 | 11.78 | 87.0 | 86.8 | 26.48 | 352.1 ± 1.8 | 142 |
| 1100 | 33.26 | 13.55 | 207.4 | 22.74 | 11.04 | 89.5 | 79.7 | 26.51 | 352.5 ± 3.3 | 150 |
| 1100 | 37.49 | 14.00 | 1.795 | 36.65 | 9.613 | 91.6 | 71.0 | 26.63 | 353.9 ± 3.0 | 175 |
| 1100 | 48.21 | 14.96 | 1.481 | 72.25 | 11.03 | 94.1 | 55.7 | 26.84 | 356.4 ± 4.2 | 214 |
| 1200 | 30.56 | 13.61 | 337.4 | 7.207 | 2.854 | 94.8 | 92.9 | 28.41 | 375.3 ± 4.9 | 196 |
| 1230 | 29.58 | 13.86 | 4.181 | 5.719 | 4.223 | 95.7 | 94.2 | 27.86 | 368.7 ± 4.6 | 234 |
| 1260 | 29.31 | 13.98 | 2.827 | 5.211 | 6.195 | 97.1 | 94.7 | 27.74 | 367.3 ± 2.7 | 251 |
| 1290 | 29.30 | 13.65 | 216.2 | 5.064 | 6.999 | 98.7 | 94.8 | 27.78 | 367.8 ± 2.8 | 207 |
| 1320 | 30.46 | 13.24 | 776.9 | 10.63 | 4.285 | 99.6 | 89.6 | 27.29 | 361.8 ± 4.4 | 139 |
| 1350 | 42.14 | 15.39 | 16.82 | 44.05 | 0.9480 | 99.8 | 69.1 | 29.10 | 383.4 ± 14 | 342 |
| 1450 | 130.5 | 21.35 | 16.53 | 362.4 | 0.6960 | 100.0 | 17.9 | 23.34 | 313.7 ± 32 | 338 |
| *Totals* | | | | 445.2 | | | | 25.14 | 335.8 ± 1.5 | |

** step lost, age estimated*

Conventional K/Ar age = 323.7 ± 2.5 Ma

$\lambda_e = 5.543 \times 10^{-10}\ a^{-1}$

Fluence monitor, GA1550 Biotite, $^{40}Ar^*/^{39}Ar_K = 6.916$

**Table B.10** *$^{40}Ar/^{39}Ar$ Step Heating Data – K-feldspar sample, MP9*

| Temp (°C) | $^{40}Ar/^{39}Ar$ | $^{38}Ar/^{39}Ar$ ($10^{-2}$) | $^{37}Ar/^{39}Ar$ ($10^{-4}$) | $^{36}Ar/^{39}Ar$ ($10^{-3}$) | $^{39}Ar$ (mol) ($10^{-15}$) | Cumulative $^{39}Ar$ (%) | $^{40}Ar^*$ (%) | $^{40}Ar^*/^{39}Ar_K$ | Calculated Age (Ma) ± 1 s.d. | Cl/K ($10^{-5}$) |
|---|---|---|---|---|---|---|---|---|---|---|
| **MP9, K-feldspar, 1.24 mg, J = 0.008148** | | | | | | | | | | |
| 450 | 86.56 | 18.57 | 6.907 | 114.8 | 0.2121 | 0.1 | 60.8 | 52.61 | 643.6 ±24 | 587 |
| 450 | 65.07 | 19.02 | 5.966 | 175.6 | 0.1449 | 0.1 | 20.2 | 13.17 | 183.8 ± 39 | 496 |
| 500 | 45.12 | 15.69 | 275.8 | 82.05 | 0.2651 | 0.2 | 46.2 | 20.84 | 283.0 ± 17 | 287 |
| 500 | 32.93 | 14.23 | 217.8 | 45.66 | 0.3699 | 0.3 | 58.9 | 19.41 | 264.9 ± 5.5 | 183 |
| 550 | 25.84 | 13.70 | 1.373 | 14.09 | 0.6308 | 0.5 | 83.8 | 21.64 | 293.0 ± 8.4 | 191 |
| 550 | 21.72 | 12.99 | 140.7 | 11.74 | 0.8435 | 0.7 | 83.9 | 18.22 | 249.7 ± 3.9 | 103 |
| 600 | 21.03 | 13.24 | 20.51 | 7.787 | 1.360 | 1.1 | 88.9 | 18.70 | 255.9 ± 2.5 | 146 |
| 600 | 20.87 | 12.55 | 0.4929 | 6.050 | 1.762 | 1.6 | 91.3 | 19.06 | 260.5 ± 2.6 | 59 |
| 650 | 23.31 | 12.89 | 85.37 | 6.204 | 2.181 | 2.2 | 92.0 | 21.45 | 290.6 ± 2.5 | 103 |
| 650 | 23.60 | 12.58 | 0.3691 | 5.172 | 2.357 | 2.9 | 93.4 | 22.04 | 298.0 ± 2.1 | 64 |
| 700 | 24.76 | 12.89 | 0.5783 | 4.064 | 2.554 | 3.6 | 95.0 | 23.54 | 316.6 ± 3.5 | 108 |
| 700 | 25.35 | 12.53 | 151.1 | 3.898 | 3.068 | 4.4 | 95.4 | 24.17 | 324.3 ± 3.0 | 61 |
| 750 | 25.43 | 12.52 | 83.28 | 2.321 | 3.319 | 5.4 | 97.2 | 24.73 | 331.1 ± 2.3 | 63 |
| 750 | 25.55 | 12.46 | 11.28 | 2.759 | 4.298 | 6.6 | 96.7 | 24.70 | 330.8 ± 1.8 | 54 |
| 800 | 25.39 | 12.71 | 89.01 | 0.6807 | 4.478 | 7.8 | 99.1 | 25.16 | 336.5 ± 1.6 | 93 |
| 800 | 25.06 | 12.46 | 55.54 | 2.105 | 5.990 | 9.5 | 97.4 | 24.41 | 327.3 ± 1.3 | 57 |
| 850 | 24.85 | 12.70 | 79.61 | 0.6983 | 5.876 | 11.2 | 99.1 | 24.61 | 329.7 ± 1.7 | 92 |
| 850 | 24.77 | 12.39 | 75.08 | 2.249 | 7.901 | 13.4 | 97.2 | 24.08 | 323.2 ± 1.7 | 46 |
| 900 | 24.79 | 12.55 | 10.49 | 1.069 | 7.221 | 15.4 | 98.6 | 24.44 | 327.6 ± 1.5 | 71 |
| 900 | 25.01 | 12.41 | 24.56 | 1.567 | 9.368 | 18.1 | 98.0 | 24.52 | 328.7 ± 0.9 | 52 |
| 950 | 24.98 | 12.40 | 0.2733 | 1.240 | 7.774 | 20.3 | 98.4 | 24.58 | 329.4 ± 1.5 | 50 |
| 950 | 25.25 | 12.49 | 0.2065 | 1.698 | 10.30 | 23.2 | 97.9 | 24.72 | 331.1 ± 1.1 | 61 |
| 950 | 25.79 | 12.38 | 40.49 | 2.651 | 11.21 | 26.3 | 96.9 | 24.97 | 334.2 ± 1.0 | 44 |
| 1000 | 25.66 | 12.44 | 0.2863 | 2.288 | 5.215 | 27.8 | 97.3 | 24.95 | 333.9 ± 1.7 | 53 |
| 1000 | 25.84 | 12.35 | 16.28 | 1.587 | 8.414 | 30.2 | 98.1 | 25.34 | 338.6 ± 1.5 | 43 |
| 1050 | 26.02 | 12.36 | 55.05 | 2.126 | 7.893 | 32.4 | 97.5 | 25.37 | 339.0 ± 2.0 | 43 |
| 1050 | 26.02 | 12.44 | 2.698 | 2.133 | 12.22 | 35.8 | 97.5 | 25.37 | 339.0 ± 0.9 | 54 |
| 1050 | 26.36 | 12.54 | 2.727 | 3.026 | 15.42 | 40.2 | 96.5 | 25.44 | 339.8 ± 0.9 | 64 |
| 1100 | 26.54 | 12.77 | 0.1814 | 2.081 | 8.271 | 42.5 | 97.6 | 25.90 | 345.4 ± 1.1 | 98 |
| 1100 | 26.39 | 12.62 | 21.88 | 2.182 | 14.75 | 46.7 | 97.5 | 25.73 | 343.4 ± 0.7 | 78 |
| 1100 | 26.61 | 12.65 | 9.389 | 2.472 | 21.78 | 52.8 | 97.2 | 25.86 | 344.9 ± 0.8 | 80 |
| 1100 | 26.82 | 12.62 | 15.95 | 3.581 | 25.61 | 60.0 | 96.0 | 25.74 | 343.5 ± 0.9 | 74 |
| 1100 | 27.29 | 12.63 | 18.16 | 4.828 | 25.25 | 67.1 | 94.7 | 25.84 | 344.7 ± 0.5 | 72 |
| 1100 | 27.96 | 12.69 | 0.08802 | 6.694 | 24.62 | 74.1 | 92.8 | 25.95 | 346.0 ± 0.9 | 75 |
| 1100 | 29.19 | 12.84 | 0.1078 | 10.89 | 20.22 | 79.8 | 88.9 | 25.95 | 346.1 ± 1.0 | 85 |
| 1100 | 31.70 | 12.87 | 8.958 | 19.61 | 21.40 | 85.8 | 81.6 | 25.87 | 345.1 ± 1.3 | 67 |
| 1200 | 26.61 | 12.68 | 5.324 | 3.221 | 7.949 | 88.0 | 96.3 | 25.63 | 342.2 ± 1.7 | 83 |
| 1230 | 26.37 | 12.64 | 0.1455 | 2.496 | 10.63 | 91.0 | 97.1 | 25.60 | 341.8 ± 1.5 | 79 |
| 1260 | 26.20 | 12.54 | 0.1712 | 1.804 | 12.91 | 94.7 | 97.9 | 25.64 | 342.3 ± 2.2 | 68 |
| 1290 | 26.06 | 12.54 | 25.12 | 2.172 | 11.79 | 98.0 | 97.4 | 25.40 | 339.4 ± 1.0 | 68 |
| 1320 | 26.51 | 12.74 | 0.3620 | 3.541 | 6.114 | 99.7 | 96.0 | 25.44 | 339.9 ± 2.2 | 89 |
| 1350 | 33.79 | 14.03 | 4.606 | 30.85 | 0.8228 | 99.9 | 72.9 | 24.64 | 330.1 ± 12 | 192 |
| 1450 | 149.7 | 22.11 | 14.66 | 399.2 | 0.2588 | 100.0 | 21.2 | 31.81 | 415.8 ± 74 | 348 |
| *Totals* | | | | | 355.0 | | | 25.30 | 338.2 ± 1.4 | |

Conventional K/Ar age = 341.3 ± 2.7 Ma

$\lambda_e = 5.543 \times 10^{-10}\ a^{-1}$ Fluence monitor, GA1550 Biotite, $^{40}Ar^*/^{39}Ar_K = 6.908$

**Table B.11** *$^{40}Ar/^{39}Ar$ Step Heating Data – K-feldspar sample, MP1*

| Temp (°C) | $^{40}Ar/^{39}Ar$ | $^{38}Ar/^{39}Ar$ ($10^{-2}$) | $^{37}Ar/^{39}Ar$ ($10^{-4}$) | $^{36}Ar/^{39}Ar$ ($10^{-3}$) | $^{39}Ar$ (mol) ($10^{-15}$) | Cumulative $^{39}Ar$ (%) | $^{40}Ar^*$ (%) | $^{40}Ar^*/^{39}Ar_K$ | Calculated Age (Ma) ± 1 s.d. | Cl/K ($10^{-5}$) |
|---|---|---|---|---|---|---|---|---|---|---|
| **MP1, K-feldspar, 1.21 mg, J = 0.008147** | | | | | | | | | | |
| 450 | 51.02 | 15.18 | 476.9 | 135.8 | 0.2252 | 0.1 | 21.3 | 10.88 | 153.2 ± 47 | 84 |
| 450 | 60.54 | 15.35 | 5.091 | 127.6 | 0.1802 | 0.1 | 37.7 | 22.81 | 307.4 ± 23 | 127 |
| 500 | 38.32 | 13.18 | 2.661 | 47.80 | 0.3450 | 0.2 | 63.1 | 24.18 | 324.4 ± 13 | 37 |
| 500 | 32.77 | 13.74 | 181.8 | 34.47 | 0.5053 | 0.3 | 68.8 | 22.56 | 304.4 ± 4.2 | 145 |
| 550 | 23.79 | 12.39 | 216.4 | 10.50 | 0.8799 | 0.6 | 86.9 | 20.66 | 280.6 ± 4.5 | 25 |
| 550 | 24.11 | 12.71 | 0.7707 | 10.59 | 1.194 | 0.9 | 86.9 | 20.95 | 284.3 ± 4.8 | 68 |
| 600 | 23.03 | 12.66 | 0.5002 | 5.649 | 1.841 | 1.4 | 92.6 | 21.33 | 289.0 ± 3.0 | 73 |
| 600 | 23.61 | 12.23 | 0.3758 | 5.512 | 2.453 | 2.1 | 93.0 | 21.95 | 296.8 ± 1.9 | 16 |
| 650 | 23.28 | 12.45 | 0.2756 | 2.598 | 3.347 | 3.0 | 96.6 | 22.49 | 303.5 ± 1.5 | 53 |
| 650 | 23.58 | 12.34 | 8.496 | 2.885 | 4.593 | 4.2 | 96.3 | 22.70 | 306.2 ± 1.5 | 38 |
| 700 | 23.77 | 12.40 | 10.65 | 0.8194 | 5.780 | 5.8 | 98.9 | 23.51 | 316.2 ± 1.4 | 51 |
| 700 | 23.86 | 12.21 | 3.199 | 1.520 | 7.587 | 7.8 | 98.0 | 23.38 | 314.6 ± 1.5 | 24 |
| 750 | 23.89 | 12.15 | 0.1976 | 1.208 | 7.945 | 10.0 | 98.4 | 23.51 | 316.2 ± 1.1 | 18 |
| 750 | 24.10 | 12.19 | 11.33 | 1.204 | 9.899 | 12.6 | 98.4 | 23.72 | 318.7 ± 0.9 | 23 |
| 800 | 24.02 | 12.17 | 0.1789 | 0.6364 | 8.787 | 15.0 | 99.1 | 23.80 | 319.8 ± 1.1 | 21 |
| 800 | 24.27 | 12.24 | 0.1508 | 1.344 | 10.44 | 17.8 | 98.3 | 23.84 | 320.2 ± 0.8 | 29 |
| 850 | 24.27 | 12.30 | 0.2774 | 0.8850 | 5.678 | 20.0 | 98.8 | 23.97 | 321.8 ± 1.2 | 37 |
| 850 | 24.51 | 12.22 | 9.053 | 0.9018 | 9.471 | 22.6 | 98.8 | 24.21 | 324.8 ± 1.4 | 26 |
| 900 | 24.59 | 12.30 | 12.47 | 1.179 | 6.988 | 24.5 | 98.5 | 24.21 | 324.8 ± 2.5 | 37 |
| 900 | 24.72 | 12.29 | 0.2662 | 1.668 | 8.468 | 26.8 | 97.9 | 24.20 | 324.6 ± 1.2 | 34 |
| 950 | 24.47 | 12.23 | 12.22 | 0.9618 | 6.264 | 28.4 | 98.7 | 24.17 | 324.2 ± 2.0 | 28 |
| 950 | 24.73 | 12.38 | 0.2778 | 1.611 | 8.127 | 30.6 | 98.0 | 24.23 | 325.0 ± 1.5 | 46 |
| 950 | 25.10 | 12.42 | 0.1833 | 2.987 | 8.644 | 33.0 | 96.4 | 24.19 | 324.5 ± 1.8 | 49 |
| 1000 | 24.88 | 12.49 | 65.56 | 1.101 | 3.554 | 33.9 | 98.6 | 24.53 | 328.7 ± 2.5 | 63 |
| 1000 | 24.92 | 12.46 | 0.2667 | 2.302 | 5.946 | 35.5 | 97.2 | 24.21 | 324.7 ± 1.0 | 55 |
| 1050 | 24.79 | 12.46 | 10.50 | 1.802 | 4.949 | 36.9 | 97.7 | 24.23 | 325.0 ± 1.5 | 56 |
| 1050 | 25.12 | 12.61 | 49.49 | 2.277 | 7.779 | 39.0 | 97.2 | 24.42 | 327.3 ± 1.2 | 76 |
| 1050 | 25.34 | 12.50 | 3.449 | 2.978 | 9.802 | 41.6 | 96.4 | 24.44 | 327.5 ± 1.5 | 58 |
| 1100 | 24.99 | 12.63 | 0.3610 | 2.136 | 4.410 | 42.8 | 97.4 | 24.34 | 326.3 ± 2.0 | 79 |
| 1100 | 25.16 | 12.68 | 3.255 | 3.077 | 8.451 | 45.1 | 96.3 | 24.22 | 324.9 ± 1.2 | 83 |
| 1100 | 25.34 | 12.69 | 0.1771 | 3.561 | 12.87 | 48.6 | 95.7 | 24.27 | 325.5 ± 1.0 | 83 |
| 1100 | 25.68 | 12.69 | 0.1399 | 5.788 | 16.33 | 53.0 | 93.2 | 23.95 | 321.6 ± 1.6 | 78 |
| 1100 | 26.13 | 12.68 | 0.1260 | 6.538 | 18.17 | 57.9 | 92.5 | 24.17 | 324.3 ± 0.9 | 74 |
| 1100 | 26.80 | 12.71 | 21.94 | 8.460 | 20.84 | 63.5 | 90.6 | 24.28 | 325.6 ± 1.1 | 74 |
| 1100 | 27.73 | 12.76 | 0.1129 | 11.93 | 20.50 | 69.1 | 87.2 | 24.18 | 324.4 ± 1.0 | 71 |
| 1100 | 30.29 | 12.87 | 0.09130 | 21.34 | 25.64 | 76.0 | 79.1 | 23.96 | 321.6 ± 1.3 | 62 |
| 1200 | 25.03 | 12.50 | 14.38 | 3.287 | 11.41 | 79.1 | 96.0 | 24.02 | 322.4 ± 1.0 | 58 |
| 1230 | 25.10 | 12.58 | 12.73 | 3.182 | 15.04 | 83.1 | 96.1 | 24.14 | 323.9 ± 0.8 | 70 |
| 1260 | 25.00 | 12.65 | 13.82 | 2.802 | 18.75 | 88.2 | 96.6 | 24.15 | 324.0 ± 1.0 | 79 |
| 1290 | 25.06 | 12.42 | 0.1107 | 2.704 | 21.21 | 93.9 | 96.7 | 24.24 | 325.1 ± 0.7 | 50 |
| 1320 | 25.35 | 12.68 | 0.1576 | 3.514 | 14.91 | 98.0 | 95.8 | 24.28 | 325.6 ± 1.0 | 81 |
| 1350 | 26.32 | 12.82 | 0.6676 | 6.918 | 6.025 | 99.6 | 92.1 | 24.26 | 325.3 ± 3.4 | 92 |
| 1450 | 56.06 | 15.17 | 722.0 | 110.4 | 1.554 | 100.0 | 41.8 | 23.44 | 315.2 ± 20 | 147 |
| *Totals* | | | | | 367.8 | | | 24.01 | 322.3 ± 1.4 | |

Conventional K/Ar age = 323.2 ± 2.5 Ma

$\lambda_e = 5.543 \times 10^{-10}\ a^{-1}$

Fluence monitor, GA1550 Biotite, $^{40}Ar^*/^{39}Ar_K = 6.909$

**Table B.12** *$^{40}Ar/^{39}Ar$ Step Heating Data – K-feldspar sample, MP6*

| Temp (°C) | $^{40}Ar/^{39}Ar$ | $^{38}Ar/^{39}Ar$ ($10^{-2}$) | $^{37}Ar/^{39}Ar$ ($10^{-4}$) | $^{36}Ar/^{39}Ar$ ($10^{-3}$) | $^{39}Ar$ (mol) ($10^{-15}$) | Cumulative $^{39}Ar$ (%) | $^{40}Ar^*$ (%) | $^{40}Ar^*/^{39}Ar_K$ | Calculated Age (Ma) ± 1 s.d. | Cl/K ($10^{-5}$) |
|---|---|---|---|---|---|---|---|---|---|---|
| **MP6, K-feldspar, 1.18 mg, J = 0.008129** | | | | | | | | | | |
| 450 | 60.90 | 19.64 | 5.259 | 139.9 | 0.2624 | 0.1 | 32.0 | 19.52 | 265.7 ± 33 | 668 |
| 450 | 68.77 | 16.65 | 3.494 | 175.4 | 0.2331 | 0.2 | 24.6 | 16.90 | 232.2 ± 20 | 180 |
| 500 | 32.11 | 15.68 | 185.5 | 42.22 | 0.4105 | 0.3 | 61.1 | 19.61 | 266.8 ± 9.1 | 385 |
| 500 | 32.16 | 13.71 | 258.4 | 40.71 | 0.6114 | 0.5 | 62.5 | 20.11 | 273.1 ± 4.7 | 126 |
| 550 | 24.27 | 14.44 | 58.77 | 15.80 | 1.033 | 0.9 | 80.6 | 19.58 | 266.4 ± 6.1 | 287 |
| 550 | 23.27 | 12.74 | 179.9 | 11.30 | 1.411 | 1.3 | 85.6 | 19.91 | 270.6 ± 3.4 | 71 |
| 600 | 21.86 | 12.87 | 0.3943 | 5.388 | 2.073 | 2.0 | 92.6 | 20.24 | 274.8 ± 1.5 | 102 |
| 600 | 22.89 | 12.48 | 89.84 | 7.301 | 2.471 | 2.9 | 90.5 | 20.71 | 280.7 ± 3.1 | 46 |
| 650 | 22.87 | 12.65 | 0.2861 | 3.750 | 2.861 | 3.8 | 95.0 | 21.74 | 293.6 ± 1.8 | 76 |
| 650 | 24.00 | 12.42 | 42.73 | 4.670 | 3.094 | 4.9 | 94.1 | 22.59 | 304.2 ± 1.4 | 44 |
| 700 | 24.03 | 12.09 | 0.4665 | 2.565 | 2.982 | 5.9 | 96.7 | 23.25 | 312.3 ± 2.9 | 6 |
| 700 | 25.10 | 12.48 | 13.19 | 5.257 | 3.205 | 7.0 | 93.7 | 23.52 | 315.7 ± 2.2 | 51 |
| 750 | 25.23 | 12.95 | 40.46 | 2.586 | 3.033 | 8.0 | 96.9 | 24.43 | 326.9 ± 2.4 | 121 |
| 750 | 25.75 | 12.30 | 0.3925 | 4.620 | 3.552 | 9.2 | 94.6 | 24.35 | 325.9 ± 2.7 | 28 |
| 800 | 25.37 | 12.76 | 34.44 | 2.914 | 3.473 | 10.4 | 96.5 | 24.49 | 327.5 ± 1.9 | 95 |
| 800 | 25.87 | 12.35 | 0.3192 | 3.638 | 4.376 | 11.8 | 95.7 | 24.77 | 331.0 ± 2.4 | 38 |
| 850 | 25.16 | 12.63 | 50.19 | 2.239 | 4.284 | 13.3 | 97.3 | 24.48 | 327.4 ± 2.2 | 78 |
| 850 | 25.60 | 12.42 | 0.3474 | 2.174 | 5.749 | 15.2 | 97.4 | 24.94 | 333.1 ± 2.0 | 51 |
| 900 | 25.54 | 12.22 | 10.40 | 2.600 | 5.376 | 17.0 | 96.9 | 24.74 | 330.6 ± 2.2 | 23 |
| 900 | 25.72 | 12.43 | 64.63 | 2.461 | 7.608 | 19.6 | 97.1 | 24.97 | 333.4 ± 1.8 | 51 |
| 950 | 25.40 | 12.47 | 12.11 | 1.888 | 6.890 | 21.9 | 97.7 | 24.82 | 331.6 ± 2.2 | 58 |
| 950 | 25.70 | 12.47 | 42.21 | 1.877 | 10.37 | 25.4 | 97.7 | 25.12 | 335.3 ± 1.0 | 59 |
| 950 | 26.17 | 12.54 | 5.897 | 3.400 | 11.78 | 29.4 | 96.1 | 25.13 | 335.4 ± 1.4 | 63 |
| 1000 | 25.97 | 12.67 | 61.40 | 2.675 | 5.375 | 31.2 | 96.9 | 25.15 | 335.6 ± 2.4 | 82 |
| 1000 | 26.05 | 12.43 | 40.00 | 2.144 | 8.573 | 34.1 | 97.5 | 25.38 | 338.4 ± 1.3 | 53 |
| 1050 | 25.90 | 12.57 | 16.32 | 2.136 | 7.248 | 36.5 | 97.5 | 25.24 | 336.7 ± 1.6 | 70 |
| 1050 | 26.15 | 12.52 | 0.1430 | 3.052 | 9.868 | 39.8 | 96.4 | 25.21 | 336.4 ± 1.3 | 61 |
| 1050 | 26.73 | 12.83 | 0.1876 | 5.017 | 10.75 | 43.5 | 94.4 | 25.23 | 336.6 ± 1.3 | 98 |
| 1100 | 26.02 | 12.88 | 94.82 | 4.112 | 4.908 | 45.1 | 95.2 | 24.78 | 331.1 ± 2.1 | 107 |
| 1100 | 26.39 | 12.84 | 0.1693 | 4.070 | 8.359 | 47.9 | 95.3 | 25.17 | 335.8 ± 1.4 | 102 |
| 1100 | 26.77 | 12.93 | 20.02 | 5.939 | 12.03 | 52.0 | 93.3 | 24.98 | 333.5 ± 2.3 | 108 |
| 1100 | 27.37 | 12.93 | 9.372 | 8.204 | 14.81 | 57.0 | 91.0 | 24.91 | 332.7 ± 1.0 | 103 |
| 1100 | 28.22 | 12.94 | 1.715 | 11.10 | 15.53 | 62.2 | 88.3 | 24.92 | 332.7 ± 1.0 | 97 |
| 1100 | 29.11 | 13.12 | 24.00 | 14.06 | 16.72 | 67.9 | 85.6 | 24.93 | 332.9 ± 1.1 | 114 |
| 1100 | 30.77 | 13.03 | 0.1288 | 19.79 | 15.95 | 73.2 | 80.9 | 24.90 | 332.5 ± 1.2 | 88 |
| 1100 | 34.38 | 13.23 | 4.014 | 32.30 | 20.65 | 80.2 | 72.2 | 24.80 | 331.4 ± 1.5 | 82 |
| 1200 | 26.59 | 12.93 | 0.1585 | 6.859 | 9.190 | 83.3 | 92.3 | 24.54 | 328.2 ± 1.1 | 107 |
| 1230 | 27.03 | 12.95 | 15.70 | 7.617 | 11.44 | 87.1 | 91.6 | 24.75 | 330.7 ± 1.2 | 107 |
| 1260 | 26.97 | 12.88 | 33.74 | 7.456 | 12.82 | 91.5 | 91.7 | 24.73 | 330.5 ± 1.5 | 98 |
| 1290 | 26.91 | 12.82 | 9.968 | 6.771 | 12.57 | 95.7 | 92.5 | 24.88 | 332.2 ± 1.0 | 92 |
| 1320 | 27.26 | 12.76 | 0.224 | 8.792 | 9.298 | 98.8 | 90.4 | 24.64 | 329.4 ± 1.5 | 78 |
| 1350 | 31.61 | 13.84 | 1.302 | 20.14 | 2.742 | 99.8 | 81.1 | 25.63 | 341.4 ± 6.3 | 194 |
| 1450 | 95.60 | 18.93 | 508.6 | 240.3 | 0.7320 | 100.0 | 25.7 | 24.59 | 328.8 ± 37 | 322 |
| *Totals* | | | | | 296.7 | | | 24.69 | 330.0 ± 1.7 | |

Conventional K/Ar age = 334.3 ± 3.5 Ma

$\lambda_e = 5.543 \times 10^{-10}\ a^{-1}$

Fluence monitor, GA1550 Biotite, $^{40}Ar^*/^{39}Ar_K = 6.924$

**Table B.13** *$^{40}Ar/^{39}Ar$ Step Heating Data – K-feldspar, sample MP4*

| Temp (°C) | $^{40}Ar/^{39}Ar$ | $^{38}Ar/^{39}Ar$ ($10^{-2}$) | $^{37}Ar/^{39}Ar$ ($10^{-4}$) | $^{36}Ar/^{39}Ar$ ($10^{-3}$) | $^{39}Ar$ (mol) ($10^{-15}$) | Cumulative $^{39}Ar$ (%) | $^{40}Ar^*$ (%) | $^{40}Ar^*/^{39}Ar_K$ | Calculated Age (Ma) ± 1 s.d. | Cl/K ($10^{-5}$) |
|---|---|---|---|---|---|---|---|---|---|---|
| **MP4, K-feldspar, 1.17 mg, J = 0.008120** | | | | | | | | | | |
| 450 | 357.7 | 172.0 | 966.5 | 208.6 | 0.3458 | 0.1 | 82.8 | 295.0 | 2209.5 ± 9.5 | 20800 |
| 450 | 104.3 | 26.78 | 195.3 | 244.3 | 0.1901 | 0.2 | 30.7 | 32.04 | 417.2 ± 37 | 1360 |
| 500 | 63.14 | 26.92 | 476.1 | 63.16 | 0.4031 | 0.3 | 70.4 | 44.45 | 556.0 ± 7.9 | 1830 |
| 500 | 41.62 | 18.73 | 151.1 | 49.70 | 0.5658 | 0.5 | 64.7 | 26.91 | 356.5 ± 4.2 | 772 |
| 550 | 40.69 | 20.96 | 178.7 | 27.44 | 0.9889 | 0.8 | 80.0 | 32.56 | 423.1 ± 4.5 | 1130 |
| 550 | 28.88 | 15.61 | 0.4802 | 14.26 | 1.240 | 1.2 | 85.3 | 24.63 | 329.0 ± 3.8 | 445 |
| 600 | 30.36 | 16.37 | 17.14 | 11.89 | 2.069 | 1.9 | 88.3 | 26.82 | 355.4 ± 2.3 | 552 |
| 600 | 25.68 | 13.82 | 0.2385 | 6.134 | 2.501 | 2.7 | 92.8 | 23.84 | 319.2 ± 1.9 | 227 |
| 650 | 28.99 | 15.75 | 56.19 | 6.433 | 3.743 | 3.9 | 93.4 | 27.06 | 358.4 ± 1.4 | 484 |
| 650 | 25.40 | 12.66 | 7.583 | 3.967 | 4.174 | 5.3 | 95.3 | 24.21 | 323.8 ± 1.0 | 78 |
| 700 | 27.86 | 14.33 | 87.17 | 3.309 | 5.464 | 7.1 | 96.4 | 26.84 | 355.7 ± 1.5 | 302 |
| 700 | 25.22 | 12.62 | 0.1763 | 3.124 | 5.758 | 9.0 | 96.2 | 24.27 | 324.5 ± 1.7 | 76 |
| 750 | 27.33 | 14.33 | 40.31 | 3.502 | 6.060 | 10.9 | 96.1 | 26.27 | 348.8 ± 1.8 | 302 |
| 750 | 25.44 | 12.70 | 17.42 | 3.406 | 6.148 | 12.9 | 95.9 | 24.41 | 326.2 ± 1.8 | 85 |
| 800 | 27.14 | 14.18 | 23.36 | 3.116 | 5.911 | 14.9 | 96.5 | 26.19 | 347.8 ± 1.3 | 283 |
| 800 | 25.55 | 12.54 | 17.02 | 3.097 | 6.410 | 17.0 | 96.3 | 24.61 | 328.7 ± 1.4 | 65 |
| 850 | 26.72 | 13.45 | 40.75 | 3.208 | 5.651 | 18.8 | 96.4 | 25.74 | 342.4 ± 1.6 | 186 |
| 850 | 25.81 | 12.37 | 27.10 | 3.606 | 6.594 | 21.0 | 95.8 | 24.71 | 329.9 ± 1.6 | 41 |
| 900 | 26.09 | 12.92 | 0.2658 | 2.244 | 5.481 | 22.7 | 97.4 | 25.39 | 338.2 ± 1.6 | 118 |
| 900 | 26.07 | 12.69 | 62.93 | 3.251 | 6.884 | 25.0 | 96.2 | 25.09 | 334.5 ± 1.6 | 84 |
| 950 | 26.50 | 13.13 | 67.72 | 2.000 | 5.471 | 26.8 | 97.7 | 25.89 | 344.2 ± 2.6 | 146 |
| 950 | 26.75 | 12.88 | 3.413 | 3.450 | 7.134 | 29.1 | 96.1 | 25.70 | 342.0 ± 1.4 | 109 |
| 950 | 27.88 | 13.22 | 30.07 | 5.513 | 7.700 | 31.6 | 94.1 | 26.23 | 348.3 ± 1.2 | 148 |
| 1000 | 27.96 | 13.64 | 96.82 | 3.677 | 3.337 | 32.7 | 96.0 | 26.85 | 355.8 ± 2.5 | 209 |
| 1000 | 28.33 | 13.87 | 38.30 | 4.344 | 5.347 | 34.4 | 95.4 | 27.03 | 358.0 ± 1.4 | 238 |
| 1050 | 28.96 | 14.76 | 21.37 | 4.183 | 4.810 | 36.0 | 95.6 | 27.69 | 365.9 ± 2.0 | 357 |
| 1050 | 29.40 | 14.61 | 25.50 | 4.983 | 7.058 | 38.3 | 94.9 | 27.91 | 368.5 ± 2.1 | 335 |
| 1050 | 31.14 | 15.07 | 4.276 | 8.156 | 8.600 | 41.1 | 92.2 | 28.70 | 377.9 ± 1.8 | 389 |
| 1100 | 32.23 | 16.57 | 22.00 | 4.059 | 8.341 | 43.8 | 96.2 | 31.01 | 405.1 ± 1.2 | 599 |
| 1100 | 31.89 | 16.30 | 54.66 | 5.601 | 14.55 | 48.6 | 94.7 | 30.22 | 395.9 ± 1.1 | 559 |
| 1100 | 32.41 | 16.57 | 23.65 | 7.745 | 21.46 | 55.6 | 92.9 | 30.10 | 394.5 ± 1.4 | 590 |
| 1100 | 33.03 | 16.76 | 14.71 | 10.25 | 23.74 | 63.3 | 90.7 | 29.97 | 393.0 ± 0.7 | 609 |
| 1100 | 34.54 | 17.25 | 4.070 | 15.81 | 17.13 | 68.9 | 86.4 | 29.84 | 391.4 ± 2.1 | 660 |
| 1100 | 38.27 | 17.14 | 34.45 | 28.00 | 11.27 | 72.6 | 78.3 | 29.97 | 392.9 ± 1.6 | 616 |
| 1100 | 41.42 | 17.27 | 9.368 | 40.40 | 10.54 | 76.0 | 71.1 | 29.46 | 386.9 ± 2.2 | 601 |
| 1100 | 48.49 | 17.70 | 2.526 | 64.54 | 14.07 | 80.6 | 60.6 | 29.38 | 386.0 ± 8.4 | 597 |
| 1200 | 31.66 | 18.24 | 48.72 | 6.849 | 9.875 | 83.9 | 93.5 | 29.61 | 388.7 ± 1.1 | 815 |
| 1230 | 31.30 | 17.95 | 27.96 | 6.584 | 15.34 | 88.9 | 93.7 | 29.33 | 385.3 ± 1.1 | 776 |
| 1260 | 30.80 | 17.46 | 23.28 | 6.561 | 15.53 | 93.9 | 93.6 | 28.85 | 379.7 ± 1.4 | 712 |
| 1290 | 30.05 | 16.11 | 0.1313 | 7.036 | 11.57 | 97.7 | 93.0 | 27.95 | 369.0 ± 1.4 | 530 |
| 1320 | 30.77 | 14.91 | 0.3562 | 13.14 | 4.267 | 99.1 | 87.3 | 26.87 | 356.0 ± 1.3 | 356 |
| 1350 | 37.69 | 16.66 | 97.34 | 34.72 | 1.465 | 99.6 | 72.7 | 27.40 | 362.4 ± 8.9 | 534 |
| 1450 | 95.11 | 21.23 | 396.6 | 225.2 | 1.310 | 100.0 | 30.0 | 28.56 | 376.2 ± 16 | 666 |
| *Totals* | | | | | 306.5 | | | 28.46 | 375.1 ± 2.0 | |

Conventional K/Ar age = 367.2 ± 2.8 Ma

$\lambda_e = 5.543 \times 10^{-10}\ a^{-1}$

Fluence monitor, GA1550 Biotite, $^{40}Ar^*/^{39}Ar_K = 6.932$

**Table B.14** *$^{40}Ar/^{39}Ar$ Step Heating Data – K-feldspar sample, MP10*

| Temp (°C) | $^{40}Ar/^{39}Ar$ | $^{38}Ar/^{39}Ar$ ($10^{-2}$) | $^{37}Ar/^{39}Ar$ ($10^{-4}$) | $^{36}Ar/^{39}Ar$ ($10^{-3}$) | $^{39}Ar$ (mol) ($10^{-15}$) | Cumulative $^{39}Ar$ (%) | $^{40}Ar^*$ (%) | $^{40}Ar^*/^{39}Ar_K$ | Calculated Age (Ma) ± 1 s.d. | Cl/K ($10^{-5}$) |
|---|---|---|---|---|---|---|---|---|---|---|
| **MP10, K-feldspar, 1.19 mg, J = 0.008109** | | | | | | | | | | |
| 450 | 189.0 | 24.34 | 1081 | 111.0 | 0.2048 | 0.1 | 82.7 | 157.2 | 1482.8 ± 40 | 1370 |
| 450 | 67.20 | 15.71 | 1132 | 120.8 | 0.2140 | 0.1 | 46.8 | 31.46 | 409.9 ± 21 | 191 |
| 500 | 43.94 | 13.22 | 375.4 | 37.94 | 0.4686 | 0.3 | 74.4 | 32.70 | 424.3 ± 11 | 68 |
| 500 | 30.80 | 12.91 | 16.01 | 24.89 | 0.8240 | 0.6 | 76.0 | 23.42 | 313.7 ± 2.1 | 59 |
| 550 | 26.68 | 12.80 | 0.4863 | 4.803 | 1.576 | 1.1 | 94.6 | 25.23 | 335.8 ± 3.7 | 95 |
| 550 | 24.37 | 12.52 | 75.06 | 4.737 | 2.434 | 2.0 | 94.2 | 22.94 | 307.8 ± 1.9 | 57 |
| 600 | 24.77 | 12.55 | 51.57 | 2.048 | 3.694 | 3.2 | 97.5 | 24.14 | 322.6 ± 1.3 | 69 |
| 600 | 24.20 | 12.42 | 13.70 | 2.223 | 4.773 | 4.8 | 97.2 | 23.52 | 314.9 ± 0.9 | 50 |
| 650 | 25.22 | 12.27 | 0.1412 | 2.166 | 5.447 | 6.7 | 97.4 | 24.56 | 327.7 ± 1.2 | 30 |
| 650 | 24.93 | 12.20 | 0.1292 | 2.846 | 5.956 | 8.7 | 96.5 | 24.07 | 321.6 ± 1.0 | 20 |
| 700 | 26.12 | 12.11 | 0.2368 | 2.069 | 5.516 | 10.6 | 97.6 | 25.48 | 338.8 ± 2.0 | 9 |
| 700 | 25.69 | 12.19 | 0.2442 | 2.203 | 5.357 | 12.4 | 97.4 | 25.00 | 333.1 ± 1.4 | 20 |
| 750 | 26.77 | 12.36 | 6.470 | 3.183 | 4.213 | 13.8 | 96.4 | 25.81 | 342.9 ± 1.7 | 41 |
| 750 | 26.09 | 12.23 | 0.3219 | 2.740 | 4.070 | 15.2 | 96.8 | 25.27 | 336.3 ± 2.4 | 24 |
| 800 | 28.39 | 12.64 | 42.89 | 3.162 | 3.085 | 16.3 | 96.6 | 27.43 | 362.3 ± 2.5 | 78 |
| 800 | 27.12 | 12.23 | 0.4034 | 5.652 | 3.252 | 17.4 | 93.7 | 25.42 | 338.1 ± 2.3 | 16 |
| 850 | 27.30 | 12.52 | 94.09 | 3.354 | 2.775 | 18.3 | 96.3 | 26.28 | 348.6 ± 4.4 | 60 |
| 850 | 27.66 | 12.69 | 221.4 | 5.863 | 3.495 | 19.5 | 93.6 | 25.90 | 344.0 ± 2.6 | 77 |
| 900 | 28.54 | 12.58 | 158.6 | 2.472 | 3.270 | 20.6 | 97.4 | 27.79 | 366.6 ± 2.6 | 71 |
| 900 | 28.81 | 12.47 | 0.4272 | 3.331 | 4.398 | 22.1 | 96.5 | 27.81 | 366.8 ± 3.0 | 55 |
| 950 | 30.10 | 12.86 | 0.4681 | 2.804 | 4.016 | 23.5 | 97.2 | 29.26 | 384.1 ± 3.0 | 107 |
| 950 | 29.55 | 13.05 | 0.3351 | 3.422 | 5.617 | 25.4 | 96.5 | 28.51 | 375.2 ± 1.9 | 131 |
| 950 | 30.69 | 13.01 | 57.92 | 5.200 | 7.113 | 27.8 | 94.9 | 29.13 | 382.6 ± 2.0 | 122 |
| 1000 | 31.60 | 13.12 | 59.53 | 3.200 | 4.475 | 29.3 | 96.9 | 30.63 | 400.2 ± 2.1 | 141 |
| 1000 | 31.50 | 13.18 | 16.02 | 3.599 | 6.796 | 31.6 | 96.5 | 30.41 | 397.6 ± 1.3 | 148 |
| 1050 | 32.33 | 13.12 | 9.767 | 2.346 | 7.842 | 34.3 | 97.8 | 31.60 | 411.6 ± 1.2 | 144 |
| 1050 | 32.82 | 13.17 | 9.746 | 2.557 | 15.33 | 39.5 | 97.6 | 32.05 | 416.8 ± 0.9 | 150 |
| 1050 | 33.75 | 13.03 | 16.94 | 3.514 | 20.14 | 46.4 | 96.8 | 32.69 | 424.2 ± 0.8 | 128 |
| 1100 | 33.91 | 13.12 | 57.43 | 2.419 | 11.79 | 50.4 | 97.8 | 33.18 | 429.9 ± 1.0 | 145 |
| 1100 | 33.67 | 12.97 | 0.07887 | 2.902 | 16.91 | 56.1 | 97.4 | 32.79 | 425.4 ± 1.1 | 122 |
| 1100 | 33.95 | 12.94 | 10.95 | 4.631 | 21.11 | 63.3 | 95.9 | 32.56 | 422.7 ± 0.9 | 114 |
| 1100 | 34.94 | 13.09 | 0.1004 | 6.733 | 19.01 | 69.8 | 94.2 | 32.92 | 426.9 ± 1.4 | 129 |
| 1100 | 36.94 | 13.16 | 0.1463 | 12.03 | 13.08 | 74.2 | 90.3 | 33.36 | 432.0 ± 1.4 | 124 |
| 1100 | 39.28 | 13.20 | 0.1626 | 18.66 | 11.82 | 78.2 | 85.9 | 33.75 | 436.4 ± 2.2 | 114 |
| 1100 | 42.45 | 13.32 | 11.93 | 28.27 | 10.51 | 81.8 | 80.3 | 34.08 | 440.2 ± 1.7 | 105 |
| 1100 | 50.16 | 13.75 | 28.46 | 52.55 | 12.64 | 86.1 | 69.0 | 34.61 | 446.3 ± 2.4 | 102 |
| 1200 | 37.07 | 12.90 | 43.35 | 4.960 | 5.063 | 87.8 | 96.0 | 35.58 | 457.4 ± 2.1 | 108 |
| 1230 | 36.01 | 12.92 | 0.1480 | 4.680 | 9.27 | 91.0 | 96.1 | 34.60 | 446.1 ± 1.1 | 112 |
| 1260 | 35.64 | 12.90 | 6.282 | 5.085 | 10.77 | 94.6 | 95.7 | 34.10 | 440.4 ± 1.5 | 106 |
| 1290 | 36.29 | 13.09 | 0.1970 | 5.090 | 9.953 | 98.0 | 95.8 | 34.76 | 448.0 ± 1.3 | 133 |
| 1320 | 37.23 | 13.26 | 0.6087 | 9.432 | 3.223 | 99.1 | 92.4 | 34.40 | 443.9 ± 3.9 | 145 |
| 1350 | 43.72 | 14.02 | 158.7 | 30.81 | 1.235 | 99.5 | 79.1 | 34.61 | 446.3 ± 17 | 192 |
| 1450 | 76.25 | 17.37 | 2.436 | 141.4 | 1.381 | 100.0 | 45.2 | 34.46 | 444.6 ± 13.4 | 362 |
| *Totals* | | | | | 294.1 | | | 31.31 | 408.2 ± 1.7 | |

Conventional K/Ar age = 388.1 ± 3.1 Ma

$\lambda_e = 5.543 \times 10^{-10}\ a^{-1}$ Fluence monitor, GA1550 Biotite, $^{40}Ar^*/^{39}Ar_K = 6.941$

**Table B.15** *$^{40}Ar/^{39}Ar$ Step Heating Data – K-feldspar sample, MP16*

| Temp (°C) | $^{40}Ar/^{39}Ar$ | $^{38}Ar/^{39}Ar$ ($10^{-2}$) | $^{37}Ar/^{39}Ar$ ($10^{-4}$) | $^{36}Ar/^{39}Ar$ ($10^{-3}$) | $^{39}Ar$ (mol) ($10^{-15}$) | Cumulative $^{39}Ar$ (%) | $^{40}Ar^*$ (%) | $^{40}Ar^*/^{39}Ar_K$ | Calculated Age (Ma) ± 1 s.d. | Cl/K ($10^{-5}$) |
|---|---|---|---|---|---|---|---|---|---|---|
| **MP16, K-feldspar, 1.68 mg, J = 0.008071** | | | | | | | | | | |
| 450 | 146.5 | 26.31 | 217.8 | 365.2 | 0.7754 | 0.3 | 26.3 | 38.50 | 488.2 ± 24 | 993 |
| 450 | 80.56 | 17.57 | 1.306 | 196.2 | 0.7450 | 0.5 | 28.0 | 22.53 | 301.4 ± 13 | 251 |
| 500 | 38.13 | 14.07 | 0.8074 | 52.50 | 1.206 | 0.9 | 59.3 | 22.61 | 302.4 ± 5.7 | 146 |
| 500 | 29.44 | 13.44 | 64.32 | 24.78 | 3.016 | 1.9 | 75.0 | 22.09 | 296.0 ± 1.4 | 130 |
| 550 | 23.21 | 12.84 | 120.2 | 5.750 | 5.537 | 3.7 | 92.6 | 21.48 | 288.4 ± 0.6 | 98 |
| 550 | 22.33 | 12.65 | 167.0 | 3.298 | 8.479 | 6.5 | 95.5 | 21.32 | 286.5 ± 0.8 | 79 |
| 600 | 21.76 | 12.58 | 399.5 | 1.632 | 9.939 | 9.8 | 97.7 | 21.26 | 285.7 ± 0.7 | 72 |
| 600 | 22.24 | 12.22 | 523.7 | 1.871 | 10.63 | 13.3 | 97.4 | 21.66 | 290.7 ± 0.6 | 25 |
| 650 | 22.66 | 12.24 | 747.6 | 1.370 | 8.238 | 16.0 | 98.1 | 22.24 | 297.8 ± 0.7 | 29 |
| 650 | 23.10 | 12.14 | 522.8 | 1.997 | 7.516 | 18.5 | 97.4 | 22.49 | 300.9 ± 0.8 | 13 |
| 700 | 23.77 | 12.28 | 399.7 | 1.515 | 5.162 | 20.2 | 98.0 | 23.31 | 311.0 ± 1.5 | 34 |
| 700 | 23.96 | 12.42 | 270.4 | 1.901 | 4.704 | 21.7 | 97.6 | 23.38 | 311.9 ± 1.5 | 52 |
| 750 | 24.53 | 12.36 | 128.7 | 3.508 | 3.241 | 22.8 | 95.7 | 23.47 | 312.9 ± 3.7 | 39 |
| 750 | 24.94 | 12.44 | 163.3 | 4.813 | 3.177 | 23.8 | 94.2 | 23.50 | 313.3 ± 2.7 | 47 |
| 800 | 25.37 | 12.82 | 176.3 | 2.936 | 2.454 | 24.6 | 96.5 | 24.48 | 325.3 ± 2.2 | 102 |
| 800 | 25.62 | 12.82 | 221.4 | 5.033 | 2.881 | 25.6 | 94.1 | 24.10 | 320.7 ± 2.3 | 97 |
| 850 | 27.10 | 12.77 | 0.8952 | 6.568 | 2.663 | 26.5 | 92.7 | 25.13 | 333.1 ± 3.6 | 86 |
| 850 | 26.75 | 12.92 | 64.79 | 3.201 | 3.101 | 27.5 | 96.4 | 25.78 | 340.9 ± 3.3 | 115 |
| 900 | 28.81 | 13.42 | 117.1 | 6.439 | 3.679 | 28.7 | 93.3 | 26.88 | 354.2 ± 2.7 | 174 |
| 900 | 28.45 | 13.61 | 116.4 | 5.996 | 4.573 | 30.2 | 93.7 | 26.65 | 351.5 ± 4.6 | 200 |
| 950 | 29.51 | 13.63 | 69.02 | 4.376 | 7.530 | 32.7 | 95.5 | 28.19 | 369.9 ± 1.5 | 205 |
| 950 | 29.54 | 13.83 | 0.2170 | 5.197 | 11.03 | 36.3 | 94.7 | 27.96 | 367.1 ± 1.2 | 231 |
| 950 | 29.88 | 14.14 | 14.95 | 5.851 | 16.48 | 41.7 | 94.1 | 28.12 | 369.0 ± 0.8 | 270 |
| 1000 | 30.11 | 14.30 | 32.22 | 4.899 | 10.70 | 45.2 | 95.1 | 28.62 | 375.0 ± 1.0 | 294 |
| 1000 | 29.62 | 14.36 | 40.46 | 5.064 | 13.36 | 49.6 | 94.9 | 28.08 | 368.5 ± 1.0 | 301 |
| 1050 | 29.78 | 14.40 | 34.27 | 4.836 | 14.25 | 54.3 | 95.1 | 28.31 | 371.3 ± 2.1 | 307 |
| 1050 | 30.01 | 14.55 | 30.80 | 4.501 | 15.66 | 59.5 | 95.5 | 28.65 | 375.2 ± 0.8 | 328 |
| 1050 | 30.77 | 14.72 | 86.36 | 5.699 | 17.60 | 65.3 | 94.4 | 29.06 | 380.1 ± 1.2 | 349 |
| 1100 | 31.03 | 14.84 | 36.82 | 4.947 | 12.86 | 69.5 | 95.2 | 29.55 | 385.8 ± 1.1 | 367 |
| 1100 | 31.18 | 14.80 | 0.1059 | 5.513 | 17.40 | 75.2 | 94.7 | 29.53 | 385.6 ± 1.0 | 359 |
| 1100 | 31.65 | 14.42 | 26.89 | 6.676 | 23.86 | 83.1 | 93.7 | 29.64 | 387.0 ± 0.7 | 306 |
| 1100 | 31.92 | 14.44 | 23.31 | 8.040 | 23.32 | 90.8 | 92.5 | 29.52 | 385.5 ± 0.9 | 306 |
| 1100 | 33.98 | 14.36 | 67.32 | 14.34 | 11.10 | 94.4 | 87.4 | 29.71 | 387.8 ± 1.9 | 279 |
| 1100 | 39.22 | 14.99 | 101.5 | 31.50 | 6.829 | 96.7 | 76.2 | 29.89 | 389.8 ± 1.9 | 320 |
| 1100 | 50.62 | 15.99 | 0.6497 | 71.11 | 4.119 | 98.0 | 58.4 | 29.59 | 386.3 ± 5.7 | 354 |
| 1100 | 77.26 | 17.69 | 95.06 | 163.5 | 3.034 | 99.0 | 37.4 | 28.92 | 378.5 ± 6.9 | 349 |
| 1200 | 34.27 | 15.29 | 1.472 | 20.12 | 1.289 | 99.4 | 82.6 | 28.29 | 371.0 ± 6.1 | 388 |
| 1230 | 34.24 | 14.63 | 1.609 | 19.34 | 1.180 | 99.8 | 83.2 | 28.49 | 373.3 ± 5.1 | 301 |
| 1260 | 48.30 | 16.81 | 385.6 | 77.21 | 0.2470 | 99.9 | 52.7 | 25.45 | 337.0 ± 43 | 448 |
| 1290 | 79.20 | 20.62 | 5214 | 234.8 | 0.1026 | 99.9 | 12.4 | 9.85 | 138.0 ± 88 | 562 |
| 1320 | 139.3 | 19.68 | 16928 | 445.5 | 0.05629 | 100.0 | 5.6 | 7.88 | 111.2 ± 257 | -90 |
| 1350 | 159.5 | 17.53 | 82.23 | 470.8 | 0.05666 | 100.0 | 12.8 | 20.38 | 274.7 ± 343 | -443 |
| 1450 | 577.8 | 91.59 | 66.58 | 1796 | 0.06992 | 100.0 | 8.1 | 46.70 | 577.0 ± 877 | 6110 |
| *Totals* | | | | | 303.8 | | | 27.17 | 357.7 ± 1.9 | |

Conventional K/Ar age = 360.1 ± 3.0 Ma

$\lambda_e = 5.543 \times 10^{-10}\ a^{-1}$ Fluence monitor, GA1550 Biotite, $^{40}Ar^*/^{39}Ar_K = 6.974$